UC San Diego

UC San Diego Electronic Theses and Dissertations

Title

Targeted Drug Delivery via Exploitation of the Tumor Microenvironment

Permalink

https://escholarship.org/uc/item/8cj741hm

Author

Callmann, Cassandra Elizabeth

Publication Date

2018

Peer reviewed|Thesis/dissertation

eScholarship.org Powered by the California Digital Library
University of California

UNIVERSITY OF CALIFORNIA, SAN DIEGO

Targeted Drug Delivery *via* Exploitation of the Tumor Microenvironment

A dissertation submitted in partial satisfaction of the
requirements for the degree Doctor of Philosophy

in

Chemistry

by

Cassandra Elizabeth Callmann

Committee in charge:

Professor Nathan C. Gianneschi, Chair
Professor Michael D. Burkart, Co-Chair
Professor Neal K. Devaraj
Professor Robert F. Mattrey
Professor Charles L. Perrin

2018

Copyright

Cassandra Elizabeth Callmann, 2018

All rights reserved.

The Dissertation of Cassandra Elizabeth Callmann is approved, and it is acceptable in quality and form for publication on microfilm and electronically:

_____

_____

_____

_____
Co-Chair

_____
Chair

University of California, San Diego

2018

Dedication

To the mice.

Epigraph

“Trust me, I’m (almost) a doctor!”

Table of Contents

List of Abbreviations

A	alanine
ABX	Abraxane®
Au	Gold
BD	biodistribution
BMDCs	bone marrow derived dendritic cells
Ca	Calcium
CAMs	cell adhesion molecules
CRS	cytokine release syndrome
D	aspartic acid
DCM	dichloromethane
DLS	dynamic light scattering
DPBS	Dulbecco's Phosphate Buffered Saline (no Ca, no Mg)
E	glutamic acid
ECM	extracellular matrix
EDAPT	Enzyme-Directed Assembly of Particle Therapeutics
EPR	enhanced permeability and retention
FRET	Förster Resonance Energy Transfer
G	glycine
Gd	gadolinium
HSA	human serum albumin
HSI	Hue-Saturation-Intensity
HPLC	high pressure liquid chromatography
IL-6	interleukin 6

Immuno-EDAPT	immunotherapeutic-based enzyme responsive nanomaterials
IP-10	interferon gamma-induced protein 10
IT	intratumoral
IV	intravenous
IQR	interquartile range
IRAEs	immune related adverse effects
keV	kiloelectron volts
K_d	dissociation constant
kD	kilodalton
L	leucine
ʎ	wavelength
M	Molar
mab	monoclonal antibody
MCP-1	monocyte chemoattractant protein 1
MDR	multidrug resistance
Mg	Magnesium
µ	micro
MMP	matrix metalloproteinase
MS	mass spectrometry
MSA	murine serum albumin
MT1-MMP	membrane type-1 MMP
MWCO	molecular weight cutoff
NanoSIMS	nanoscale secondary ion mass spectrometry
NIR	near-infrared
n	nano
NP	nanoparticle

ODDA	octadecanedioic acid
P	proline
PBS	phosphate buffered saline
PBSt	PBS with 0.05% Tween 20
PD1	prodrug-1
PD1C	prodrug-1 control
PEG	polyethylene gylcol
PF1	profluorophore-1
PF1C	profluorophore-1 control
Pgp	P-glycoprotein
Ph	phenyl
PK	pharmacokinetics
PPA	peptide-polymer amphiphile
PS	peptide substrate
PSC	peptide substrate control
Pt	Platinum
Pt-EDAPT	Platinum(II)-based enzyme responsive nanomaterials
PTX	paclitaxel
PTX-EDAPT	paclitaxel-based enzyme responsive nanomaterials
q7dx4	injections once every 7 days, for 4 total injections
R	arginine
RAFT	reversible addition-fragmentation chain transfer
ROI	region of interest
ROMP	ring opening metathesis polymerization
ROS	reactive oxygen species
R_f	retention factor

RP-HPLC	reverse-phase HPLC
SE	standard error
SEC-MALS	size exclusion chromatography, multi angle light scattering
SEM	standard error of the mean
SIM	Structural Illumination Microscopy
SLS	static light scattering
SPARC	secreted protein acidic and rich in cysteine
TLC	thin layer chromatography
TI	therapeutic index
TME	tumor microenvironment
VEGF	vascular endothelial growth factors

List of Figures

List of Tables

Acknowledgements

This thesis work, and indeed my graduate career, would have never been possible without the help and support that I have been extremely fortunate to have received from my amazing family, friends, and colleagues. As such, the list of people I need to thank is long.

First and foremost, I sincerely thank my advisor, **Professor Nathan Gianneschi**. It has been quite an exciting adventure since he first took me on as a graduate student at UCSD in 2012. You will see many of the results of our work together in the thesis herein, but that only scratches the surface. Nathan has taught me how to think like a scientist and how to craft a well-written document, whether it be a grant application or a response to reviewers. He has given me the opportunity to travel the world to engage with others about science, from San Francisco, to Italy, to Washington D.C., to Switzerland, and to several other beautiful places along the way, including a ~6 month stint in Chicago at the end of my graduate studies. He has fully supported me at all points along this path, and I am proud to say that I consider him not only a mentor, but also a friend.

One of the coolest things about joining Nathan's group when I did is that I have had the opportunity to get to know nearly everyone who has been a member of our lab so far. Research doesn't happen in a bubble, and I am grateful for the insight and diverse backgrounds of the members I've had the chance to work alongside. The list of people is too long to fit into one acknowledgements section (I have personally shared the lab with 66 group members in total!), so I want to generally thank all the Gianneschi Group members, past and present. Together, we have done some great work, and I look forward to seeing what the future brings, not only for our lab, but for our careers, as well.

I want to especially thank the following colleagues who have made life in graduate school fun and without whom I would have floundered: **Andrea Carlini**, for her absolutely

unwavering friendship throughout grad school. We met on one of the very first days of orientation at UCSD, and have been best friends pretty much ever since – love you, girl. **Christopher Barback**, for teaching me everything I know about *in vivo* work, and for continuously being there for technical (and often emotional!) support; also, for keeping me company on nights and weekends, and sometimes even on holidays, in the vivarium. **Rob Hennis**, for teaching *me* how to be a mentor, and for always coming into work with an air of positivity and enthusiasm. **Dr. Matthew Thompson**, for working directly with me from my very first day in the lab straight through to now, and for being a constant source of scientific insight, profound conversations, and 90s music. **Dr. Swagat Sahu**, for being the first person in the lab to be actually friendly to me – without him, I may not have joined our group. **Dr. Angela Blum**, for teaching me to how critically evaluate science, and for her friendship, mentorship, and fellow love of dogs. **Dr. Gina Policastro**, for being someone I could always rely on not only for scientific discussions, but also for great conversations and laughs. **Dr. Maria Proetto**, for being my lab vecina for the first 4 years of grad school and a wonderful international travel partner. **Nanzhi Zang**, **Mollie Touve**, and **Dr. Daniel Wright**, for our colorful office conversations at Northwestern, which kept me positive even when I didn't want to be. **Dr. Christopher Forman**, for being an absolutely superb roommate in Evanston (along with Andrea, we three are THE Judson Jokers). **Dr. Clare LeGuyader**, for her refreshing and pragmatic views on science and the world in general. **Dr. Julia Michaelis** and **Dr. Alex Roloff**, for being the coolest Germans I know.

I want to also thank my family, including my parents, **Maurine and Luther Callmann**, and my little brother, **Austin Callmann**, for being my biggest cheerleaders and for nurturing my curiosity about the world around me from a young age. Without them, I would not be where I am today.

Grad school can be incredibly demanding, and so I thank the members of **Capoeira Luanda San Diego** and **Capoeira Brasil Chicago** for providing me with a positive outlet for my stress, as well as a diverse network of wonderful people. *Se berimbau toca, tu me chama***…**

Most importantly, I need to thank my fiancé, **Raymond Hartnedy**, for joining me on this incredible journey and for supporting me throughout the highs and lows of my graduate career. He may not understand all the science jargon I throw at him, but he always takes a genuine interest in what I'm doing, which is, perhaps, the most important thing of all. And, of course, special thanks to **Cinnabear** and **Oso** for all their cuddles, kisses, and unconditional love, especially during the dissertation writing process (who's a good boy?).

And now for the necessary acknowledgements to my co-authors:

Chapter 1.2 is adapted, in part, from material currently being prepared for submission for publication. Callmann, Cassandra; Thompson, Matthew; and Nathan Gianneschi. The dissertation author is the primary author of this pending manuscript.

Chapter 2.2 is adapted, in part, from material as it appears in Advanced Materials 2015. Callmann, Cassandra; Barback, Christopher.; Thompson, Matthew; Hall, David; Mattrey, Robert; and Nathan Gianneschi. The dissertation author was the primary author of this paper.

Chapter 2.3 is adapted, in part, from material currently being prepared for submission for publication. Proetto, Maria; Callmann, Cassandra; Cliff, John; Szymanski, Craig; Hu, Dehong; Howell, Stephen; Evans, James; Orr, Galya; and Nathan Gianneschi. The dissertation author is a contributing author of this pending manuscript.

Chapter 3 is adapted, in part, from material currently being prepared as a revised manuscript for resubmission for publication. Callmann, Cassandra; Thompson, Matthew; Yao, Shiyin; Hayashi, Tomoko; Carson, Dennis; and Nathan Gianneschi. The dissertation author is the primary author of this pending manuscript.

Chapter 4 is adapted, in part, from material as it appears in Chemical Communications 2016. Daniel, Kevin; Callmann, Cassandra; Gianneschi, Nathan; and Seth Cohen. The dissertation author is co-first author of this paper.

Chapter 5 is adapted, in part, from material currently being prepared for submission for publication. Callmann, Cassandra; Thompson, Matthew; Barback, Christopher; LeGuyader, Clare; Hennis, Robert; Henrickson, Niel; Jeremko, Matthew; Chan, Warren; Momper, Jeremiah; Bertin, Paul; and Nathan Gianneschi. The dissertation is the primary author of this pending manuscript.

Vita

2012 Bachelor of Science, Biochemistry
West Chester University

2014 Master of Science, Chemistry
University of California, San Diego

2018 Doctor of Philosophy, Chemistry
University of California, San Diego

Publications

Callmann, C.E., Gianneschi, N.C., et al. "A Paclitaxel-Octadecanedioic Acid Ester for Albumin-Mediated Delivery to Tumors." *Manuscript in preparation.*

Callmann, C.E., Thompson, M.P., and Gianneschi, N.C. "The Chemistry and Biology of Peptide Brush Polymers." *Accounts of Chemical Research; Invited contribution, manuscript in preparation.*

Callmann, C.E., Thompson, M.P., Yao, S., Hayashi, T., Carson, D.A., and Gianneschi, N.C. "Immunotherapeutic Enzyme-Responsive Nanomaterials Inhibit Lung Metastasis in a Orthotopic Syngeneic Breast Cancer Model." *In revision*.

Proetto, M.P., **Callmann, C.E.**, Cliff, J., Szymanski, C.J., Hu, D., Evans, J.E.; Orr, G., Howell, S.B., and Gianneschi, N.C. "Nanoscaled Multimodal Imaging of Targeted Enzyme-Responsive Pt(II)-loaded Nanoparticles." *Manuscript in preparation*.

Rolloff, A., Carlini, A.S., **Callmann, C.E.**, and Gianneschi, N.C. "Micellar Thrombin-Binding Aptamers: Reversible Nanoscale Anticoagulants." *Journal of the American Chemical Society; 2017,* 139, 16442–16445.

Callmann, C.E. and Gianneschi, N.C. "Enzyme-Responsive Nanoparticles for the Treatment of Disease." *Methods in Molecular Biology*; *2017*, 1570, 223-238.

Daniel, K.B.*, **Callmann, C.E.***, Cohen, S.M., and Gianneschi, N.C. "Enzyme-Responsive Nanoparticles Release Cargo Upon Exposure to Matrix Metalloproteinase and Reactive Oxygen Species." *Chemical Communications; 2016*, 52, 2126-2128.

Callmann, C.E., Barback, C.V., Thompson, M.P., Hall, D.J., Mattrey, R.F., and Gianneschi, N.C. "Therapeutic Enzyme-Responsive Nanoparticles for Targeted Delivery and Accumulation in Tumors." *Advanced Materials; 2015*, 27, 4611–4615.

Blum, A. P., Kammeyer, J. K.*, Rush, A. M.*, **Callmann, C. E.,** Hahn, M. E., and Gianneschi, N. C. “Stimuli-Responsive Nanomaterials for Biomedical Applications.” *Journal of the American Chemical Society; 2014,* 137, 2140-2154.

* = equal contribution

Patents

Callmann, C.E., Thompson, M.T., Gianneschi, N.C., LeGuyader, C.L., Bertin, P.A. “Modified Cytotoxins and Their Therapeutic Use.” Publication No. 20170080094. Filed September 21, 2015. Published March 23, 2017.

LeGuyader, C.L., Thompson, M.T., **Callmann, C.E.**, Ditri, T., Bertin, P.A., Gianneschi, N.C. “Modified MRI Contast Agents and Uses Thereof.” Application No. US62/491159. Filed April 2017.

ABSTRACT OF THE DISSERTATION

Targeted Drug Delivery *via* Exploitation of the Tumor Microenvironment

by

Cassandra Elizabeth Callmann

Doctor of Philosophy

University of California, San Diego, 2018

Professor Nathan C. Gianneschi, Chair
Professor Michael D. Burkart, Co-Chair

Targeted therapeutics should accumulate at disease sites in higher quantities relative to other locations in the body. In cancer therapy, one strategy towards this is to exploit features of the tumor microenvironment (TME) for drug delivery. Herein, drug delivery strategies focusing on the TME are investigated.

First, nanomaterials designed to respond to matrix metalloproteinases (MMPs) are explored for delivery of cytotoxins to tumors. Ring opening metathesis polymerization (ROMP) is employed to generate amphiphilic diblock copolymers containing paclitaxel (PTX) prodrugs and MMP-responsive peptides. These polymers form 20 nm nanoparticles that rearrange to microscale aggregates upon MMP exposure. This process is observed and efficacy evaluated in a fibrosarcoma xenograft model. Critically, these materials have equivalent efficacy to PTX at equivalent doses, but with a 16-fold higher maximum tolerated dose (MTD). Further,

nanoparticles containing an MMP-responsive peptide together with platinum (Pt) drugs, ^{15}N-labelled moieties, and near infrared (NIR) fluorophores are developed. These materials are evaluated for their therapeutic efficacy *in vivo* and the simultaneous, yet independent, tracking of carrier and drug is completed *ex vivo* using correlative microscopy techniques.

This platform is then extended to the delivery of immunotherapeutics. MMP-responsive nanoparticles containing an immunotherapeutic compound (1V209) are developed and assessed *in vitro* for immunogenicity and *in vivo* for efficacy. In a syngeneic orthotopic breast cancer model, 1V209-containing nanoparticles do not cause nonspecific cytokine upregulation and significantly inhibit lung metastasis formation relative to 1V209, non-responsive nanoparticles, and saline.

Dual-responsive nanomaterials are also explored that are designed to respond to two separate features of the TME. Polymers and nanoparticles are designed to release cargo only when both MMPs and reactive oxygen species (ROS) are present.

Finally, a biomaterial-based delivery strategy is explored using human serum albumin (HSA) as a drug carrier of long chain fatty acids (LCFAs) to the TME. Mono-functionalizing octadecanedioic acid (ODDA) with PTX affords a fatty acid-PTX ester prodrug that retains one carboxylic acid moiety to form stable electrostatic interactions with HSA in its natural binding sites for LCFAs. This prodrug is capable of binding to HSA and shows differentiated pharmacokinetics, as well as remarkable tolerability and efficacy *in vivo*, relative to clinical formulations in multiple xenograft models.

Chapter 1

Introduction

1.1 Drug Delivery and The Tumor Microenvironment (TME)

1.1.1 The Quest for the Magic Bullet

Paul Ehrlich is considered by many to be the father of chemotherapy[1-2], and first envisioned the concept of a "magic bullet" for cancer therapy in the early 1900s[3], whereby drugs are designed to go straight to their intended targets upon administration without harming other tissues[2, 4-5]. Over 100 years after it was first postulated, this concept is still far from realized. This is largely because there is no true magic bullet for cancer therapy, as tumors are a complex collection of both malignant and non-transformed cells[6] that leave few completely unique targets to lock onto, as many of the features of cancerous tissue also appear in other parts of the body. Thus, the challenge lies in sufficiently targeting the tumor site while avoiding significant off-target accumulation of potent cancer therapeutics.

In place of the all-elusive magic bullet, researchers have instead focused their efforts on exploiting features of the tumor microenvironment (TME) to preferentially localize therapeutic cargo at the site of interest. Some cases, such as the antibody-based therapeutics trastuzumab and bevacuzimab (discussed in more detail in Chapter 1.1.4), come *close* to Ehrlich's magic bullet, but are still limited by off-target toxicities[7-9]. Thus, one of the main aims

of modern chemotherapy has been to expand the therapeutic index (TI) of treatments through clever TME targeting strategies[10]. The TI is defined as the ratio of the toxic dose of a drug to that of the effective dose[11], and when the TI is small, dosing becomes challenging as there is a fine line between the dose that can be safely administered without toxicity and the dose that will have a significant therapeutic effect. By designing chemotherapeutics to target features of the TME while also shielding the drug from the body and the body from the drug, the effect on TI can be two-fold: firstly, limiting drug exposure to off-target organs may increase the dose necessary to observe toxicity; secondly, increasing the on-target accumulation may decrease the amount of drug that needs to be administered in the first place. Therefore, the key is to identify features of the TME that can be targeted with much greater specificity than other parts of the body, thus preventing drug accumulation in off-target sites.

1.1.2 Introduction to Targets within the TME

Tumors are composed not only of malignant cells, but also of non-transformed cells, blood vessels, and a complex milieu of enzymes and other proteins in the extracellular matrix (ECM) (**Figure 1.1.2**)[6, 12]. Together, these biomaterials compose an organ-like mass that has its own set of features that provide appealing targets for chemotherapeutics. Further, a hallmark of many cancers is a dysregulated metabolism due to unrestricted cellular proliferation[13] that is not proportional to nutrient availability, which means that it may be possible to hijack biomaterials utilized in metabolic processes to deliver therapeutic payloads (discussed in more detail in **Chapter 1.3**). There are several features of the TME that researchers have sought to exploit for therapeutic targeting purposes that will be introduced in this chapter, including endothelial cells and receptors[14-16], cell surface receptors[17-19], extracellular proteases[20-22], pH gradients (both global and intracellular)[23-25], redox environments and upregulation of reactive oxygen species (ROS)[26-28], and the enhanced

permeability and retention (EPR) effect[29-30]. The dissertation herein utilizes two different features of the TME to accumulate drug cargo within the tumor space – matrix metalloproteinases (MMPs) in **Chapters 2-4**, and human serum albumin (HSA) transport mechanism and features in **Chapter 5**.

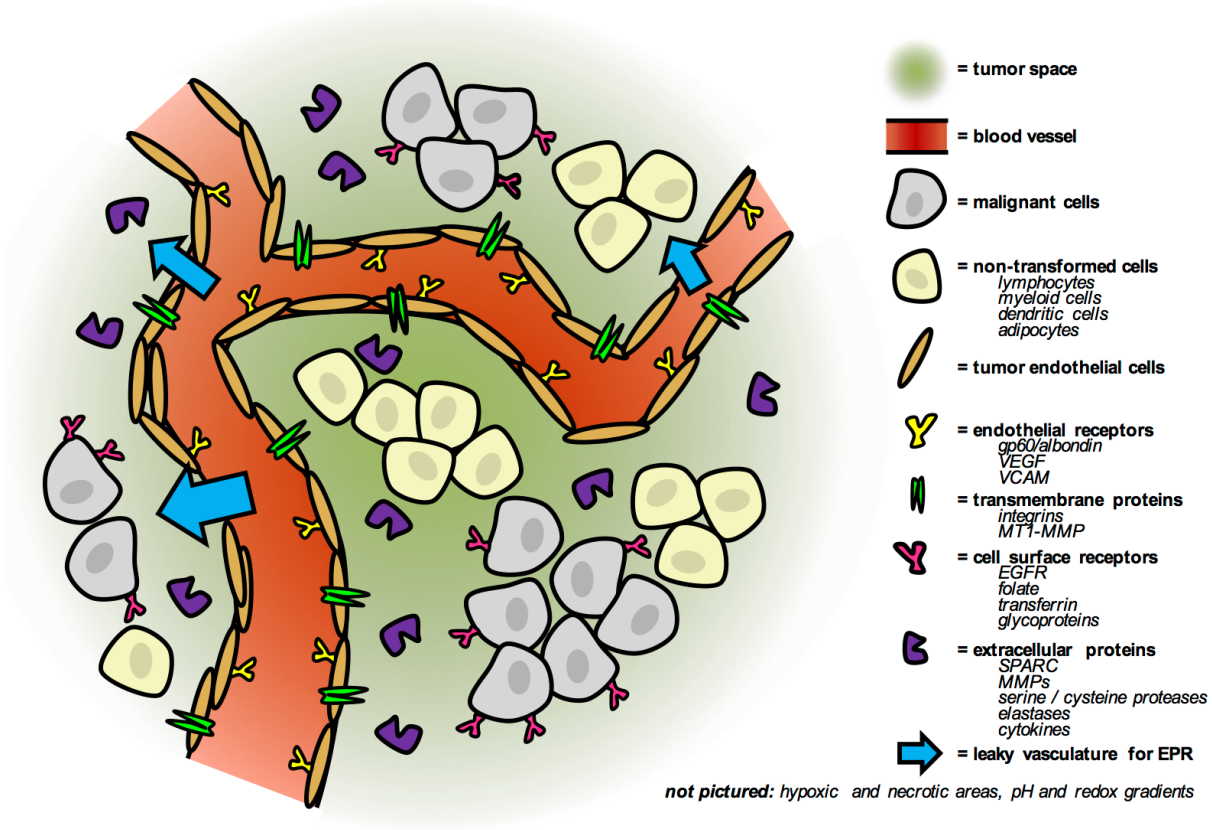

Figure 1.1.1. Components of the tumor microenvironment. The TME contains a wide variety of cells, proteins, and other biological components that form a complex, organ-like mass. Some examples of TME components are depicted above, and described in more detail the sections that follow. The dissertation work utilizes features of the TME to preferentially deliver therapeutic cargo to tumors; specifically, extracellular MMPs (**Chapters 2-4**) and HSA-based transport (**Chapter 5**).

1.1.3 Tumor Endothelium

Tumor endothelial receptors are one class of targets for infiltrating the TME. Tumor endothelial cells line the wall between blood vessels and the tumor ECM[31], and have roles in angiogenesis and tumor infiltration and metastasis[6]. As such, these cell populations have been

of interest in the field of targeted drug delivery, as it is possible to directly bind endothelial cell surface receptors directly following intravenous (IV) administration[12]. Further, many tumor endothelial receptors have been shown to be ubiquitous across a range of cancer types[12]. However, the efficacy of ligand binding to tumor endothelial receptors is inherently dependent upon the K_d between ligand and receptor, as it must be high enough for ligand to bind its intended target before being swept away in the bloodstream.

Examples of tumor endothelial cell receptors and transmembrane proteins that are highly upregulated include gp60/albondin[32-33], vascular endothelial growth factor (VEGF) receptors[34-35], endothelial cell adhesion molecules (CAMs)[36], integrins[15, 37-38], and membrane type-1 matrix metalloproteinase (MT1-MMP)[39-40]. The gp60 receptor will be discussed in more detail in **Chapter 1.3**, but it is an endothelial receptor for human serum albumin (HSA), and Abraxane® is an FDA approved "nanoparticle" composed of HSA paclitaxel (PTX) that has been proposed to enter the tumor space, in part, through transcytosis *via* the gp60 receptor[41-42]. Avastin®, or bevacuzimab, is an FDA approved monoclonal antibody (mab) designed to bind high affinity VEGF receptors, including VEGFR-1 and VEGF-R1[43]. It is used as a first-line treatment of colorectal cancer as a combination therapy with chemotherapeutics, and works by preventing angiogenesis[44]. Vascular cell adhesion molecule-1 (VCAM-1) is a type of CAM that is upregulated in multiple cancers[45] and has been proposed as a target for antibody therapy[46] in preventing metastasis. Another common endothelial target is the αvβ3 integrin[47], which also plays a role in tumor angiogenesis and is highly overexpressed on cancer endothelial cells[48]. Etaracizumab is a mab currently in clinical trials as an angiogenesis inhibitor that targets αvβ3[49-50]. Beyond antibody therapy, the cyclic RGD peptide has been an attractive target as an antagonist of αvβ3 integrin[48, 51] and indeed a cyclic RGD pentapeptide is currently in Phase III for glioblastomas[52]. Finally, MT1-MMP is part of the MMP family (discussed in more detail in **Chapter 1.2**) and is overexpressed on the tumor endothelium[46]. Peptide-based

inhibitors of MT1-MMP[53] have shown promise in reducing tumor growth *in vivo*[54], though high doses were necessary for efficacy.

1.1.4 Tumor Cell Surface Receptors

An alternate strategy for targeting material within the TME are overexpressed cell surface receptors. A major benefit of this strategy is direct cell killing upon internalization[12], thus nearly guaranteeing a 1:1 targeting:outcome ratio. However, targeting and cellular internalization relies on overexpression of surface receptors on cancer cells, and as is the case with endothelial receptor targeting, the efficiency also relies on the K_d between ligand and receptor.

Examples of cell surface receptors and transmembrane proteins that are highly upregulated on tumor cells within the TME include epidermal growth factor receptors (EGFRs)[55-57], folate receptors[58-59], transferrin receptors[18, 60-61], and certain glycoproteins[62-65]. There has been much clinical success with EGFR-based targeting, as evidenced by three FDA approved EGFR therapeutics, Herceptin® (trastuzumab), Erbitux® (cetuximab) and Iressa® (gefitinib) developed to inhibit multiple members of the EGFR family[66], including HER-2. The folate receptor is an interesting target for chemotherapy, as internalization of cargo through this mechanism retains material within endosomes for direct cytosolic delivery, rather than lysosome-mediated entry, due to the nature of folic acid uptake by cells[58]. Methotrexate is a notorious chemotherapeutic that acts as an antifolate[67]. The transferrin receptor is upregulated on many tumor types, and has thus been an attractive target for receptor-binding molecules including antibodies and peptides[60]. In terms of glycoproteins, P-glycoprotein (Pgp) has been implicated in affording multidrug resistance (MDR) to cancer cells, making it an attractive target for inhibitors[63]. Further, lectin-functionalized nanoparticles[68] have shown promise in targeting materials for cellular internalization in tumor tissues.

1.1.5 Extracellular Proteins

Extracellular proteases and other proteins in the ECM provide an attractive target within the TME. Advantage of targeting the ECM include a localization of material within the tumor interstitium for prolonged release and retention, and there is no need for direct cellular internalization for cargo to be delivered. However, as with targeting tumor cell surfaces, therapeutics designed to interact with extracellular proteins in the TME still need to penetrate the tumor endothelium to act.

Examples of extracellular proteins that can be highly upregulated within the TME include osteonectin or secreted protein acidic and rich in cysteine (SPARC)[69-70], MMPs[71-72], serine and cysteine proteases[73-74], elastases[75-77], and various cytokines[78-79]. SPARC, discussed further in **Chapter 1.3**, is a known HSA transporter[33] that acts in conjunction with the endothelial gp60 receptor to transport HSA from the bloodstream to cells. As such, it has also been proposed that Abraxane® is shuttled by SPARC to tumor cells[80]. The Gianneschi Group has developed a method of accumulating nanomaterials within tumor tissue in response to MMPs[21, 81-85] (see **Chapter 1.1.9**), and indeed much of the thesis herein builds on this concept. Protease-activated prodrugs[73] are therapeutics that are inert until acted upon by proteases that are upregulated in the TME. An elegant example of this is targeting doxorubicin to the TME by generating a prodrug susceptible to action by prostate-specific antigen[86], a serine protease. Neutrophil elastase, secreted by neutrophils in the TME[76], is useful as a prognostic marker in cancer and inhibition of this enzyme has been shown to reduce tumor growth *in vivo*[75]. Finally, much of immunotherapy is dedicated to interfacing with cytokines and the immune system within the TME[87]; thus it is impossible to cover it all in this introduction.

1.1.6 Extrinsic TME Properties

Instead of targeting features of specific cells in the TME, an alternative strategy is to utilize extrinsic properties of the TME, i.e., collective characteristics of the tumor space that evolve when enough cells produce similar conditions in their surrounding environment. Many of these features arise due to the dysfunctional metabolism of cancer cells[88-89] (discussed further in **Chapter 1.3**). An advantage of targeting these features is that it is much less likely that normal tissues show these properties. However, tumors are heterogenous and have many local environments even within the TME; thus, it is unlikely that the entire tumor space can be targeted based on these features.

Examples of extrinsic TME properties include hypoxic areas[90-91], a more acidic pH[92-94], and highly redox reactive environments[95-96], depending on the specific type and state of cancer progression. Hypoxia arises in tumors due to lack of oxygen, and hypoxic areas within the TME are attractive targets for cancer therapeutics[97]. Hypoxia-inducible factors (HIFs) are upregulated in hypoxic environments that have roles in angiogenesis and cancer progression, and inhibition of HIFs has led to tumor regression[98]. Sufficient hypoxia can lead to anaerobic glycolysis in tumor cells, causing lactate secretion and resulting in local extracellular acidification[93]. These acidic environments have been the target of many polymeric and nanoparticle drug delivery systems[99-102]. Highly redox reactive environments within the TME also arise from inadequate oxygen supplies. Reactive oxygen species (ROS) are major components of these environments[103] that have been of interest in the field of responsive nanomaterials for drug delivery[104], and indeed the work discussed in **Chapter 4** includes ROS-reactive materials.

1.1.7 Reprogrammed Metabolism

A key feature of the TME the altered metabolic state[105-106] found in many cancers. Indeed, reprogrammed metabolism is a hallmark of cancer[106], though exactly how and why this process occurs is still under investigation. Regardless, cancer cells exhibit increased glucose metabolism[107], increased fatty acid uptake[108-109], as well as increased HSA uptake[110], among others, depending on the cancer state (e.g., when nascent tumors begin to experience nutrient deficits, or during metastasis)[106]. A key advantage of using tumor metabolism for drug delivery is that this altered state is observed across virtually every cancer type, regardless of genetic or histological heterogeneity[111]. However, direct inhibition of metabolic enzymes may be systemically toxic, as normal cells still utilize some of the same pathways.

Increased glucose and glutamine metabolism, termed the Warburg Effect[107], describes how many cancer cells produce energy through aerobic glycolysis and lactic acid fermentation, regardless of oxygen availability. This effect is well-documented, and indeed F-18 fluoro-2-deoxyglucose positron emission tomography (FDG-PET) is used clinically as a diagnostic agent[88], as it accumulates in cancer cells following uptake of this glucose derivative. Increased fatty acid uptake[112-113], as well as HSA uptake[33, 110], is gaining increasing attention as a way to target cancer metabolism, and will be discussed in more detail in **Chapter 1.3**, as part of the dissertation work herein (see **Chapter 5**) uses materials generated from fatty acids to bind to HSA for delivery to tumor tissue *in vivo*.

1.1.8 The EPR Effect

Finally, the most common TME targeting feature employed by researchers has been the EPR effect. All the features of the TME discussed thus far have relied on active targeting strategies, whereas the EPR effect relies on physical characteristics of tumor tissue[29] to passively accumulate material. Once crossing a threshold of about 2 mm^3, tumors experience

rapid angiogenesis to prevent, among other things, necrosis due to lack of oxygen and nutrients caused by insufficient vascularization. This rapid and haphazard growth has been demonstrated to produce “leaky” vasculature in mouse models, including large fenestrations and poorly formed vessel walls[114]. This allows for enhanced permeability of “large” structures, such as nanomaterials, into the tumor space. Coupled with this is a reduced clearance of materials from the tumor space due to slow lymphatic drainage[115], proposed to result in an overall long retention of materials within the tumor space.

Many nanoparticles in preclinical and clinical development rely on the EPR effect for delivery to tumor tissue[116], with the effect being termed the “royal gate” for drug carriers to enter tumors without toxicity to normal tissues[117]. Indeed, Doxil®, the first FDA-approved nanomedicine, is a pegylated liposome containing noncovalently encapsulated doxorubicin that is proposed to accumulate in tumor tissues due to leaky vasculature and slow lymphatic drainage[118]. However, there is increasing controversy surrounding the prevalence of the EPR effect in human tumors[10, 119-120], partially because of the little improvement in overall tumor accumulation has been observed for nanoparticle-based formulations over free drug[119], and also because there is much clinical data to suggest that human tumors are not nearly as “leaky” as their murine, preclinical counterparts[121]. The latter could be because murine subcutaneous models grow much faster than their human counterparts, as well as reach a much larger mass, relative to the rest of the body[10]. Overall, the current prevalent sentiment is that the EPR effect needs to be evaluated on a case-by-case basis in regards to its clinical applicability.

1.1.9 Nanomedicine and the TME

Various types of nanomaterials for cancer therapy have been widely studied[122]. As stated in **Chapter 1.1.8**, many nanomedicines rely upon the EPR effect for localization within the TME. Given the controversy surrounding the EPR effect in clinical settings, it is not

completely surprising that the clear majority of nanomedicines have, as of yet, failed to reach the clinic[123-125]. Indeed, in a meta-analysis by Chan and coworkers of nanomedicine literature over the past 10 years, only 0.7% of the administered nanoparticle dose reaches the tumor[124].

There are many reasons, reliance on EPR effect aside, that this could be the case. For example, it has been demonstrated that nanoparticle occlusion by biomolecules is a major issue for nanomaterials functionalized with targeting ligands, inhibiting the interaction with receptors on both tumor endothelium and cell surface[126]. Further, positively-charged nanoparticles are readily taken up and cleared by the reticuloendothelial system (RES) and other immune cells, including macrophages[127-129]. Additionally, insufficient drug release from the nanocarrier before eventual clearance from the body could be contributing to this modest success in the clinic.

Nanomaterials for drug delivery are developed in **Chapters 2-4** in this dissertation, and seek an alternative approach to traditional EPR-based or receptor/ligand-based targeting strategies, thus potentially sidestepping some of the problems preventing general nanoparticle translation. However, several key areas of improvement are discussed, as is typical with all nanomedicines in development today.

1.1.9 TME Features Exploited in This Dissertation

The dissertation herein utilizes, in part, MMPs to accumulate polymeric nanomaterials within the TME. Briefly, amphiphilic copolymers assemble into nanomaterials whose shells contain MMP-responsive peptides. Upon interaction with MMPs in the TME, a drastic change in size and shape occurs within the nanomaterials, resulting in microscale aggregates that remain in the tumor space. **Chapter 1.2** introduces background of how these materials were developed in the Gianneschi Group, and **Chapter 2.1** discusses the mechanism by which

these nanomaterials are accumulated in the TME. **Chapters 2-4** cover the development of nanomaterials for therapeutic delivery based on this concept.

The work in **Chapter 5** utilizes a different feature of the TME to deliver therapeutic cargo – the uptake of human serum albumin (HSA) by tumors, as well as the high affinity binding of fatty acids to HSA for improved circulation half-lives. Briefly, octadecanedioic acid is mono-esterified with PTX to produce a prodrug capable of binding to HSA in its natural binding pockets for long-chain fatty acids. **Chapter 1.3** will go into more detail about the role of HSA and other biomaterials, including fatty acids, in cancer as well as HSA-fatty acid interactions.

1.2 Peptide-Containing Polymers for Targeting the TME

1.2.1 Introduction to Peptide-Containing Polymers and the TME

The work covered in **Chapters 2-4** is based around peptide-containing polymer systems that form nanoparticles upon dialysis from organic solvent into aqueous media. The key to the targeting of these polymeric nanoparticles is that the hydrophilic block of the polymer, which ultimately forms the shell of the nanoparticle, contains MMP-responsive peptides. The idea behind the development of these systems was based on physical trapping of material within the tumor space, following enzyme activation. The choice of peptide motif was inspired by the work of Tsien et. al.[130-132], on activatable cell-penetrating peptides (ACPPs) that contain a recognition sequence for MMPs between the cationic and anionic domain of the peptide. Upon enzymatic cleavage of this peptide sequence, the CPP portion of the material is released and can enter cells. In a similar manner, enzymatic cleavage of the peptide substrate on the shell of our nanoparticles induces a morphology change of the polymeric material from discrete nanoparticles to microscale aggregates, which become too large to exit the vasculature. A more thorough explanation of this process is described in **Chapter 2.1**.

At the onset of our research into these types of polymeric materials, the graft-through polymerization of peptides via ring opening metathesis polymerization (ROMP) had been increasingly demonstrated in the literature[133-138]. In addition, the high glass transition temperature (T_g) of polynorbornene[139] (which form the backbone of ROMP polymers) made this motif attractive for the generation of kinetically trapped, robust nanoparticle systems. Thus, we sought to generate peptide-containing polymers through ROMP and evaluate the utility and properties of said polymers.

Herein, an account of how the Gianneschi Group developed these systems is provided, as context for the materials described in the dissertation. Discussed will be the synthesis of peptide containing polymers, including graft-through and graft-to approaches; sequence scope, properties, and function of peptide-containing polymers; and an insight into applications of these systems for disease imaging, as this application is not the focus of the current thesis work.

1.2.2 Synthesis of Peptide-Containing Polymers

Our work on peptide-polymer conjugates altogether demonstrates the capability of generating functional, hybrid materials using complex peptides; however, these systems required significant optimization and several challenges had to be overcome through the course of their development. In general, graft-to polymerization strategies, wherein peptides are covalently bound to polymers containing reactive groups post-polymerization (**Figure 1.2.1a**), requires an added purification step following conjugation which can be nontrivial and lead to significant product loss, depending on the peptide sequence and conjugation technique. Additionally, there is little ability to control the spacing and number of peptides conjugated per polymer, which makes characterization difficult and limits batch-to-batch reproducibility. An alternative strategy, which many of our systems employ, is graft-through polymerization, wherein the peptide is first modified with a polymerizable moiety, then directly incorporated into the growing polymer chain (**Figure 1.2.1b**). This allows for precise control of the spacing and density of the peptide on the polymer. With graft-through techniques, however, there are several important parameters that need to be considered to successfully polymerize peptides, and one of the most important is the peptide sequence. Many functional peptides contain amino acid residues capable of reacting with polymerization initiators, so suitable protecting groups may have to be used or the sequence itself modified in a way that removes

the problematic residue yet maintains the overall peptide function[133, 140-141] . Further, the peptide needs to be soluble in the polymerization solvent and remain so throughout the duration of polymerization. Our systems utilize DMF as the solvent, but certainly other solvents could be used depending on the tolerability of the initiator and polymerization technique employed. Additionally, many peptides are inherently slow to polymerize[142], which, coupled with the fact that many initiators are oxygen-sensitive, means that polymerizations need to be completed in a rigorously oxygen-free environment. Overall, significant thought needs to be given when designing graft-through peptide-polymer systems and parameters need to be evaluated and optimized on a system-by-system basis, often through trial-and-error.

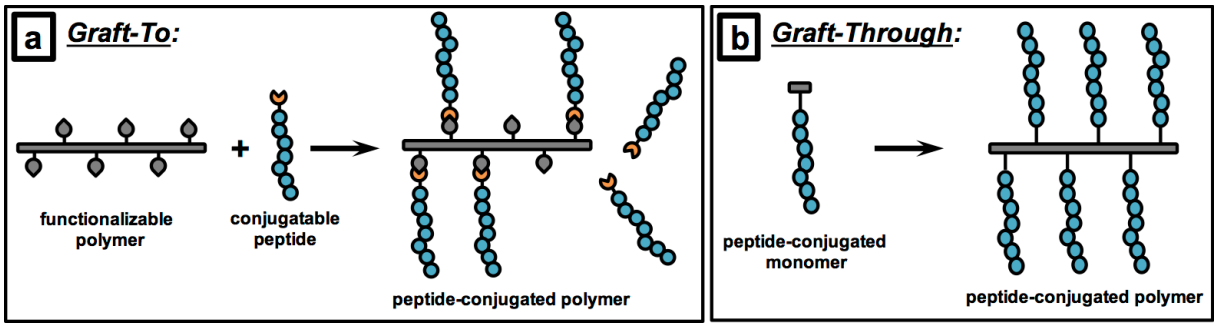

Figure 1.2.1. Generation of peptide-containing polymers. a) graft-to polymerization strategy, whereby a functionalizable moiety is polymerized, and then conjugated to a peptide post-polymerization. b) graft-through polymerization strategy, whereby peptides are first conjugated to a polymerizable moiety, then directly polymerized as a block polymer.

Whether it be graft-to or graft-through, our work on peptide-polymers utilizes ring opening metathesis polymerization (ROMP). There are several characteristics that make ROMP ideal for the synthesis of peptide-polymer materials. First, ROMP is a living polymerization method[143] that allows for the generation of polymers with low dispersity. Second, the initiators, particularly the Grubbs' Ruthenium-based initiators [144-146], display excellent functional group tolerance which permits the incorporation of a diverse array of functionalized monomers, including complex peptides. Third, there are multiple opportunities

for the incorporation of functionality in the polymers through the choice of initiator, monomers, and chain transfer agent (CTA). The driving force for ROMP is relief of ring strain. Our systems utilize norbornene, as it is easily functionalized and has a high ring strain[147]. **Figure 1.2.2** outlines a typical ROMP experiment, which begins with the polymerization of *n* equivalents of monomer relative to Ru initiator. Upon complete consumption of the monomer, the polymer can either be terminated to produce a homopolymers by addition of a CTA or can be elongated by adding *m* equivalents of a second monomer to ultimately produce a block copolymer with blocks of lengths *n* and *m* repeating units, respectively. Other polymerization techniques could be envisioned for the generation of peptide-polymers; however, the precision and living characteristics of ROMP make it an ideal method to develop well-defined, highly reproducible systems.

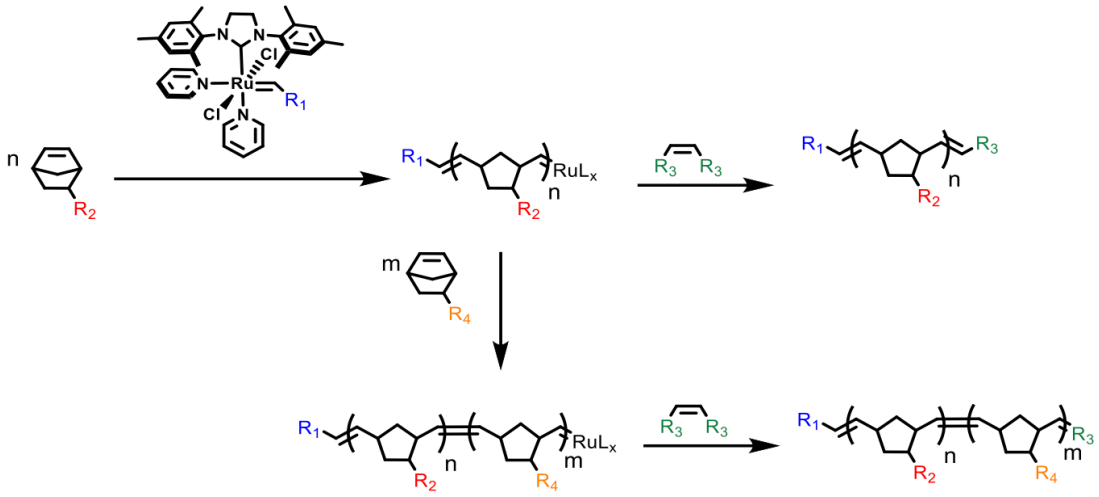

Figure 1.2.2. General ROMP scheme. *n* equivalents of a monomer, relative to Ru initiator, are combined and allowed to polymerize, affording a polymer, which can either be terminated to produce a homopolymer (rightmost arrow, top) or combined with a second monomer (downward arrow, middle), that can be terminated to afford a block copolymer (rightmost arrow, bottom).

1.2.3 Initial Design of Peptide-Polymers: Graft-To Approach

A central goal of our research on peptide-polymer materials is to explore the generality of controlling nanoparticle behavior through the employment of biomolecules covalently bound

to polymer backbones as programmable, stimuli-responsive moieties. Indeed, to date we have demonstrated the capability of polymerizing not only peptides[21, 81-85, 142, 148-151], but also DNA[152-154] and oligonucleotides[155-157]. Our initial work on peptide-polymer materials sought to replicate our success in controlling the morphology of DNA-functionalized block copolymers, where we demonstrated that the morphology of polymeric nanoparticles could be manipulated by altering the length of DNA contained within the hydrophilic polymer block *in situ*. DNA-polymer amphiphiles synthesized via a graft-to approach between CPG-bound DNA and the hydrophilic block of a block copolymer (containing activated N-hydroxysuccinimide (NHS) moieties) assembled into spherical micelles with DNA forming the nanoparticle shell. An RNA base was included within the DNA sequence of these materials to serve as an enzymatic cleavage site for DNA-based phosphodiesterases (DNAzymes). Addition of a DNAzyme to these spherical micelles resulted in complete and rapid cleavage of the DNA on the nanoparticle shell, leaving only a short ssDNA sequence on the polymer backbone. This, in turn, resulted in a sphere-to-cylinder morphology change of the assembled system as the "new" DNA amphiphiles reorganized to minimize packing parameters. The morphology change was shown to be reversible upon addition of a 19-base DNA sequence that formed a 9-base double helix with the truncated DNA in the shell of the cylinder. This was our first proof-of-concept work on controlling and manipulating the morphology of biomolecule-containing polymer amphiphiles using exogenous stimuli.

Spurred by the success of our DNA-based systems, we designed analogous "shape-shifting" polymer systems using peptides[149]. To this end, we first focused on a graft-to approach for synthesizing peptide-polymer amphiphiles (PPAs), where we programmed the peptide sequence to be responsive to four different cancer-associated enzymes: protein kinase A (PKA), protein phosphatase-1 (PP1) and matrix-metalloproteinases 2 and 9, (MMP-2 and MMP-9). Two different amphiphilic peptide brush block copolymer systems were prepared from

a block copolymer containing an inert hydrophobic block and a reactive NHS ester block. Two peptide sequences, differing only in their relative ordering of enzyme recognition site, were conjugated at their N-terminus to the activated NHS ester of the polymer backbones. In one set of PPAs, the cleavage site for MMP-2/9 was close to the polymer backbone; on the other set, the cleavage site was near the C-terminus of the peptide. The conjugation efficiency in both PPAs was determined to be approximately 33% and well-defined micelles approximately 30 nm in diameter formed upon transitioning the PPAs from a 1:1 DMSO:DMF solution to buffered water (**Figure 1.2.3a**). Exposing the materials to PKA phosphorylated the serine residues on the peptides and produced a dramatic change in morphology (**Figure 1.2.3b**). As in our DNA-based systems, this morphology change could be reversed by treatment of the phosphorylated micelles with PP1 (**Figure 1.2.3c**). In a separate set of experiments, the PPAs were treated with MMP-2 and MMP-9 to cleave the peptide substrate. Though both sets of PPAs were susceptible to proteolysis by MMP, a morphology change from sphere-to-aggregate (**Figure 1.2.3d-e**) was only observed when the cleavage site was close to the polymer backbone. This result indicated that the position of the cleavage site within in the amphiphile has a critical role in how the morphology of the micelle is affected by proteolysis, with cleavage sites closer to the backbone giving rise to greater changes in morphology. Together these results demonstrate the ability of controlling morphology of polymer materials with peptides programmed to be responsive to multiple stimuli.

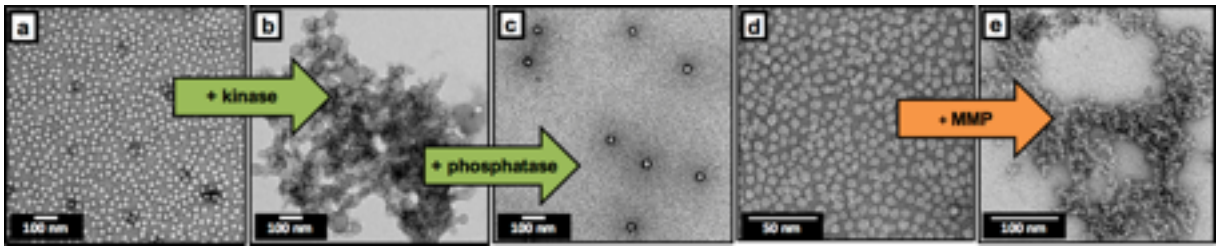

Figure 1.2.3. Enzyme Response of PPAs. a) TEM of PPA before enzyme exposure. b) TEM of PPA after exposure to PKA. c) TEM of materials in panel b to PP1. d) TEM of PPAs before MMP exposure. e) TEM of PPAs after exposure to MMP.

1.2.4 Graft-Through, Direct Polymerization of Peptides

Although graft-through incorporation of peptides into polymers allowed us to generate materials with interesting attributes, we reckoned that precise control over peptide location and density on the polymer backbone would afford greater control on the overall materials properties. Direct incorporation of peptides on the growing polymer chain provides complete control over spacing and number of peptides incorporated per polymer, allowing for the generation of highly reproducible polymer systems with minimal polymer-to-polymer and batch-to-batch variation. This, in turn, enables systematic analysis of design parameters of peptide-polymers; namely, how peptide brush density and degree of polymerization impacts function. Prior work on the graft-through polymerization of peptides was mainly limited to aromatic and aliphatic residues, or resulted in polymers with high dispersity and low overall peptide incorporation[134, 158-160]. For peptides with more complex functionalities, suitable protecting groups had to be employed and subsequently removed post-polymerization[133, 140-141]. Our work sought to establish ROMP as a viable strategy for the graft-through polymerization of peptides with diverse functionalities, through the analysis of how peptide identity, density, degree of polymerization impacts function of resulting materials.

Our first demonstration of the graft-through polymerization of peptides elucidated that the spatial arrangement and density of peptides allows for the programming of a material's susceptibility to proteolytic cleavage, and thus the ability to undergo a change in morphology or function. In this work[161], we synthesized two PPAs by directly polymerizing an inert hydrophobic block followed by a norbornenyl-modified peptide as the hydrophilic block via ROMP using a modified version of Grubbs' second generation Ru catalyst. As in our graft-to systems, the peptide sequences were designed to be substrates for MMP-2 and -9. This method generated well-defined PPAs where the density and number of peptides per polymer were precisely known, which in turn formed micellar nanoparticles of uniform size and shape.

In stark contrast to our graft-to systems, however, minimal or no cleavage of the peptide substrate was observed when the nanoparticles were treated with MMPs. This important finding demonstrates that spatial arrangement of the peptide on the polymer has a large impact on the resulting function of the material.

1.2.5 Sequence Scope, Properties, and Function

Inspired by the results of our study on graft-through generated PPAs, we hypothesized that susceptibility to proteolysis could be mediated by packaging peptides as high-density brush polymers. A key challenge with peptide-based therapeutics is short circulation times in the blood due to cleavage by serum proteases and rapid clearance because of their relatively low molecular weights[162]. Therefore, packaging peptides as high-density, high molecular weight polymers could be a strategy to deliver bioactive peptides with extended circulation half-lives. Many therapeutic and bioactive peptides contain amino acid residues that had never previously been polymerized in a graft-through fashion prior to our entrance to the field. Thus, we examined the substrate scope of protecting-group free peptides for graft-through ROMP, and then, using this knowledge, generated bioactive peptide-based systems and probed their activity and properties.

We explored the limits of ROMP for the direct polymerization of protecting-group free peptides[142]. Towards this end, a library of 31 norbornenyl-modified, protecting-group free pentapeptides that altogether incorporated all 21 naturally occurring amino acids was generated and the rate and degree of polymerization was quantified by a combination of NMR (**Figure 1.2.4a**) and SEC-MALs. All monomers polymerized completely except those containing cysteine residues. Protecting the cysteine residues with Acm protecting groups, however, resulted in complete polymerization within 3 hours. We also found that polymers with carboxylic acid-containing residues tended to “gel” upon polymerization, but that this can be

mitigated by the protection of the carboxylic acid moieties with tert-butyl groups. Further, sequences containing guanidinium moieties (Arg and Lys residues) performed poorly at high degrees of polymerization, but protecting the primary ε-amino group of Lys mitigated this problem. Additionally, spacing the peptide sequence further from the norbornyl group using a longer, 6-aminohexanoic acid linker increased the polymerization rates of monomers containing unprotected Lys residues. Together, these results broadened our understanding of the limitations and scope of graft-through polymerization of peptides via ROMP, so we could then use this knowledge to design complex, bioactive systems.

Some final work in our study on substrate scope suggested that in addition to cleavage site location within the peptide sequence, polymerization density affects the bioactivity of the construct. Thus, we explored the potential of using high-density brush polymers to protect bioactive peptides from proteolysis. Towards this end, we generated high density brush polymers of two cell-penetrating peptides (CPPs), Tat and Arg8, and analyzed their proteolytic susceptibility and bioactivity by terminating each peptide-polymer with a fluorescein moiety as a model cargo. Both CPP peptide-polymers displayed greater cellular uptake than both their monomeric peptide counterparts and two “control” peptides with no cell penetration capability (**Figure 1.2.4b**). The proteolytic susceptibility of the CPP peptide-polymers was evaluated by exposing the materials to high concentrations of proteases and assaying for peptide cleavage by HPLC and bioactivity by flow cytometry and live-cell confocal microscopy (**Figure 1.2.4c**). No evidence of proteolysis was observed for CPP-containing polymers, whereas there was complete consumption of the monomeric peptide. Following enzyme exposure, materials were incubated with cells. Treatment with proteases had no effect on the cell-penetration capability of peptide-polymers; however, the monomeric peptides displayed greater than 90% signal loss. The generality of this approach was further investigated through polymerization of peptide substrates for thrombin and MT1-MMP. As observed for the CPP materials, homopolymers of

these peptide sequences were resistant to enzymatic degradation, whereas their monomeric counterparts were readily degraded (**Figure 1.2.4d**). Importantly, we also found that proteolytic susceptibility of peptide-polymers could be tuned by "spacing" the peptides farther away from one another along the polymer backbone by adding a non-peptide diluent monomer during polymerization (**Figure 1.2.4e**).

Having insight on the capabilities and scope of incorporating peptides as high density brush polymers, we investigated the potential of using this motif to enable cellular uptake of otherwise impenetrable peptides[148]. We hypothesized that the incorporation of positively charged Arg or Lys residues into non-cell penetrating peptides, followed by polymerization as a high-density brush, would enable cellular uptake of otherwise impermeable peptide sequences. Towards this end, we synthesized a non-CPP peptide and added 1 or 2 Arg or Lys residues at either the N- or C-terminus and polymerized it via ROMP, together with a water-soluble OEG block (**Figure 1.2.4f**). We compared these constructs to their monomeric peptide counterparts, and found that only the peptide-polymers containing the positively charged amino acid residues enter cells. Further, we determined that adding the Arg or Lys to the C-terminus of the peptide results in greater uptake than if it is "buried" closer to the polymer backbone at the N-terminus of the peptide. Additionally, the extent of uptake of peptide-polymers is enhanced when the degree of polymerization and/or concentration is increased. Together, these results provide a set of design-rules for generating peptide-polymer systems programmed to resist proteolysis and penetrate cells.

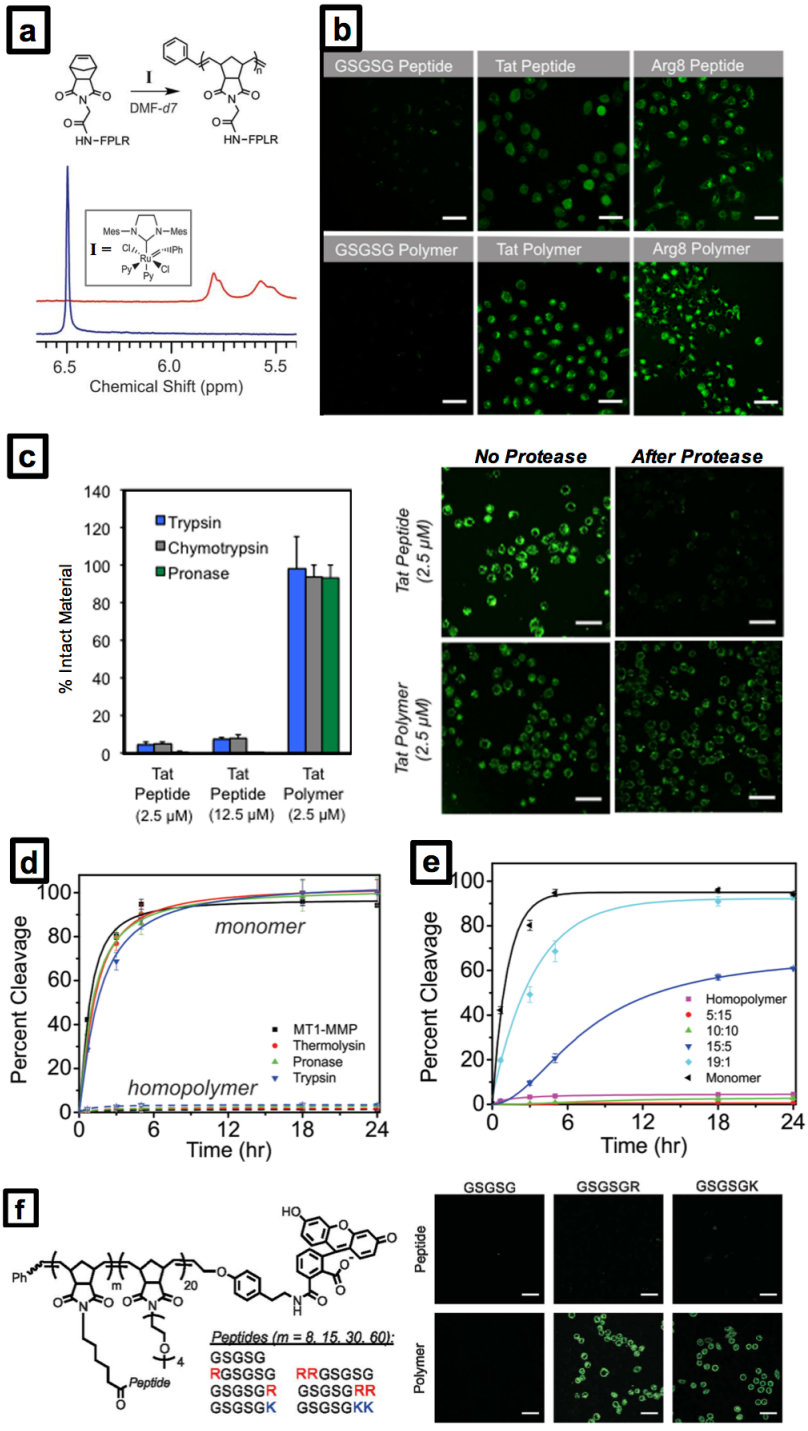

Figure 1.2.4. Substrate scope of directly polymerized peptides. a) General strategy for analysis of polymerization of peptide-based monomers. b) uptake of peptides, both cell penetrating and non-cell penetrating, (top panel) and their brush polymer analogs (bottom panel). c) Protease susceptibility (left) and subsequent cell-penetrating capability (right) of Tat peptide and Tat polymer. d) Degradation kinetics of peptide monomers and polymers to various proteases. e) Effect of spacing within the polymer block on susceptibility of peptide proteolysis. f) Polymer structure of peptide-containing polymers with R or K residues (left) and analysis of these materials for their cell penetrating capability (right).

1.2.6 Applications for Disease Imaging

Beyond *in vitro* proof-of-concept and *in cellulo* uptake experiments, we envisioned that peptide-polymer materials could be used to interface with complex biological systems and diseased tissue *in vivo*. Indeed, enzyme-responsive peptides had been previously demonstrated to respond to MMPs at tumor sites[130-132]. We reasoned that PPAs designed to change morphology in response to MMP exposure to form large, slow-clearing aggregates could be used to accumulate materials *in vivo* at disease sites where MMPs are upregulated for applications in imaging and drug delivery. As in our initial work on PPAs with switchable morphologies, we designed enzyme-responsive peptide-polymer amphiphiles (PPAs) with hydrophilic polymer blocks containing peptides with recognition sequences only for MMPs. Prior to MMP exposure, the PPAs assemble into nanoparticles <50 nm in diameter. When incubated with MMPs, the enzyme cleaves the peptide, altering the hydrophobic-to-hydrophilic ratio of the polymers and resulting in a shift in morphology from discrete nanoparticles to micro-scale aggregates (**Figure 1.2.5a**).

To date, we have demonstrated that fluorophore-labelled enzyme-responsive PPAs have utility in the imaging of disease states *in vivo* in cancer[21, 82-83, 150], post-myocardial infarction (MI)[150], and inflammatory diseases, such as peripheral artery disease[151]. The first generation of disease-imaging enzyme-responsive PPAs was designed based on our early successes with graft-to approaches. In this scheme (**Figure 1.2.6**), a hydrophobic phenyl-based norbornenyl moiety was polymerized via ROMP, followed by the polymerization of a hydrophilic conjugatable NHS-ester. At this point, the batch of growing polymer was split in half and terminated with either a fluorescein- or rhodamine-based chain transfer agent (FRET donor and acceptor, respectively)[163]. The hydrophilic blocks were further modified with peptides containing MMP recognition sequences post-polymerization, then dialyzed to afford fluorescein- (PPA_F) or rhodamine- (PPA_R) tagged, MMP-responsive nanoparticles. As discrete

nanoparticle systems, PPA_F and PPA_R did not produce a FRET signal, even when co-incubated for several months, indicating no inter-particle mixing of polymers occurs and that these are kinetically trapped constructs. However, exposure of these systems to MMP induced a morphology change and resulted in the generation of a FRET signal, indicating a rearrangement in polymer ordering that brings FRET donor-bearing materials (PPA_F) within the Föerster radius of FRET acceptor-bearing materials (PPA_R).

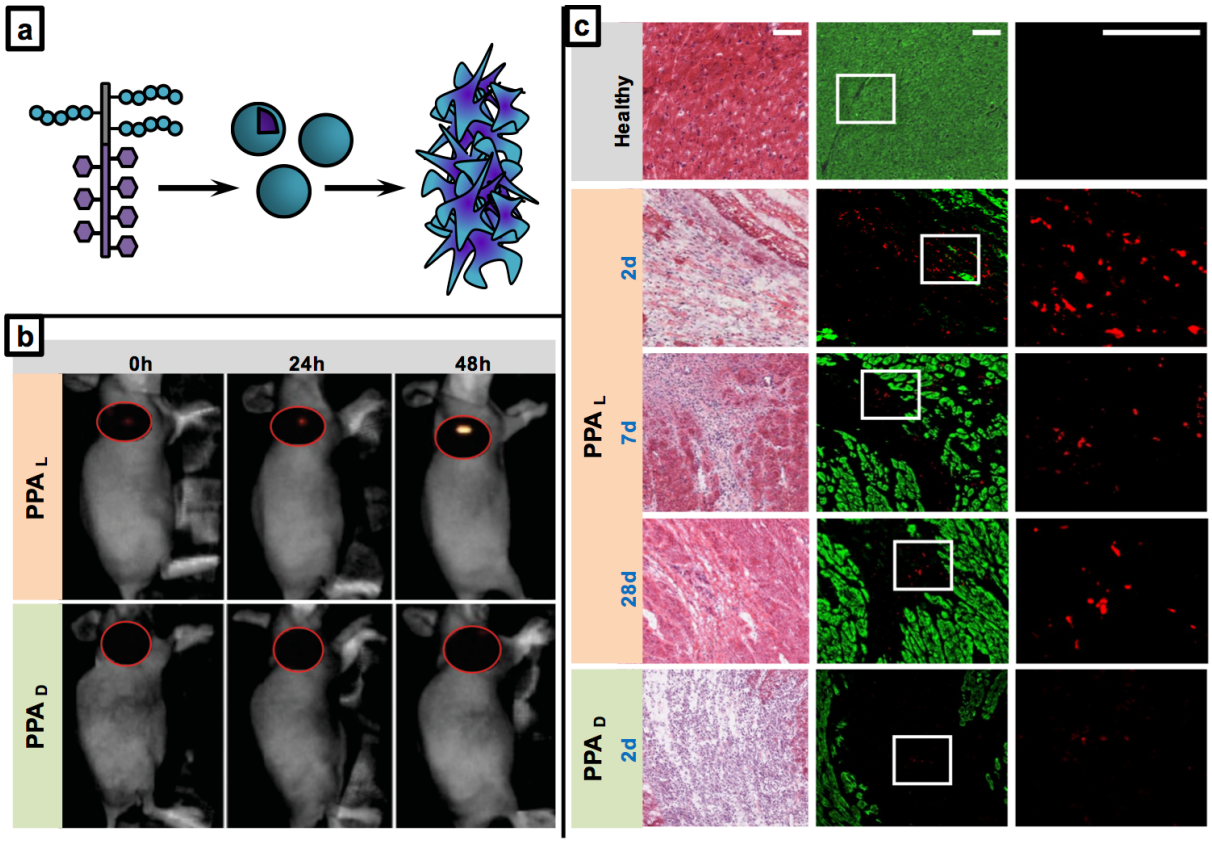

Figure 1.2.5. Application of enzyme-responsive nanomaterials for imaging. a) general schematic of diblock copolymer amphiphiles that assemble into core-shell micelles, and subsequently react with MMPs to generate large aggregates. b) Visualization of this nanoparticle-to-aggregate process in tumor tissue, using live-animal fluorescence imaging. Top panel: live animal imaging analysis for FRET, following IV administration of PPA_L. Bottom panel: live animal imaging analysis following IV administration of PPA_D. c) Visualization of accumulated nanoparticles in infarcted heart tissue. Left panel: H&E stained images; middle panel: neighboring fluorescent sections, with myocardium stained with anti-α-actinin in green and nanoparticles shown in red; right panel: zoomed in region of white box in panel b.

As an initial proof-of concept, this motif was studied in HT-1080 fibrosarcoma murine xenografts. HT-1080 was chosen as a model system because it is known to highly overexpress

MMPs in its progression[164]. A key design feature of these PPA systems is that analogous polymers and nanoparticles can be rapidly generated using peptide sequences composed of *d*-amino acids. These peptides are not recognized by enzymes as substrates because of their enantiomeric configuration, thus systems generated with *d*-amino acids (*d*-PPA) are incapable of undergoing morphology changes when exposed to MMPs and serve as a true negative control for this process. In HT-1080 xenografts, the enzyme-responsive PPA (*l*-PPA) systems can be visualized in tumor tissue as a function of FRET signal *via* live-animal fluorescence imaging up to two days following intravenous (IV) injection, indicating that MMPs are acting upon the nanomaterials and eliciting the morphology change (**Figure 1.2.5b**). In contrast, the tumors remain dark in animals treated with *d*-PPA systems. Together, these results confirm that enzyme-responsive peptide-polymer systems accumulate in tumor tissue only following stimulus response and have utility in imaging tumor tissue.

We have found that fluorophore-containing PPAs are also useful in imaging damaged heart tissue following acute myocardial infarction (MI)[150]. As in cancer, MMPs are upregulated following MI during the left ventricle (LV) remodeling process[165], thus providing a targeting scheme for our enzyme-responsive PPA systems. Fluorophore-labelled enzyme-responsive PPA nanoparticles were intravenously injected at 24 hours post-MI, and retention of material was evaluated by *ex vivo* fluorescence at various timepoints up to 28 days post-injection (**Figure 1.2.5c**). Throughout the course of the study, enzyme-responsive PPAs (*l*-PPA) are visualizable in infarcted tissue. Additionally, no accumulation is observed in healthy animals administered *l*-PPA Conversely, very little fluorescence signal is observed at 2 days post-injection in infarcted animals administered the non-responsive controls (*d*-PPA), indicating that the enzyme-response, not the EPR effect observed acutely post-MI[166], is necessary for retention of these materials. Together, these results demonstrate the utility of the FRET-

labelled PPA system in the *in vivo* imaging of disease states. See **Chapters 2-4** for the application of these types of system for drug delivery.

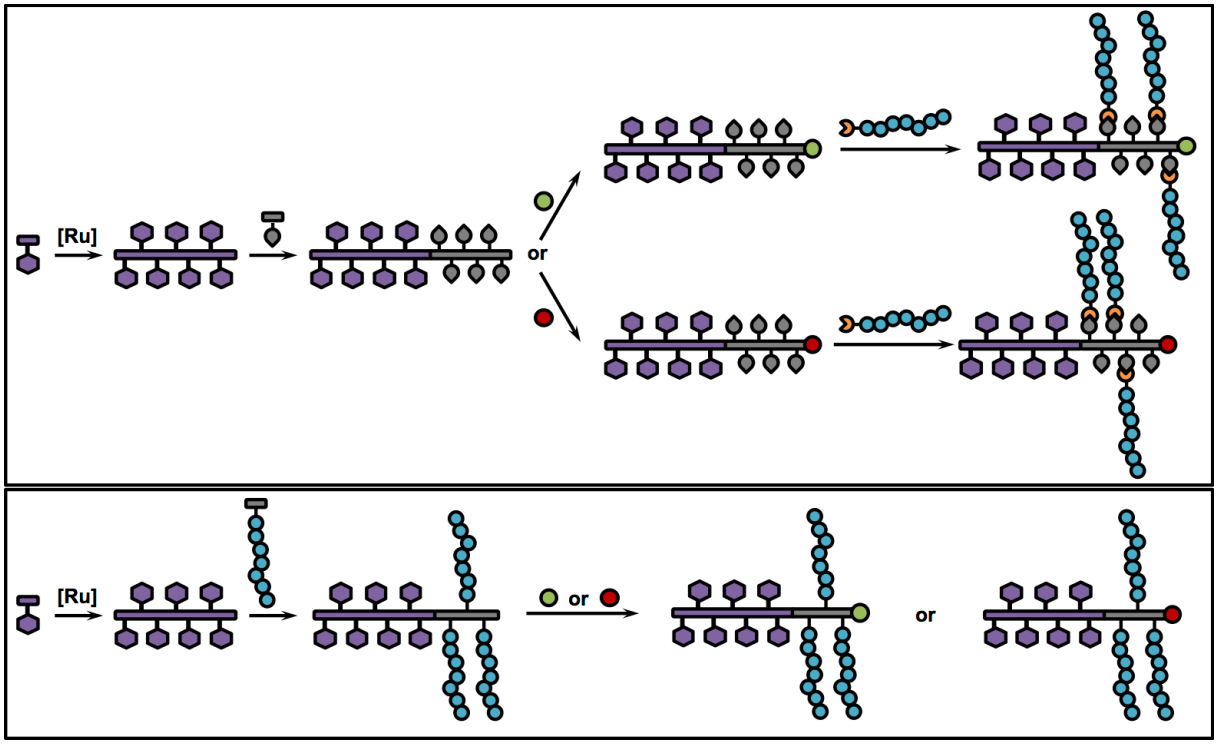

Figure 1.2.6. Synthesis of fluorophore-labelled enzyme-responsive PPAs. Top panel: graft-to approach for generating two different sets of fluorescent polymers. Bottom panel: graft-through approach to generating fluorescent polymers. Note that the spacing of peptides within the block copolymers is expected to be much more uniform and identical using the graft-through approach.

1.3 HSA as a Drug Carrier to the TME

1.3.1 Introduction to HSA, Fatty Acids, and the TME

The work in **Chapter 5** involves the development of a fatty acid-based PTX delivery system, designed to noncovalently bind to HSA with high affinity. This design is predicated on the relationship between HSA and cancer, fatty acid and cancer, and HSA with fatty acids. Herein, a brief introduction is given specifically to HSA and fatty acids with respect to their roles in tumor pathophysiology (**Figure 1.3.1**), and their history as drug delivery systems for cancer therapy.

It is being increasingly recognized that HSA is a key nutrient for growing tumors[33, 80, 167], and given its unique properties (see **Chapter 1.3.2**), it provides an attractive strategy for delivering therapeutic cargo to the TME. As mentioned in **Chapter 1.1.3**, the gp60 receptor, also known as albondin, facilitates endothelial transport of HSA and transcytosis into the tumor space, and it has been proposed that over 50% of HSA leaves the blood through binding to gp60[168-171]. It has been demonstrated that gp60 binds albumin-bound drugs in the same fashion as native HSA[172]; thus, this may provide a clever way of accumulating drug cargo within the TME.

After entering the TME, SPARC (mentioned in **Chapter 1.1.5**) has been proposed to facilitate the accumulation of HSA in the tumor space[172-176]. Indeed, SPARC expression has been used as a prognostic tool in cancer patients[176-178], though there is controversy surrounding its overall prognostic value[179]. In normal physiology, SPARC expression is limited to bone and gut endothelium, as well as tissues undergoing remodeling and repair[180]. However, SPARC expression is high in certain types of cancer, including melanoma, glioblastoma, breast cancer, and prostate cancer[178] as a key component of the TME. Further,

SPARC and gp60 have been shown to share a native albumin-binding domain[172], and increased SPARC expression has been correlated with increased uptake of fluorophore-labelled HSA in cells[181]. Studies of Abraxane®, the HSA-PTX nanoparticle, have also indicated that interaction of Abraxane® with SPARC in the TME enhances the overall tumor accumulation of the drug[175-176].

It has been shown that Ras-driven cancers, among others, utilize micropinocytosis to internalize HSA[182-183], where it is catabolized to be used as a source of amino acids by the cells[184-187]. Of special importance is HSA as a source of glutamine, as it can be used to power the TCA cycle under metabolic stress and for macromolecular synthesis for cell replication[88, 188-189]. Indeed, pancreatic tumors show a lower overall glutamine level than normal tissues, suggesting that any available glutamine is readily metabolized by the cells[182].

In addition to HSA, fatty acid uptake by cancer cells is of increasing interest in the field[32, 109, 113, 190-191]. Cancer cells need lipids for cell membranes, as signaling molecules, and for powering the TCA cycle[192-194]. Either must come from exogenous sources or *de novo* synthesis. Fatty acids provide more energy than carbohydrates for ATP synthesis, thus making them attractive nutrients to growing tumors[191]. Additionally, specific fatty acid binding proteins, including FABP4 and CD36, have been implicated in cancer progression[195-199], and inhibition of these proteins or inactivation of pathways that involve fatty acid binding proteins has remarkably stalled tumor growth in some cases[198].

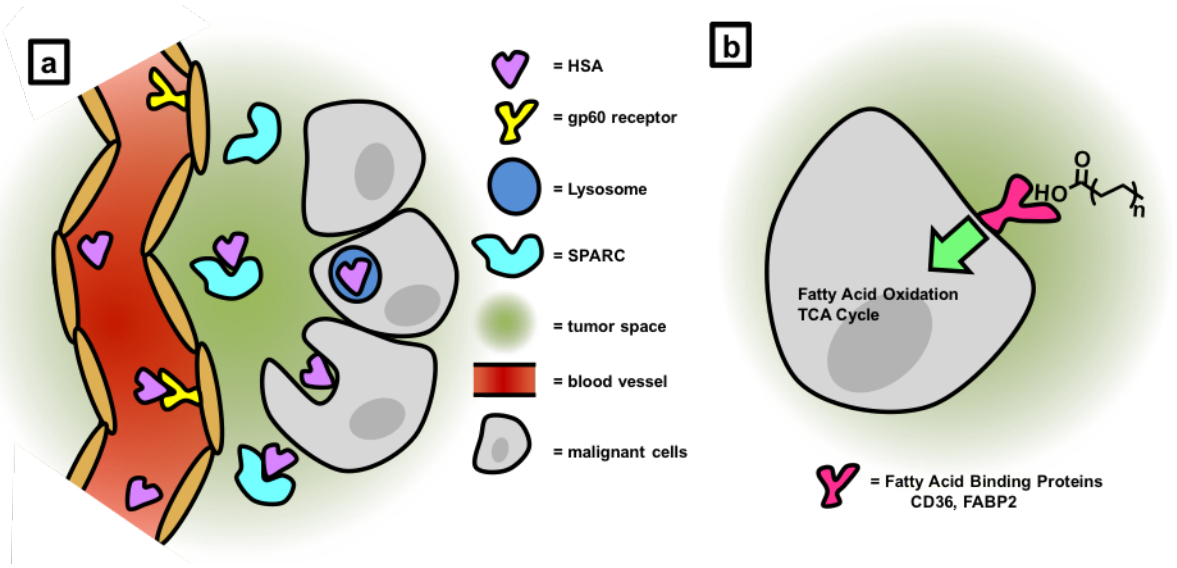

Figure 1.3.1. Diagram of HSA and FA uptake by cancer cells. a) HSA and the TME. In recent years, the role of HSA and fatty acid uptake by tumors and their accumulation in the TME has been of increasing interest. HSA entry into the tumor space can be facilitated by the gp60 receptor. SPARC may mediate the accumulation of HSA in the TME, and has been used as a prognostic indicator in certain cancer types. Further, HSA can be utilized as a fuel source by cancer cells, either by specific entry through receptors or by micropinocytosis. b) Fatty acid and lipid metabolism has been implicated to play an important role in cancer progression. Fatty acid binding proteins include FABP4 and CD36. As with HSA, fatty acids can fuel the TCA cycle in tumor cells.

1.3.2 HSA as a Drug Carrier

HSA is a heart shaped ~67 kD protein, and is the most abundant component of blood plasma and constitutes about 50% of whole blood[33]. It is produced in the liver, and has many functions, including maintaining osmotic pressure and transporting hydrophobic and lipophilic molecules, including both endogenous ligands (including fatty acids)[200-201] and exogenous ligands (including many drugs)[202-204]. Indeed, HSA serum levels have been shown to impact the half-lives of drugs in the bloodstream[80]. Normally, HSA has a half-life of ~20 days in the blood[205], which makes strategies of using HSA as a drug carrier appealing.

The concept of using HSA as a drug carrier is not new; in fact, HSA-based drug delivery has seen increasing interest in the field[33, 80, 206]. Abraxane® is an FDA-approved formulation of HSA with PTX[175] developed primarily as a Cremophor®-free formulation of PTX, and has been proposed to utilize SPARC and gp60, among others, to accumulate drug cargo in the TME[175-

[176]. In addition, several imaging agents designed to interact with HSA have been clinically approved[207-209].

One notable strategy towards increasing the TI of drug cargo, as well as targeting the TME, has been the development of drugs (both small molecules and biologicals) that "hitchhike" on human serum albumin (HSA)[80, 210]. Directed interactions between HSA and drug partners have, to date, involved either coincidental, non-specific "sticking" to HSA in shallow hydrophobic clefts and pockets or through direct surface conjugation via covalent methodologies. Nano- and biomaterials designed to specifically interact with HSA have been demonstrated utility[211-213] indicative of this upswing in interest of HSA as a drug carrier[214]. This could partially be attributed to the fact that upon entering the bloodstream, most nanomaterials are immediately coated in serum proteins, including HSA[215-218], forming a so-called "protein corona". Therefore, exploiting this already-known phenomenon by designing materials to specifically interact with HSA may improve the properties of nano- and biomaterials for drug delivery. Given the controversy surrounding the prevalence of EPR effect in human tumors (see **Chapter 1.1.8**), it may be possible that HSA-mediated transport of nanomaterials is actually what is responsible for accumulation of nanomaterials in tumors. However, this is difficult to study, and as of yet has been unexplored.

1.3.3 Fatty Acids for Drug Delivery

A main class of ligands that binds HSA are medium- and long-chain fatty acids. As many as 7 high affinity binding sites for fatty acids on HSA have been identified[200, 219-222], which are composed of hydrophobic channels with cationic residues deep within the pockets. These residues form salt bridges with the carboxylate moiety of the fatty acid, and this interaction is responsible for the nanomolar dissociation constants observed for native fatty acids[223].

Given their role in tumorigenesis, fatty acids and lipids are being increasingly explored for their potential as drug carriers to tumor tissue. In fact, conjugation of lipids to small molecule drugs is not a new idea, and much of the performance of these materials is likely attributed to them adhering to HSA[80, 224-227]. However, to date, these strategies have largely involved conjugation of drugs to the critical carboxylic acid functionalities on various fatty acids, primarily palmitic and stearic acids. These strategies have not been ultimately successful; competition against native ligands for binding to fatty acid transport/processing proteins, like HSA, is eliminated when esters or other functional groups are made at the carboxylic acid sites. Indeed, it is known that these contacts are involved in fatty acid shuttling between pathway proteins[228]. There are a few notable examples of fatty acid-conjugated drugs that utilize HSA as a transporter, including the FDA-approved diabetes drug Levemir®[206].

1.4 Acknowledgements

Chapter 1.2 is adapted, in part, from material currently being prepared for submission for publication. Callmann, Cassandra; Thompson, Matthew; and Nathan Gianneschi. The dissertation author is the primary author of this pending manuscript.

1.5 References

1. Kaufmann, S. H. E., Paul Ehrlich: founder of chemotherapy. *Nature Reviews Drug Discovery* **2008,** *7*, 373.

2. Strebhardt, K.; Ullrich, A., Paul Ehrlich's magic bullet concept: 100 years of progress. *Nature Reviews Cancer* **2008,** *8*, 473.

3. Ehrlich, P., *Aus theorie und praxis der chemotherapie*. W. Klinkhardt: 1911.

4. Bosch, F.; Rosich, L., The Contributions of Paul Ehrlich to Pharmacology: A Tribute on the Occasion of the Centenary of His Nobel Prize. *Pharmacology* **2008,** *82* (3), 171-179.

5. Winau, F.; Westphal, O.; Winau, R., Paul Ehrlich — in search of the magic bullet. *Microbes and Infection* **2004,** *6* (8), 786-789.

6. Balkwill, F. R.; Capasso, M.; Hagemann, T., The tumor microenvironment at a glance. *Journal of Cell Science* **2012,** *125* (23), 5591-5596.

7. Seidman, A.; Hudis, C.; Pierri, M. K.; Shak, S.; Paton, V.; Ashby, M.; Murphy, M.; Stewart, S. J.; Keefe, D., Cardiac dysfunction in the trastuzumab clinical trials experience. *Journal of clinical oncology : official journal of the American Society of Clinical Oncology* **2002,** *20* (5), 1215-21.

8. Byrd, J. C.; Waselenko, J. K.; Maneatis, T. J.; Murphy, T.; Ward, F. T.; Monahan, B. P.; Sipe, M. A.; Donegan, S.; White, C. A., Rituximab therapy in hematologic malignancy patients with circulating blood tumor cells: association with increased infusion-related side effects and rapid blood tumor clearance. *Journal of clinical oncology : official journal of the American Society of Clinical Oncology* **1999,** *17* (3), 791-5.

9. Piccart-Gebhart , M. J.; Procter , M.; Leyland-Jones , B.; Goldhirsch , A.; Untch , M.; Smith , I.; Gianni , L.; Baselga , J.; Bell , R.; Jackisch , C.; Cameron , D.; Dowsett , M.; Barrios , C. H.; Steger , G.; Huang , C.-S.; Andersson , M.; Inbar , M.; Lichinitser , M.; Láng , I.; Nitz , U.; Iwata , H.; Thomssen , C.; Lohrisch , C.; Suter , T. M.; Rüschoff , J.; Sütő , T.; Greatorex , V.; Ward , C.; Straehle , C.; McFadden , E.; Dolci , M. S.; Gelber , R. D., Trastuzumab after Adjuvant Chemotherapy in HER2-Positive Breast Cancer. *New England Journal of Medicine* **2005,** *353* (16), 1659-1672.

10. Danhier, F., To exploit the tumor microenvironment: Since the EPR effect fails in the clinic, what is the future of nanomedicine? *Journal of controlled release : official journal of the Controlled Release Society* **2016,** *244* (Pt A), 108-121.

11. Muller, P. Y.; Milton, M. N., The determination and interpretation of the therapeutic index in drug development. *Nature reviews. Drug discovery* **2012,** *11* (10), 751-61.

12. Danhier, F.; Feron, O.; Preat, V., To exploit the tumor microenvironment: Passive and active tumor targeting of nanocarriers for anti-cancer drug delivery. *Journal of controlled release : official journal of the Controlled Release Society* **2010,** *148* (2), 135-46.

13. Hirschey, M. D.; DeBerardinis, R. J.; Diehl, A. M. E.; Drew, J. E.; Frezza, C.; Green, M. F.; Jones, L. W.; Ko, Y. H.; Le, A.; Lea, M. A.; Locasale, J. W.; Longo, V. D.; Lyssiotis, C. A.; McDonnell, E.; Mehrmohamadi, M.; Michelotti, G.; Muralidhar, V.; Murphy, M. P.; Pedersen, P. L.; Poore, B.; Raffaghello, L.; Rathmell, J. C.; Sivanand, S.; Vander Heiden, M. G.; Wellen, K. E., Dysregulated metabolism contributes to oncogenesis. *Seminars in cancer biology* **2015,** *35 Suppl*, S129-s150.

14. Nanda, A.; St Croix, B., Tumor endothelial markers: new targets for cancer therapy. *Current opinion in oncology* **2004,** *16* (1), 44-9.

15. Desgrosellier, J. S.; Cheresh, D. A., Integrins in cancer: biological implications and therapeutic opportunities. *Nature reviews. Cancer* **2010,** *10* (1), 9-22.

16. Byrne, J. D.; Betancourt, T.; Brannon-Peppas, L., Active targeting schemes for nanoparticle systems in cancer therapeutics. *Advanced Drug Delivery Reviews* **2008,** *60* (15), 1615-1626.

17. Low, P. S.; Kularatne, S. A., Folate-targeted therapeutic and imaging agents for cancer. *Current opinion in chemical biology* **2009,** *13* (3), 256-62.

18. Daniels, T. R.; Delgado, T.; Helguera, G.; Penichet, M. L., The transferrin receptor part II: targeted delivery of therapeutic agents into cancer cells. *Clinical immunology (Orlando, Fla.)* **2006,** *121* (2), 159-76.

19. Mamot, C.; Drummond, D. C.; Greiser, U.; Hong, K.; Kirpotin, D. B.; Marks, J. D.; Park, J. W., Epidermal growth factor receptor (EGFR)-targeted immunoliposomes mediate specific and efficient drug delivery to EGFR- and EGFRvIII-overexpressing tumor cells. *Cancer research* **2003,** *63* (12), 3154-61.

20. Lee, M.; Fridman, R.; Mobashery, S., Extracellular proteases as targets for treatment of cancer metastases. *Chemical Society reviews* **2004,** *33* (7), 401-9.

21. Callmann, C. E.; Barback, C. V.; Thompson, M. P.; Hall, D. J.; Mattrey, R. F.; Gianneschi, N. C., Therapeutic Enzyme-Responsive Nanoparticles for Targeted Delivery and Accumulation in Tumors. *Advanced Materials* **2015,** *27* (31), 4611-4615.

22. Takashi, S.; Miwa, Y.; Satoshi, T.; Takashi, F.; Jun-Ichi, Y., Neutrophil Elastase Inhibition: A New Cancer Therapy. *Current Enzyme Inhibition* **2008,** *4* (2), 82-85.

23. Liu, J.; Huang, Y.; Kumar, A.; Tan, A.; Jin, S.; Mozhi, A.; Liang, X. J., pH-sensitive nano-systems for drug delivery in cancer therapy. *Biotechnology advances* **2014,** *32* (4), 693-710.

24. Kim, D.; Lee, E. S.; Oh, K. T.; Gao, Z. G.; Bae, Y. H., Doxorubicin-loaded polymeric micelle overcomes multidrug resistance of cancer by double-targeting folate receptor and early endosomal pH. *Small (Weinheim an der Bergstrasse, Germany)* **2008,** *4* (11), 2043-50.

25. Lee, E. S.; Na, K.; Bae, Y. H., Polymeric micelle for tumor pH and folate-mediated targeting. *Journal of Controlled Release* **2003,** *91* (1), 103-113.

26. Tao, W.; He, Z., ROS-responsive drug delivery systems for biomedical applications. *Asian Journal of Pharmaceutical Sciences*.

27. Liou, G.-Y.; Storz, P., Reactive oxygen species in cancer. *Free radical research* **2010,** *44* (5), 10.3109/10715761003667554.

28. Nikitovic, D.; Corsini, E.; Kouretas, D.; Tsatsakis, A.; Tzanakakis, G., ROS-major mediators of extracellular matrix remodeling during tumor progression. *Food and Chemical Toxicology* **2013,** *61* (Supplement C), 178-186.

29. Maeda, H., The enhanced permeability and retention (EPR) effect in tumor vasculature: the key role of tumor-selective macromolecular drug targeting. *Advances in enzyme regulation* **2001,** *41*, 189-207.

30. Maeda, H.; Wu, J.; Sawa, T.; Matsumura, Y.; Hori, K., Tumor vascular permeability and the EPR effect in macromolecular therapeutics: a review. *Journal of controlled release : official journal of the Controlled Release Society* **2000,** *65* (1-2), 271-84.

31. Chouaib, S.; Kieda, C.; Benlalam, H.; Noman, M. Z.; Mami-Chouaib, F.; Ruegg, C., Endothelial cells as key determinants of the tumor microenvironment: interaction with tumor cells, extracellular matrix and immune killer cells. *Critical reviews in immunology* **2010,** *30* (6), 529-45.

32. Frei, E., Albumin binding ligands and albumin conjugate uptake by cancer cells. *Diabetology & Metabolic Syndrome* **2011,** *3*, 11-11.

33. Merlot, A. M.; Kalinowski, D. S.; Richardson, D. R., Unraveling the mysteries of serum albumin—more than just a serum protein. *Frontiers in Physiology* **2014,** *5*, 299.

34. Shadidi, M.; Sioud, M., Selective targeting of cancer cells using synthetic peptides. *Drug resistance updates : reviews and commentaries in antimicrobial and anticancer chemotherapy* **2003,** *6* (6), 363-71.

35. Lin, P.; Sankar, S.; Shan, S.; Dewhirst, M. W.; Polverini, P. J.; Quinn, T. Q.; Peters, K. G., Inhibition of tumor growth by targeting tumor endothelium using a soluble vascular endothelial growth factor receptor. *Cell Growth Differ* **1998,** *9* (1), 49-58.

36. Kobayashi, H.; Boelte, K. C.; Lin, P. C., Endothelial cell adhesion molecules and cancer progression. *Current medicinal chemistry* **2007,** *14* (4), 377-86.

37. Pasqualini, R.; Koivunen, E.; Ruoslahti, E., αv Integrins as receptors for tumor targeting by circulating ligands. *Nature Biotechnology* **1997,** *15*, 542.

38. Alghisi, G. C.; Ruegg, C., Vascular integrins in tumor angiogenesis: mediators and therapeutic targets. *Endothelium : journal of endothelial cell research* **2006,** *13* (2), 113-35.

39. Genis, L.; Galvez, B. G.; Gonzalo, P.; Arroyo, A. G., MT1-MMP: universal or particular player in angiogenesis? *Cancer metastasis reviews* **2006,** *25* (1), 77-86.

40. Remacle, A. G.; Golubkov, V. S.; Shiryaev, S. A.; Dahl, R.; Stebbins, J. L.; Chernov, A. V.; Cheltsov, A. V.; Pellecchia, M.; Strongin, A. Y., Novel MT1-MMP small-molecule inhibitors based on insights into hemopexin domain function in tumor growth. *Cancer research* **2012,** *72* (9), 2339-49.

41. Zhao, M.; Lei, C.; Yang, Y.; Bu, X.; Ma, H.; Gong, H.; Liu, J.; Fang, X.; Hu, Z.; Fang, Q., Abraxane, the Nanoparticle Formulation of Paclitaxel Can Induce Drug Resistance by Up-Regulation of P-gp. *PLOS ONE* **2015,** *10* (7), e0131429.

42. Miele, E.; Spinelli, G. P.; Miele, E.; Tomao, F.; Tomao, S., Albumin-bound formulation of paclitaxel (Abraxane(®) ABI-007) in the treatment of breast cancer. *International Journal of Nanomedicine* **2009,** *4*, 99-105.

43. Ferrara, N.; Hillan, K. J.; Novotny, W., Bevacizumab (Avastin), a humanized anti-VEGF monoclonal antibody for cancer therapy. *Biochemical and biophysical research communications* **2005,** *333* (2), 328-35.

44. Ferrara, N.; Hillan, K. J.; Gerber, H.-P.; Novotny, W., Discovery and development of bevacizumab, an anti-VEGF antibody for treating cancer. *Nature Reviews Drug Discovery* **2004,** *3*, 391.

45. Dienst, A.; Grunow, A.; Unruh, M.; Rabausch, B.; Nor, J. E.; Fries, J. W.; Gottstein, C., Specific occlusion of murine and human tumor vasculature by VCAM-1-targeted recombinant fusion proteins. *Journal of the National Cancer Institute* **2005,** *97* (10), 733-47.

46. Chen, Q.; Massague, J., Molecular pathways: VCAM-1 as a potential therapeutic target in metastasis. *Clin Cancer Res* **2012,** *18* (20), 5520-5.

47. Liu, Z.; Wang, F.; Chen, X., Integrin α(v)β(3)-Targeted Cancer Therapy. *Drug development research* **2008,** *69* (6), 329-339.

48. Liu, S., Radiolabeled Cyclic RGD Peptides as Integrin α(v)β(3)-Targeted Radiotracers: Maximizing Binding Affinity via Bivalency. *Bioconjugate chemistry* **2009,** *20* (12), 2199-2213.

49. Mulgrew, K.; Kinneer, K.; Yao, X. T.; Ward, B. K.; Damschroder, M. M.; Walsh, B.; Mao, S. Y.; Gao, C.; Kiener, P. A.; Coats, S.; Kinch, M. S.; Tice, D. A., Direct targeting of alphavbeta3 integrin on tumor cells with a monoclonal antibody, Abegrin. *Molecular cancer therapeutics* **2006,** *5* (12), 3122-9.

50. Delbaldo, C.; Raymond, E.; Vera, K.; Hammershaimb, L.; Kaucic, K.; Lozahic, S.; Marty, M.; Faivre, S., Phase I and pharmacokinetic study of etaracizumab (Abegrin), a humanized monoclonal antibody against alphavbeta3 integrin receptor, in patients with advanced solid tumors. *Investigational new drugs* **2008,** *26* (1), 35-43.

51. Dechantsreiter, M. A.; Planker, E.; Mathä, B.; Lohof, E.; Hölzemann, G.; Jonczyk, A.; Goodman, S. L.; Kessler, H., N-Methylated Cyclic RGD Peptides as Highly Active and Selective αVβ3 Integrin Antagonists. *Journal of Medicinal Chemistry* **1999,** *42* (16), 3033-3040.

52. Mas-Moruno, C.; Rechenmacher, F.; Kessler, H., Cilengitide: The First Anti-Angiogenic Small Molecule Drug Candidate. Design, Synthesis and Clinical Evaluation. *Anti-Cancer Agents in Medicinal Chemistry* **2010,** *10* (10), 753-768.

53. Zucker, S.; Cao, J., Selective matrix metalloproteinase (MMP) inhibitors in cancer therapy: Ready for prime time? *Cancer biology & therapy* **2009,** *8* (24), 2371-2373.

54. Koivunen, E.; Arap, W.; Valtanen, H.; Rainisalo, A.; Medina, O. P.; Heikkila, P.; Kantor, C.; Gahmberg, C. G.; Salo, T.; Konttinen, Y. T.; Sorsa, T.; Ruoslahti, E.; Pasqualini, R., Tumor targeting with a selective gelatinase inhibitor. *Nat Biotechnol* **1999,** *17* (8), 768-74.

55. Ciardiello, F.; Tortora, G., Epidermal growth factor receptor (EGFR) as a target in cancer therapy: understanding the role of receptor expression and other molecular determinants that could influence the response to anti-EGFR drugs. *European Journal of Cancer* **2003,** *39* (10), 1348-1354.

56. Arteaga, C., Targeting HER1/EGFR: A molecular approach to cancer therapy. *Seminars in Oncology* **2003,** *30* (3, Supplement 7), 3-14.

57. Acharya, S.; Dilnawaz, F.; Sahoo, S. K., Targeted epidermal growth factor receptor nanoparticle bioconjugates for breast cancer therapy. *Biomaterials* **2009,** *30* (29), 5737-5750.

58. Low, P. S.; Antony, A. C., Folate receptor-targeted drugs for cancer and inflammatory diseases. *Advanced Drug Delivery Reviews* **2004,** *56* (8), 1055-1058.

59. Yang, J.; Vlashi, E.; Low, P., Folate-linked drugs for the treatment of cancer and inflammatory diseases. *Sub-cellular biochemistry* **2012,** *56*, 163-79.

60. Daniels, T. R.; Bernabeu, E.; Rodriguez, J. A.; Patel, S.; Kozman, M.; Chiappetta, D. A.; Holler, E.; Ljubimova, J. Y.; Helguera, G.; Penichet, M. L., The transferrin receptor and the targeted delivery of therapeutic agents against cancer. *Biochimica et biophysica acta* **2012,** *1820* (3), 291-317.

61. Tortorella, S.; Karagiannis, T. C., Transferrin receptor-mediated endocytosis: a useful target for cancer therapy. *The Journal of membrane biology* **2014,** *247* (4), 291-307.

62. Breier, A.; Gibalova, L.; Seres, M.; Barancik, M.; Sulova, Z., New insight into p-glycoprotein as a drug target. *Anticancer Agents Med Chem* **2013,** *13* (1), 159-70.

63. Lehne, G., P-glycoprotein as a drug target in the treatment of multidrug resistant cancer. *Current drug targets* **2000,** *1* (1), 85-99.

64. Xiao, H.; Woods, E. C.; Vukojicic, P.; Bertozzi, C. R., Precision glycocalyx editing as a strategy for cancer immunotherapy. *Proceedings of the National Academy of Sciences* **2016,** *113* (37), 10304-10309.

65. Minko, T., Drug targeting to the colon with lectins and neoglycoconjugates. *Adv Drug Deliv Rev* **2004,** *56* (4), 491-509.

66. Xu, H.; Yu, Y.; Marciniak, D.; Rishi, A. K.; Sarkar, F. H.; Kucuk, O.; Majumdar, A. P., Epidermal growth factor receptor (EGFR)-related protein inhibits multiple members of the EGFR family in colon and breast cancer cells. *Molecular cancer therapeutics* **2005,** *4* (3), 435-42.

67. Hagner, N.; Joerger, M., Cancer chemotherapy: targeting folic acid synthesis. *Cancer Management and Research* **2010,** *2*, 293-301.

68. Sinha, R.; Kim, G. J.; Nie, S.; Shin, D. M., Nanotechnology in cancer therapeutics: bioconjugated nanoparticles for drug delivery. *Molecular cancer therapeutics* **2006,** *5* (8), 1909-1917.

69. Clark, C. J.; Sage, E. H., A prototypic matricellular protein in the tumor microenvironment--where there's SPARC, there's fire. *Journal of cellular biochemistry* **2008,** *104* (3), 721-32.

70. Whatcott, C. J.; Hanl, H.; Von Hoff, D. D., Orchestrating the Tumor Microenvironment to Improve Survival for Patients With Pancreatic Cancer Normalization, Not Destruction. *Cancer journal (Sudbury, Mass.)* **2015,** *21* (4), 299-306.

71. Cathcart, J.; Pulkoski-Gross, A.; Cao, J., Targeting matrix metalloproteinases in cancer: Bringing new life to old ideas. *Genes & Diseases* **2015,** *2* (1), 26-34.

72. Overall, C. M.; Kleifeld, O., Validating matrix metalloproteinases as drug targets and anti-targets for cancer therapy. *Nature Reviews Cancer* **2006,** *6*, 227.

73. Vandooren, J.; Opdenakker, G.; Loadman, P. M.; Edwards, D. R., Proteases in cancer drug delivery. *Adv Drug Deliv Rev* **2016,** *97*, 144-55.

74. Choi, K. Y.; Swierczewska, M.; Lee, S.; Chen, X., Protease-Activated Drug Development. *Theranostics* **2012,** *2* (2), 156-178.

75. Sato, T.; Takahashi, S.; Mizumoto, T.; Harao, M.; Akizuki, M.; Takasugi, M.; Fukutomi, T.; Yamashita, J., Neutrophil elastase and cancer. *Surgical oncology* **2006,** *15* (4), 217-22.

76. Hunt, K. K.; Wingate, H.; Yokota, T.; Liu, Y.; Mills, G. B.; Zhang, F.; Fang, B.; Su, C.-H.; Zhang, M.; Yi, M.; Keyomarsi, K., Elafin, an inhibitor of elastase, is a prognostic indicator in breast cancer. *Breast Cancer Research : BCR* **2013,** *15* (1), R3-R3.

77. Sun, Z.; Yang, P., Role of imbalance between neutrophil elastase and α1-antitrypsin in cancer development and progression. *The Lancet Oncology* **2004,** *5* (3), 182-190.

78. Landskron, G.; De la Fuente, M.; Thuwajit, P.; Thuwajit, C.; Hermoso, M. A., Chronic Inflammation and Cytokines in the Tumor Microenvironment. *Journal of Immunology Research* **2014,** *2014*, 19.

79. Mocellin, S.; Wang, E.; Marincola, F. M., Cytokines and immune response in the tumor microenvironment. *Journal of immunotherapy (Hagerstown, Md. : 1997)* **2001,** *24* (5), 392-407.

80. Larsen, M. T.; Kuhlmann, M.; Hvam, M. L.; Howard, K. A., Albumin-based drug delivery: harnessing nature to cure disease. *Molecular and Cellular Therapies* **2016,** *4*, 3.

81. Callmann, C. E.; Gianneschi, N. C., Enzyme-Responsive Nanoparticles for the Treatment of Disease. In *Biomedical Nanotechnology: Methods and Protocols*, Petrosko, S. H.; Day, E. S., Eds. Springer New York: New York, NY, 2017; pp 223-238.

82. Chien, M.-P.; Carlini, A. S.; Hu, D.; Barback, C. V.; Rush, A. M.; Hall, D. J.; Orr, G.; Gianneschi, N. C., Enzyme-Directed Assembly of Nanoparticles in Tumors Monitored by in Vivo Whole Animal Imaging and ex Vivo Super-Resolution Fluorescence Imaging. *Journal of the American Chemical Society* **2013,** *135* (50), 18710-18713.

83. Chien, M.-P.; Thompson, M. P.; Barback, C. V.; Ku, T.-H.; Hall, D. J.; Gianneschi, N. C., Enzyme-Directed Assembly of a Nanoparticle Probe in Tumor Tissue. *Advanced Materials* **2013,** *25* (26), 3599-3604.

84. Chien, M.-P.; Thompson, M. P.; Lin, E. C.; Gianneschi, N. C., Fluorogenic enzyme-responsive micellar nanoparticles. *Chemical Science* **2012,** *3* (9), 2690-2694.

85. Daniel, K. B.; Callmann, C. E.; Gianneschi, N. C.; Cohen, S. M., Dual-responsive nanoparticles release cargo upon exposure to matrix metalloproteinase and reactive oxygen species. *Chemical Communications* **2016,** *52* (10), 2126-2128.

86. DeFeo-Jones, D.; Garsky, V. M.; Wong, B. K.; Feng, D. M.; Bolyar, T.; Haskell, K.; Kiefer, D. M.; Leander, K.; McAvoy, E.; Lumma, P.; Wai, J.; Senderak, E. T.; Motzel, S. L.; Keenan, K.; Van Zwieten, M.; Lin, J. H.; Freidinger, R.; Huff, J.; Oliff, A.; Jones, R. E., A peptide-doxorubicin 'prodrug' activated by prostate-specific antigen selectively kills prostate tumor cells positive for prostate-specific antigen in vivo. *Nature medicine* **2000,** *6* (11), 1248-52.

87. Tang, H.; Qiao, J.; Fu, Y. X., Immunotherapy and tumor microenvironment. *Cancer letters* **2016,** *370* (1), 85-90.

88. Vander Heiden, M. G.; Cantley, L. C.; Thompson, C. B., Understanding the Warburg Effect: The Metabolic Requirements of Cell Proliferation. *Science* **2009,** *324* (5930), 1029-1033.

89. Kim, J.-w.; Dang, C. V., Cancer's Molecular Sweet Tooth and the Warburg Effect. *Cancer research* **2006,** *66* (18), 8927-8930.

90. Brown, J. M., Tumor hypoxia in cancer therapy. *Methods in enzymology* **2007,** *435*, 297-321.

91. Semenza, G. L., The hypoxic tumor microenvironment: A driving force for breast cancer progression. *Biochimica et Biophysica Acta (BBA) - Molecular Cell Research* **2016,** *1863* (3), 382-391.

92. Griffiths, J. R., Are cancer cells acidic? *British Journal of Cancer* **1991,** *64* (3), 425-427.

93. Kato, Y.; Ozawa, S.; Miyamoto, C.; Maehata, Y.; Suzuki, A.; Maeda, T.; Baba, Y., Acidic extracellular microenvironment and cancer. *Cancer Cell International* **2013,** *13*, 89-89.

94. Tannock, I. F.; Rotin, D., Acid pH in tumors and its potential for therapeutic exploitation. *Cancer research* **1989,** *49* (16), 4373-84.

95. Acharya, A.; Das, I.; Chandhok, D.; Saha, T., Redox regulation in cancer: A double-edged sword with therapeutic potential. *Oxidative Medicine and Cellular Longevity* **2010,** *3* (1), 23-34.

96. Cook, J. A.; Gius, D.; Wink, D. A.; Krishna, M. C.; Russo, A.; Mitchell, J. B., Oxidative stress, redox, and the tumor microenvironment. *Seminars in radiation oncology* **2004,** *14* (3), 259-66.

97. Wigerup, C.; Påhlman, S.; Bexell, D., Therapeutic targeting of hypoxia and hypoxia-inducible factors in cancer. *Pharmacology & Therapeutics* **2016,** *164* (Supplement C), 152-169.

98. Semenza, G. L., Targeting HIF-1 for cancer therapy. *Nature reviews. Cancer* **2003,** *3* (10), 721-32.

99. Du, J.-Z.; Du, X.-J.; Mao, C.-Q.; Wang, J., Tailor-Made Dual pH-Sensitive Polymer–Doxorubicin Nanoparticles for Efficient Anticancer Drug Delivery. *Journal of the American Chemical Society* **2011,** *133* (44), 17560-17563.

100. Lv, Y.; Hao, L.; Hu, W.; Ran, Y.; Bai, Y.; Zhang, L., Novel multifunctional pH-sensitive nanoparticles loaded into microbubbles as drug delivery vehicles for enhanced tumor targeting. *Scientific Reports* **2016,** *6*, 29321.

101. She, W.; Luo, K.; Zhang, C.; Wang, G.; Geng, Y.; Li, L.; He, B.; Gu, Z., The potential of self-assembled, pH-responsive nanoparticles of mPEGylated peptide dendron–doxorubicin conjugates for cancer therapy. *Biomaterials* **2013,** *34* (5), 1613-1623.

102. Zhou, K.; Wang, Y.; Huang, X.; Luby-Phelps, K. K.; Sumer, B. D.; Gao, J., Tunable, Ultra-Sensitive pH Responsive Nanoparticles Targeting Specific Endocytic Organelles in Living Cells. *Angewandte Chemie (International ed. in English)* **2011,** *50* (27), 6109-6114.

103. Policastro, L. L.; Ibanez, I. L.; Notcovich, C.; Duran, H. A.; Podhajcer, O. L., The tumor microenvironment: characterization, redox considerations, and novel approaches for reactive oxygen species-targeted gene therapy. *Antioxidants & redox signaling* **2013,** *19* (8), 854-95.

104. Daniel, K. B.; Callmann, C. E.; Gianneschi, N. C.; Cohen, S. M., Dual-responsive nanoparticles release cargo upon exposure to matrix metalloproteinase and reactive oxygen species. *Chemical communications (Cambridge, England)* **2016,** *52* (10), 2126-8.

105. Vander Heiden, M. G., Exploiting tumor metabolism: challenges for clinical translation. *The Journal of Clinical Investigation* **2013,** *123* (9), 3648-3651.

106. DeBerardinis, R. J.; Chandel, N. S., Fundamentals of cancer metabolism. *Science Advances* **2016,** *2* (5), e1600200.

107. Vander Heiden, M. G.; Cantley, L. C.; Thompson, C. B., Understanding the Warburg Effect: The Metabolic Requirements of Cell Proliferation. *Science (New York, N.Y.)* **2009,** *324* (5930), 1029-1033.

108. Carracedo, A.; Cantley, L. C.; Pandolfi, P. P., Cancer metabolism: fatty acid oxidation in the limelight. *Nature reviews. Cancer* **2013,** *13* (4), 227-232.

109. Currie, E.; Schulze, A.; Zechner, R.; Walther, T. C.; Farese, R. V., Cellular Fatty Acid Metabolism and Cancer. *Cell metabolism* **2013,** *18* (2), 153-161.

110. Trajkovska, M., Macropinocytosis supports cancer cell proliferation. *Nature Cell Biology* **2013,** *15*, 729.

111. Cantor, J. R.; Sabatini, D. M., Cancer Cell Metabolism: One Hallmark, Many Faces. *Cancer Discovery* **2012,** *2* (10), 881-898.

112. Currie, E.; Schulze, A.; Zechner, R.; Walther, T. C.; Farese, R. V., Jr., Cellular fatty acid metabolism and cancer. *Cell Metab* **2013,** *18* (2), 153-61.

113. Carracedo, A.; Cantley, L. C.; Pandolfi, P. P., Cancer metabolism: fatty acid oxidation in the limelight. *Nature reviews. Cancer* **2013,** *13* (4), 227-32.

114. Dvorak, H. F.; Nagy, J. A.; Dvorak, J. T.; Dvorak, A. M., Identification and characterization of the blood vessels of solid tumors that are leaky to circulating macromolecules. *The American Journal of Pathology* **1988,** *133* (1), 95-109.

115. Matsumura, Y.; Maeda, H., A new concept for macromolecular therapeutics in cancer chemotherapy: mechanism of tumoritropic accumulation of proteins and the antitumor agent smancs. *Cancer research* **1986,** *46* (12 Pt 1), 6387-92.

116. Ragelle, H.; Danhier, F.; Preat, V.; Langer, R.; Anderson, D. G., Nanoparticle-based drug delivery systems: a commercial and regulatory outlook as the field matures. *Expert opinion on drug delivery* **2017,** *14* (7), 851-864.

117. Greish, K., Enhanced permeability and retention of macromolecular drugs in solid tumors: a royal gate for targeted anticancer nanomedicines. *Journal of drug targeting* **2007,** *15* (7-8), 457-64.

118. Barenholz, Y., Doxil(R)--the first FDA-approved nano-drug: lessons learned. *Journal of controlled release : official journal of the Controlled Release Society* **2012,** *160* (2), 117-34.

119. Nichols, J. W.; Bae, Y. H., EPR: Evidence and fallacy. *Journal of Controlled Release* **2014,** *190* (Supplement C), 451-464.

120. Nakamura, Y.; Mochida, A.; Choyke, P. L.; Kobayashi, H., Nanodrug Delivery: Is the Enhanced Permeability and Retention Effect Sufficient for Curing Cancer? *Bioconjug Chem* **2016,** *27* (10), 2225-2238.

121. Jain, R. K.; Stylianopoulos, T., Delivering nanomedicine to solid tumors. *Nature Reviews Clinical Oncology* **2010,** *7*, 653.

122. Shi, J.; Kantoff, P. W.; Wooster, R.; Farokhzad, O. C., Cancer nanomedicine: progress, challenges and opportunities. *Nature Reviews Cancer* **2016,** *17*, 20.

123. Stirland, D. L.; Nichols, J. W.; Miura, S.; Bae, Y. H., Mind the gap: A survey of how cancer drug carriers are susceptible to the gap between research and practice. *Journal of Controlled Release* **2013,** *172* (3), 1045-1064.

124. Wilhelm, S.; Tavares, A. J.; Dai, Q.; Ohta, S.; Audet, J.; Dvorak, H. F.; Chan, W. C. W., Analysis of nanoparticle delivery to tumours. *Nature Reviews Materials* **2016,** *1*, 16014.

125. Wilhelm, S.; Tavares, A. J.; Chan, W. C. W., Reply to “Evaluation of nanomedicines: stick to the basics”. *Nature Reviews Materials* **2016,** *1*, 16074.

126. Monopoli, M. P.; Åberg, C.; Salvati, A.; Dawson, K. A., Biomolecular coronas provide the biological identity of nanosized materials. *Nature Nanotechnology* **2012,** *7*, 779.

127. Dobrovolskaia, M. A.; McNeil, S. E., Immunological properties of engineered nanomaterials. *Nat Nanotechnol* **2007,** *2* (8), 469-78.

128. Aggarwal, P.; Hall, J. B.; McLeland, C. B.; Dobrovolskaia, M. A.; McNeil, S. E., Nanoparticle interaction with plasma proteins as it relates to particle biodistribution, biocompatibility and therapeutic efficacy. *Adv Drug Deliv Rev* **2009,** *61* (6), 428-37.

129. Dobrovolskaia, M. A.; Aggarwal, P.; Hall, J. B.; McNeil, S. E., Preclinical studies to understand nanoparticle interaction with the immune system and its potential effects on nanoparticle biodistribution. *Molecular pharmaceutics* **2008,** *5* (4), 487-95.

130. Jiang, T.; Olson, E. S.; Nguyen, Q. T.; Roy, M.; Jennings, P. A.; Tsien, R. Y., Tumor imaging by means of proteolytic activation of cell-penetrating peptides. *Proceedings of the National Academy of Sciences of the United States of America* **2004,** *101* (51), 17867-17872.

131. Olson, E. S.; Jiang, T.; Aguilera, T. A.; Nguyen, Q. T.; Ellies, L. G.; Scadeng, M.; Tsien, R. Y., Activatable cell penetrating peptides linked to nanoparticles as dual probes for in vivo fluorescence and MR imaging of proteases. *Proc Natl Acad Sci U S A* **2010,** *107* (9), 4311-6.

132. Olson, E. S.; Aguilera, T. A.; Jiang, T.; Ellies, L. G.; Nguyen, Q. T.; Wong, E. H.; Gross, L. A.; Tsien, R. Y., In vivo characterization of activatable cell penetrating peptides for targeting protease activity in cancer. *Integrative biology : quantitative biosciences from nano to macro* **2009,** *1* (5-6), 382-93.

133. Maynard, H. D.; Okada, S. Y.; Grubbs, R. H., Synthesis of Norbornenyl Polymers with Bioactive Oligopeptides by Ring-Opening Metathesis Polymerization. *Macromolecules* **2000,** *33* (17), 6239-6248.

134. Biagini, S. C. G.; Parry, A. L., Investigation into the ROMP copolymerization of peptide- and PEG-functionalized norbornene derivatives. *Journal of Polymer Science Part A: Polymer Chemistry* **2007,** *45* (15), 3178-3190.

135. Breitenkamp, R. B.; Ou, Z.; Breitenkamp, K.; Muthukumar, M.; Emrick, T., Synthesis and Characterization of Polyolefin-graft-oligopeptide Polyelectrolytes. *Macromolecules* **2007,** *40* (21), 7617-7624.

136. Conrad, R. M.; Grubbs, R. H., Tunable, Temperature-Responsive Polynorbornenes with Side Chains Based on an Elastin Peptide Sequence. *Angewandte Chemie International Edition* **2009,** *48* (44), 8328-8330.

137. Roberts, K. S.; Sampson, N. S., Increased Polymer Length of Oligopeptide-Substituted Polynorbornenes with LiCl. *The Journal of Organic Chemistry* **2003,** *68* (5), 2020-2023.

138. Parry, A. L.; Bomans, P. H. H.; Holder, S. J.; Sommerdijk, N. A. J. M.; Biagini, S. C. G., Cryo Electron Tomography Reveals Confined Complex Morphologies of Tripeptide-Containing Amphiphilic Double-Comb Diblock Copolymers. *Angewandte Chemie International Edition* **2008,** *47* (46), 8859-8862.

139. Haselwander, T. F. A.; Heitz, W.; Krügel, S. A.; Wendorff, J. H., Polynorbornene: synthesis, properties and simulations. *Macromolecular Chemistry and Physics* **1996,** *197* (10), 3435-3453.

140. Hopkins, T. E.; Wagener, K. B., ADMET Synthesis of Polyolefins Targeted for Biological Applications. *Macromolecules* **2004,** *37* (4), 1180-1189.

141. Patel, P. R.; Kiser, R. C.; Lu, Y. Y.; Fong, E.; Ho, W. C.; Tirrell, D. A.; Grubbs, R. H., Synthesis and Cell Adhesive Properties of Linear and Cyclic RGD Functionalized Polynorbornene Thin Films. *Biomacromolecules* **2012,** *13* (8), 2546-2553.

142. Kammeyer, J. K.; Blum, A. P.; Adamiak, L.; Hahn, M. E.; Gianneschi, N. C., Polymerization of protecting-group-free peptides via ROMP. *Polymer Chemistry* **2013,** *4* (14), 3929-3933.

143. Bielawski, C. W.; Grubbs, R. H., Living ring-opening metathesis polymerization. *Progress in Polymer Science* **2007,** *32* (1), 1-29.

144. Sanford, M. S.; Love, J. A.; Grubbs, R. H., Mechanism and Activity of Ruthenium Olefin Metathesis Catalysts. *Journal of the American Chemical Society* **2001,** *123* (27), 6543-6554.

145. Sanford, M. S.; Love, J. A.; Grubbs, R. H., A Versatile Precursor for the Synthesis of New Ruthenium Olefin Metathesis Catalysts. *Organometallics* **2001,** *20* (25), 5314-5318.

146. Bielawski, C. W.; Grubbs, R. H., Highly Efficient Ring-Opening Metathesis Polymerization (ROMP) Using New Ruthenium Catalysts Containing N-Heterocyclic Carbene Ligands. *Angewandte Chemie International Edition* **2000,** *39* (16), 2903-2906.

147. Walker, R.; Conrad, R. M.; Grubbs, R. H., The Living ROMP of trans-Cyclooctene. *Macromolecules* **2009,** *42* (3), 599-605.

148. Blum, A. P.; Kammeyer, J. K.; Yin, J.; Crystal, D. T.; Rush, A. M.; Gilson, M. K.; Gianneschi, N. C., Peptides Displayed as High Density Brush Polymers Resist Proteolysis and Retain Bioactivity. *Journal of the American Chemical Society* **2014,** *136* (43), 15422-15437.

149. Ku, T.-H.; Chien, M.-P.; Thompson, M. P.; Sinkovits, R. S.; Olson, N. H.; Baker, T. S.; Gianneschi, N. C., Controlling and Switching the Morphology of Micellar Nanoparticles with Enzymes. *Journal of the American Chemical Society* **2011,** *133* (22), 8392-8395.

150. Nguyen, M. M.; Carlini, A. S.; Chien, M.-P.; Sonnenberg, S.; Luo, C.; Braden, R. L.; Osborn, K. G.; Li, Y.; Gianneschi, N. C.; Christman, K. L., Enzyme-Responsive Nanoparticles for Targeted Accumulation and Prolonged Retention in Heart Tissue after Myocardial Infarction. *Advanced Materials* **2015,** *27* (37), 5547-5552.

151. Ungerleider, J. L.; Kammeyer, J. K.; Braden, R. L.; Christman, K. L.; Gianneschi, N. C., Enzyme-targeted nanoparticles for delivery to ischemic skeletal muscle. *Polymer Chemistry* **2017,** *8* (34), 5212-5219.

152. Rush, A. M.; Thompson, M. P.; Tatro, E. T.; Gianneschi, N. C., Nuclease-Resistant DNA via High-Density Packing in Polymeric Micellar Nanoparticle Coronas. *ACS Nano* **2013,** *7* (2), 1379-1387.

153. Chien, M.-P.; Thompson, M. P.; Gianneschi, N. C., DNA-nanoparticle micelles as supramolecular fluorogenic substrates enabling catalytic signal amplification and detection by DNAzyme probes. *Chemical Communications* **2011,** *47* (1), 167-169.

154. Chien, M.-P.; Rush, A. M.; Thompson, M. P.; Gianneschi, N. C., Programmable Shape-Shifting Micelles. *Angewandte Chemie International Edition* **2010,** *49* (30), 5076-5080.

155. James, C. R.; Rush, A. M.; Insley, T.; Vuković, L.; Adamiak, L.; Král, P.; Gianneschi, N. C., Poly(oligonucleotide). *Journal of the American Chemical Society* **2014,** *136* (32), 11216-11219.

156. Rush, A. M.; Nelles, D. A.; Blum, A. P.; Barnhill, S. A.; Tatro, E. T.; Yeo, G. W.; Gianneschi, N. C., Intracellular mRNA Regulation with Self-Assembled Locked Nucleic Acid Polymer Nanoparticles. *Journal of the American Chemical Society* **2014,** *136* (21), 7615-7618.

157. Roloff, A.; Carlini, A. S.; Callmann, C. E.; Gianneschi, N. C., Micellar Thrombin-Binding Aptamers: Reversible Nanoscale Anticoagulants. *Journal of the American Chemical Society* **2017,** *139* (46), 16442-16445.

158. Coles, M. P.; Gibson, V. C.; Mazzariol, L.; North, M.; Teasdale, W. G.; Williams, C. M.; Zamuner, D., Amino acid derived homochiral polymers via ring-opening metathesis polymerisation. *Journal of the Chemical Society, Chemical Communications* **1994,** (21), 2505-2506.

159. C. G. Biagini, S.; Gareth Davies, R.; North, M.; C. Gibson, V.; R. Giles, M.; L. Marshall, E.; A. Robson, D., The synthesis and ring-opening metathesis polymerization of peptide functionalized norbornenes. *Chemical Communications* **1999,** (3), 235-236.

160. Ayres, L.; Vos, M. R. J.; Adams, P. J. H. M.; Shklyarevskiy, I. O.; van Hest, J. C. M., Elastin-Based Side-Chain Polymers Synthesized by ATRP. *Macromolecules* **2003,** *36* (16), 5967-5973.

161. Hahn, M. E.; Randolph, L. M.; Adamiak, L.; Thompson, M. P.; Gianneschi, N. C., Polymerization of a peptide-based enzyme substrate. *Chemical Communications* **2013,** *49* (28), 2873-2875.

162. Gregoriadis, G.; Jain, S.; Papaioannou, I.; Laing, P., Improving the therapeutic efficacy of peptides and proteins: A role for polysialic acids. *International Journal of Pharmaceutics* **2005,** *300* (1), 125-130.

163. Didenko, V. V., DNA Probes Using Fluorescence Resonance Energy Transfer (FRET): Designs and Applications. *BioTechniques* **2001,** *31* (5), 1106-1121.

164. Morodomi, T.; Ogata, Y.; Sasaguri, Y.; Morimatsu, M.; Nagase, H., Purification and characterization of matrix metalloproteinase 9 from U937 monocytic leukaemia and HT1080 fibrosarcoma cells. *The Biochemical journal* **1992,** *285 (Pt 2)*, 603-11.

165. Phatharajaree, W.; Phrommintikul, A.; Chattipakorn, N., Matrix metalloproteinases and myocardial infarction. *The Canadian Journal of Cardiology* **2007,** *23* (9), 727-733.

166. Horwitz, L. D.; Kaufman, D.; Keller, M. W.; Kong, Y., Time course of coronary endothelial healing after injury due to ischemia and reperfusion. *Circulation* **1994,** *90* (5), 2439-47.

167. Elsadek, B.; Kratz, F., Impact of albumin on drug delivery--new applications on the horizon. *Journal of controlled release : official journal of the Controlled Release Society* **2012,** *157* (1), 4-28.

168. Milici, A. J.; Watrous, N. E.; Stukenbrok, H.; Palade, G. E., Transcytosis of albumin in capillary endothelium. *The Journal of cell biology* **1987,** *105* (6 Pt 1), 2603-12.

169. Schnitzer, J. E., gp60 is an albumin-binding glycoprotein expressed by continuous endothelium involved in albumin transcytosis. *The American journal of physiology* **1992,** *262* (1 Pt 2), H246-54.

170. Schnitzer, J. E.; Oh, P., Albondin-mediated capillary permeability to albumin. Differential role of receptors in endothelial transcytosis and endocytosis of native and modified albumins. *The Journal of biological chemistry* **1994,** *269* (8), 6072-82.

171. Tiruppathi, C.; Finnegan, A.; Malik, A. B., Isolation and characterization of a cell surface albumin-binding protein from vascular endothelial cells. *Proc Natl Acad Sci U S A* **1996,** *93* (1), 250-4.

172. Schnitzer, J. E.; Oh, P., Antibodies to SPARC inhibit albumin binding to SPARC, gp60, and microvascular endothelium. *The American journal of physiology* **1992,** *263* (6 Pt 2), H1872-9.

173. Porter, P. L.; Sage, E. H.; Lane, T. F.; Funk, S. E.; Gown, A. M., Distribution of SPARC in normal and neoplastic human tissue. *The journal of histochemistry and cytochemistry : official journal of the Histochemistry Society* **1995,** *43* (8), 791-800.

174. Podhajcer, O. L.; Benedetti, L. G.; Girotti, M. R.; Prada, F.; Salvatierra, E.; Llera, A. S., The role of the matricellular protein SPARC in the dynamic interaction between the tumor and the host. *Cancer metastasis reviews* **2008,** *27* (4), 691-705.

175. Desai, N. P.; Trieu, V.; Hwang, L. Y.; Wu, R.; Soon-Shiong, P.; Gradishar, W. J., Improved effectiveness of nanoparticle albumin-bound (nab) paclitaxel versus polysorbate-based docetaxel in multiple xenografts as a function of HER2 and SPARC status. *Anti-cancer drugs* **2008,** *19* (9), 899-909.

176. Desai, N.; Trieu, V.; Damascelli, B.; Soon-Shiong, P., SPARC Expression Correlates with Tumor Response to Albumin-Bound Paclitaxel in Head and Neck Cancer Patients. *Translational oncology* **2009,** *2* (2), 59-64.

177. Gundewar, C.; Sasor, A.; Hilmersson, K. S.; Andersson, R.; Ansari, D., The role of SPARC expression in pancreatic cancer progression and patient survival. *Scandinavian Journal of Gastroenterology* **2015,** *50* (9), 1170-1174.

178. Zhao, Z. S.; Wang, Y. Y.; Chu, Y. Q.; Ye, Z. Y.; Tao, H. Q., SPARC is associated with gastric cancer progression and poor survival of patients. *Clin Cancer Res* **2010,** *16* (1), 260-8.

179. Huang, Y.; Zhang, J.; Zhao, Y.-Y.; Jiang, W.; Xue, C.; Xu, F.; Zhao, H.-Y.; Zhang, Y.; Zhao, L.-P.; Hu, Z.-H.; Yao, Z.-W.; Liu, Q.-Y.; Zhang, L., SPARC expression and prognostic value in non-small cell lung cancer. *Chinese Journal of Cancer* **2012,** *31* (11), 541-548.

180. Chin, D.; Boyle, G. M.; Williams, R. M.; Ferguson, K.; Pandeya, N.; Pedley, J.; Campbell, C. M.; Theile, D. R.; Parsons, P. G.; Coman, W. B., Novel markers for poor prognosis in head and neck cancer. *International journal of cancer* **2005,** *113* (5), 789-97.

181. Jo, J.; Song, M. G.; Park, J. Y.; Youn, H.; Chung, J.-K.; Jeong, J. M.; Lee, Y.-S.; Kang, K. W., Fluorescence labeled human serum albumin as an imaging agent for a SPARC(secreted protein acidic and rich in cysteine) expressing glioblastoma. *Journal of Nuclear Medicine* **2017,** *58* (supplement 1), 53.

182. Commisso, C.; Davidson, S. M.; Soydaner-Azeloglu, R. G.; Parker, S. J.; Kamphorst, J. J.; Hackett, S.; Grabocka, E.; Nofal, M.; Drebin, J. A.; Thompson, C. B.; Rabinowitz, J. D.; Metallo, C. M.; Vander Heiden, M. G.; Bar-Sagi, D., Macropinocytosis of protein is an amino acid supply route in Ras-transformed cells. *Nature* **2013,** *497* (7451), 633-7.

183. White, E., Exploiting the bad eating habits of Ras-driven cancers. *Genes & Development* **2013,** *27* (19), 2065-2071.

184. Hradec, J., Metabolism of serum albumin in tumour-bearing rats. *Br J Cancer* **1958,** *12* (2), 290-304.

185. Andersson, C.; Iresjo, B. M.; Lundholm, K., Identification of tissue sites for increased albumin degradation in sarcoma-bearing mice. *The Journal of surgical research* **1991,** *50* (2), 156-62.

186. Schilling, U.; Friedrich, E. A.; Sinn, H.; Schrenk, H. H.; Clorius, J. H.; Maier-Borst, W., Design of compounds having enhanced tumour uptake, using serum albumin as a carrier--Part II. In vivo studies. *International journal of radiation applications and instrumentation. Part B, Nuclear medicine and biology* **1992,** *19* (6), 685-95.

187. Stehle, G.; Sinn, H.; Wunder, A.; Schrenk, H. H.; Stewart, J. C.; Hartung, G.; Maier-Borst, W.; Heene, D. L., Plasma protein (albumin) catabolism by the tumor itself--implications for tumor metabolism and the genesis of cachexia. *Critical reviews in oncology/hematology* **1997,** *26* (2), 77-100.

188. Yang, C.; Ko, B.; Hensley, Christopher T.; Jiang, L.; Wasti, Ajla T.; Kim, J.; Sudderth, J.; Calvaruso, Maria A.; Lumata, L.; Mitsche, M.; Rutter, J.; Merritt, Matthew E.; DeBerardinis, Ralph J., Glutamine Oxidation Maintains the TCA Cycle and Cell Survival during Impaired Mitochondrial Pyruvate Transport. *Molecular Cell 56* (3), 414-424.

189. Guarente, L., The Many Faces of Sirtuins: Sirtuins and the Warburg effect. *Nature medicine* **2014,** *20*, 24.

190. Omabe, M.; Ezeani, M.; Omabe, K. N., Lipid metabolism and cancer progression: The missing target in metastatic cancer treatment. *Journal of Applied Biomedicine* **2015,** *13* (1), 47-59.

191. Liu, Q.; Luo, Q.; Halim, A.; Song, G., Targeting lipid metabolism of cancer cells: A promising therapeutic strategy for cancer. *Cancer letters* **2017,** *401*, 39-45.

192. Baenke, F.; Peck, B.; Miess, H.; Schulze, A., Hooked on fat: the role of lipid synthesis in cancer metabolism and tumour development. *Disease Models & Mechanisms* **2013,** *6* (6), 1353.

193. Beloribi-Djefaflia, S.; Vasseur, S.; Guillaumond, F., Lipid metabolic reprogramming in cancer cells. *Oncogenesis* **2016,** *5*, e189.

194. Santos, C. R.; Schulze, A., Lipid metabolism in cancer. *FEBS Journal* **2012,** *279* (15), 2610-2623.

195. Guaita-Esteruelas, S.; Bosquet, A.; Saavedra, P.; Guma, J.; Girona, J.; Lam, E. W.; Amillano, K.; Borras, J.; Masana, L., Exogenous FABP4 increases breast cancer cell proliferation and activates the expression of fatty acid transport proteins. *Molecular carcinogenesis* **2017,** *56* (1), 208-217.

196. Nieman, K. M.; Kenny, H. A.; Penicka, C. V.; Ladanyi, A.; Buell-Gutbrod, R.; Zillhardt, M. R.; Romero, I. L.; Carey, M. S.; Mills, G. B.; Hotamisligil, G. S.; Yamada, S. D.; Peter, M. E.; Gwin, K.; Lengyel, E., Adipocytes promote ovarian cancer metastasis and provide energy for rapid tumor growth. *Nature medicine* **2011,** *17*, 1498.

197. Harjes, U.; Bridges, E.; McIntyre, A.; Fielding, B. A.; Harris, A. L., Fatty acid binding protein 4, a point of convergence for angiogenic and metabolic signalling pathways in endothelial cells. *Journal of Biological Chemistry* **2014**.

198. Pascual, G.; Avgustinova, A.; Mejetta, S.; Martín, M.; Castellanos, A.; Attolini, C. S.-O.; Berenguer, A.; Prats, N.; Toll, A.; Hueto, J. A.; Bescós, C.; Di Croce, L.; Benitah, S. A., Targeting metastasis-initiating cells through the fatty acid receptor CD36. *Nature* **2016,** *541*, 41.

199. Hale, J. S.; Otvos, B.; Sinyuk, M.; Alvarado, A. G.; Hitomi, M.; Stoltz, K.; Wu, Q.; Flavahan, W.; Levison, B.; Johansen, M. L.; Schmitt, D.; Neltner, J. M.; Huang, P.; Ren, B.; Sloan, A. E.; Silverstein, R. L.; Gladson, C. L.; DiDonato, J. A.; Brown, J. M.; McIntyre, T.; Hazen, S. L.; Horbinski, C.; Rich, J. N.; Lathia, J. D., Cancer stem cell-specific scavenger receptor CD36 drives glioblastoma progression. *Stem cells (Dayton, Ohio)* **2014,** *32* (7), 1746-1758.

200. Curry, S.; Brick, P.; Franks, N. P., Fatty acid binding to human serum albumin: new insights from crystallographic studies. *Biochimica et biophysica acta* **1999,** *1441* (2-3), 131-40.

201. van der Vusse, G. J., Albumin as fatty acid transporter. *Drug metabolism and pharmacokinetics* **2009,** *24* (4), 300-7.

202. Petitpas, I.; Bhattacharya, A. A.; Twine, S.; East, M.; Curry, S., Crystal Structure Analysis of Warfarin Binding to Human Serum Albumin: ANATOMY OF DRUG SITE I. *Journal of Biological Chemistry* **2001,** *276* (25), 22804-22809.

203. SUDLOW, G.; BIRKETT, D. J.; WADE, D. N., Further Characterization of Specific Drug Binding Sites on Human Serum Albumin. *Molecular Pharmacology* **1976,** *12* (6), 1052-1061.

204. Hein, K. L.; Kragh-Hansen, U.; Morth, J. P.; Jeppesen, M. D.; Otzen, D.; Møller, J. V.; Nissen, P., Crystallographic analysis reveals a unique lidocaine binding site on human serum albumin. *Journal of Structural Biology* **2010,** *171* (3), 353-360.

205. Neumann, E.; Frei, E.; Funk, D.; Becker, M. D.; Schrenk, H.-H.; Müller-Ladner, U.; Fiehn, C., Native albumin for targeted drug delivery. *Expert opinion on drug delivery* **2010,** *7* (8), 915-925.

206. Kratz, F., Albumin as a drug carrier: design of prodrugs, drug conjugates and nanoparticles. *Journal of controlled release : official journal of the Controlled Release Society* **2008,** *132* (3), 171-83.

207. Caravan, P., Strategies for increasing the sensitivity of gadolinium based MRI contrast agents. *Chemical Society reviews* **2006,** *35* (6), 512-23.

208. Liu, Z.; Chen, X., Simple bioconjugate chemistry serves great clinical advances: albumin as a versatile platform for diagnosis and precision therapy. *Chemical Society reviews* **2016,** *45* (5), 1432-1456.

209. Caravan, P.; Cloutier, N. J.; Greenfield, M. T.; McDermid, S. A.; Dunham, S. U.; Bulte, J. W.; Amedio, J. C., Jr.; Looby, R. J.; Supkowski, R. M.; Horrocks, W. D., Jr.; McMurry, T. J.; Lauffer, R. B., The interaction of MS-325 with human serum albumin and its effect on proton relaxation rates. *J Am Chem Soc* **2002,** *124* (12), 3152-62.

210. Yamasaki, K.; Chuang, V. T.; Maruyama, T.; Otagiri, M., Albumin-drug interaction and its clinical implication. *Biochimica et biophysica acta* **2013,** *1830* (12), 5435-43.

211. Sarett, S. M.; Werfel, T. A.; Lee, L.; Jackson, M. A.; Kilchrist, K. V.; Brantley-Sieders, D.; Duvall, C. L., Lipophilic siRNA targets albumin in situ and promotes bioavailability, tumor penetration, and carrier-free gene silencing. *Proceedings of the National Academy of Sciences* **2017,** *114* (32), E6490-E6497.

212. Lacroix, A.; Edwardson, T. G. W.; Hancock, M. A.; Dore, M. D.; Sleiman, H. F., Development of DNA Nanostructures for High-Affinity Binding to Human Serum Albumin. *J Am Chem Soc* **2017,** *139* (21), 7355-7362.

213. Capomaccio, R.; Jimenez, I. O.; Colpo, P.; Gilliland, D.; Ceccone, G.; Rossi, F.; Calzolai, L., Determination of the structure and morphology of gold nanoparticle-HSA protein complexes. *Nanoscale* **2015,** *7* (42), 17653-7.

214. Karimi, M.; Bahrami, S.; Ravari, S. B.; Zangabad, P. S.; Mirshekari, H.; Bozorgomid, M.; Shahreza, S.; Sori, M.; Hamblin, M. R., Albumin nanostructures as advanced drug delivery systems. *Expert opinion on drug delivery* **2016,** *13* (11), 1609-1623.

215. Wang, Y.; Ni, Y., New insight into protein-nanomaterial interactions with UV-visible spectroscopy and chemometrics: human serum albumin and silver nanoparticles. *The Analyst* **2014,** *139* (2), 416-24.

216. Lundqvist, M.; Stigler, J.; Elia, G.; Lynch, I.; Cedervall, T.; Dawson, K. A., Nanoparticle size and surface properties determine the protein corona with possible implications for biological impacts. *Proceedings of the National Academy of Sciences* **2008,** *105* (38), 14265-14270.

217. Verma, A.; Stellacci, F., Effect of surface properties on nanoparticle-cell interactions. *Small (Weinheim an der Bergstrasse, Germany)* **2010,** *6* (1), 12-21.

218. Saptarshi, S. R.; Duschl, A.; Lopata, A. L., Interaction of nanoparticles with proteins: relation to bio-reactivity of the nanoparticle. *Journal of Nanobiotechnology* **2013,** *11* (1), 26.

219. Curry, S.; Mandelkow, H.; Brick, P.; Franks, N., Crystal structure of human serum albumin complexed with fatty acid reveals an asymmetric distribution of binding sites. *Nature structural biology* **1998,** *5* (9), 827-35.

220. Simard, J. R.; Zunszain, P. A.; Hamilton, J. A.; Curry, S., Location of high and low affinity fatty acid binding sites on human serum albumin revealed by NMR drug-competition analysis. *Journal of molecular biology* **2006,** *361* (2), 336-51.

221. Simard, J. R.; Zunszain, P. A.; Ha, C. E.; Yang, J. S.; Bhagavan, N. V.; Petitpas, I.; Curry, S.; Hamilton, J. A., Locating high-affinity fatty acid-binding sites on albumin by x-ray crystallography and NMR spectroscopy. *Proceedings of the National Academy of Sciences of the United States of America* **2005,** *102* (50), 17958-17963.

222. Zunszain, P. A.; Ghuman, J.; McDonagh, A. F.; Curry, S., Crystallographic Analysis of Human Serum Albumin Complexed with 4Z,15E-Bilirubin-IXα. *Journal of molecular biology* **2008,** *381* (2), 394-406.

223. Scheider, W., Dissociation rate of serum albumin-fatty acid complex from stop-flow dielectric study of ligand exchange. *Biophysical Journal* **1978,** *24* (1), 260-262.

224. Schneider, E. K.; Huang, J. X.; Carbone, V.; Han, M.; Zhu, Y.; Nang, S.; Khoo, K. K.; Mak, J.; Cooper, M. A.; Li, J.; Velkov, T., Plasma Protein Binding Structure–Activity

Relationships Related to the N-Terminus of Daptomycin. *ACS Infectious Diseases* **2017,** *3* (3), 249-258.

225. Dong, D.; Xia, G.; Li, Z.; Li, Z., Human Serum Albumin and HER2-Binding Affibody Fusion Proteins for Targeted Delivery of Fatty Acid-Modified Molecules and Therapy. *Molecular pharmaceutics* **2016,** *13* (10), 3370-3380.

226. di Masi, A.; Leboffe, L.; Trezza, V.; Fanali, G.; Coletta, M.; Fasano, M.; Ascenzi, P., Drugs modulate allosterically heme-Fe-recognition by human serum albumin and heme-fe-mediated reactivity. *Current pharmaceutical design* **2015,** *21* (14), 1837-47.

227. Liu, F.; Mu, J.; Xing, B., Recent advances on the development of pharmacotherapeutic agents on the basis of human serum albumin. *Current pharmaceutical design* **2015,** *21* (14), 1866-88.

228. Zhivkova, Z. D., Studies on drug-human serum albumin binding: the current state of the matter. *Current pharmaceutical design* **2015,** *21* (14), 1817-30.

Chapter 2

Enzyme-Responsive Nanomaterials for the Delivery of Cytotoxins

2.1 Enzyme-Directed Assembly of Particle Therapeutics (EDAPT)

2.1.1 Introduction

Targeted therapeutics are designed to accumulate at the site of disease in higher quantities relative to other locations in the body. To achieve this, nanomaterials capable of acting as carriers or reservoirs of therapeutics have been of interest, as they can carry multiple copies of functional small molecules, can display multiple targeting groups on their surface, and are small enough to be safely intravenously administered[1-2]. As discussed in Chapter 1, researchers have traditionally sought long-circulating nanoparticles reliant on passive accumulation via the enhanced permeability and retention (EPR) effect[3] or "specific" targeting by incorporation of targeting groups[4]. However, despite this, nanoparticles frequently suffer low degrees of penetration and poor retention in tumor tissue, leading to poor performance[5]. Indeed, in published analyses of available data from across the field, it has been revealed that

less than 0.1% of intravenously administered nanoparticles typically reach neoplastic cells inside the tumor[5-7]. This means that the vast majority of systems do not appreciably alter the therapeutic index of the drug they are carrying versus standard delivery approaches. Clearly, significant challenges face current nanomedicine strategies, with a need for new approaches to address those challenges.

Our group has sought to address the challenge of poor particle accumulation and retention in tumor tissue by developing an entirely different targeting strategy for amplified accumulation of nanoparticles by virtue of a supramolecular assembly event specific to tumor tissue, occurring in response to a specific signal. We term this platform **"Enzyme Directed Assembly of Particle Therapeutics" (EDAPT)**. These phase-changing EDAPT materials undergo physical trapping within tumor tissue. We hypothesized that the most desirable approach to stimuli-induced targeting is to utilize an *endogenous* signal, specific to the diseased tissue itself, capable of actively targeting materials introduced via intravenous (IV) injection [8]. We have developed nanoparticles capable of assembling *in vivo*, in tumors, in response to selective, endogenous, biomolecular signals. We utilize enzymes as stimuli, rather than other recognition events, because they are uniquely capable of propagating a signal via catalytic amplification. The enzymes are matrix metalloproteinases (MMPs), known to be overexpressed in many aggressive cancers[9-10].

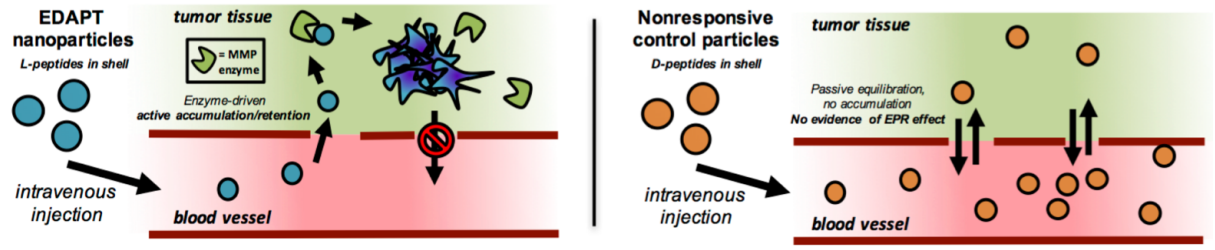

Figure 2.1.1. Schematic representation of enzyme-driven assembly. Enzyme-responsive nanomaterials (EDAPT), whose shells contain *L*-peptides, form large assemblies in response to MMP enzymes upregulated in the tumor space, leading to a physical, morphology change to form micron-scale aggregates that trap the material in the extracellular matrix. By contrast, non-responsive control nanoparticles, whose shells contain *D*-peptides (poor substrates for MMPs) passively equilibrate and clear.

2.1.2 General EDAPT Overview

The concept of selective deposition of exogenous material in tumor tissue to a much greater degree than in normal tissue forms the basis of our EDAPT platform for selective treatment of malignant disease[11]. Our work is predicated on the idea that if one can achieve the selective deposition of a synthetic material within malignant tumors, the tumor can be effectively treated. EDAPT is designed to make use of hyperactive enzymatic biomarkers (MMPs) to mediate marked structural changes in the synthetic particles through the cleavage of peptide substrates on the nanoparticle shell, ultimately leading to their selective accumulation and active trapping in the tumor[11-14] (**Figure 2.1.1**). The platform does not rely on the dissociation constant of a nanoparticle bound ligand with an overexpressed receptor to target, where occlusion has been an issue[15], but rather relies on the second order rate constant of an enzyme acting catalytically on the particle as a substrate. As a control for this process, analogous nanoparticles are generated using peptides constructed from *D*-amino acids, thus they are nearly identical in composition to the active systems, but do not interact with MMPs in tumors (**Figure 2.1.1**).

Ring Opening Metathesis Polymerization (ROMP)[16-20] is employed to generate amphiphilic block copolymers that contain *1)* a peptide substrate for MMP2/9 in the hydrophilic block and 2) either a drug or inert moiety in the hydrophobic block (**Figure 2.1.2a**). Upon dialysis from a favorable solvent for both blocks into aqueous solution, polymers assemble into micellar nanoparticles whose shell contains MMP-responsive peptides. When exposed to MMPs, the peptide substrates are cleaved, causing a significant change in morphology from nanoscale spheres (**Figure 2.1.2b**), to microscale networks (**Figure 2.1.2c**). This change in morphology has been confirmed in our laboratories through a number of high resolution microscopy and whole animal imaging studies[11-12], verifying a true phase change, not simply a precipitation. Upon morphology switch *in vivo*, the material is retained in tumor tissue as

micron-sized species, which are visualizable if a label is used (**Figure 2.1.2d**)[11-14]. As a negative control for this enzymatically-driven process, we generate "non-responsive" nanoparticles, which consist of peptides composed of *D*-amino acids. In this way, the nanoparticles generated have nearly identical physical properties as their enzyme-responsive counterparts, but are not recognized by MMPs in the body and thus, do not undergo morphology change upon enzyme exposure. Upon IV injection, the non-responsive particles stay as micellar spherical nanoparticles, and show no sign of accumulation and no retention (**Figure 2.1.2e**).

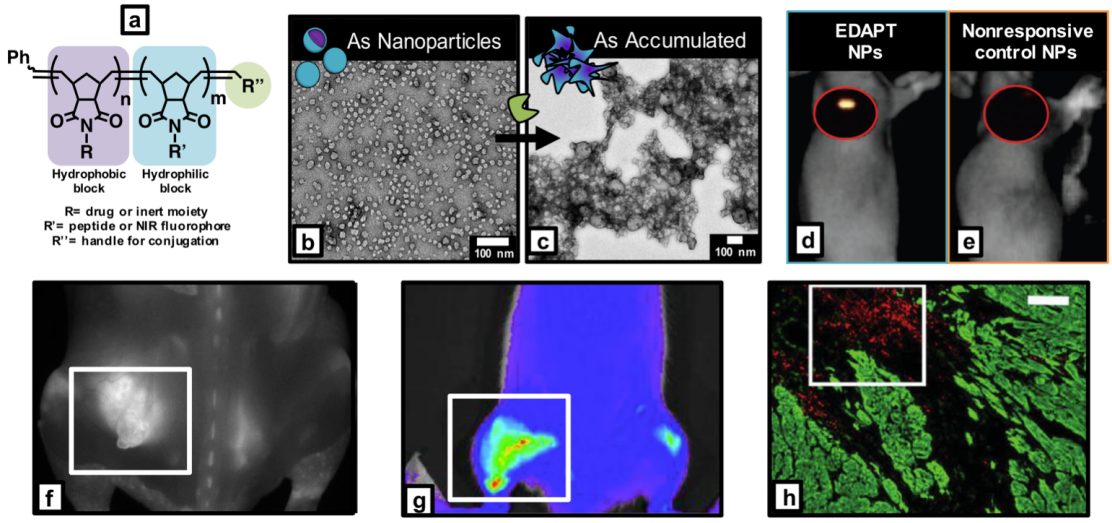

Figure 2.1.2. General performance of EDAPT *in vivo*. a) General polymer structure of EDAPT polymers generated through ROMP. The hydrophobic block of the polymer (purple, R) forms the core of the nanoparticle following dialysis. The hydrophilic block (blue, R') carries an MMP-responsive peptide and forms the shell of the particle. The polymer chain end (green, R'') can be modified to include various types of cargo[21]. Core-shell micellar nanoparticles have morphologies defined by the hydrophilic to hydrophobic ratios, and hence structures can be perturbed by enzymatic activity that cleaves peptides in the shell of micelles made from these amphiphiles. b) TEM micrograph of EDAPT nanoparticles. c) TEM micrograph of EDAPT materials after exposure to MMP enzymes. d) live-animal fluorescence image of animals IV injected with fluorescently-labelled, enzyme-responsive nanoparticles. Accumulation is visible in the tumor, which is circled in red. e) live-animal fluorescence image[11] of animal IV injected with nonresponsive, fluorescently-labelled control nanoparticles. No evidence of accumulation is seen in the tumor area, circled in red. f) Whole-animal fluorescence image of mice bearing HNSCC xenografts. EDAPT accumulation is visible in the tumor region (white box). g) live-animal fluorescence image of EDAPT accumulating in ischemic tissue (white box) in an animal model of PAD with upregulated MMPs following IV injection. h) *Ex vivo* analysis of EDAPT retention in infarct tissue in rat hearts from a rat myocardial infarction model. Particles were injected at 7 days post-MI, and tissues harvested at 6 days post-injection. Particles are visible in red, and myocardium (labelled with anti-α-actinin) is shown in green. Black region is the site of infarct – targeted following IV injection.

2.1.3 Additional EDAPT Applications

By incorporating fluorophores into polymer backbones of these materials, we have been able to observe this enzyme-driven retention in multiple disease models where MMPs are known to be upregulated. including Cal-27 human head and neck squamous cell carcinoma (HNSCC) (**Figure 2.1.2f**), peripheral artery disease (PAD)[22], (**Figure 2.1.2g**) and post-myocardial infarction (MI)[14] (**Figure 2.1.2h**). These studies demonstrate the robustness of the approach to enzymatically amplified targeting to leaky, inflamed tissue in various animal models.

2.2 EDAPT for Delivery of Paclitaxel

2.2.1 Introduction

The goal of nanomedicine is to treat disease through selective accumulation of therapeutics in diseased tissue. Nanoparticles offer the potential to package large quantities of drug cargo per carrier entity, to be decorated with targeting moieties in a multivalent fashion, and to have the potential to decrease off-target effects associated with conventional treatment regimes, while simultaneously increasing efficacy.[23-24] With respect to cancer therapy, the enhanced permeability and retention (EPR) effect has been implicated, albeit somewhat controversially,[25-27] as a mechanism by which nanomaterials accumulate in the fenestrated vasculature of tumor tissue. However, among other factors, this effect is limited to diseases that undergo rapid angiogenesis in their pathology.[3] Furthermore, the EPR effect is a passive mechanism of accumulation. To achieve active targeting, nanoparticle drug carriers have utilized receptor-mediated endocytosis[28] and hence, rely on the overexpression of surface receptors on disease-associated cells. Therefore, researchers have focused on a recurring set of ligand-receptor combinations, including RGD with integrin $\alpha_v\beta_3$,[29-34] NGR with aminopeptidase N,[35-38] and folic acid with the folate receptor.[39-43]

As discussed in Section 2.1, we envisioned a different targeting method termed **EDAPT**, wherein an enzymatic signal endogenous to tumor tissue directs a build-up of material selectively at the tumor site.[11-12, 44-46] Specifically, we utilized matrix metalloproteinases (MMPs), overexpressed in an array of cancer types and present as catalytic, extracellular or membrane-bound tumor markers.[8, 47-49] In this strategy, nanoparticles have shells decorated with peptides containing a substrate for MMPs. Upon exposure to the enzyme, the materials undergo a nano- to microscale change in size, coupled with a change in morphology[11]. In this way, the tumor guides the accumulation process through MMP expression patterns resulting in active accumulation through catalytic amplification. To date, we have demonstrated this

targeting method for the accumulation of fluorescent probes with the aim of developing approaches for guided surgery[50] and for diagnostic purposes.[11-12, 46]

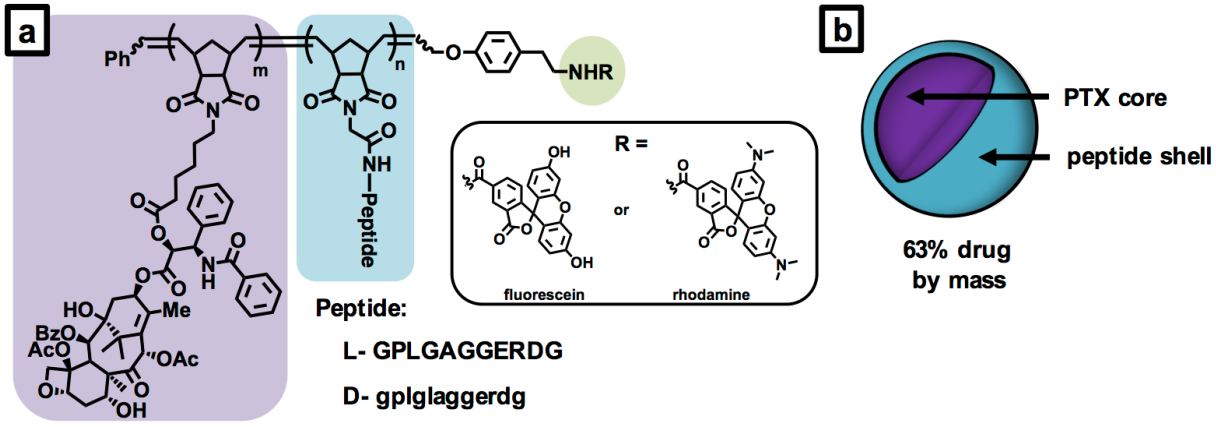

Figure 2.2.1. PTX-EDAPT polymer scheme. a) Structure of PTX-containing ROMP polymer. PTX is directly polymerized as part of the hydrophobic polymer block (shaded in purple), followed by either an enzyme responsive peptide composed of *L*-amino acids (sequence denoted in capital letters) or an enzyme nonresponsive peptide composed of *D*-amino acids (sequence denoted in lowercase letters) as the hydrophilic block (shaded in blue), and terminated with a fluorophore (shaded in green) to enable visualization and tracking *in vivo*. b) Schematic representation of **PTX-EDAPT** nanoparticles formed from the polymers shown in panel a. Upon dialysis of the polymers from organic solvent against aqueous media, spherical nanoparticles self-assemble as shown in **Figure 2.1.2**. PTX is covalently bound within the nanoparticle core and comprises 63% of the structure by mass. The nanoparticle shell contains the peptide sequence (comprised of either *L*- or *D*- amino acids).

Given our experience with targeting fluorescent probes[11], we hypothesized that an MMP-targeted nanoparticle platform could be employed as a tool for the delivery of chemotherapeutics (**Figure 2.2.1**). Towards this end, we generated micellar nanoparticles through the direct diblock copolymerization of a novel paclitaxel (PTX) conjugate with a MMP substrate and end-functionalized with a fluorophore (**Figure 2.2.1a**). Both functional monomers were synthesized as norbornene analogues amenable to ring opening metathesis polymerization (ROMP),[16-20, 51-53] utilizing a highly functional group tolerant Ru-based initiator[20, 54-57] capable of producing polymers with low dispersity in a highly reproducible manner.[55, 57] The resulting amphiphilic block copolymers assemble into micellar nanoparticles with a surface comprised of shell of MMP-substrates and a hydrophobic paclitaxel core (**Figure 2.2.1b**).

Notably, the drug is polymerized directly and is covalently bound via a biodegradable ester linkage. Upon exposure to MMP, the peptide shell is cleaved and the nanoparticles undergo a drastic change in morphology from discrete, spherical micelles 20 nm in diameter to form micron-scale assemblies visualized by transmission electron microscopy (see **Figure 2.1.2b-c** and **Figure 2.2.2**).[11-12] This transition amounts to a tumor-guided implantation of the polymer-bound drug conjugate via intravenous (IV) injection.

We utilized PTX in the hydrophobic block of the copolymer and as the therapeutic moiety in this motif, as it is a potent microtubule-stabilizing agent[58-59] and standard component of chemotherapy regimes for many malignant and metastatic cancers. The free 2'-hydroxyl group of PTX is absolutely required for its antitumor activity[60], but is available for conjugation via a biodegradable ester formed with a carboxylic acid-functionalized norbornene (PTX-norbornenyl ester) (**Figure 2.2.1a**) This ensures PTX is completely inactivated, and thus is delivered as a prodrug prior to hydrolysis from the polymer scaffold. The peptide sequence GPLGLAGGERDG was employed as the hydrophilic moiety and MMP recognition sequence, along with its fully D-amino acid analog, gplglaggerdg. The sequence was amenable to graft-through polymerization affording precise control of the polymer chemistry and subsequent enzymatic response.[53, 61] Fluorescein- or rhodamine-based chain transfer agents (CTAs) were included in the polymerization scheme so that the resulting polymers and nanoparticles could be visualized as a function of FRET (Förster Resonance Energy Transfer), as fluorescein and rhodamine form a FRET pair. The presence of a viable FRET signal can be observed by exciting the donor, fluorescein, at 470 nm and monitoring the emission of the acceptor, rhodamine, at 590 nm. FRET is only manifest when donor and acceptor molecules are within the Förster radius, as they are in these materials. The use of a FRET signal, rather than a single-dye system, eliminates much of the background signal caused by autofluorescence.

2.2.2 Results and Discussion

ROMP was employed to generate, and static light scattering (SLS) used to analyze, amphiphilic diblock copolymers containing norbornenyl-bound PTX as the first, hydrophobic block, followed by a second block of either the fully L-amino acid peptide sequence GPLGLAGGERDG or fully D-amino acid peptide sequence gplglaggerdg. From these polymers, uniform nanoparticles with high drug loading (63% by weight per polymer) spontaneously assembled upon dialysis of the copolymers initially dissolved in DMSO against aqueous solution. Two analogous nanoparticle systems whose hydrophilic blocks were comprised of either all *L*- or all *D*-amino acid peptides, were generated to afford enzyme-responsive (**PTX-EDAPT$_L$**) or nonresponsive, negative control (**PTX-EDAPT$_D$**) nanoparticles respectively. Additionally, both systems were split into two batches during polymerization of the second block, and terminated with either fluorescein or rhodamine, which form a FRET pair when formulated into a single particle[11, 46] to enable tracking of these materials *in vivo*.

With both responsive (**PTX-EDAPT$_L$**) and nonresponsive (**PTX-EDAPT$_D$**) nanoparticles in hand, we confirmed the ability of these materials to respond to MMP and aggregate *in vitro*. Catalytic exposure of **PTX-EDAPT$_L$** to MMP-12 for 4 hours led to the aggregated material (**Figure 2.2.2a**). Conversely, **PTX-EDAPT$_D$** showed no change in structure when exposed to the same conditions (**Figure 2.2.2b**). Further, HPLC analysis of both nanoparticle solutions following enzyme exposure reveals that authentic peptide cleavage product is only observed in **PTX-EDAPT$_L$** (**Figure 2.2.2c**). On the basis of these observations, we hypothesized that **PTX-EDAPT$_L$** would collect within tumor tissue upon IV injection, or be retained following intratumoral (IT) injection. This would lead, in turn, to release of PTX within the tumor tissue achieving a measurable therapeutic dose via hydrolysis induced by the tumor microenvironment. By contrast, **PTX-EDAPT$_D$** would not be retained, but rather clear from the tumor tissue, before PTX hydrolysis and release could lead to a therapeutic dose.

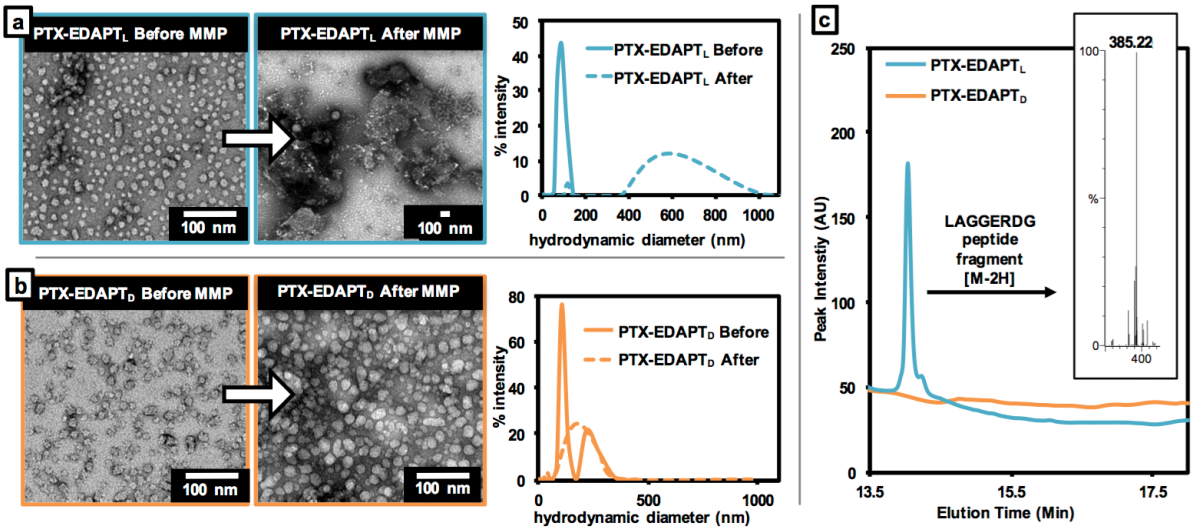

Figure 2.2.2. Enzyme response of PTX-EDAPT *in vitro*. a) TEM micrographs and DLS plots of **PTX-EDAPT$_L$** before and after MMP exposure. After dialysis, polymers assemble into ~20 nm spherical nanoparticles, which assemble into network-like structures after incubation with MMP for 4 hours. b) TEM micrographs and DLS plots of **PTX-EDAPT$_D$** before and after MMP exposure. These materials also form ~20 nm spherical micelles, but unlike their enzyme-responsive analogs, they do not change shape after incubation with MMP under identical conditions. c) HPLC plot and MS analysis (inset) of **PTX-EDAPT$_L$** and **PTX-EDAPT$_D$** after MMP exposure for 4 hours. The authentic peptide cleavage fragment, LAGGERDG, is only seen in the enzyme-responsive system.

We examined the safety and efficacy of PTX-loaded NPs in three proof-of-concept *in vivo* studies (**Figure 2.2.3**); 1) maximum tolerated dose (MTD) following IV administration; 2) efficacy post-IT injection; and 3) efficacy post-IV injection. For these studies, employed an HT-1080 fibrosarcoma xenograft cancer model known to overexpress MMPs[62] and to rapidly proliferate in a predictable manner after subcutaneous implantation. All animal procedures were approved by the University of California, San Diego's institutional animal care and use committee (IACUC).

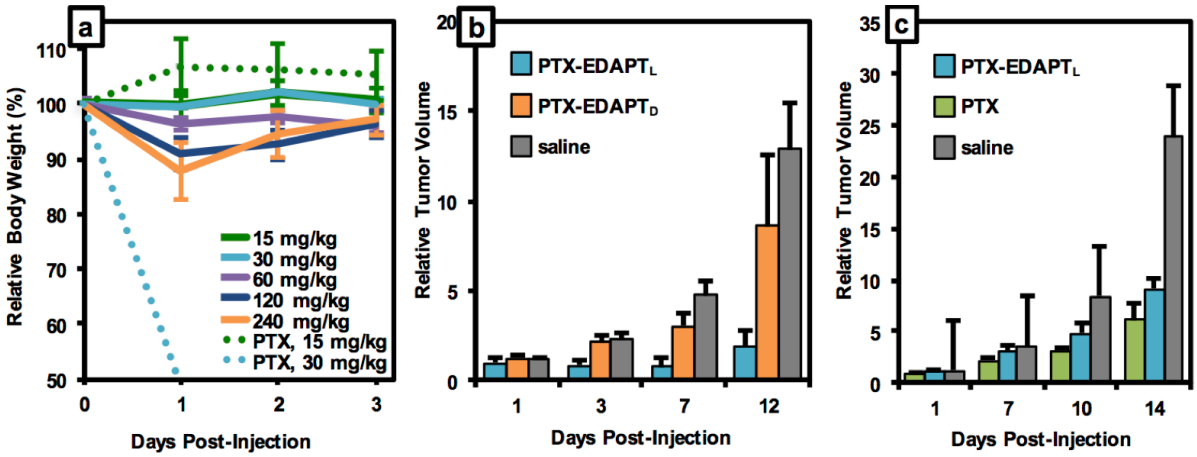

Figure 2.2.3. *In vivo* analysis of PTX-EDAPT. a) MTD analysis of **PTX-EDAPT$_L$** (solid lines) and clinically formulated PTX (dashed lines) following single, tail-vein IV injection. Note: LD_{50} of clinical PTX is 30 mg/kg and MTD is 15 mg/kg in our hands, whereas no overt toxicity is observed in any animal given **PTX-EDAPT$_L$**. b) Comparison of **PTX-EDAPT$_L$** to **PTX-EDAPT$_D$** following IT injection**. PTX-EDAPT$_L$** effectively inhibits tumor growth up to 12 days post-injection, whereas **PTX-EDAPT$_D$** has no observable effect, providing evidence that morphology change is necessary to have therapeutic effect and be retained. Note: clinical PTX cannot be IT injected without severe adverse effects (ulceration). c) Comparison of **PTX-EDAPT$_L$** to clinical PTX following a single tail vein IV injection. Throughout the duration of the study, equivalent efficacy is observed.

To examine the safety of our system, an MTD was determined in healthy nu/nu mice. In animal models, toxicity was secondarily measured as a function of animal body weight,[63-64] with lethality and/or weight loss of greater than 20% suggestive of severe adverse reactions. The MTD in mice of clinically formulated PTX as a suspension in 1:1 Cremophor EL (polyoxyethylated castor oil) to ethanol has been previously established as being in a range between 10-30 mg/kg.[65-67] In our hands the clinical formulation had a MTD of 15 mg/kg when administered via single tail-vein IV injection. Conversely, we were able to administer **PTX-EDAPT$_L$** via tail vein IV at a dose of 240 mg/kg. Therefore, NP_L exhibited a MTD 16 times greater than PTX without overt clinical toxicity, except for a 10% weight loss at 1 day with slow recovery over the next 3 days (**Figure 2.2.3a**). This suggests our enzyme-responsive materials are safely administered, even at exceptionally high doses.

To examine efficacy, **PTX-EDAPT$_L$** was tested against **PTX-EDAPT$_D$**, clinically formulated PTX, and saline in a series of IT (**Figure 2.2.3b**) and IV (**Figure 2.2.3c**) studies,

with all injection concentrations standardized to the equivalent of a 15 mg/kg dose of PTX. In brief, tumor xenografts of HT-1080 were established by inoculating each mouse subcutaneously with ~10^6 cells. Drug treatments were initiated once the tumors reached approximately 50 mm^3 in size. Tumor growth was assessed by daily measurement of tumor diameter through B-Mode Ultrasound (US) (**Figure 2.2.4**).[68]

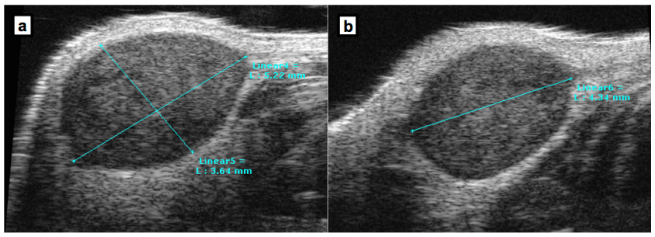

Figure 2.2.4. Representative example of tumor measurement by ultrasound. Tumor volume was determined by ultrasound, as described above. a) Ultrasound of X and Y axes of tumor. b) Ultrasound image of tumor Z axis.

To confirm that morphology change is necessary to retain our materials and further, to determine whether this accumulation event leads to a release of drug cargo at the tumor site, we conducted an efficacy study in which the effect on tumor growth of **PTX-EDAPT$_L$** was compared to that of both **PTX-EDAPT$_D$** and saline (negative control) following IT injection. Live-animal fluorescence imaging (**Figure 2.2.5**) was used to monitor the retention of our materials post-injection as a function of FRET signal with the eXplore Optix preclinical scanner (λ_{ex}= 470 nm and λ_{em}= 590 nm). As shown in **Figure 2.2.5a**, FRET is observable up to 3 days following IT injection of **PTX-EDAPT$_L$**, suggesting these materials are accumulating and being retained over a long time-scale. Importantly, FRET is only observed for the first 3 hours following IT injection of **PTX-EDAPT$_D$** (**Figure 2.2.5b**), indicative of rapid clearance of the material, presumably due to the lack of MMP-induced morphology change. Excitingly, we observed superior tumor growth suppression by **PTX-EDAPT$_L$** up to 12 days post-IT injection (see **Figure 2.2.3b**), and in fact, one animal in the cohort experienced complete remission beyond two months post-treatment. Conversely, there is no observable difference between **PTX-**

EDAPT$_D$ and saline throughout the duration of the study. These results provide evidence that morphology change is required for the function of these materials.

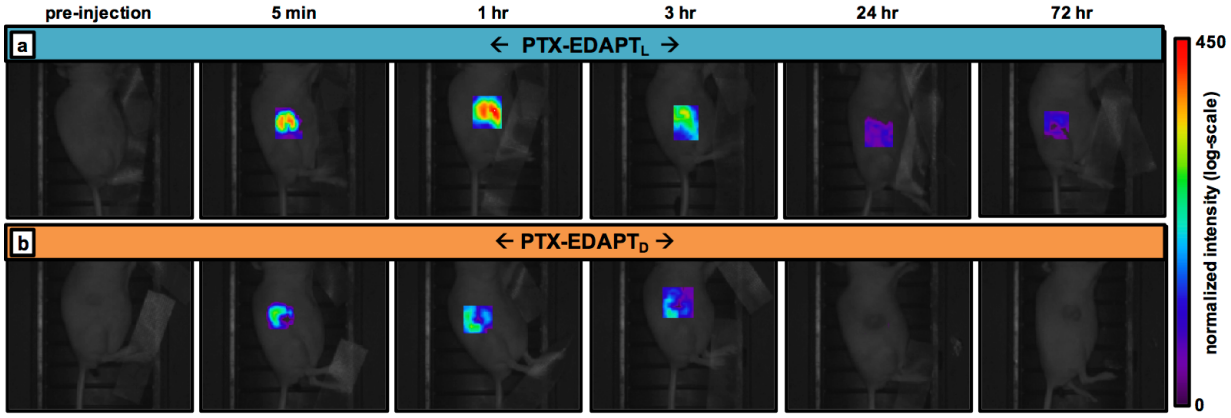

Figure 2.2.5. Live-animal fluorescence imaging of PTX-EDAPT. a) Time-course analysis of FRET signal in tumor-bearing nu/nu mouse following IT injection of **PTX-EDAPT$_L$**. Signal can be detected in the tumor out to 72 hours post-injection, indicating retention of the material. b) Time-course analysis of FRET signal in tumor-bearing nu/nu mouse following IT injection of **PTX-EDAPT$_D$**. Rapid signal loss is observed within the first 3 hours post-IT injection, indicating that materials are being cleared from the tumor, unlike their enzyme-responsive analogs.

Further evidence of efficacy was elucidated through a preliminary IV study. The effect on tumorigenesis of **PTX-EDAPT$_L$** was compared to that of clinically formulated PTX (positive control) and of saline (negative control), following a single tail vein IV injection (**Figure 2.2.3c**). In the literature, it is accepted that *in* vivo tumor growth follows an exponential curve until it reaches a lethal tumor volume of 10^9 cells (1 cubic centimeter).[69-70] After 10 days post-injection, mice in the saline cohort experienced rapid proliferation until reaching nearly lethal tumor volume within 14 days. By contrast, **PTX-EDAPT$_L$** successfully suppressed tumor growth for up to two weeks post-treatment, and in fact, paralleled that of PTX, within standard error, throughout the duration of the study. This, coupled with the MTD data, suggests that at equivalent doses, enzyme-responsive nanoparticle scaffolds have potentially very low toxicity for equivalent efficacy.

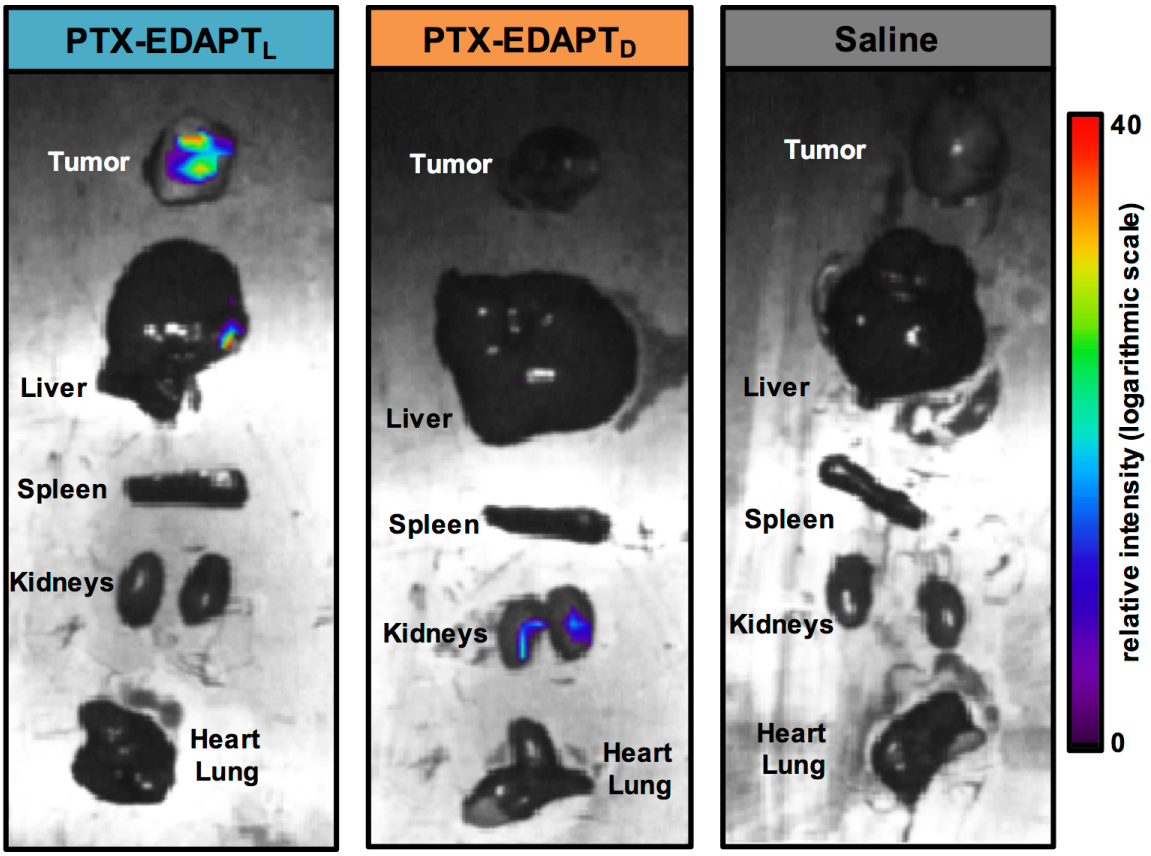

Figure 2.2.6. *Ex vivo* FRET analysis. Representative FRET fluorescence images of **PTX-EDAPT$_L$** (left), **PTX-EDAPT$_D$** (middle), and saline (right) cohorts at 14 days post-IV injection. Organs were imaged immediately after excision, and include tumor, liver, spleen, kidneys, heart, and lung, from top to bottom in each panel. FRET is observed in tumors from animals administered **PTX-EDAPT$_L$**, with minimal accumulation observed elsewhere.

In conjunction with the IV efficacy study, the targeting capabilities of our materials following IV injection were analyzed via fluorescence imaging to monitor for FRET signal generation at the tumor site. Indeed, *ex vivo* tissue analysis of animals sacrificed at 14 days post-injection (**Figure 2.2.6**) reveals that FRET is only observable in organs of animals administered **PTX-EDAPT$_L$** system. Further, the highest fluorescence signal intensity is observed in the excised tumors, with fluorescence observed to a lesser extent in the liver, spleen, and kidneys. This suggests that a mode of clearance of our system is through the reticuloendothelial system (RES).[71] However, the limited toxicity established in the MTD study suggests that although RES-associated organs may sequester these materials, they are not

being processed to release their payloads at off-target sites at a rate high enough to achieve toxic doses in the animals. Full pharmacokinetic analysis of these materials will be completed prior to optimization of the system, but preliminary biodistribution analysis following IV injection (**Figure 2.2.7**) reveals comparable accumulation of **PTX-EDAPT$_L$** in both the tumor, liver, and spleen, which is promising, as many nanoparticle systems suffer from extensive accumulation in the clearance organs, relative to the target organ[72-73] .

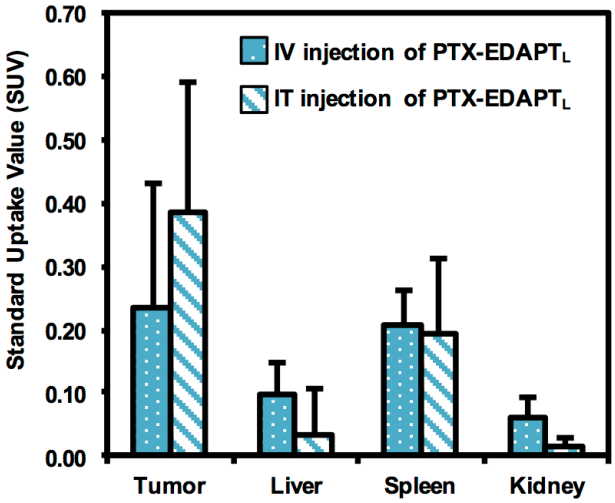

Figure 2.2.7. Biodistribution of PTX-EDAPT$_L$ as a function of injection type. The biodistribution of **PTX-EDAPT$_L$** in tumor, liver, spleen, and kidneys was assessed by measuring FRET signal at 48 hours following IV injection (blue dots) or IT injection (blue stripes). Using tissue-specific calibration curves, fluorescence counts were converted to polymer concentrations. These values were then normalized by the injected dose and animal weight, and background autofluorescence was subtracted (based on fluorescence from organs in animals administered saline) to calculate standardized uptake values.

2.2.3 Study Conclusions

Together, the foregoing results in Section 2.2.2 demonstrate that this novel, innovative class of nanoscale carrier can transport small molecule chemotherapeutics specifically and selectively to the disease site while limiting off-target toxicity. A distinct advantage of this system is that therapeutic moieties are incorporated into the nanoparticle scaffold *via* labile covalent bonds enabling high drug-loading, highly reproducible synthesis, and no observable release of material until accumulation occurs at the tumor site. Furthermore, these systems are potentially generalizable, as any therapeutic capable of conjugation to a norbornene handle can be incorporated into the center of the nanoparticle scaffold, which will be discussed

in later chapters. Future studies will center on the optimization of this system, and include investigation of higher PTX doses, exploration of the effect of surface chemistry on RES uptake, and tuning the biodegradation of the drug-to-polymer bond via incorporation of linkages sensitive to other stimuli present in tumor tissue, such as lowered pH and oxidative stress. Finally, we note the promising effects observed for IT administration. Although IV administration is certainly the gold standard for development of chemotherapeutics, there are several instances in which IT administration is used clinically, and is highly efficacious against primary and metastatic disease,[74-78] thus this route may prove a powerful translational tool. In summary, the system introduced here constitutes a new paradigm in the design of drug-carrying nanomaterials: the use of switchable morphology to guide *in vivo* accumulation for enhanced safety and efficacy.

2.2.4 Experimental

In Vitro Studies—General Materials and Methods: All reagents were obtained from Sigma Aldrich or Fisher Scientific and used without further purification. Polymerizations were performed in a dry, nitrogen atmosphere with anhydrous solvents. MMP-2, -9, and -12 were obtained from Calbiochem as a solution in 200 mM NaCl, 50 mM tris-HCl, 5 mM $CaCl_2$, 1 μM $ZnCl_2$, 0.05% BRIJ® 35 Detergent, 0.05% NaN_3, at pH 7.0. HPLC analyses of all products and peptides were performed on a Jupiter 4μ Proteo 90A Phenomenex column (150 x 4.60 mm) with a binary gradient, using a Hitachi-Elite LaChrom 2130 pump that was equipped with a Hitachi-Elite LaChrom L-2420 UV-Vis detector. Separation was achieved with a flow rate of 1 mL min^{-1} and the following mobile phase: 0.1% trifluoroacetic acid in H_2O (A) and 0.1% trifluoroacetic acid in ACN (B). Starting with 100% A and 0% B, a linear gradient was run for 30 min to a final solvent mixture of 33% A and 67% B, which was held for 5 min before ramping up to 0% A and 100% B over the course of 2 min and holding at this level for an additional 4

minutes, before ramping back down to 100% A and 0% B, with constant holding at this level for 4 additional minutes. Mass spectrometry (MS) of all synthesized compounds and peptides was performed at the Molecular Mass Spectrometry Facility (MMSF) in the Department of Chemistry and Biochemistry at the University of California, San Diego. Polymer dispersities and molecular weights were determined by size-exclusion chromatography (Phenomenex Phenogel 5u 10, 1K-75K, 300 x 7.80 mm in series with a Phenomenex Phenogel 5u 10, 10K-100K, 300 x 7.80 mm) in 0.05 M LiBr in DMF, using a Shimatzu pump that was equipped with a multi-angle light scattering detector (DAWN-HELIOS, Wyatt Technology) and a refractive index detectors (Wyatt Optilab T-rEX) normalized to a 30,000 MW polystyrene standard. Hydrodynamic radius (R_h) was determined by DLS, through a Wyatt Dynapro NanoStar. Transmission Electron Microscopy was performed on an FEI Tecnai G2 Sphera at 200 KV. TEM grids were prepared with a 1% uranyl acetate stain on carbon grids from Ted Pella, Inc. *In vitro* fluorescence measurements were taken on a PTI QuantaMaster Spectrofluorometer. Chemical shifts (^{1}H) are reported in δ (ppm), relative to the residual proton peak of $CDCl_3$ (7.27 ppm). Chemical shifts (^{13}C) are reported in δ (ppm), relative to the carbon peak of $CDCl_3$ (77.00 ppm).

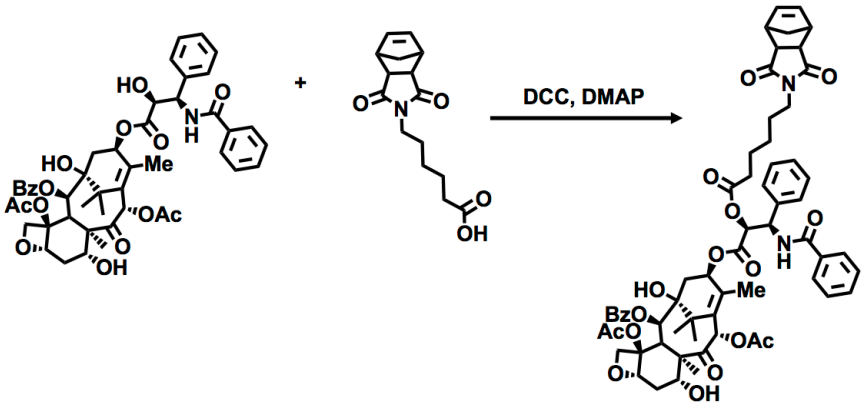

Figure 2.2.8. Synthetic scheme of PTX monomer. PTX is esterified through it's 2'-hydroxyl group with a norbornenyl derivative to afford the PTX ROMP monomer used in Chapter 2.2.

Paclitaxel (PTX) Monomer Synthesis: To a solution of paclitaxel ($2.34x10^{-5}$ mol, 1.0 equiv.) with *N*-(hexanoic acid)-*cis*-5-norbornene-*exo*-dicarboximide ($2.34x10^{-4}$ mol, 1.0 equiv., prepared from published protocol[79]) in 50 mL dry DMF in a 100 mL round bottom flask under N_2, was added 4-(Dimethylamino)pyridine ($2.34x10^{-6}$ mol, 0.1 equiv.). After stirring for 5 minutes at 0°C in an ice bath, *N,N'*-Dicyclohexylcarbodiimide ($2.58x10^{-6}$ mol, 1.1 equiv.) was dripped into the reaction mixture and allowed to stir for 7 hours. Reaction progress was monitored via TLC (1:1 hexane:ethyl acetate, R_f =0.3). Precipitated urea was removed via suction filtration, and the filter cake washed with DCM. The solvent was removed via rotary evaporation and the resulting crude product was dissolved in 30 mL $CHCl_3$. Purification was achieved through extraction with water (1 x 30 mL), followed by 0.5M HCl (3 x 10 mL), and finally saturated $NaHCO_3$ (3 x 10 mL). The organic phase was dried over $MgSO_4$ and solvent removed via rotary evaporation to afford the purified product in 90% yield. ^{1}H NMR (400 MHz, $CDCl_3$): δ (ppm) 1.14-1.33 (m, 8H, 2×CH_3. 1×CH_2) 1.53 (m, 2H, CH_2) 1.58 (m, 2H, CH_2) 1.68 (m, 3H, CH_3) 1.81 (s, 3H, CH_3) 1.88 (m, 2H, CH_2) 1.93 (t, 2H, CH_2) 2.02 (s, 1H, OH) 2.22 (s, 3H, CH_3) 2.34-2.39 (m, 5H, CH_3, CH_2) 2.47 (s, 1H, OH) 3.21 (m, 2H, CH) 3.37-3.48 (m, 2H, CH), 3.80 (d, 1H, CH) 4.19-4.45 (m, 3H, CH_2, CH) 4.96 (t, 1H, CH) 5.51 (d, 1H, CH) 5.68 (d, 1H, CH) 5.98 (t, 1H, CH) 6.22-6.30 (m, 4H, CH) 7.12-7.33 (d, 1H, NH) 7.34-7.75 (m, 18H, 3×Ar). ^{13}C NMR (400 MHz, DMSO): 10.2, 14.3, 23.1, 24.3, 26.02, 27.2, 30.83, 32.15, 33.81, 36.23, 38.00, 43.40, 44.91, 47.67, 54.43, 57.83, 70.86, 71.28, 74.95, 77.17, 80.71, 84.07, 125.75, 127.84, 128.77, 129.34, 230.03, 134.64, 137.77, 138,06, 139.82, 154.02, 157.07, 162.74, 165.66, 166.79, 169.18, 170.09, 172.75, 178.03, 202.81. ESI-MS(+): *m/z* 1136.40 $[M+Na]^+$.

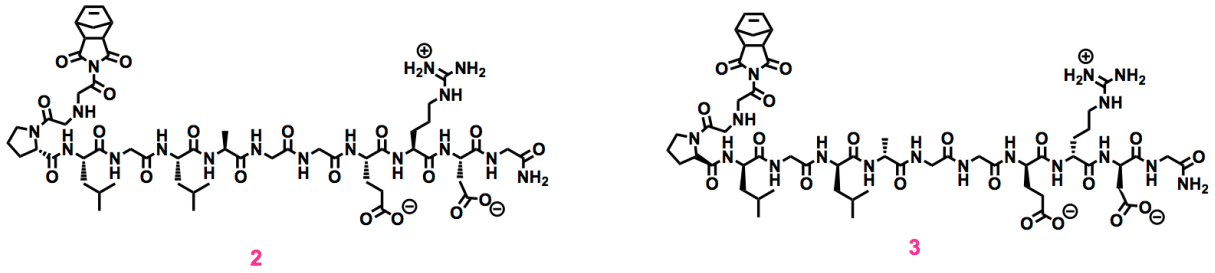

Figure 2.2.9. Peptide Structures. Structure of enzyme-responsive peptide, containing *L*-amino acids, is shown as compound **2**. Structure of nonresponsive peptide, containing *D*- amino acids, is shown as compound **3**.

Peptide Synthesis: Peptides were synthesized using an AAPPTEC Focus XC automated synthesizer. Both L- and D-amino acids were purchased from AAPPTEC and NovaBiochem. *N*-(glycine)-*cis*-5-norbornene-*exo*-dicarboximide (NorGly) was prepared as described above. Peptide monomers were synthesized via standard FMOC-based peptide synthesis using Rink Amide MBHA resin (AAPTEC) in a standardized fashion. FMOC was deprotected using a solution of 20% 4-methylpiperidine in DMF. Amino acid couplings were carried out using HBTU and DIPEA (resin/amino acid/HBTU/DIPEA 1:3.5:3.4:4). The final peptide monomers were cleaved from the resin using a mixture of TFA/H_2O/TIPS (95:2.5:2.5) for 90 minutes. The peptides were precipitated and washed with cold ether. For purification and analysis, the peptides were dissolved in a solution of 0.1% TFA in water and analyzed via RP-HPLC and purified via preparative HPLC. Peptide identities and purities were confirmed using ESI-MS and RP-HPLC monitoring at I_{abs} = 214 nm. Peptide monomer sequence: NorGly-Gly-Pro-Leu-Gly-Leu-Ala-Gly-Gly-Glu-Arg-Asp-Gly. *L*-amino acids were used exclusively for the preparation of **2** (**Figure 2.2.9**), and *D*-amino acids were used exclusively for the preparation of **3**. RP- HPLC retention time was 13 minutes (linear gradient of 0-67% B over 30 minutes). Preparative HPLC retention time was 33 minutes (linear gradient of 20-40% over 60 minutes). ESI-MS(+): 1300.54 $[M+H]^+$.

Fluorescein-Terminated Diblock Copolymers (**4L, 4D in Figure 2.2.10**): To a stirred solution of PTX-norbornene (compound **1, Figure 2.2.10**) (143 mg, 1.3 x10^{-4} mol, 10 equiv) in dry DMF (1600 µL) was added a solution of the catalyst ($(IMesH_2)(C_5H_5N_2)(Cl)_2Ru$=CHPh) (9.22 mg, 1.3x$10^{-5}$ mol, 1.0 equiv) in dry DMF (230 µL). The reaction was allowed to stir under N_2 for 2 hours, after which an aliquot (30 µL) was removed and quenched with ethyl vinyl ether for SLS analysis. The remaining solution of **1** + catalyst (1800 µL) was split into two separate reaction vessels. To one reaction vessel was added a solution of **2** (50 mg, 3.8x10^{-5} mol, 3 equiv) in 800 µL dry DMF (to ultimately afford **4L**). To the second vessel was added a solution of **3** (50 mg, 3.8x10^{-5} mol, 3 equiv) in 800 µL dry DMF (to ultimately afford **4D**). After three additional hours, a small aliquot was removed from each reaction vessel (30 µL each) and terminated with ethyl vinyl ether for SLS analysis. To each of the remaining solutions, **TA-1** (prepared via previously published protocol[2]) was added (4.5 mg, 6.3x10^{-6} mol, 1.2 equiv) and stirred for 1 hour. Afterwards, 10 µL ethyl vinyl ether was added to ensure the polymerizations were fully terminated. 30 µL NH_4OH was then added to both solutions and allowed to stir for an additional 20 minutes to deprotect **TA-1**. The fully terminated and deprotected polymers were precipitated with a cold 1:1 ether:methanol solution to afford the block copolymers as dark yellow solids (**4L**, **4D)**.

Rhodamine-Terminated Diblock Copolymers (**5L, 5D in Figure 2.2.10**): To a stirred solution of **1** (143 mg, 1.3 x10^{-4} mol, 10 equiv) in dry DMF (1600 µL) was added a solution of the catalyst ($(IMesH_2)(C_5H_5N_2)(Cl)_2Ru$=CHPh) (9.22 mg, 1.3x$10^{-5}$ mol, 1.0 equiv) in dry DMF (230 µL). The reaction was allowed to stir under N_2 for 2 hours, after which an aliquot (30 µL) was removed and quenched with ethyl vinyl ether for SLS analysis. The remaining solution of **1** + catalyst (1800 µL) was split into two separate reaction vessels. To one reaction vessel was added a solution of **2** (50 mg, 3.8x10^{-5} mol, 3 equiv) in 800 µL dry DMF (To ultimately afford **5L**). To the second vessel was added a solution of **3** (50 mg, 3.8x10^{-5} mol, 3 equiv) in 800 µL

dry DMF (To ultimately afford **5D**). After three additional hours, a small aliquot was removed from each reaction vessel (30 µL each) and terminated with ethyl vinyl ether for SLS analysis. To each of the remaining solutions, **TA-2** (prepared via previously published protocol[46]) was added (4.5 mg, $6.3x10^{-6}$ mol, 1.2 equiv) and stirred for 1 hour. Afterwards, 10 µL ethyl vinyl ether was added to ensure the polymerizations were fully terminated. The fully terminated polymers were then precipitated with a cold 1:1 ether:methanol solution to afford the block copolymers as deep magenta solids **(5L**, **5D)**.

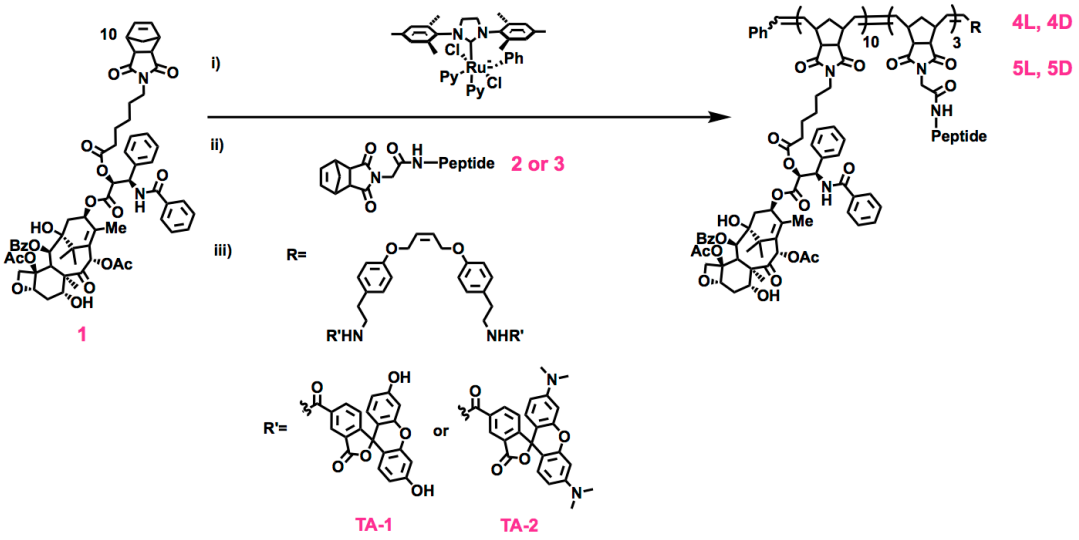

Figure 2.2.10. Synthetic scheme of PTX-EDAPT polymers. The PTX-based monomer (compound **1**) is first polymerized through ROMP, followed by a second block composed of either *L*- or *D*- peptides (compound **2** or **3**, respectively), and finally terminated with either a fluorescein (compound **TA-1**) or rhodamine (compound **TA-2**) chain transfer agent. This ultimately affords 4 polymers: Fluorescein-labelled, enzyme responsive polymers (**4L**), fluorescein-labelled, nonresponsive polymers (**4D**), rhodamine-labelled, enzyme responsive polymers (**5L**), and rhodamine-labelled, nonresponsive polymers (**5D**).

Homopolymer of **4L** and **4D**: M_n = 13330, PDI = 1.016, hydrophobic block length = 10

Copolymer of **4L**: M_n = 17240, PDI = 1.035, hydrophilic block length = 3

Copolymer of **4D**: M_n = 18830, PDI = 1.069, hydrophilic block length = 4

Homopolymer of **5L** and **5D**: M_n = 8345, PDI = 1.024, hydrophobic block length = 8

Copolymer of **5L**: 10015, PDI = 1.027, hydrophilic block length = 2

Copolymer of **5D**: M_n = 13030, PDI = 1.117, hydrophilic block length = 4

Nanoparticle Preparation (**PTX-EDAPT$_L$** and **PTX-EDAPT$_D$**): 10 mg of polymer was dissolved in 1 mL of DMSO and an additional 1 mL of 1X DPBS (Dulbecco's Phosphate Buffered Saline, no Ca, no Mg) was added over the course of 2 hours. This solution was transferred to a 3500 MWCO snakeskin dialysis tubing, and dialyzed against 1 L of 1X DPBS at pH 7.4 over 2 days with 2 buffer changes. The resulting solution was analyzed by DLS and TEM.

In vitro Nanoparticle Degradation via MMP-12: 500 µL **PTX-EDAPT$_L$** (concentration with respect to peptide), **PTX-EDAPT$_D$**, or PTX were incubated with MMP-12 (100 nU) at 37 degrees Celsius. After 4 hours, the assay was quenched by inactivation of MMP-12 at 65 °C for 20 minutes. Aliquots of these quenched samples were removed and analyzed via RP-HPLC (absorbance = 214 nm) to monitor for the presence of peptide cleavage fragment, whose sequence is LAGGERDG. ESI-MS was conducted on the peak eluted at 14 minutes on the spectrum to determine fragment MW. Only in **PTX-EDAPT$_L$** does this fragment appear (**Figure 2.2.2c**), which confirms that enzymatic degradation of the peptide shell will only occur if the sequence is composed of *L*-amino acids. Analogous experiments were run using MMP-2 and MMP-9, whose results are the same.). Samples were also analyzed by DLS and negative stain TEM to monitor for aggregation following MMP cleavage. This aggregation event only occurs in the **PTX-EDAPT$_L$** system, as evidenced by TEM and DLS (**Figure 2.2.2a-b**).

In Vivo Studies – General Methods: Paclitaxel Injection USP (Hospira, Inc.) was graciously donated by UCSD Moores Cancer Center (3855 Health Sciences Drive, La Jolla, CA). Tumors grown from HT-1080 fibrosarcoma cells (ATCC) were used for the model system, as this cell line overexpress MMPs[62]. Nu/nu mice were obtained through the UCSD in-house colony. Animals were inoculated with ~10^6 cells as a subcutaneous bolus, and treatments began once tumor mass reached ~50 mm^3. Animals were sacrificed at 14 days post-treatment,

or when their tumor burdens exceeded 1500 mm^3. B-mode ultrasound (US) (Visualsonics Inc, Vevo 770-120) was used to record tumor volume daily over the course of the study. Absolute tumor volume was approximated with the formula[68] V = length (mm) x width (mm) x depth (mm), as determined from US images. Relative tumor volume was determined by the formula:

$$(1) \qquad V_{relative} = \frac{V}{V_i} * 100$$

where **V** is the absolute tumor volume on the day of measurement and $\mathbf{V_i}$ is the absolute tumor volume on the first day of treatment. Live-animal imaging was taken on a GE Art Optix instrument.

For optical imaging, animals were anesthetized with isofluorane with an induction dose of 3% and a maintenance dose of 1.5% in an oxygen gas stream. After injection, animals were imaged at given timepoints using a GE ART eXplore Optix Instrument (λ_{ex}= 470 nm and λ_{em}= 590 nm). Animals were sacrificed after experiments. Organs (liver, spleen, lung, kidney, heart, and lung) and tumor were harvested and frozen for tissue slice preparation and analysis. To examine chronic *in vivo* toxicity, histological examination was conducted on sections of liver and kidney, 14 days post-IV injection of **PTX-EDAPT$_L$** and **PTX-EDAPT$_D$**. Organs were removed and frozen using cryoprotection and OCT. The tissue was then sectioned with a cryostat at 5 μm thickness, and stained with haemoatoxylin and eosin.

Maximum Tolerated Dose (MTD) of **PTX-EDAPT$_L$**: 15 healthy nu/nu female mice were separated into 5 groups (3 mice per cohort) and treated with **PTX-EDAPT$_L$** at the dosage equivalent of 15, 30, 60, 120, or 240 mg/kg with respect to PTX as a single, tail vein IV injection. Mouse weight was recorded once daily until all animals in the cohort returned to, or surpassed, their weight on the day of injection. Adverse toxicity is measured as a function of lethality and/or weight loss, with >20% weight loss suggestive of severe adverse events.[63-64] No animals in any cohort given **PTX-EDAPT$_L$** died. Two additional cohorts (6 mice, 3 per group) were treated with 15 mg/kg and 30 mg/kg of clinically formulated paclitaxel (a 6 mg/mL suspension in 1:1

ethanol: Cremophor EL®, diluted with 1X DPBS prior to injection). Animals in the 15 mg/kg PTX cohort experienced similar weight-loss as those in the 15 mg/kg PTX-NP cohort (see Figure 2A), but with serious reactions as a result of the method of injection (tails necrosed below the injection site and subsequently fell off). In the 30 mg/kg group, 1 out of the 3 animals died within 30 minutes post-injection. An additional animal was given 30 mg/kg and also died within an hour of injection.

Intravenous Efficacy: 20 tumor-bearing nu/nu female mice were randomly sorted into 4 groups (5 mice per cohort) and treated with **PTX-EDAPT$_L$**, **PTX-EDAPT$_D$**, PTX, or saline at the dosage equivalent of 15 mg/kg of PTX as a single, tail-vein IV injection. Mouse weight and tumor volume were recorded once daily over the course of the 14-day study. Animals were imaged at 0, 1, 3, 5, 24, 48, 72, and 126 hours post-injection via live-animal optical imaging. To assess efficacy, relative tumor volume (see equation (1) above) was calculated for each data point. The average relative tumor volume of each cohort at each time point was then calculated, along with standard deviation and standard error. Animals were sacrificed at 14 days post-injection. Tumor, liver, spleen, kidneys, heart, and lungs were excised from each animal and treated as in above protocol.

Intratumoral Efficacy: 15 tumor-bearing nu/nu female mice were randomly sorted into 3 groups (5 mice per cohort) and treated with **PTX-EDAPT$_L$**, **PTX-EDAPT$_D$**, or saline at the dosage equivalent of 15 mg/kg of PTX as a single intratumoral injection. Mouse weight and tumor volume were recorded once daily over the course of the 12-day study. Animals were imaged at 0, 1, 3, 24, 48, and 72 hours post-injection via live-animal optical imaging. To assess efficacy, relative tumor volume (see equation (1) above) was calculated for each data point. The average relative tumor volume of each cohort at each time point was then calculated, along with standard deviation and standard error. Animals were sacrificed at 12 days post-injection. Tumor, liver, spleen, kidneys, heart, and lungs were excised from each animal and

treated as in above protocol. An additional tumor-bearing mouse was administered 15 mg/kg of PTX, also as a single intratumoral injection. Following treatment, the animal experienced severe ulceration at the tumor site within two days of treatment, and thus had to be sacrificed and excluded from the study.

Biodistribution by Standardized Uptake Values*:* 6 tumor-bearing nu/nu female mice were sorted randomly into 2 groups (3 mice per cohort) and treated with **PTX-EDAPT$_L$** at the dosage equivalent of 15 mg/kg of PTX, as either an IT or IV injection. An additional cohort of 3 tumor-bearing mice was given no treatment, to serve as a handle for baseline tissue fluorescence. At 48 hours post-injection, all animals were sacrificed. Tumor, liver, spleen, and kidneys of all animals were harvested, weighed, and transferred to individual 15 mL conical tubes. Lysis buffer (0.25mg/mL Proteinase K, 0.1mg/mL DNAse, 150 mM NaCl, 10mM tris pH 8, 0.2% SDS) was added to each conical tube as a ratio of 9 µL buffer per 1 mg tissue. All tissues were then cut into small pieces and homogenized for 30 seconds using an ultrasonicator, transferred to 1.5 mL eppendorf tubes, and incubated overnight at 55^{o}C.

Calibration curves for each tissue type (liver, spleen, kidney, tumor) were generated via the following protocol: 90 µL of homogenated tissue from animals treated with saline were pipetted into a 96-well plate and fluorescence measured to obtain background. 10 µL of **PTX-EDAPT$_L$** was added at varying polymer concentrations and the fluorescence measured ($\lambda_{excitation}$ = 545 nm, $\lambda_{excitation}$ = 580 nm), to generate a plot of fluorescence counts vs. polymer concentration. The data obtained from each curve was fitted linearly to use for measuring polymer concentration in experimental tissues.

To assess the effect of injection method on the biodistribution of **PTX-EDAPT$_L$**, the fluorescence count of **PTX-EDAPT$_L$** in tumor, liver, spleen, and kidneys after either IT or IV injection was measured. 100 µL of each homogenated tissue (see details above) was added to an individual well of a 96-well plate. Fluorescent counts of each well ($\lambda_{excitation}$ = 545 nm,

$\lambda_{excitation}$ = 580 nm) were converted to polymer concentrations using tissue-specific calibration curves generated as described above, and were then normalized by the injected dose and animal weight to calculate standardized uptake values (SUV). SUV = (moles of polymer in tissue/mass of tissue) / (mols of polymer injected/weight of animal).

2.3 EDAPT For Delivery of Pt-Based Drugs

2.3.1 Introduction

Following the success in delivery of PTX to tumor tissue using our EDAPT system (**Section 2.2**), we hypothesized that this platform could be extended to the delivery of other small molecule cytotoxins. We had previously demonstrated the feasibility of delivering ROMP-based, Pt(II)-loaded nanoparticles to cells[80] through the copolymerization of a Pt-II norbornenyl complex together with a hydrophobic ^{15}N-labelled Ph monomer, hydrophilic PEG monomer, and NIR dye. In that work, the *in cellulo* uptake of the nanoparticles was monitored and the nanocarrier and drug were tracked separately to understand the pathway for drug release and cytotoxic effects within the cell. Importantly, this system showed equivalent cytotoxicity as the parent Pt drug, and demonstrated the power of combined optical and isotopic nanoscopy techniques to study the delivery and the intracellular distribution of Pt(II)-loaded nanoparticles in tumor cells.

Based on these promising results, we reckoned that a Pt(II)-based EDAPT nanoparticle system would also show efficacy *in vivo*, and that incorporation of the same types of isotopic and NIR labels as in our previous study would enable visualization of the carrier and drug in tissues following administration. Thus, we designed a system wherein a Pt(II) complex was copolymerized with an ^{15}N-labelled Ph, an NIR fluorophore, and an MMP-responsive peptide, termed **Pt-EDAPT** (**Figure 2.3.1**). We applied a similar imaging technique as in our previous work[80] to study the distribution of this drug-loaded, enzyme responsive nanoparticle system *in vivo* following intratumoral (IT) administration to HT-1080 xenografts.

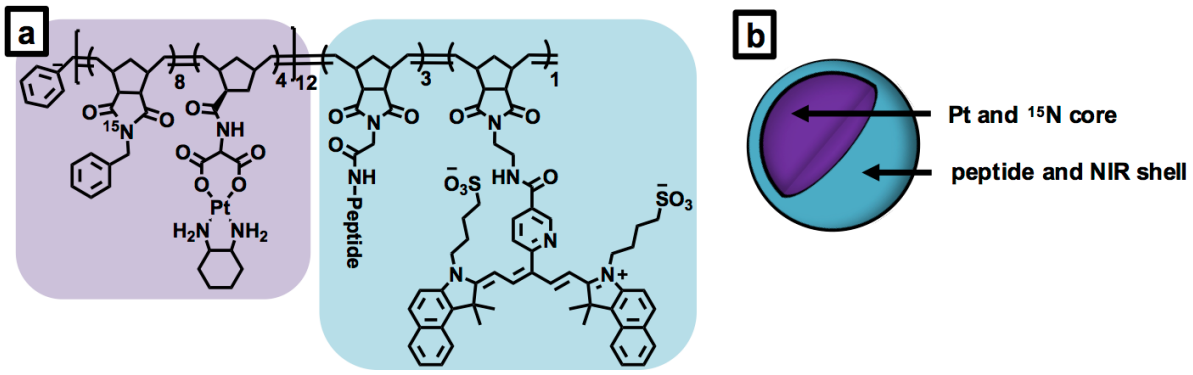

Figure 2.3.1. Pt-EDAPT structure. a) Structure of Pt-containing, enzyme responsive polymer containing isotopic and fluorescent labels. Pt is directly polymerized as part of the hydrophobic block (purple shading) together as a blend with a ^{15}N-labelled Ph moiety. This blended block is then followed by either an enzyme responsive peptide composed of *L*-amino acids (discussed in Chapter 2.2) or nonresponsive peptide composed of *D*-amino acids and a single NIR fluorophore as two separate blocks of the hydrophobic portion of the polymer (blue shading). b) Schematic representation of **Pt-EDAPT** nanoparticles formed from the polymers depicted in panel a. Upon dialysis, spherical nanoparticles assemble, wherein the Pt-drug and ^{15}N-isotopic label are covalently bound within the core (depicted in green), and the peptide and NIR fluorophore are contained on the shell (depicted in pink). Together, this forms a nanoparticle drug delivery system amenable to visualization and tracking using correlated optical and isotopic nanoscopy techniques.

It should be noted that there are considerable challenges that face nanomaterials that relate to the ability to characterize these materials *in vitro*, *in vivo*, and *ex vivo* to determine their interactions with biological cells and tissues. Despite important advances in characterizing nanostructures as single entities,[81-84] understanding their behavior once in a complex living organism, and more specifically, observing their state and distribution in the target tissues at the nanometer length scale, remains challenging.[85-86]

To characterize the location of **Pt-EDAPT**, we employed an approach that correlates optical and isotopic nanoscopy, which has been recently introduced for multimodal imaging at the nanometer length scale.[80, 87] In this case, Nanoscale Secondary Ion Mass Spectrometry (NanoSIMS; high special resolution, sensitivity and mass resolution)[88-89] is linked with super-resolution microscopy techniques for the study of biological systems. Although still methodologically complex, this combination of techniques has gained attention and it has been

applied to the study of systems such as biological processes in neuron cells, as well as intracellular distribution of metal-based drugs.[87, 90]

2.3.2 Results and Discussion

Amphiphilic block copolymers containing an oxaliplatin analog and MMP-responsive peptides were generated through ring opening metathesis polymerization (ROMP).[91] The monomers were specifically designed to form polymers which would self-assemble into a nanoparticle with three main characteristics. It should *(1)* specifically accumulate in tumor tissue; *(2)* demonstrate antitumor properties in a murine xenograft of a cancer that overexpresses MMPs in its pathology; and *(3)* provide contrast for optical and isotopic imaging techniques. Thus, polymers were synthesized using 4 different ROMP monomers: *(a)* an oxaliplatin analogue monomer containing a norbornene polymerizable moiety,[81] known to be cytotoxic to a variety of cancer cells and useful as an isotopic label because of the lack of Pt in biological samples; *(b)* a ^{15}N-labeled phenyl monomer which serves as a isotopic label for the polymer backbone of the nanocarrier; *(c)* a peptide substrate monomer as an MMP recognition sequence (*L*-amino acid sequence “GPLGLAGGERDG and *D*-amino acid sequence “gplglaggerdg”); and *(d)* a Cyanine 5.5 dye (NIR) monomer as a fluorescent polymer label for super-resolution fluorescence microscopy (**Figure 2.3.1a**)

Copolymerization of the Pt-monomer with the ^{15}N-monomer in a 2:1 ratio as the hydrophobic block, followed by the peptide as the hydrophilic block and NIR monomer as a third block generated an amphiphilic block copolymer. From this, nanoparticles were generated by dialyzing the polymers from DMSO into water as drug-containing, enzymae responsive, isotopically and fluorescently labeled **Pt-EDAPT$_L$** (**Figure 2.3.1b**). Non-responsive, negative control nanoparticles were synthesized by incorporating *D*-amino acid peptides into the hydrophilic block of the polymers (**Pt-EDAPT$_D$**).

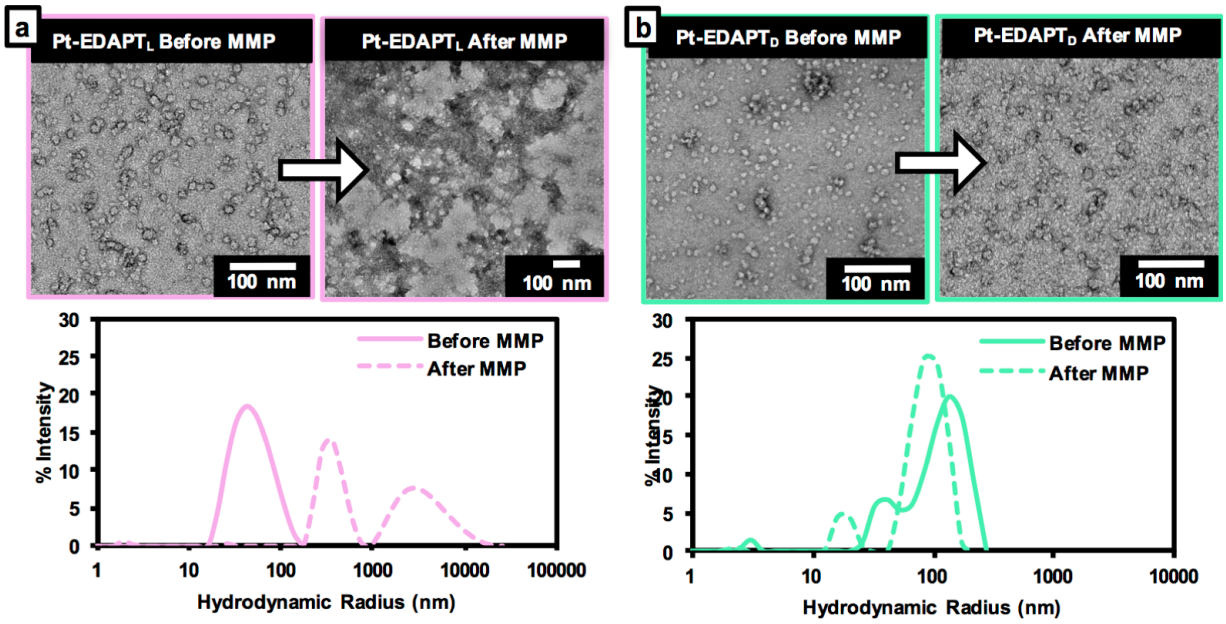

Figure 2.3.2. Enzyme response of Pt-EDAPT. a) TEM micrographs (top panels) and DLS plots (lower panel) of **Pt-EDAPT$_L$** before and after MMP exposure. Upon dialysis from DMSO against aqueous media, polymers assemble into nanoparticles. Incubation with MMP overnight induces a morphology change from spherical assemblies to microscale network structures. b) TEM micrographs (top panels) and DLS plots (lower panel) of **Pt-EDAPT$_D$** before and after MMP exposure. Upon dialysis, polymers assemble into nanoparticles, but unlike their enzyme-responsive analogs, no change is seen in the particle morphology following overnight incubation with MMP.

After confirming the ability of **Pt-EDAPT$_L$** to aggregate upon MMP exposure *in vitro* using methods like those described in Section 2.2 (**Figure 2.3.2**), we examined the *in vivo* capability of the material to be retained in tumor tissue and to inhibit tumor growth. We utilized human HT-1080 fibrosarcoma subcutaneous xenografts for these studies, as this line overexpresses MMPs[92] and we have had previous success in delivering other therapeutic enzyme responsive nanoparticles in this model.[13] Thus, mice bearing HT-1080 tumors were injected IT with either **Pt-EDAPT$_L$** or **Pt-EDAPT$_D$** at 2.5 mg/kg with respect to Pt content and monitored over the course of 12 days for retention and efficacy. A third cohort received saline alone as an additional negative control. The efficacy of **Pt-EDAPT$_L$** was also compared to that of oxaliplatin at equivalent Pt doses.

Importantly, **Pt-EDAPT$_L$** inhibited tumor growth relative to both the saline and **Pt-EDAPT$_D$** controls (**Figure 2.3.3a**). Additionally, **Pt-EDAPT$_L$** performed as well as its clinical counterpart, oxaliplatin, suggesting that packaging the Pt drug in a nanocarrier does not adversely affect its therapeutic capabilities. Further, live animal fluorescence microscopy was used to monitor the retention of both **Pt-EDAPT$_L$** (**Figure 2.3.3.b**) and **Pt-EDAPT$_D$** (**Figure 2.2.3c**) post-injection by tracking the NIR fluorophore on the polymer backbone of both systems (λ_{em} = 635 nm and λ_{ex} =693 nm). Fluorescence was observable up to 5 d following IT injection of **Pt-EDAPT$_L$**, suggesting that these materials were retained over a long timescale. Further, *ex vivo* analysis of tumor, liver, spleen, kidney, heart, and lung showed the highest accumulation of **Pt-EDAPT$_L$** in the tumor. Importantly, fluorescence was only observed for the first 5 h following IT injection of **Pt-EDAPT$_D$**, indicative of rapid clearance of the material, and presumably due to the lack of MMP-induced morphology change, and no enhanced fluorescence in the tumor is observed through *ex vivo* analysis.

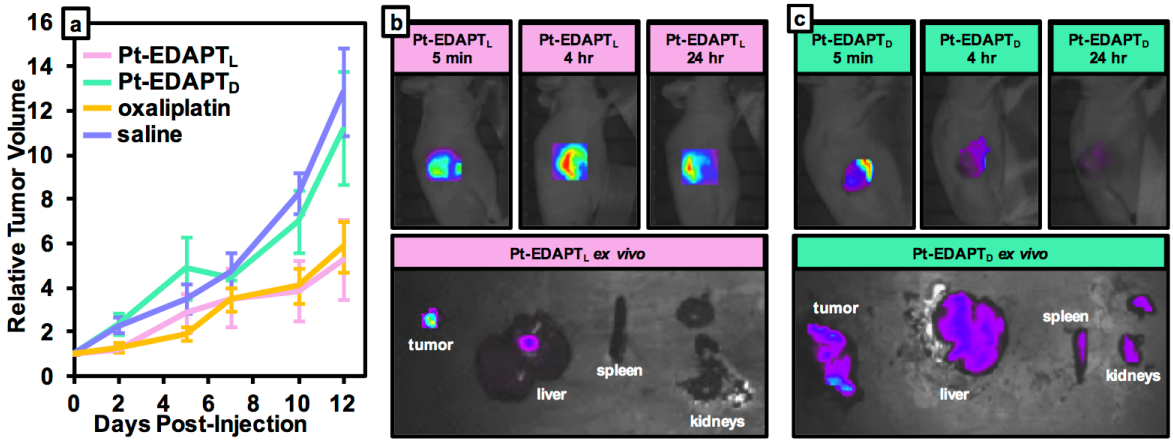

Figure 2.3.3. *In vivo* analysis of Pt-EDAPT. a) Comparison of **Pt-EDAPT$_L$** (pink curve) to **Pt-EDAPT$_D$** (green curve), oxaliplatin (orange curve), and saline (blue curve). Throughout the duration of the study, **Pt-EDAPT$_L$** has equivalent efficacy to that of oxaliplatin. Conversely, no evidence of efficacy is seen in animals treated with **Pt-EDAPT$_D$**, relative to saline-treated controls. b) Time course of live-animal fluorescence imaging (top three panels) and *ex* vivo analysis at 24 hr (bottom panel) following IT injection of **Pt-EDAPT$_L$** to evaluate retention as a function of NIR fluorescence. The material is visualizable out to 24 hr, and the highest accumulation is observed in the tumor. c) Time course of live-animal fluorescence imaging (top three panels) and *ex* vivo analysis (bottom panel) following IT injection of **Pt-EDAPT$_D$** to evaluate retention. Unlike the responsive system, rapid signal loss is observed within 5 hr post-injection of the nonresponsive control, with nearly no detectable signal at 24 hr post-injection. Note: All signal intensities in b) and c) are on the same, relative scale.

After demonstrating the efficacy of our system as a drug delivery vehicle and assessing its retention in tumor tissue, we investigated the material *ex vivo* utilizing a multimodal super-resolution imaging approach that combines optical (Structural Illumination Microscopy or SIM) with isotopic (NanoSIMS) nanoscopy. The combination of these techniques allows for the determination of not only the distribution of the nanocarrier and the drug within the tumor, but also their specific cellular and intracellular localization. We aimed to track the permeation of **Pt-EDAPT$_L$** within the tumor and to visualize its aggregation in the extracellular matrix upon cleavage of the peptide shell by MMPs. Exposure of the aggregated material to complex tissue milieu conditions is expected to promote drug release and cytotoxic effects in tumor cells by virtue of oxaliplatin binding to nuclear DNA.[93-94]

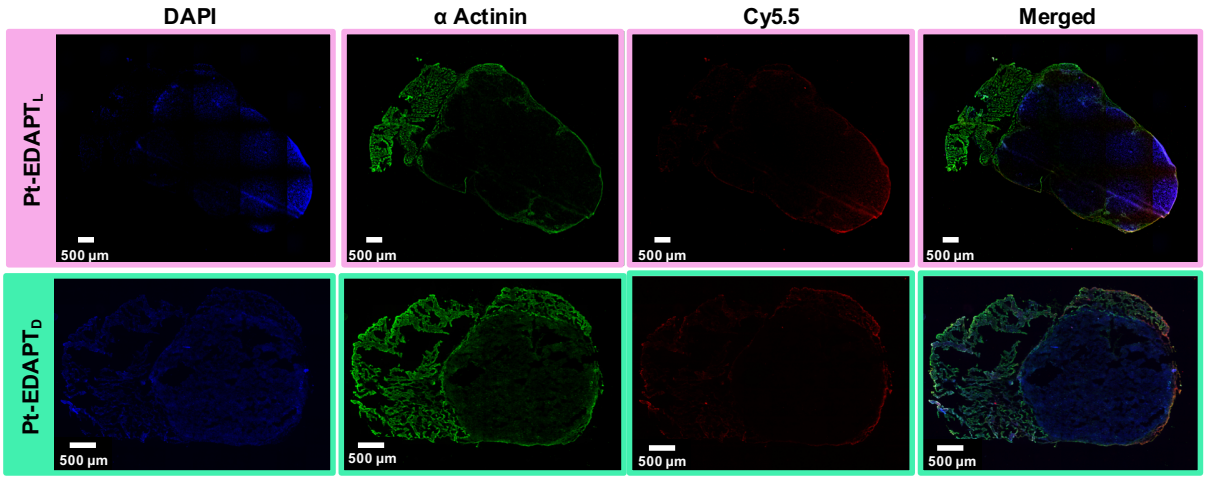

Figure 2.3.4. SIM of tumor sections. 10X magnification fluorescence image of tumor sections from mice treated with **Pt-EDAPT$_L$** (top) and **Pt-EDAPT$_D$** (bottom). In both cases, the signal from the nanoparticles (Cy5.5) is concentrated on the periphery of the sections.

To validate the proposed nanoparticle activation pathway, we performed super-resolution imaging of tumor tissue and tracked the nanocarrier (the polymer NIR dye label with SIM and the ^{15}N label with NanoSIMS) and the Pt(II)-drug (NanoSIMS) separately. As before, tumor-bearing mice were injected IT with either **Pt-EDAPT$_L$**, **Pt-EDAPT$_D$**, or saline solution and sacrificed 24 hours later. The tumors were harvested and cryo-sectioned into 5 µm sections

and placed on Indium-Tin-Oxide (ITO) coverslips. Immunostaining was performed on the sections with an anti-α-actinin antibody to label cytoplasmic dense structures (α-actinin, AF 488). Samples were subsequently stained with DAPI as a cell nucleus indicator. Samples were finally dehydrated through a series of ethanol solutions of increasing concentration.

Because of the non-destructive nature of SIM, fluorescent images at different magnifications were obtained as part of preliminary investigations. Low magnification images showed fluorescent signals from both **Pt-EDAPT$_L$** and **Pt-EDAPT$_D$** mainly distributed in the periphery of the tumor tissue (**Figure 2.3.4**).

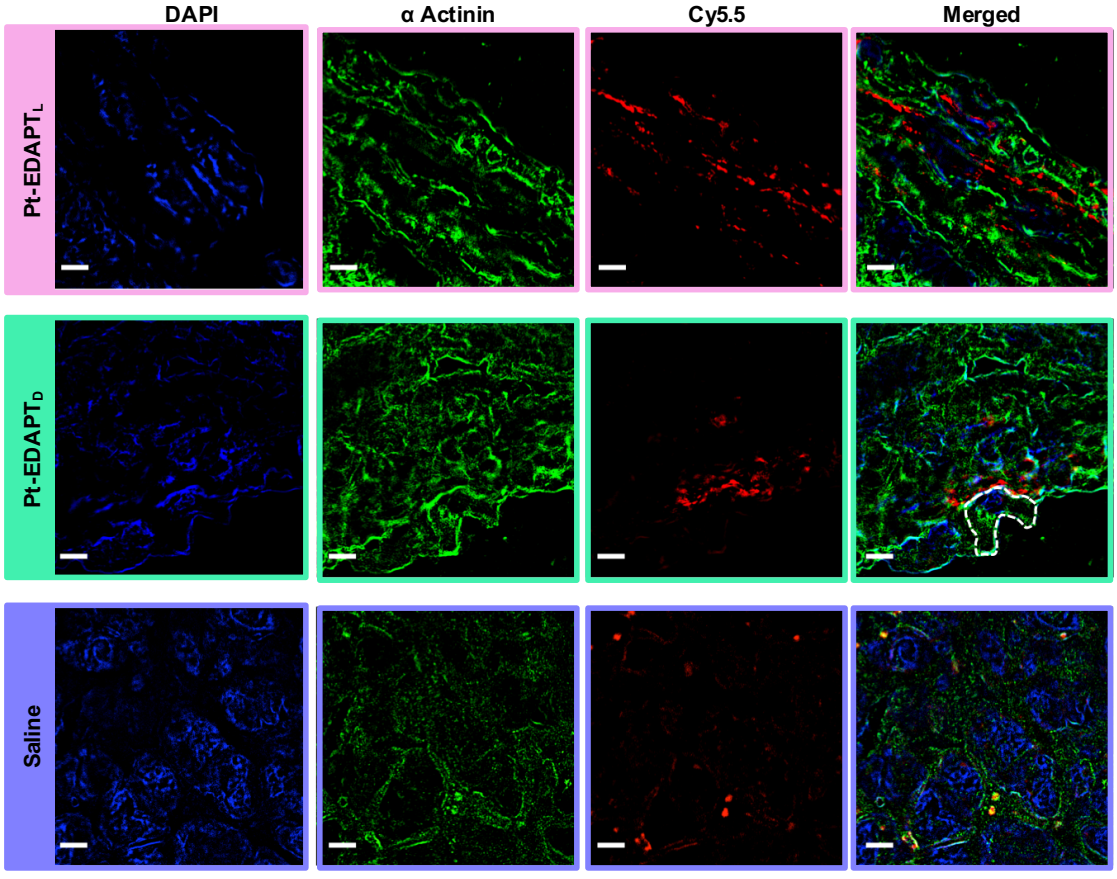

Figure 2.3.5. Magnified SIM of tumor sections. SIM analysis of 5 μm thick tumor tissue sections of animals treated with **Pt-EDAPT$_L$** (top), **Pt-EDAPT$_D$** (middle), or saline (bottom). From these images, it is clear that the signal for the enzyme responsive nanoparticles is the nonresponsive controls is not correlated with nuclear and actin staining, suggesting an extracellular localization of the nanomaterials. Interestingly, samples from animals treated with saline solution showed fluorescent signals in the far-red channel, attributed to tissue autofluorescence. The dashed line outlines a cell boundary. Scale bar represents 5 μm.

As previously observed on the time-course of live animal fluorescence, only a minimal amount of Cy5.5 signal was detected for **Pt-EDAPT$_D$**, most likely due to its reduced retention in tumor tissues. Increased magnification reveled the polymeric probes preferentially accumulating in the extracellular space, as the fluorescent signal associated with the polymer backbone (Cy5.5) was only poorly correlated with green actin filaments (**Figure 2.3.5**).

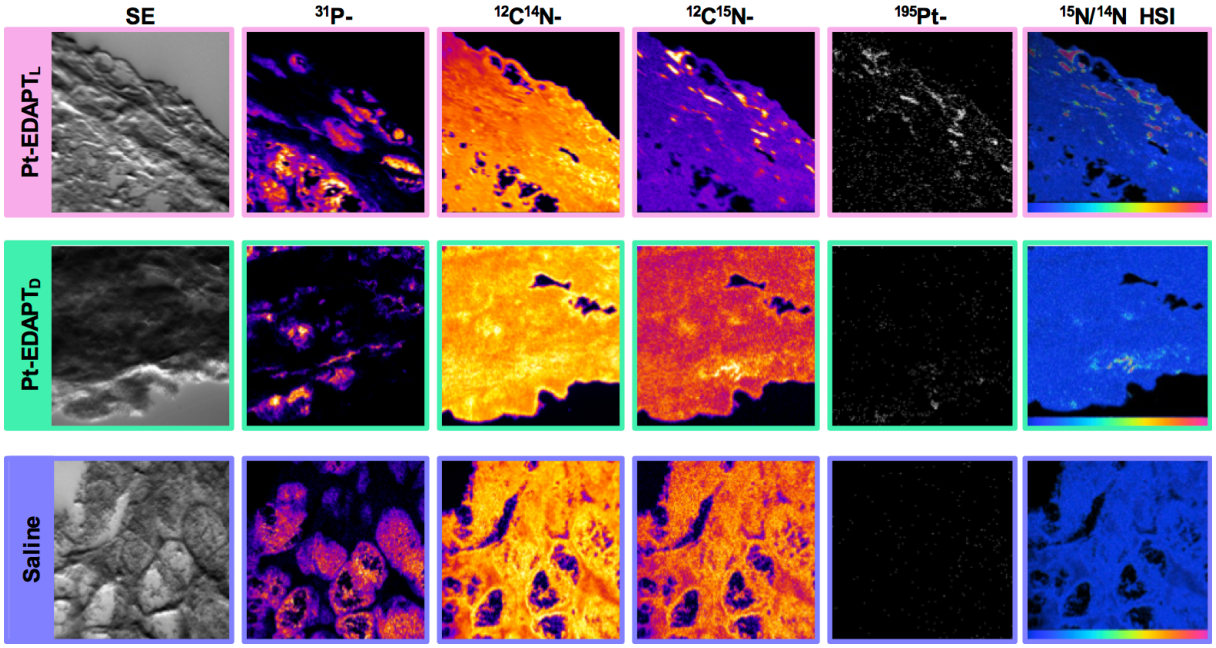

Figure 2.3.6. NanoSIMS imaging of tissue slices. Secondary Electron images (SE) and NanoSIMS ion maps of dehydrated 5 µm tumor tissue sections of mice treated with **Pt-EDAPT$_L$** (top), **Pt-EDAPT$_D$** (middle), or saline (bottom). $^{31}P^-$, $^{12}C^{14}N^-$, $^{12}C^{15}N^-$, and $^{195}Pt^-$ ion maps were obtained simultaneously and intensities are shown in a fire scale, except for the $^{195}Pt^-$ ion map which is shown in white/black. HSI images represent the $^{12}C^{15}N/^{12}C^{14}N$ ratio and highlight specifically enriched areas as can be seen for **Pt-EDAPT$_L$** and **Pt-EDAPT$_D$** samples. The scales on the HSI images were adjusted depending on the relative intensities for each sample. Thus, the scale for **Pt-EDAPT$_L$** is .0037-.02, for **Pt-EDAPT$_D$** is .0037-.11 and for the saline solution sample .0037-.15. Images, in all cases, represent an area of 48 µm × 48 µm.

However, the fact that tumor regression was previously observed presumes Pt permeated into the cellular structures and bound to DNA. To test this hypothesis, the tissue sections previously imaged by SIM were further analyzed with NanoSIMS (**Figure 2.3.6**). Under our experimental conditions we collected a Secondary Electron (SE) image and four

masses of interest to create elemental maps of each sample: ^{31}P as a nuclear indicator because of the phosphorus-rich DNA; $^{12}C^{14}N$ as an indicator for organic matter; $^{12}C^{15}N$ as a polymer backbone indicator and ^{195}Pt as a drug label. A Hue-Saturation-Intensity (HSI) representation of the $^{12}C^{15}N/^{12}C^{14}N$ ratio map as a color scaled image was constructed to specifically identify ^{15}N-rich areas, representative of aggregated material (**Figure 2.3.6, rightmost panel**).

In addition to the tumor tissue, a sample of yeast was imaged daily and used to calibrate the $^{12}C^{15}N/^{12}C^{14}N$ measurements relative to air (*vide infra*). ^{195}Pt counts obtained from images of samples of animals pretreated with saline solution were set as baseline counts and the ^{15}N distribution was in accordance with ^{15}N natural abundance. It is important to note that fluorescent images from these saline, control samples (**Figure 2.3.4, bottom row**) showed signals in the far red channel (Cy5) attributed to autofluorescence, since no specific ^{195}Pt or elevated ^{15}N signals were observed by NanoSIMS (**Figure 2.3.6, bottom panels**). This highlights the need and importance of multimodal imaging when studying labeled materials in complex biological systems.

As seen in **Figure 2.3.6**, samples exposed to both **Pt-EDAPT$_L$** and **PT-EDAPT$_D$** show colocalization of ^{195}Pt with high ^{15}N enriched areas. Some of these hotspots correlate with NIR fluorescent signals on the SIM images (**Figure 2.3.7**). This suggests that, in certain areas of the tumor, the three labels incorporated in the polymer are still associated with the aggregated nanomaterials. However, there is a higher concentration of counts for samples for both labels (^{15}N and Pt) in tissues that had been exposed to **Pt-EDAPT$_L$** than those exposed to **Pt-EDAPT$_D$**, which aligns with the greater retention in tumor tissues of the responsive material previously observed by fluorescence spectroscopy.

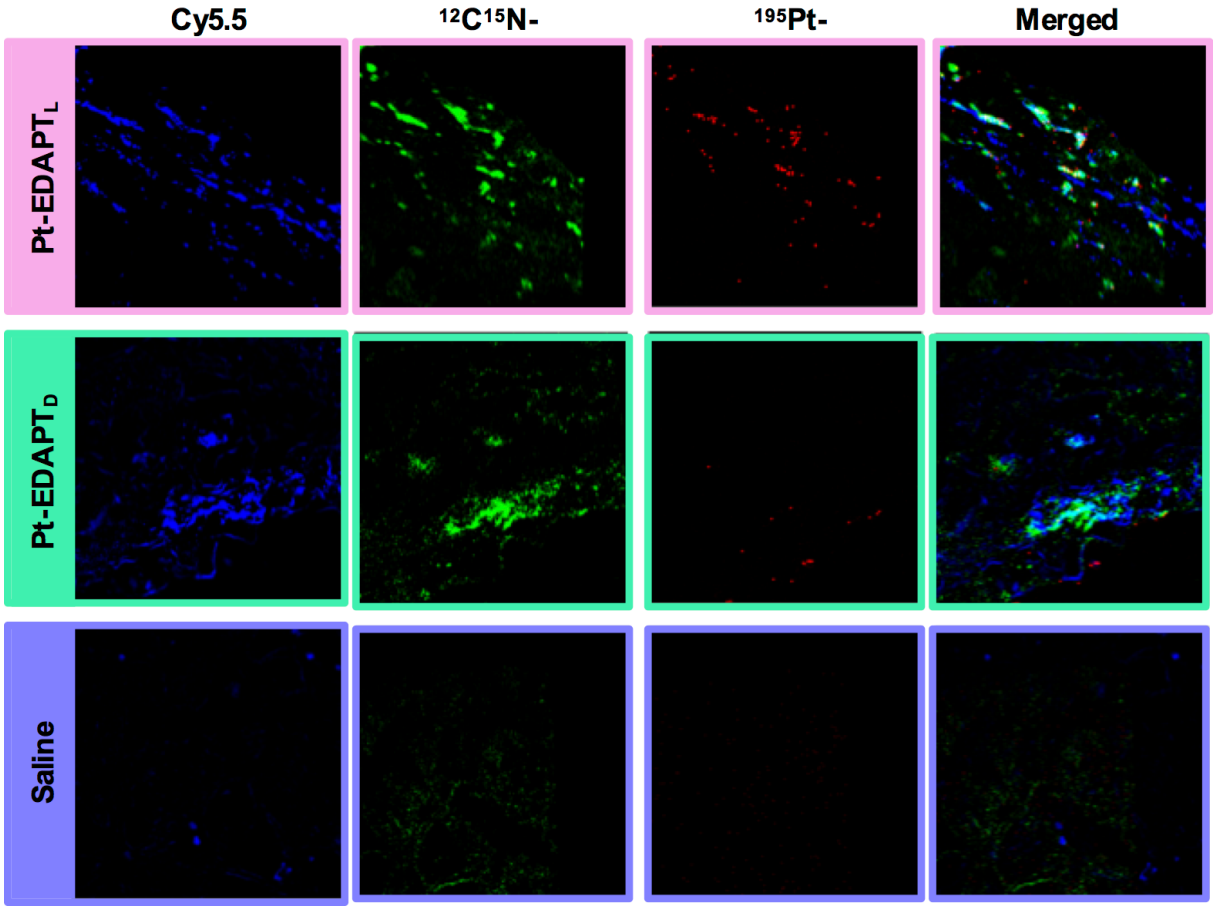

Figure 2.3.7. Overlay between the 3 different labels introduced in the polymers. Cy5.5 in blue (nanocarrier), $^{12}C^{15}N^-$ in green (nanocarrier) and $^{195}Pt^-$ in red (Pt-drug). The correlation was carried out for images from the three different studied conditions: tumor sections from mice treated with **Pt-EDAPT$_L$** (top), **Pt-EDAPT$_D$** (middle) and saline solution (bottom). While Cy5.5 and $^{12}C^{15}N^-$ images show large areas of overlap for **Pt-EDAPT$_L$** **Pt-EDAPT$_D$**, $^{195}Pt^-$ shows hotspots which correlate only partially. As expected, saline samples show only low signal (Cy5.5) or counts for $^{12}C^{15}N^-$ and $^{195}Pt^-$.

To better understand the distribution of nanocarrier drug in the tissue, regions of interest (ROIs) on the NanoSIMS images were defined, based on areas within the samples where high concentrations of each label was observed. These ROIs were used to quantify the accumulation of the nanocarrier and drug labels *within* (on) and *outside* (off) of ROIs. Thus, two types of ROIs were analyzed: *within* (on) or *outside* (off) highly ^{15}N-rich areas (on/off ^{15}N ROIs, defined from the corresponding HSI images, representing high concentrations aggregated polymer, **Figure 2.3.8a**) and *within* (on) or *outside* (off) ^{31}P-rich areas (on/off ^{31}P

ROIs, defined from the corresponding $^{31}P^-$ images, representing the nucleus of cells, **Figure 2.3.8b**), to analyze accumulation of the labels on the aggregated nanomaterial and on the nucleus of cells, respectively.

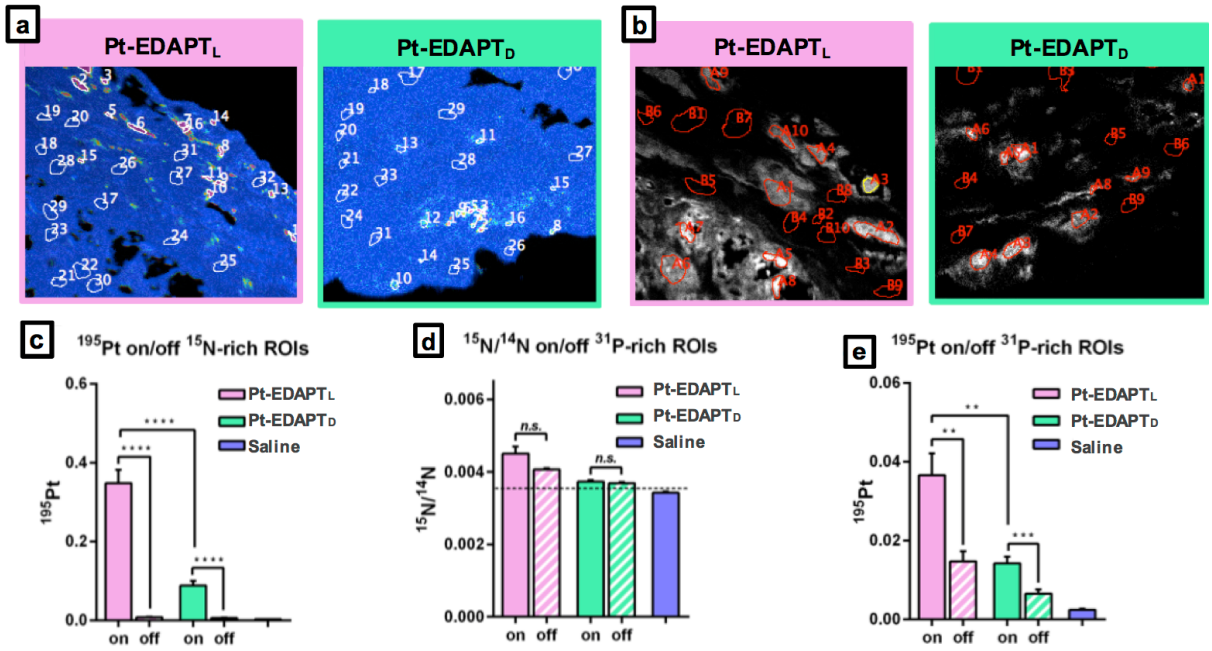

Figure 2.3.8. **Quantitative analysis of ^{15}N and ^{195}Pt enrichment.** a) ROIs were defined according to ^{15}N accumulation as "high ^{15}N/^{14}N" (ROI number 1-16) and "low ^{15}N/^{14}N" enrichment (ROI number 17-32). ^{15}N ROIs of the **Pt-EDAPT$_L$** HSI image are in the pink panel, and ^{15}N ROIs on the **Pt-EDAPT$_D$** HSI image in the green panel. b) ^{31}P ROIs on the **Pt-EDAPT$_L$** ^{31}P ion map (pink panel) ^{31}P ROIs on the **Pt-EDAPT$_D$** ^{31}P ion map image (green panel). c) ^{195}Pt enrichment on and off ^{15}N-rich ROIs. d) ^{15}N/^{15}N on and off ^{31}P-rich ROIs. e) ^{195}Pt enrichment on and off ^{31}P-rich ROIs. Note that Pt^- was collected as $^{196}Pt^-$ for the saline sample. Pt counts on saline ROIs were normalized to ^{195}Pt by multiplying by 1.34, according to their isotopic abundance (33.8/25.2). Enrichment values were obtained from at least two independent images of each sample. A summary of these results and its statistical analysis can be found in **Table 2.3.4**. Minimum significant difference was defined as a *p*-value < 0.05.

In analyzing the localization of ^{195}Pt with respect to the polymer backbone within the tissue, there is a significantly higher ^{195}Pt concentration within the ^{15}N-enriched areas than off the ^{15}N-ROI (**Figure 2.3.8c**), suggesting that at this time point, much of the Pt drug is still closely associated with the polymer. In analyzing the localization of materials in the cell nucleus by NanoSIMS, no significant difference was observed for ^{15}N between on and off ^{31}P-ROIs, indicating that there is no differential accumulation of polymer backbone within the nucleus, regardless of treatment (**Figure 2.3.8d**). However, differences between samples and between

the local sample distribution was observed for Pt, with a higher concentration of Pt on the nucleus and for the samples exposed to **Pt-EDAPT$_L$** (**Figure 2.3.8e**), which could be responsible for the enhanced efficacy of **Pt-EDAPT$_L$** *in vivo*.

2.3.3 Study Conclusions

In summary, these results demonstrate that the EDAPT platform is translatable to other small molecule cytotoxins, and that it is possible to analyze the components of the system simultaneously, yet independently from one another using SIM and NanoSIMS. The larger concentration of both ^{15}N and ^{195}Pt in tumor sections exposed to the responsive **Pt-EDAPT$_L$** is in agreement with the extended retention of this system observed *in vivo* over the non-responsive **Pt-EDAPT$_D$**. Tumor growth inhibition was only observed in animals administered **Pt-EDAPT$_L$**, suggesting that the Pt-drug is being released from the nanocarrier and binding to intracellular targets. Indeed, a higher ^{195}Pt concentration was observed on ^{31}P-rich ROIs (representing cell nuclei), and in respect to ^{15}N enrichment, for samples treated with the responsive nanoparticles, suggesting a specific association of Pt with ^{31}P-rich structures, such as DNA.

In addition to expanding the scope of the EDAPT platform, this study serves as a demonstration of the potential of correlated optical and isotopic nanoscopy for the study of nanomaterials in complex biological systems. Fluorescent microscopy enabled the differentiation of cellular structures and compartments in respect to the nanoparticle system by utilizing specific fluorescent markers. Further, NanoSIMS imaging revealed the specific accumulation of the nanoprobe in tumor tissue and showed the dissociation of the drug from the nanocarrier for enzyme-responsive system than for the non-responsive control system. Further, by comparing the specific localization of the nanocarrier and the drug at the nanometer scale, we could track *in situ*, in an unprecedented manner, the specific association of the Pt-

drug with the nuclear DNA of tumor tissues *in vivo*. We believe such new correlative approaches utilizing multi-element labeled systems are widely applicable for the study of many different systems. In the case of nanomaterials serving as delivery vehicles, these techniques can elucidate the pathway followed by the cargo and the nanocarrier and their performance following *in vivo* delivery.

2.3.4 Experimental Details

General Materials and Methods: All reagents were purchased from VWR, Alfa Aesar, or Sigma-Aldrich and used without further purification. Sealed ampules of DMF-d_7 (Cambridge Isotopes) were used without further purification. Modified second generation Grubbs' ruthenium initiator, $(IMesH_2)(C_5H_5N)_2(Cl)_2Ru{=}CHPh$, was prepared as previously described[18]. Drug, ^{15}N, peptide, and Cy5.5 monomers were synthesized as previously reported[80]. MMP-9 (catalytic domain) was obtained from Enzo Life Sciences as a solution in 50 mM TRIS, pH 7.5, containing 1 mM calcium chloride, 300 mM sodium chloride, 5 μM zinc chloride, 0.1% Brij-35 and 15% glycerol. HPLC analyses of all products and peptides were performed on a Jupiter 4u Proteo 90A Phenomenex column (150 x 4.60 mm) with a binary gradient, using a Hitachi-Elite LaChrom 2130 pump that was equipped with a Hitachi-Elite LaChrom L-2420 UV-Vis detector. Separation was achieved with a flow rate of 1 mL min^{-1} and the following mobile phase: 0.1% trifluoroacetic acid in H_2O (A) and 0.1% trifluoroacetic acid in ACN (B). Starting with 100% A and 0% B, a linear gradient was run for 30 min to a final solvent mixture of 33% A and 67% B, which was held for 5 min before ramping up to 0% A and 100% B over the course of 2 min and holding at this level for an additional 4 minutes, before ramping back down to 100% A and 0% B, with constant holding at this level for an additional 4 minutes. Mass

spectrometry (MS) of all synthesized compounds and peptides was performed at the Molecular Mass Spectrometry Facility (MMSF) in the Department of Chemistry and Biochemistry at the University of California, San Diego. Polymer dispersities and molecular weights were determined by size-exclusion chromatography (Phenomenex Phenogel 5u 10, 1k-75k, 300 x 7.80 mm in series with a Phenomex Phenogel 5u 10, 10K-1000K, 300 x 7.80 mm (0.05 M LiBr in DMF)) using a Shimadzu pump equipped with a multi-angle light scattering detector (DAWN-HELIOS: Wyatt Technology) and a refractive index detector Wyatt Optilab TrEX normalized to a 30,000 MW polystyrene standard. Particle diameters were determined by dynamic light scattering (DLS, D_{DLS}) using a Wyatt Dynapro NanoStar. TEM images were acquired on carbon grids (Ted Pella, INC.) using a FEI Tecnai G2 Sphera at 200 KV. TEM grids were prepared with a 1% uranyl acetate stain on carbon grids from Ted Pella, Inc.

General *in* vivo materials and Methods: Oxaliplatin Injection USP (Hospira, Inc.) was graciously donated by UCSD Moores Cancer Center (3855 Health Sciences Drive, La Jolla, CA). Tumors grown from HT-1080 fibrosarcoma cells (ATCC) were used for the model system, as this cell line overexpress MMPs. Nu/nu mice were obtained through the UCSD in-house breeding colony. Animals were inoculated with ~10^6 cells as a subcutaneous bolus, and treatments began once tumor mass reached ~50 mm^3. Animals were sacrificed at 12 days post-treatment. Calipers were used to record tumor volume daily over the course of the study. Absolute tumor volume was approximated with the formula: (1) V = 0.5 *length (mm) x $width^2$ (mm). Relative tumor volume was determined by the formula: (2) $V_{relative} = (V/V_i) * 100$, where V is the absolute tumor volume on the day of measurement and V_i is the absolute tumor volume on the first day of treatment. Live-animal imaging was taken on a GE Art Optix instrument. For optical imaging, animals were anesthetized with isofluorane with an induction dose of 3% and a maintenance dose of 1.5% in an oxygen gas stream. After injection, animals were imaged at given timepoints using a GE ART eXplore Optix Instrument (λ_{ex}= 635 nm and λ_{em}= 693 nm).

After sacrifice, tumors were harvested and frozen for tissue section preparation and analysis. Tumors were removed and frozen using cryoprotection and Optimum Cutting Temperature (O.C.T.) formulation. The tissue was then sectioned with a cryostat at 5 µm thickness and places on a ITO coverslip. A Zeiss ELYRA super resolution microscope located within the Environmental Molecular Sciences Laboratory at PNNL in Richland, WA was used for SIM imaging. A NanoSIMS 50L (Cameca, France) located within the Environmental Molecular Sciences Laboratory at PNNL in Richland, WA was used for secondary ion mass spectrometry imaging.

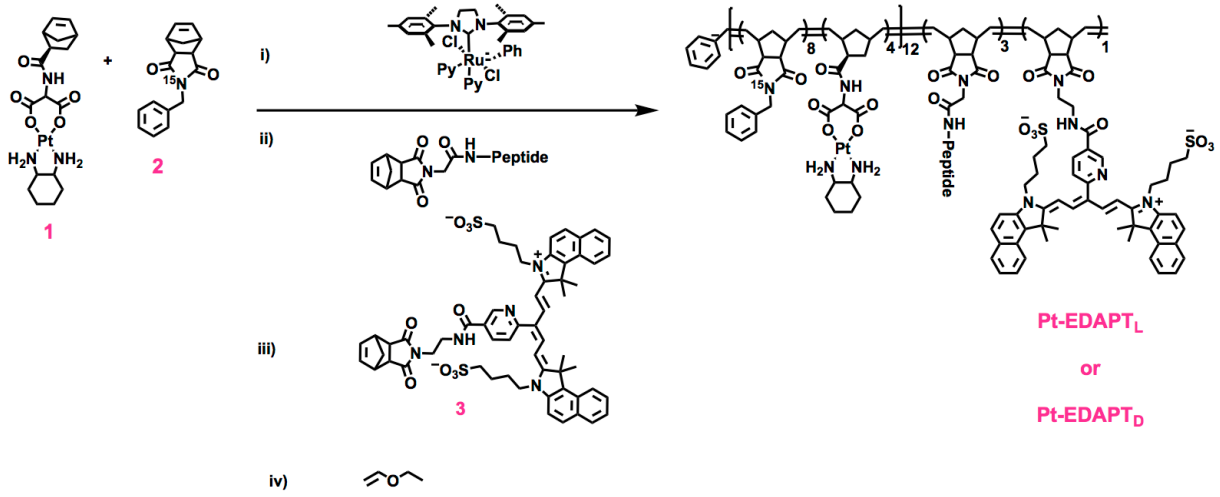

Figure 2.3.9. Synthetic scheme of Pt-EDAPT polymers. The Pt-based monomer (compound **1**) is first copolymerized with the ^{15}N-labelled monomer (compound **2**) through ROMP, followed by a second block composed of either *L*- or *D*- peptides, followed by one unit of Cy5.5 monomer (compound **3**), and terminated with ethyl vinyl ether to afford either **Pt-EDAPT$_L$** or **Pt-EDAPT$_D$**.

Polymer Synthesis: To a stirred solution of **1** (**Figure 2.3.9**) (6.59 mg, 2.6 x10-^{5} mol, 8.4 equiv) in dry DMF (140 µL) was added a solution of the catalyst ((IMesH$_2$)(C$_5$H$_5$N$_2$)(Cl)$_2$Ru=CHPh) (2.36 mg, 3.2x10^{-6} mol, 1.05 equiv) in dry DMF (105 µL) and a solution of **2** (7.08 mg, 1.3x10^{-5} mol, 4.2 equiv) in dry DMF (1700 µL). The reaction was allowed to stir under N$_2$ for 2 hours, after which an aliquot (30 µL) was removed and quenched with ethyl vinyl ether for Static Light Scattering (SLS) analysis. The remaining solution of **1** + **2**

+ catalyst (1800 µL) was split into two separate reaction vessels. To one reaction vessel was added a solution of L-peptide (See **Figure 2.2.9**, compound **2** for structure) (6.02 mg, $4.6x10^{-6}$ mol, 3 equiv) in 200 µL dry DMF (to ultimately afford **Pt-EDAPT$_L$**). To the second vessel was added a solution of D-peptide See **Figure 2.2.9**, compound **3** for structure) (6.02 mg, $4.6x10^{-6}$ mol, 3 equiv) in 200 µL dry DMF (to ultimately afford **Pt-EDAPT$_D$**). After three additional hours, a small aliquot was removed from each reaction vessel (30 µL each) and terminated with ethyl vinyl ether for SLS analysis. Then, to each of the polymer solutions was added **3** (1.16 mg, $1.2x10^{-6}$ mol, 0.75 equiv) and was allowed to stir for an additional two hours, before fully quenching the polymer solutions with ethyl vinyl ether. The fully terminated polymers were precipitated with a cold 1:1 ether:methanol solution to afford the block copolymers as dark yellow solids.

Table 2.3.1. Polymer analysis by SLS

		Mn	Mw	Dispersity
Pt-EDAPT$_L$	Block 1	6726	6856	1.019
	Full Polymer	8540	8980	1.051
	Block 2	1814	2124	--
Pt-EDAPT$_D$	Block 1	10870	11630	1.069
	Full Polymer	16010	17420	1.089
	Block 2	5140	5790	--

Nanoparticle Preparation and Characterization**:** Polymers (either *L*-peptide containing or *D*-peptide containing) were dissolved in DMSO at a concentration of 1.0 mg/mL with respect to polymer, and an additional 1 mL of 1X DPBS (Dulbecco's Phosphate Buffered Saline, no Ca, no Mg) was added over the course of 2 hours. These solutions were transferred to 3500 MWCO snakeskin dialysis tubing, and dialyzed against 1 L of 1X DPBS at pH 7.4 over 2 days with 2 buffer changes. The resulting solution was analyzed by DLS and TEM (**Figure 2.3.2**).

In Vitro Nanoparticle Degradation via MMP-12: 500 μM **Pt-EDAPT$_L$** (concentration with respect to peptide) or **Pt-EDAPT$_D$** were incubated with MMP-9 (100 nU) at 37 degrees Celsius. After 24 hours, samples were analyzed via RP-HPLC (λ = 254 nm) to monitor for the presence of peptide cleavage fragments, with sequence LAGGERDG. Samples were also analyzed by DLS and negative stain TEM to monitor for aggregation following MMP cleavage. This aggregation event only occurs in the **Pt-EDAPT$_L$** system, as evidenced by TEM and DLS (**Figure 2.3.2**).

Intratumoral Efficacy: 16 tumor-bearing nu/nu female mice were randomly sorted into 4 groups (4 mice per cohort) and treated with **Pt-EDAPT$_L$**, **Pt-EDAPT$_D$**, oxaliplatin, or saline at the dosage equivalent of 2.5 mg/kg of Pt as a single intratumoral injection. Mouse weight and tumor volume were recorded once daily over the course of the 12-day study. Animals were imaged at 0, 4, 24, 48, and 72 hours post-injection via live-animal optical imaging (see **Figure 2.3.3**). To assess efficacy, relative tumor volume (see equation (1) above) was calculated for each data point. The average relative tumor volume of each cohort at each time point was then calculated, along with standard deviation and standard error of the mean. Animals were sacrificed at 12 days post-injection. Tumor, liver, spleen, kidneys, heart, and lungs were excised from each animal and treated as in the above protocols.

Fluorescent IHC Staining of Tissue Sections: Tissue sections on 18 mm^2 ITO coverslips (70-100 Ω, 6462-AB, SPI supplies) were fixed for 10 min with acetone at room temperature and washed three times with PBSt (0.05% Tween in PBS). Sections were incubated with blocking solution (1% BSA in PBSt) for 15 min. The primary antibody mouse anti-alpha-actinin (A7811, Sigma Aldrich) was added in a 1/200 dilution in blocking buffer and incubated at 4 °C overnight. Tissues were washed three times with PBSt and the secondary antibody goat anti-mouse AlexaFluor 488 (A11001, Life Technologies) was added in a 1/400 dilution in blocking buffer and incubated for 30 min. Tissue sections were washed three times with PBSt and were

incubated for 10 min with a 300 nM solution of DAPI. The tissue sections were finally washed three times with PBSt and then subjected to a series of dehydration washes with 30%, 50%, 70%, 80% ethanol solutions and 3 times with 100% ethanol (30 min each).

Fluorescence Imaging by Wide-field and Structural Illumination Microscopy (SIM): SIM and wide-field fluorescence imaging was performed on the Elyra S1 inverted fluorescence microscope (Zeiss). To survey a large area of a tissue section, wide-field fluorescence microscopy with a 10X magnification objective was used. Multiple images were tiled to cover a large area. SIM was used to obtain high magnification, high resolution images, an oil immersion objective with 100X magnification and 1.4 numerical aperture was used in this study. The same set of lasers and fluorescence filters were used for wide-field fluorescence and SIM imaging. For every sample, 3 tracks were recorded sequentially to: (1) image the NPs (Cy5.5) using 642 nm laser excitation with emission wavelength longer than 655 nm; (2) image the cellular bodies (alpha-actinin) using 488 nm laser excitation with emission band 495 nm to 550 nm; and (3) image the nucleus (DAPI) using 405 nm laser excitation with emission band 420 nm to 480 nm. The laser power was adjusted accordingly due to the difference in signal level from different objectives. 3 rotations and 5 phases were taken for each SIM image. The resolution in the raw images was 80 nm per pixel, and in the resulting super resolution images was 40 nm per pixel. The camera exposure time was 100 ms per image. In SIM, the multi-phase/rotation/track data were later processed to obtain super resolution images using the ZEN software (Zeiss).

NanoSIMS Imaging: For NanoSIMS analyses, the samples were coated with 10 nm of Au prior to analysis to minimize sample charging. Samples were presputtered with about 2×10^{16} ions cm^{-2} after which, images sized 48 μm × 48 μm containing 256 pixel × 256 pixel were acquired with a 16 keV, ~1.5 pA Cs^+ primary ion beam (width ~115 nm) using magnetic peak switching, where in the first two planes $^{12}C^{14}N^-$, $^{31}P^-$ and $^{195}Pt^-$ were collected (13.5 ms/pixel).

After the first two planes, the detector collecting $^{12}C^{14}N^-$ was moved to collect $^{12}C^{15}N^-$ and in the second scan of the plane $^{12}C^{15}N^-$, $^{31}P^-$ and $^{195}Pt^-$ were collected in two consecutive planes at 13.5 ms/pixel). Secondary electron images (SE) were also collected for all analyses. Data was processed using OpenMIMS (National Resource for Imaging Mass Spectrometry, Harvard University, Cambridge), which is an ImageJ plugin (U. S. National Institutes of Health, Bethesda, Maryland) in which pixel by pixel deadtime (44 ns) and QSA ($\beta = 0.5$) corrections were applied. Data from ROIs were further processed in a spreadsheet. Prior to tumor analyses, yeast standards with known $\delta^{15}N$ were imaged each day with identicle analysis conditions to those used with the tumor sections. 16 ROIs were drawn around the yeast and used to correct each day's data. There appeared to be a minor interference associated with ^{195}Pt as evidenced in a small background, however Pt-treated cells had hotspots that were significantly higher than background.

SIM and NanoSIMS Correlated Images: NanoSIMS images were transformed using Matlab software to correlate with SIM images acquired on similar areas. Thus, all three signals observed on SIM images can be correlated with the seven acquired NanoSIMS images representing different ion maps.

Statistical Analysis of NanoSIMS Data: The first step for NanoSIMS data processing involved correcting the counts obtained for ^{15}N and ^{14}N against the standard yeast sample, which was measured each day before any of the samples. Thus, this yeast standard was used to correct the $^{15}N/^{14}N$ ratio relative to air, $\delta^{15}N \sim 0.35‰$. Those were called "corrected $^{15}N/^{14}N$ values" and were used for all further calculations. Note that Pt^- was collected as ^{196}Pt for the saline sample. Pt counts on saline ROIs were normalized to ^{195}Pt by multiplying by 1.34, according to their isotopic abundance (33.8/25.2).

On/off ^{15}N-rich ROIs: For samples containing nanoparticles, 16/16 ROIs on/off ^{15}N were selected from 3 independent images. On the saline sample, 16 ROIs were selected on tissue

from 2 different images. Each ROI value was obtained as the average counts per pixel in the ROI.

On/off ^{31}P-rich ROIs: 10/10 ROIs on/off ^{31}P were selected from 3 independent images for the samples containing **Pep-Pt-NP** and from 2 independent images for the saline samples.

ROI counts (as a ratio counts/area), were averaged for the different groups, leaving out of the average of those considered as outliers (values higher or lower to IQR*1.5).

Those averages and corresponding SE are listed in **Table 2.3.2** and **Table 2.3.3**. Additional statistical analyses were performed with Graphpad software with these values to compare bars on graphs of Figure 5 in the main text. The results of unpaired *t* tests are shown in **Table 2.3.4**.

Table 2.3.2. $^{15}N/^{14}N$ and ^{195}Pt counts for ROIs of selected on and off ^{15}N areas. Values are mean ± 1 SE.

	Pt-EDAPT$_L$	**Pt-EDAPT$_D$**	**Saline**
$^{15}N/^{14}N$ on	0.02966 ± 0.00132	0.00597 ± 0.00021	0.00346 ± 0.00002
$^{15}N/^{14}N$ off	0.00499 ± 0.00002	0.00369 ± 0.00002	
^{195}Pt on	0.3480 ± 0.0339	0.0882 ± 0.0114	0.0030 ± 0.0005
^{195}Pt off	0.0080 ± 0.0012	0.0057 ± 0.0010	

Table 2.3.3. $^{15}N/^{14}N$ and ^{195}Pt counts for ROIs selected on and off ^{31}P areas. Values are means ± 1 SE.

	Pt-EDAPT$_L$	**Pt-EDAPT$_D$**	**Saline**
$^{15}N/^{14}N$ on	0.00450 ± 0.00019	0.00373 ± 0.00004	0.00343 ± 0.00003
$^{15}N/^{14}N$ off	0.00407 ± 0.00003	0.00369 ± 0.00003	
^{195}Pt on	0.0365 ± 0.0056	0.0147 ± 0.0017	0.0023 ± 0.0004
^{195}Pt off	0.0147 ± 0.0026	0.0065 ± 0.0011	

Table 2.3.4. Statistical analysis for graphs in **Figure 2.3.8**

From Figure 2.3.8c: ^{195}Pt on/off ^{15}N-rich ROIs		
Variables analyzed	***p* value**	**Significance**
Pt-EDAPT$_L$ on *vs.* **Pt-EDAPT$_L$** off	$p \leq 0.0001$	****
Pt-EDAPT$_D$ on *vs.* **Pt-EDAPT$_D$** off	$p \leq 0.0001$	****
Pt-EDAPT$_L$ on *vs.* **Pt-EDAPT$_D$** on	$p \leq 0.0001$	****
Pt-EDAPT$_L$ off *vs.* **Pt-EDAPT$_D$** off	0.1739	ns
Pt-EDAPT$_L$ off *vs.* saline	0.0086	**
Pt-EDAPT$_D$ off *vs.* saline	0.3702	ns
From Figure 2.3.8d: ^{15}N/^{14}N on/off ^{31}P-rich ROIs		
Variables analyzed	***p* value**	**Significance**
Pt-EDAPT$_L$ on *vs.* **Pt-EDAPT$_L$** off	0.1392	ns
Pt-EDAPT$_D$ on *vs.* **Pt-EDAPT$_D$** off	0.5494	ns
Pt-EDAPT$_L$ on *vs.* **Pt-EDAPT$_D$** on	$p \leq 0.0001$	****
Pt-EDAPT$_L$ off *vs.* **Pt-EDAPT$_D$** off	$p \leq 0.0001$	****
Pt-EDAPT$_L$ off *vs.* saline	$p \leq 0.0001$	****
Pt-EDAPT$_D$ off *vs.* saline	$p \leq 0.0001$	****
From Figure 2.3.8e: ^{195}Pt on/off ^{31}P-rich ROIs		
Variables analyzed	***p* value**	**Significance**
Pt-EDAPT$_L$ on *vs.* **Pt-EDAPT$_L$** off	0.0017	**
Pt-EDAPT$_D$ on *vs.* **Pt-EDAPT$_D$** off	0.0002	***
Pt-EDAPT$_L$ on *vs.* **Pt-EDAPT$_D$** on	0.0025	**
Pt-EDAPT$_L$ off *vs.* **Pt-EDAPT$_D$** off	0.0279	*
Pt-EDAPT$_L$ off *vs.* saline	$p \leq 0.0001$	****
Pt-EDAPT$_D$ off *vs.* saline	0.0007	***

2.4 Perspectives and Future Studies

Chapter 2 encompasses much of the work-to-date on the employment of EDAPT for the delivery of cytotoxins to tumor tissue. Chapter 2.1, in particular, serves as a worthy proof-of-concept for this novel targeting mechanism for drug delivery. However, there are several areas where this platform can be expanded upon for optimizing the delivery of cytotoxins, as well as considerations that will make this platform more robust moving forward.

For example, the dose-response of **PTX-EDAPT** has not been fully evaluated and optimized. We completed a preliminary investigation of dose-response following a single IV injection, but did not observe a proportional increase in efficacy to injected dose (**Figure 2.4.1**).

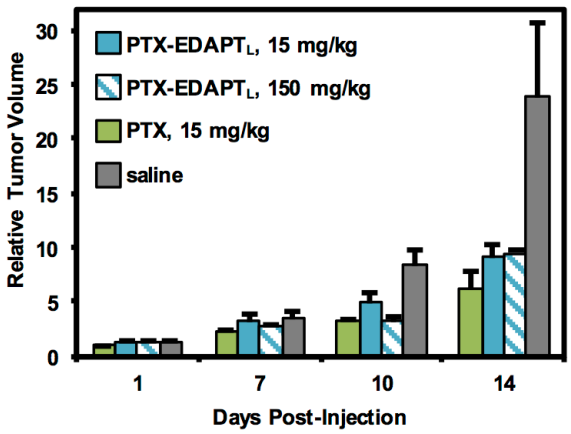

Figure 2.4.1. Dose-response investigation of PTX-EDAPT$_L$. The efficacy **of PTX-EDAPT$_L$** at elevated doses was preliminary investigated following single tail vein IV injection. Although no evidence of toxicity was observed (see **Figure 2.2.3a**), there was also no evidence that increasing the dose increased the response observed in the tumor. This may be perhaps be mitigated by altering the electronics of the drug-polymer bond, or altering the overall degradation rate of the aggregated material by introducing other polymerization methods.

One reason for this may be because PTX is bound to the polymer backbone via ester linkage. Although esters are labile covalent bonds, the timescale on which ester hydrolysis occurs *in vivo* may not be very fast, relative to overall clearance rate. Additionally, it is unknown how much of the hydrophobic PTX core may be sequestered in the interior of the aggregate post-accumulation, which would make it difficult for esterases to access these substrates. Thus, introducing more labile linkages between the drug and polymer backbone may provide an enhanced dose-response in the **PTX-EDAPT** system. For example, carbonate, carbamate, and cyclic acetal linkages differ in their stability with respect to hydrolysis and pH changes and

have shown promise for use in drug delivery [95-103]. Of course, tuning the electronics of the PTX-nanoparticle bond may affect the MTD of the system, as well, meaning there is the potential to develop an array of systems with unique drug release rates that influence efficacy and toxicity following administration.

Additionally, the efficacy of **PTX-EDAPT** following repeat injections has not been investigated, but is an important parameter to consider. As will be discussed in Chapter 5, the dosing schedule of chemotherapeutics can have a profound effect on the overall efficacy and toxicity of the warhead. Although a minimal increase in efficacy was observed for **PTX-EDAPT** at highly elevated doses, that may not matter if repeated injections at low dose result in complete tumor regression and minimal off-target toxicity. In addition, if an array of **PTX-EDAPT** nanoparticles with differing drug-polymer linkages were to be developed, it may be possible to optimize both the dosing schedule and cytotoxin release profiles for maximum efficacy and minimum toxicity.

Further, a full investigation of the pharmacokinetics (PK) and biodistribution (BD) of the **PTX-EDAPT** platform is warranted, given the promising preliminary data described in Chapter 2.2. Although efforts on the **Pt-EDAPT** system in Chapter 2.3 provide fundamental insight on the tissue distribution of both warhead and drug carrier, the overall PK and BD has not yet been fully established for any EDAPT-based system. Information on where the drug and nanocarrier are distributed throughout the body at any given timepoint would be beneficial for the development of EDAPT platforms moving forward, and can be achieved if the appropriate radiolabels are used. Further, knowing exactly when and where the drug dissociates from the carrier is critical, and efforts such as those described in Chapter 2.3 are the beginning of this front.

Beyond just tuning the drug-polymer bond, EDAPT systems containing biodegradable backbones may be better suited to clinical translation than their ROMP-based, glassy-

backboned counterparts. Indeed, work is ongoing in our lab towards the development of biodegradable EDAPT systems using reversible addition-fragmentation chain transfer (RAFT) polymerization techniques, such that there is no long-term retention in the body after completion of the desired function. This may also alter the release and efficacy profile of the therapeutic payload, and provide another avenue towards optimization of the drug delivery vehicle. Ultimately, this may be more translatable in general, as the degradation products are generally regarded as safe by the FDA, and there would be no leftover Ru to purify away from the polymer, as this polymerization technique is metal-free.

Of course, cytotoxins other than PTX and Pt may be even better suited for delivery using the EDAPT platform. Both PTX and Pt are good as initial proof-of-concept cytotoxins because they have clinically used counterparts. However, because we observe such a high MTD in the HT1080 model for the **PTX-EDAPT** system, we may be able to use this platform to deliver extremely cytotoxic that cannot be currently delivered at all using conventional delivery and formulation methods (indeed, Chapter 3 will investigate the use of EDAPT for the delivery of immunotherapeutics, which constitute a different class of therapeutics that are known to be acutely toxic and have their own sets of benefits and limitations that will be discussed therein). For example, we had initially investigated doxorubicin as an additional model cargo for the EDAPT platform, and although the norbornenyl monomer is accessible synthetically (**Figure 2.3.2a**) and forms nanoparticles when polymerized as a block copolymer with MMP-responsive peptides that aggregate in response to MMP exposure (**Figure 2.3.2b-c**), technical considerations hindered its development. Additionally, other cytotoxins may also be amenable to delivery through the EDAPT platform.

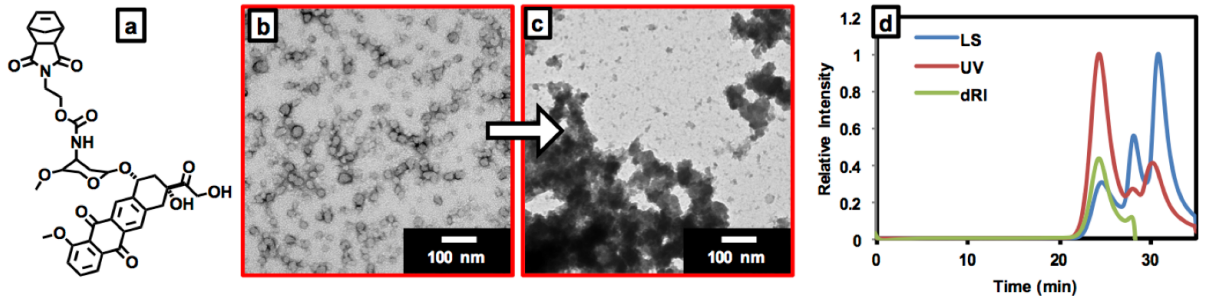

Figure 2.4.2. Doxorubicin-EDAPT development. a) structure of norbornenyl-doxorubicin (Dr. Steven Nguyen). Notably, the drug is bound *via* a carbamate linkage. b) after being copolymerized with MMP-responsive peptides as an amphiphilic diblock copolymer, nanoparticles form upon transition from DMF to aqueous solution. c) As their PTX-EDAPT and Pt-EDAPT counterparts, these doxorubicin-containing nanoparticles aggregate in response to enzyme exposure. d) SLS trace of doxorubicin homopolymer. Although the light scattering (LS) trace is strong, the calculated molecular weight is 500-fold higher than the theoretical molecular weight. This was observed multiple times, until it was determined that the doxorubicin molecule interferes with the SLS detector.

Finally, Chapter 2 serves as an insight to the feasibility of EDAPT as a strategy for *active accumulation and retention* of nanoparticles in tumors, which is non-reliant on the EPR effect discussed in Chapter 1. This process may be further enhanced if a suitable targeting ligand is grafted to the surface of the nanoparticles to instill *active tumor penetration*. Indeed, explorations in collaboration with the Proteogenomics Research Institute for Systems Medicine (PRISM) are ongoing on this front.

2.5 Acknowledgements

Chapter 2.2 is adapted, in part, from material as it appears in Advanced Materials 2015. Callmann, Cassandra; Barback, Christopher.; Thompson, Matthew; Hall, David; Mattrey, Robert; and Nathan Gianneschi. The dissertation author was the primary investigator and author of this paper.

Chapter 2.3 is adapted, in part, from material currently being prepared for submission for publication. Proetto, Maria; Callmann, Cassandra; Cliff, John; Szymanski, Craig; Hu, Dehong; Howell, Stephen; Evans, James; Orr, Galya; and Nathan Gianneschi. The dissertation author is a contributing author of this pending manuscript.

2.6 References

1. Chapman, S.; Dobrovolskaia, M.; Farahani, K.; Goodwin, A.; Joshi, A.; Lee, H.; Meade, T.; Pomper, M.; Ptak, K.; Rao, J.; Singh, R.; Sridhar, S.; Stern, S.; Wang, A.; Weaver, J. B.; Woloschak, G.; Yang, L., Nanoparticles for cancer imaging: The good, the bad, and the promise. *Nano today* **2013,** *8* (5), 454-460.

2. Chu, K. S.; Hasan, W.; Rawal, S.; Walsh, M. D.; Enlow, E. M.; Luft, J. C.; Bridges, A. S.; Kuijer, J. L.; Napier, M. E.; Zamboni, W. C.; DeSimone, J. M., Plasma, tumor and tissue pharmacokinetics of Docetaxel delivered via nanoparticles of different sizes and shapes in mice bearing SKOV-3 human ovarian carcinoma xenograft. *Nanomedicine* **2013,** *9* (5), 686-93.

3. Maeda, H.; Wu, J.; Sawa, T.; Matsumura, Y.; Hori, K., Tumor vascular permeability and the EPR effect in macromolecular therapeutics: a review. *Journal of Controlled Release* **2000,** *65* (1), 271-284.

4. Alexis, F.; Pridgen, E.; Molnar, L. K.; Farokhzad, O. C., Factors Affecting the Clearance and Biodistribution of Polymeric Nanoparticles. *Molecular Pharmaceutics* **2008,** *5* (4), 505-515.

5. Dvorak, H. F.; Nagy, J. A.; Dvorak, A. M., Structure of solid tumors and their vasculature: implications for therapy with monoclonal antibodies. *Cancer Cells* **1991,** *3*, 77-85.

6. Huang, X.; Molema, G.; King, S.; Watkins, L.; Edgington, T. S.; Thorpe, P. E., Tumor infarction in mice by antibody-directed targeting of tissue factor to tumor vasculature. *Science* **1997,** *275*, 547-550.

7. Wilhelm, S.; Tavares, A. J.; Dai, Q.; Ohta, S.; Audet, J.; Dvorak, H. F.; Chan, W. C. W., Analysis of nanoparticle delivery to tumours. *Nature Reviews Materials* **2016,** *1* (5), 16014.

8. Olson, E. S.; Jiang, T.; Aguilera, T. A.; Nguyen, Q. T.; Ellies, L. G.; Scadeng, M.; Tsien, R. Y., Activatable cell penetrating peptides linked to nanoparticles as dual probes for in vivo fluorescence and MR imaging of proteases. *Proceedings of the National Academy of Sciences* **2010,** *107* (9), 4311-4316.

9. Uloza, V.; Liutkevičius, V.; Pangonytė, D.; Šaferis, V.; Lesauskaitė, V., Expression of matrix metalloproteinases (MMP-2 and MMP-9) in recurrent respiratory papillomas and laryngeal carcinoma: clinical and morphological parallels. *Eur Arch Otorhinolaryngol* **2011,** *268* (6), 871-878.

10. Malemud, C. J., Matrix metalloproteinases (MMPs) in health and disease: an overview. *Frontiers in Bioscience* **2006,** *11*, 1696-1701.

11. Chien, M.-P.; Thompson, M. P.; Barback, C. V.; Ku, T.-H.; Hall, D. J.; Gianneschi, N. C., Enzyme-Directed Assembly of a Nanoparticle Probe in Tumor Tissue. *Advanced Materials* **2013,** *25* (26), 3599-3604.

12. Chien, M.-P.; Carlini, A. S.; Hu, D.; Barback, C. V.; Rush, A. M.; Hall, D. J.; Orr, G.; Gianneschi, N. C., Enzyme-Directed Assembly of Nanoparticles in Tumors Monitored by in Vivo Whole Animal Imaging and ex Vivo Super-Resolution Fluorescence Imaging. *Journal of the American Chemical Society* **2013,** *135* (50), 18710-18713.

13. Callmann, C. E.; Barback, C. V.; Thompson, M. P.; Hall, D. J.; Mattrey, R. F.; Gianneschi, N. C., Therapeutic Enzyme-Responsive Nanoparticles for Targeted Delivery and Accumulation in Tumors. *Adv Mater* **2015,** *27* (31), 4611-4615.

14. Nguyen, M. M.; Carlini, A. S.; Chien, M.-P.; Sonnenberg, S.; Luo, C.; Braden, R. L.; Osborn, K. G.; Li, Y.; Gianneschi, N. C.; Christman, K. L., Enzyme-Responsive Nanoparticles for Targeted Accumulation and Prolonged Retention in Heart Tissue after Myocardial Infarction. *Advanced Materials* **2015,** *27* (37), 5547-5552.

15. Monopoli, M. P.; Åberg, C.; Salvati, A.; Dawson, K. A., Biomolecular coronas provide the biological identity of nanosized materials. *Nature Nanotechnology* **2012,** *7*, 779.

16. Bielawski, C. W.; Grubbs, R. H., Highly Efficient Ring-Opening Metathesis Polymerization (ROMP) Using New Ruthenium Catalysts Containing N-Heterocyclic Carbene Ligands. *Angewandte Chemie International Edition* **2000,** *39* (16), 2903-2906.

17. Grubbs, R. H., Olefin metathesis. *Tetrahedron* **2004,** *60* (34), 7117-7140.

18. Sanford, M. S.; Love, J. A.; Grubbs, R. H., A Versatile Precursor for the Synthesis of New Ruthenium Olefin Metathesis Catalysts. *Organometallics* **2001,** *20* (25), 5314-5318.

19. Sanford, M. S.; Love, J. A.; Grubbs, R. H., Mechanism and Activity of Ruthenium Olefin Metathesis Catalysts. *Journal of the American Chemical Society* **2001,** *123* (27), 6543-6554.

20. Scholl, M.; Ding, S.; Lee, C. W.; Grubbs, R. H., Synthesis and Activity of a New Generation of Ruthenium-Based Olefin Metathesis Catalysts Coordinated with 1,3-Dimesityl-4,5-dihydroimidazol-2-ylidene Ligands. *Organic Letters* **1999,** *1* (6), 953-956.

21. Thompson, M. P.; Randolph, L. M.; James, C. R.; Davalos, A. N.; Hahn, M. E.; Gianneschi, N. C., Labelling polymers and micellar nanoparticles via initiation, propagation and termination with ROMP. *Polymer Chemistry* **2014,** *5* (6), 1954-1964.

22. Ungerleider, J. L.; Kammeyer, J. K.; Braden, R. L.; Christman, K. L.; Gianneschi, N. C., Enzyme-targeted nanoparticles for delivery to ischemic skeletal muscle. *Polymer Chemistry* **2017,** *8* (34), 5212-5219.

23. Davis, M. E.; Chen, Z.; Shin, D. M., Nanoparticle therapeutics: an emerging treatment modality for cancer. *Nat Rev Drug Discov* **2008,** *7* (9), 771-782.

24. Blum, A. P.; Kammeyer, J. K.; Rush, A. M.; Callmann, C. E.; Hahn, M. E.; Gianneschi, N. C., Stimuli-Responsive Nanomaterials for Biomedical Applications. *Journal of the American Chemical Society* **2015,** *137* (6), 2140-2154.

25. Bae, Y. H.; Park, K., Targeted drug delivery to tumors: Myths, reality and possibility. *Journal of Controlled Release* **2011,** *153* (3), 198-205.

26. Kobayashi, H.; Watanabe, R.; Choyke, P. L., Improving Conventional Enhanced Permeability and Retention (EPR) Effects; What Is the Appropriate Target? *Theranostics* **2014,** *4* (1), 81-89.

27. Jain, R. K.; Stylianopoulos, T., Delivering nanomedicine to solid tumors. *Nat Rev Clin Oncol* **2010,** *7* (11), 653-664.

28. Danhier, F.; Feron, O.; Préat, V., To exploit the tumor microenvironment: Passive and active tumor targeting of nanocarriers for anti-cancer drug delivery. *Journal of Controlled Release* **2010,** *148* (2), 135-146.

29. Arap, W.; Pasqualini, R.; Ruoslahti, E., Cancer Treatment by Targeted Drug Delivery to Tumor Vasculature in a Mouse Model. *Science* **1998,** *279* (5349), 377-380.

30. Horton, M. A., The αvβ3 integrin “vitronectin receptor”. *The International Journal of Biochemistry & Cell Biology* **1997,** *29* (5), 721-725.

31. Jin, H.; Varner, J., Integrins: roles in cancer development and as treatment targets. *Br J Cancer* **2004,** *90* (3), 561-565.

32. Temming, K.; Schiffelers, R. M.; Molema, G.; Kok, R. J., RGD-based strategies for selective delivery of therapeutics and imaging agents to the tumour vasculature. *Drug Resistance Updates* **2005,** *8* (6), 381-402.

33. Pierschbacher, M. D.; Ruoslahti, E., Cell attachment activity of fibronectin can be duplicated by small synthetic fragments of the molecule. *Nature* **1984,** *309* (5963), 30-33.

34. Lawler, J.; Weinstein, R.; Hynes, R. O., Cell attachment to thrombospondin: the role of ARG-GLY-ASP, calcium, and integrin receptors. *The Journal of Cell Biology* **1988,** *107* (6), 2351-2361.

35. Pasqualini, R.; Koivunen, E.; Kain, R.; Lahdenranta, J.; Sakamoto, M.; Stryhn, A.; Ashmun, R. A.; Shapiro, L. H.; Arap, W.; Ruoslahti, E., Aminopeptidase N Is a Receptor for Tumor-homing Peptides and a Target for Inhibiting Angiogenesis. *Cancer Research* **2000,** *60* (3), 722-727.

36. Curnis, F.; Sacchi, A.; Borgna, L.; Magni, F.; Gasparri, A.; Corti, A., Enhancement of tumor necrosis factor [alpha] antitumor immunotherapeutic properties by targeted delivery to aminopeptidase N (CD13). *Nat Biotech* **2000,** *18* (11), 1185-1190.

37. Garde, S. V.; Forté, A. J.; Ge, M.; Lepekhin, E. A.; Panchal, C. J.; Rabbani, S. A.; Wu, J. J., Binding and internalization of NGR-peptide-targeted liposomal doxorubicin (TVT-DOX) in CD13-expressing cells and its antitumor effects. *Anti-Cancer Drugs* **2007,** *18* (10), 1189-1200.

38. Pastorino, F.; Brignole, C.; Marimpietri, D.; Cilli, M.; Gambini, C.; Ribatti, D.; Longhi, R.; Allen, T. M.; Corti, A.; Ponzoni, M., Vascular Damage and Anti-angiogenic Effects of Tumor Vessel-Targeted Liposomal Chemotherapy. *Cancer Research* **2003,** *63* (21), 7400-7409.

39. Low, P. S.; Antony, A. C., Folate receptor-targeted drugs for cancer and inflammatory diseases. *Advanced Drug Delivery Reviews* **2004,** *56* (8), 1055-1058.

40. Stella, B.; Arpicco, S.; Peracchia, M. T.; Desmaële, D.; Hoebeke, J.; Renoir, M.; D'Angelo, J.; Cattel, L.; Couvreur, P., Design of folic acid-conjugated nanoparticles for drug targeting. *Journal of Pharmaceutical Sciences* **2000,** *89* (11), 1452-1464.

41. Leamon, C. P.; Reddy, J. A., Folate-targeted chemotherapy. *Advanced Drug Delivery Reviews* **2004,** *56* (8), 1127-1141.

42. Lee, R. J.; Low, P. S., Folate-mediated tumor cell targeting of liposome-entrapped doxorubicin in vitro. *Biochimica et Biophysica Acta (BBA) - Biomembranes* **1995,** *1233* (2), 134-144.

43. Leamon, C.; Low, P., Selective Targeting of Malignant Cells with Cytotoxin-Folate Conjugates. *Journal of Drug Targeting* **1994,** *2* (2), 101-112.

44. Galande, A. K.; Hilderbrand, S. A.; Weissleder, R.; Tung, C.-H., Enzyme-Targeted Fluorescent Imaging Probes on a Multiple Antigenic Peptide Core. *Journal of Medicinal Chemistry* **2006,** *49* (15), 4715-4720.

45. Nguyen, Q. T.; Olson, E. S.; Aguilera, T. A.; Jiang, T.; Scadeng, M.; Ellies, L. G.; Tsien, R. Y., Surgery with molecular fluorescence imaging using activatable cell-penetrating peptides decreases residual cancer and improves survival. *Proceedings of the National Academy of Sciences* **2010,** *107* (9), 4317-4322.

46. Chien, M.-P.; Thompson, M. P.; Lin, E. C.; Gianneschi, N. C., Fluorogenic enzyme-responsive micellar nanoparticles. *Chemical Science* **2012,** *3* (9), 2690-2694.

47. Kessenbrock, K.; Plaks, V.; Werb, Z., Matrix Metalloproteinases: Regulators of the Tumor Microenvironment. *Cell* **2010,** *141* (1), 52-67.

48. Bremer, C.; Bredow, S.; Mahmood, U.; Weissleder, R.; Tung, C.-H., Optical Imaging of Matrix Metalloproteinase–2 Activity in Tumors: Feasibility Study in a Mouse Model. *Radiology* **2001,** *221* (2), 523-529.

49. Jiang, T.; Olson, E. S.; Nguyen, Q. T.; Roy, M.; Jennings, P. A.; Tsien, R. Y., Tumor imaging by means of proteolytic activation of cell-penetrating peptides. *Proceedings of the National Academy of Sciences of the United States of America* **2004,** *101* (51), 17867-17872.

50. Metildi, C.; Felsen, C.; Savariar, E.; Nguyen, Q.; Kaushal, S.; Hoffman, R.; Tsien, R.; Bouvet, M., Ratiometric Activatable Cell-Penetrating Peptides Label Pancreatic Cancer, Enabling Fluorescence-Guided Surgery, Which Reduces Metastases and Recurrence in Orthotopic Mouse Models. *Ann Surg Oncol* **2014**, 1-6.

51. Trnka, T. M.; Grubbs, R. H., The Development of L2X2RuCHR Olefin Metathesis Catalysts: An Organometallic Success Story. *Accounts of Chemical Research* **2001,** *34* (1), 18-29.

52. Slugovc, C., The Ring Opening Metathesis Polymerisation Toolbox. *Macromolecular Rapid Communications* **2004,** *25* (14), 1283-1297.

53. Kammeyer, J. K.; Blum, A. P.; Adamiak, L.; Hahn, M. E.; Gianneschi, N. C., Polymerization of protecting-group-free peptides via ROMP. *Polymer Chemistry* **2013,** *4* (14), 3929-3933.

54. C. G. Biagini, S.; Gareth Davies, R.; North, M.; C. Gibson, V.; R. Giles, M.; L. Marshall, E.; A. Robson, D., The synthesis and ring-opening metathesis polymerization of peptide functionalized norbornenes. *Chemical Communications* **1999,** (3), 235-236.

55. Leitgeb, A.; Wappel, J.; Slugovc, C., The ROMP toolbox upgraded. *Polymer* **2010,** *51* (14), 2927-2946.

56. Maynard, H. D.; Okada, S. Y.; Grubbs, R. H., Synthesis of Norbornenyl Polymers with Bioactive Oligopeptides by Ring-Opening Metathesis Polymerization. *Macromolecules* **2000,** *33* (17), 6239-6248.

57. Sutthasupa, S.; Shiotsuki, M.; Sanda, F., Recent advances in ring-opening metathesis polymerization, and application to synthesis of functional materials. *Polym J* **2010,** *42* (12), 905-915.

58. Schiff, P. B.; Fant, J.; Horwitz, S. B., Promotion of microtubule assembly in vitro by taxol. *Nature* **1979,** *277* (5698), 665-667.

59. Band Horwitz, S., Mechanism of action of taxol. *Trends in Pharmacological Sciences* **1992,** *13* (0), 134-136.

60. Rowinsky, E. K.; Donehower, R. C., Paclitaxel (Taxol). *New England Journal of Medicine* **1995,** *332* (15), 1004-1014.

61. Blum, A. P.; Kammeyer, J. K.; Yin, J.; Crystal, D. T.; Rush, A. M.; Gilson, M. K.; Gianneschi, N. C., Peptides Displayed as High Density Brush Polymers Resist Proteolysis and Retain Bioactivity. *Journal of the American Chemical Society* **2014,** *136* (43), 15422-15437.

62. Yoon, S.-O.; Kim, M.-M.; Chung, A.-S., Inhibitory Effect of Selenite on Invasion of HT1080 Tumor Cells. *Journal of Biological Chemistry* **2001,** *276* (23), 20085-20092.

63. Cao, S.; Black, J. D.; Troutt, A. B.; Rustum, Y. M., Interleukin 15 offers selective protection from irinotecan-induced intestinal toxicity in a preclinical animal model. *Cancer Res* **1998,** *58* (15), 3270-4.

64. Cao, S.; Rustum, Y. M., Synergistic Antitumor Activity of Irinotecan in Combination with 5-Fluorouracil in Rats Bearing Advanced Colorectal Cancer: Role of Drug Sequence and Dose. *Cancer Research* **2000,** *60* (14), 3717-3721.

65. Huang, G. S.; Lopez-Barcons, L.; Freeze, B. S.; Smith, A. B.; Goldberg, G. L.; Horwitz, S. B.; McDaid, H. M., Potentiation of Taxol Efficacy by Discodermolide in Ovarian Carcinoma Xenograft-Bearing Mice. *Clinical Cancer Research* **2006,** *12* (1), 298-304.

66. Yamori, T.; Sato, S.; Chikazawa, H.; Kadota, T., Anti-tumor Efficacy of Paclitaxel against Human Lung Cancer Xenografts. *Japanese Journal of Cancer Research* **1997,** *88* (12), 1205-1210.

67. Trail, P. A.; Willner, D.; Bianchi, A. B.; Henderson, A. J.; TrailSmith, M. D.; Girit, E.; Lasch, S.; Hellström, I.; Hellström, K. E., Enhanced Antitumor Activity of Paclitaxel in Combination with the Anticarcinoma Immunoconjugate BR96-Doxorubicin. *Clinical Cancer Research* **1999,** *5* (11), 3632-3638.

68. Ayers, G. D.; McKinley, E. T.; Zhao, P.; Fritz, J. M.; Metry, R. E.; Deal, B. C.; Adlerz, K. M.; Coffey, R. J.; Manning, H. C., Volume of preclinical xenograft tumors is more accurately assessed by ultrasound imaging than manual caliper measurements. *Journal of ultrasound in medicine : official journal of the American Institute of Ultrasound in Medicine* **2010,** *29* (6), 891-901.

69. Simpson-Herren, L.; Lloyd, H. H., Kinetic parameters and growth curves for experimental tumor systems. *Cancer chemotherapy reports. Part 1* **1970,** *54* (3), 143.

70. Yorke, E. D.; Fuks, Z.; Norton, L.; Whitmore, W.; Ling, C. C., Modeling the Development of Metastases from Primary and Locally Recurrent Tumors: Comparison with a Clinical Data Base for Prostatic Cancer. *Cancer Research* **1993,** *53* (13), 2987-2993.

71. Gref, R.; Domb, A.; Quellec, P.; Blunk, T.; Müller, R. H.; Verbavatz, J. M.; Langer, R., The controlled intravenous delivery of drugs using PEG-coated sterically stabilized nanospheres. *Advanced Drug Delivery Reviews* **1995,** *16* (2–3), 215-233.

72. Blanco, E.; Shen, H.; Ferrari, M., Principles of nanoparticle design for overcoming biological barriers to drug delivery. *Nature biotechnology* **2015,** *33* (9), 941-951.

73. Choi, H. S.; Gibbs, S. L.; Lee, J. H.; Kim, S. H.; Ashitate, Y.; Liu, F.; Hyun, H.; Park, G.; Xie, Y.; Bae, S.; Henary, M.; Frangioni, J. V., Targeted zwitterionic near-infrared fluorophores for improved optical imaging. *Nat Biotech* **2013,** *31* (2), 148-153.

74. Goldberg, E. P.; Hadba, A. R.; Almond, B. A.; Marotta, J. S., Intratumoral cancer chemotherapy and immunotherapy: opportunities for nonsystemic preoperative drug delivery. *Journal of Pharmacy and Pharmacology* **2002,** *54* (2), 159-180.

75. Walter, K. A.; Tamargo, R. J.; Olivi, A.; Burger, P. C.; Brem, H., Intratumoral Chemotherapy. *Neurosurgery* **1995,** *37* (6), 1129-1145.

76. Tong, Y.; Song, W.; Crystal, R. G., Combined Intratumoral Injection of Bone Marrow-derived Dendritic Cells and Systemic Chemotherapy to Treat Pre-existing Murine Tumors. *Cancer Research* **2001,** *61* (20), 7530-7535.

77. Lammers, T.; Peschke, P.; Kühnlein, R.; Subr, V.; Ulbrich, K.; Huber, P.; Hennink, W.; Stormy, G., Effect of Intratumoral Injection on the Biodistribution and the Therapeutic Potential of HPMA Copolymer-Based Drug Delivery Systems. *Neoplasia (New York, N.Y.)* **2006,** *8* (10), 788-795.

78. Celikoglu, F.; Celikoglu, S. I.; Goldberg, E. P., Bronchoscopic intratumoral chemotherapy of lung cancer. *Lung Cancer* **2008,** *61* (1), 1-12.

79. Patel, P. R.; Kiser, R. C.; Lu, Y. Y.; Fong, E.; Ho, W. C.; Tirrell, D. A.; Grubbs, R. H., Synthesis and Cell Adhesive Properties of Linear and Cyclic RGD Functionalized Polynorbornene Thin Films. *Biomacromolecules* **2012,** *13* (8), 2546-2553.

80. Proetto, M. T.; Anderton, C. R.; Hu, D.; Szymanski, C. J.; Zhu, Z.; Patterson, J. P.; Kammeyer, J. K.; Nilewski, L. G.; Rush, A. M.; Bell, N. C.; Evans, J. E.; Orr, G.; Howell, S. B.; Gianneschi, N. C., Cellular Delivery of Nanoparticles Revealed with Combined Optical and Isotopic Nanoscopy. *ACS Nano* **2016**.

81. Proetto, M. T.; Rush, A. M.; Chien, M.-P.; Abellan Baeza, P.; Patterson, J. P.; Thompson, M. P.; Olson, N. H.; Moore, C. E.; Rheingold, A. L.; Andolina, C.; Millstone, J.; Howell, S. B.; Browning, N. D.; Evans, J. E.; Gianneschi, N. C., Dynamics of Soft Nanomaterials Captured by Transmission Electron Microscopy in Liquid Water. *Journal of the American Chemical Society* **2014,** *136* (4), 1162-1165.

82. Patterson, J. P.; Proetto, M. T.; Gianneschi, N. C., Soft nanomaterials analysed by in situ liquid TEM: Towards high resolution characterisation of nanoparticles in motion. *Perspectives in Science* **2015,** *6*, 106-112.

83. Rao, C. N. R.; Biswas, K., Characterization of Nanomaterials by Physical Methods. *Annu Rev Anal Chem* **2009,** *2*, 435-462.

84. Lin, P. C.; Lin, S.; Wang, P. C.; Sridhar, R., Techniques for physicochemical characterization of nanomaterials. *Biotechnol Adv* **2014,** *32* (4), 711-726.

85. Battistella, C.; Klok, H. A., Controlling and Monitoring Intracellular Delivery of Anticancer Polymer Nanomedicines. *Macromol Biosci* **2017**.

86. Ivask, A.; Mitchell, A. J.; Malysheva, A.; Voelcker, N. H.; Lombi, E., Methodologies and approaches for the analysis of cell-nanoparticle interactions. *Wiley Interdiscip Rev Nanomed Nanobiotechnol* **2017**.

87. Saka, S. K.; Vogts, A.; Kröhnert, K.; Hillion, F.; Rizzoli, S. O.; Wessels, J. T., Correlated optical and isotopic nanoscopy. *Nat Commun* **2014,** *5*.

88. Lee, R. F. S.; Theiner, S.; Meibom, A.; Koellensperger, G.; Keppler, B. K.; Dyson, P. J., Application of imaging mass spectrometry approaches to facilitate metal-based anticancer drug research. *Metallomics* **2017,** *9* (4), 365-381.

89. Nunez, J.; Renslow, R.; Cliff, J. B.; Anderton, C. R., NanoSIMS for biological applications: Current practices and analyses. *Biointerphases* **2018,** *13* (3).

90. Legin, A. A.; Schintlmeister, A.; Jakupec, M. A.; Galanski, M.; Lichtscheidl, I.; Wagner, M.; Keppler, B. K., NanoSIMS combined with fluorescence microscopy as a tool for subcellular imaging of isotopically labeled platinum-based anticancer drugs. *Chemical Science* **2014,** *5* (8), 3135-3143.

91. Xia, Y.; Olsen, B. D.; Kornfield, J. A.; Grubbs, R. H., Efficient Synthesis of Narrowly Dispersed Brush Copolymers and Study of Their Assemblies: The Importance of Side Chain Arrangement. *Journal of the American Chemical Society* **2009,** *131* (51), 18525-18532.

92. Yoon, S. O.; Kim, M. M.; Chung, A. S., Inhibitory effect of selenite on invasion of HT1080 tumor cells. *Journal of Biological Chemistry* **2001,** *276* (23), 20085-20092.

93. Wheate, N. J.; Walker, S.; Craig, G. E.; Oun, R., The status of platinum anticancer drugs in the clinic and in clinical trials. *Dalton Transactions* **2010,** *39* (35), 8113-8127.

94. Wedlock, L. E.; Kilburn, M. R.; Liu, R.; Shaw, J. A.; Berners-Price, S. J.; Farrell, N. P., NanoSIMS multi-element imaging reveals internalisation and nucleolar targeting for a highly-charged polynuclear platinum compound. *Chemical Communications* **2013,** *49* (62), 6944-6946.

95. Yang, Y.-h.; Aloysius, H.; Inoyama, D.; Chen, Y.; Hu, L.-q., Enzyme-mediated hydrolytic activation of prodrugs. *Acta Pharmaceutica Sinica B* **2011,** *1* (3), 143-159.

96. de Groot, F. M. H.; Busscher, G. F.; Aben, R. W. M.; Scheeren, H. W., Novel 20-Carbonate Linked Prodrugs of Camptothecin and 9-Aminocamptothecin Designed for Activation by Tumour-Associated Plasmin. *Bioorganic & Medicinal Chemistry Letters* **2002,** *12* (17), 2371-2376.

97. Greenwald, R. B.; Pendri, A.; Conover, C. D.; Zhao, H.; Choe, Y. H.; Martinez, A.; Shum, K.; Guan, S., Drug Delivery Systems Employing 1,4- or 1,6-Elimination: Poly(ethylene glycol) Prodrugs of Amine-Containing Compounds. *J Med Chem* **1999,** *42* (18), 3657-3667.

98. Jordan, A. M.; Khan, T. H.; Malkin, H.; Osborn, H. M. I., Synthesis and analysis of urea and carbamate prodrugs as candidates for melanocyte-directed enzyme prodrug therapy (MDEPT). *Bioorganic & Medicinal Chemistry* **2002,** *10* (8), 2625-2633.

99. Meng, Q.; Luo, H.; Liu, Y.; Li, W.; Zhang, W.; Yao, Q., Synthesis and evaluation of carbamate prodrugs of SQ109 as antituberculosis agents. *Bioorganic & Medicinal Chemistry Letters* **2009,** *19* (10), 2808-2810.

100. Nomura, M.; Shuto, S.; Matsuda, A., Synthesis of the cyclic and acyclic acetal derivatives of 1-(3-C-Ethynyl-β-d-ribo-pentofuranosyl)cytosine, a potent antitumor nucleoside. Design of prodrugs to be selectively activated in tumor tissues via the bio-Reduction–Hydrolysis mechanism. *Bioorganic & Medicinal Chemistry* **2003,** *11* (11), 2453-2461.

101. Binauld, S.; Stenzel, M. H., Acid-degradable polymers for drug delivery: a decade of innovation. *Chemical Communications* **2013,** *49* (21), 2082-2102.

102. Kaihara, S.; Matsumura, S.; Fisher, J. P., Synthesis and characterization of cyclic acetal based degradable hydrogels. *European Journal of Pharmaceutics and Biopharmaceutics* **2008,** *68* (1), 67-73.

103. Gillies, E. R.; Goodwin, A. P.; Fréchet, J. M. J., Acetals as pH-Sensitive Linkages for Drug Delivery. *Bioconjugate Chemistry* **2004,** *15* (6), 1254-1263.

Chapter 3

Enzyme-Responsive Nanomaterials for the Delivery of Immunotherapeutics

3.1 Introduction

While Chapter 2 explores the utility of the EDAPT platform for the delivery of cytotoxins to tumor tissue (for an explanation of EDAPT, see Chapter 2.1), Chapter 3 serves as the first investigation of using enzyme-responsive nanomaterials to deliver small molecule immune agonists to tumors. While the goal of materials developed in Chapter 2 is to use EDAPT to tackle significant limitations facing traditional cytotoxic drug delivery, namely the frequently narrow therapeutic indexes and significant off-target toxicities, a problem inherent to nearly all chemotherapeutics is acquired resistance. Towards this end, immunotherapy has been proposed as a strategy to bypass acquired resistance by stimulation of a host immune response for long-lasting tumor destruction [1-2]. Thus, the goal of Chapter 3 is to utilize EDAPT to accumulate small molecule immune activators within tumor tissue at high concentrations and for extended periods of time following systemic administration (IV). The central objective

of this work was to develop highly efficient, actively targeted nanoparticle immunotherapeutics with minimal systemic toxicity.

Materials that activate the innate immune system against tumors have great potential as cancer therapeutics, as evidenced by the vast increase in the number of immunotherapy-based treatments in clinical trials in recent years[3-4]. Despite this promise, immunotherapeutics face significant challenges. As is the case for numerous classes of drugs, many powerful immunostimulatory molecules suffer from solubility and stability issues that prevent their direct translation as clinical therapeutics.[5-8] Further, as the field continues to develop potent immunotherapies, the risk of cytokine release syndrome (CRS) is vastly increased. CRS is a serious adverse event where high-level immune activation occurs within hours to weeks following administration of immunotherapeutics, which can have life-threatening consequences for the patient.[9-11] Indeed, several immunotherapeutics have failed in clinical trials or have been removed from the market due to the severity of CRS toxicity.[12-16] Thus, it is necessary to develop novel formulations that overcome immune related adverse effects (IRAEs)[17] and poor solubility while maintaining therapeutic efficacy. In an effort to solve these problems, there has been an increased interest in recent years in the development of nanoparticle systems designed to enhance the action of immunotherapy.[18-22] However, this field is still in its infancy with no synthetic nanoparticle delivery strategy having been translated to the clinic in this context.

To address the problems associated with solubility and CRS, we hypothesized that packaging an immunopharmacophore in a tumor-targeted nanocarrier could increase solubility and reduce the risk of IRAEs (**immuno-EDAPT**, **Figure 3.1.1a**). As discussed in Chapter 2, our laboratory has developed a polymeric nanoparticle delivery platform that utilizes endogenous enzymes associated with inflammation[23-25] to localize and retain nanomaterials within diseased tissues.[26-32] These materials are generated through the self-assembly of

amphiphilic diblock copolymers. The polymers are designed such that the hydrophilic polymer block, which ultimately forms the shell of the nanoparticle, is comprised of enzyme-responsive peptides, while the hydrophobic polymer block, which forms the core of the nanoparticle, contains the warhead of interest[26]. The key to the targeting of this nanoparticle system lies in the incorporation of enzyme-responsive peptides into the nanoparticle shell. Specifically, these hydrophilic peptides contain substrates for matrix metalloproteinases (MMPs), which are overexpressed in many cancers (**Figure 3.1.1b**).[33-35] Notably, this enzyme-responsive platform has been used to safely intravenously deliver therapeutic doses of paclitaxel to tumor tissue with efficacy matching that of the parent compound at equivalent dose, but with a significantly higher maximum tolerated dose (MTD).[26] Given these results, we hypothesized that we could exploit this technology to carry an immunopharmacophore and to reduce systemic cytokine release and subsequent IRAEs.

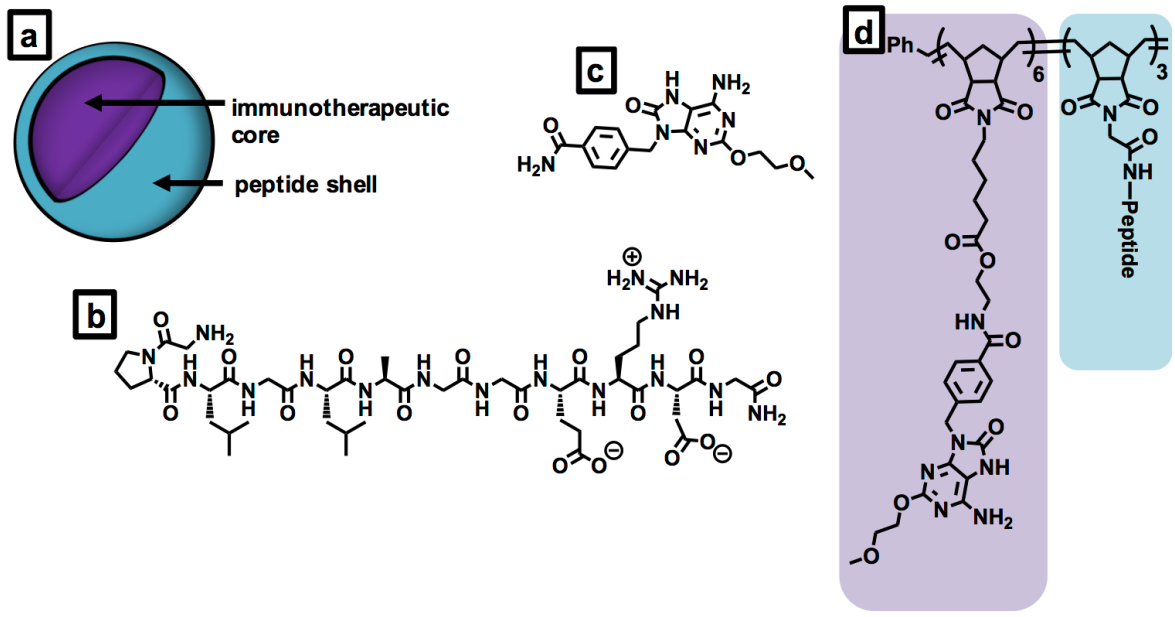

Figure 3.1.1. Immunotherapeutic enzyme-responsive nanoparticles (immuno-EDAPT). a) Schematic representation of **immuno-EDAPT**, where the nanoparticle core, represented in blue, contains the immunotherapeutic of interest, while the nanoparticle shell, represented in orange, contains the enzyme-responsive peptide. b) Structure of MMP-responsive peptide. c) Structure of TLR7 agonist 1V209. d) Structure of amphiphilic diblock copolymers containing norbornenyl-1V209 and MMP-responsive peptide.

Herein, 1V209 (Figure **3.1.1c**), a small molecule agonist of Toll-like receptor 7 (TLR7) developed in the Carson laboratory,[7] was chosen as a proof-of-concept for the delivery of immunotherapeutic pharmacophores using the enzyme-responsive platform. Toll-like receptors (TLRs) are part of the innate immune system that recognize Pathogen-Associated Molecular Patterns (PAMPs) and activate the adaptive immune system. TLR ligands promote maturation of myeloid derived suppressor cells (MDSC) to matured dendritic cells and activation of tumor associated suppressor macrophages (M2 macrophages) to tumoricidal macrophages (M1 macrophages). TLR ligands have also been shown to enhance tumor specific adaptive immune response, which in turn inhibits metastasis formation.[36] TLR7, located in the endosomal compartments of immune cells, binds single-stranded RNA and is an established target for small molecules capable of reviving the immune system to act against tumor tissues.[37-38] Though a potent immunostimulant, 1V209 is poorly water soluble and systemic administration can result in rapid systemic cytokine release and acute lethality (see **Figure 3.5.3**), presumably from CRS (*vide infra*). Clinical trials have been previously performed using TLR ligands but have failed for three primary reasons similar to those described above: 1) serious adverse events, most notably CRS, occurring with systemic administration; 2) modes of administration had not been optimized, leading to immune tolerance; and 3) poor specificity of the previous agents led to a minimal type 1 interferon response [39-40]. Thus, we hypothesized that covalently sequestering potent immunotherapeutics, using 1V209 as a model compound, in the core of enzyme-responsive nanomaterials, could address these issues.

3.2 Results and Discussion

Amphiphilic, diblock copolymers (**Figure 3.1.1d**) that incorporate both 1V209 and MMP-responsive peptides were generated through ring opening metathesis polymerization (ROMP) using a pyridine modified Grubbs' second-generation initiator.[41-44] ROMP enables the generation of highly reproducible polymers with narrow molecular weight dispersities, providing precise control over polymer block length and identity. Both 1V209 and the MMP-responsive peptide were modified with norbornenyl groups for polymerization (**Figure 3.2.1**).

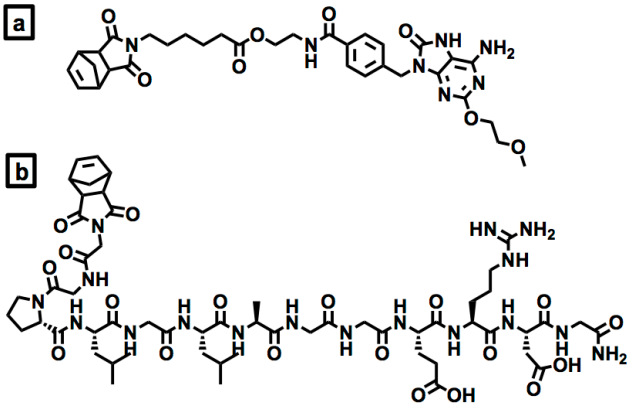

Figure 3.2.1. Structure of ROMP monomers. a) structure of norbornenyl-modified 1V209. Note: parent molecule had to be appended with an ethanolamine spacer (for parent molecule, see **Figure 3.2.1b**) to allow for efficient conjugation to the norbornenyl moiety. b) structure of norbornenyl-modified, enzyme-responsive peptide.

Norbornenyl-1V209 was polymerized as the hydrophobic block, followed by either an MMP-responsive peptide composed of all *L*-amino acids, or a nonresponsive peptide composed of all *D*- amino acids (for more in depth explanation of enzyme-responsive peptides, see Chapter 2.1), to afford two different amphiphilic diblock copolymer systems: **immuno-EDAPT$_L$** (composed of the *L*-peptides) and **immuno-EDAPT$_D$** (composed of the *D*-peptides that are not recognized by MMPs as efficient substrates). Upon dialysis from DMSO against aqueous media, **immuno-EDAPT$_L$** formed spherical nanoparticles visualizable by TEM and DLS (**Figure 3.2.2a**). Incubation of **immuno-EDAPT$_L$** with MMP-9 at 37°C overnight confirmed the ability of the nanoparticle system to respond to enzymes (100:1 peptide:enzyme). As expected, a shift in morphology was observed, as evidenced by dynamic light scattering and

TEM. Upon dialysis from DMSO against aqueous media, **immuno-EDAPT$_D$** also formed spherical nanoparticles visualizable by TEM and DLS (**Figure 3.2.2b**). However, no change in morphology was observed for **immuno-EDAPT$_D$** when exposed to the same enzyme digestion conditions as **immuno-EDAPT$_L$** This data indicates that MMP exposure is necessary for the shape change of these materials.

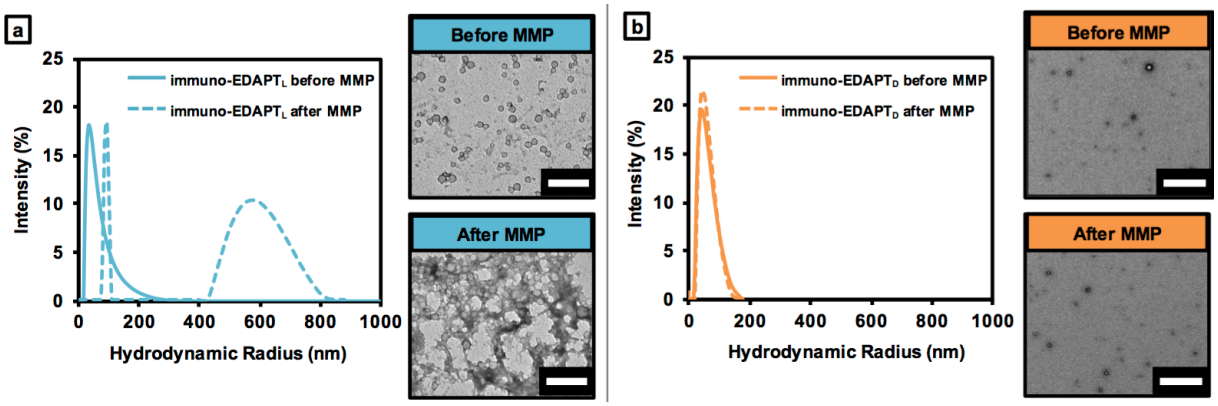

Figure 3.2.2. Analysis of immuno-EDAPT systems before and after MMP. a) Prior to MMP incubation, **immuno-EDAPT$_L$** forms spherical nanoparticles that are visualizable by DLS (dotted line on on graph) and dry-state TEM (top right panel). Exposure to MMP-9 overnight at 37°C induces a morphology change that is visualizable by DLS (solid line, left graph) and dry-state TEM (bottom right panel). b) **immuno-EDAPT$_D$** forms spherical nanoparticles that are visualizable by DLS (dotted line on graph) and dry-state TEM (top right panel). Exposure to MMP-9 overnight at 37°C has no effect on particle morphology change by neither DLS (solid line on graph) nor dry-state TEM (bottom right panel). Scale bar = 500 nm.

When appending moieties to molecules designed to interact with proteins based on their ability to fit into the target binding site, it is necessary to ensure that derivatization of the warhead does not negatively impact the therapeutic capability. Thus, we first examined the immunogenicity of norbornenyl-1V209 in comparison to the parent therapeutic. Importantly, derivatization did not affect its potency, as evidenced by its ability to stimulate TNFα production in RAW246.7 cells *in vitro* (**Figure 3.2.4a**).

After confirming that derivatization of the parent molecule, the ability of **immuno-EDAPT$_L$** to function as an immune stimulator was then evaluated *in vitro*. Briefly, murine primary bone marrow derived dendritic cells (BMDCs) were incubated for 18 hours with

immuno-EDAPT$_L$, with or without pre-treatment with MMP-9, and the subsequent production of IL-6 was measured (**Figure 3.2.4b**). Additionally, cells were incubated with **immuno-EDAPT$_D$**, with and without pre-treatment with MMP, to further examine the effect of MMP exposure and enzyme-driven morphology change on cytokine production. Minimal release of IL-6 was observed when cells were incubated with **immuno-EDAPT$_L$** without MMP pretreatment. However, significantly higher levels of IL-6 were detected in the culture supernatant of cells incubated with **immuno-EDAPT$_L$** that had been pre-treated with MMP-9. Conversely, no increase was observed when incubated with **immuno-EDAPT$_L$** with MMP pre-treatment, demonstrating that MMP did not affect IL-6 release and, further, that morphology change is necessary to generate the immunostimulatory effects. Taken together, these data indicate that these materials are poorly immunogenic as nanoparticles, but are potent as aggregates.

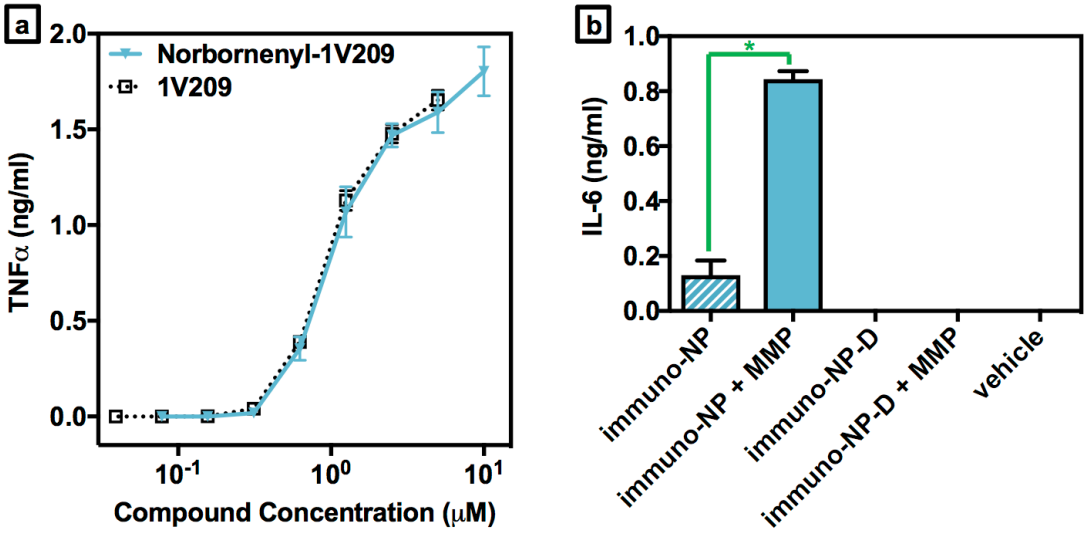

Figure 3.2.4. *In vitro* cytokine upregulation. a) TNFα release was evaluated by ELISA after incubation with 1V209 and norbornenyl-1V209. No change in cytokine release levels was observed, indicating that modifying 1V209 with a norbornenyl moiety does not affect its potency. b) IL-6 release in the culture supernatant was measured after incubating 10^6/mL murine BMDCs with **immuno-EDAPT$_L$** (with or without pretreatment with MMP), **immuno-EDAPT$_D$** (with or without pretreatment with MMP), 1V209, or saline at 100 μM with respect to immunotherapeutic content. *P values were calculated by one way ANOVA with Dunnet's post hoc testing and $p<0.05$ was considered as statistically significant.

The first evaluation of **immuno-EDAPT** *in vivo* was a pilot study to determine whether the delivery vehicle would inhibit the action of the conjugated immunotherapeutic *in vivo*. In this study, a syngeneic murine model of SCC-7 (squamous cell carcinoma) was employed, and animals (n=8 per group) were intratumorally administered either **immuno-EDAPT$_L$**, 1V209 (positive control), or saline (negative control). When tumors reached 3-5 mm in diameter, treatment was initiated as daily IT injections of 100 µg/animal for 5 days (qdx5) (**Figure 3.2.5**). Throughout the duration of the study, **immuno-EDAPT$_L$** demonstrated equivalent efficacy to the parent compound, suggesting that the delivery vehicle should not inhibit immunotherapeutic performance.

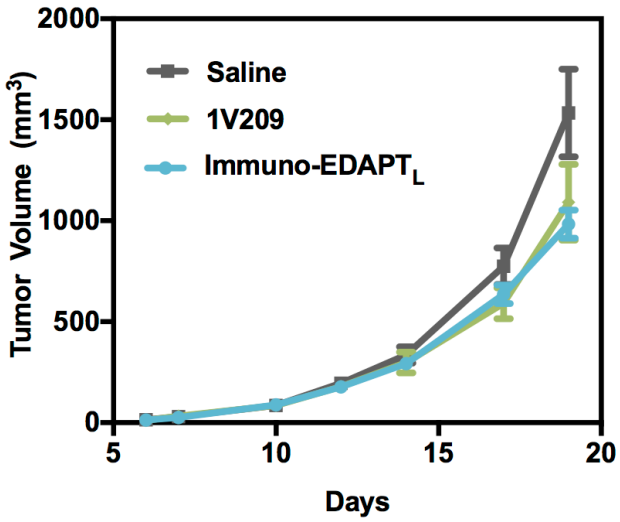

Figure 3.2.5. *In vivo* efficacy of immuno-EDAPT$_L$ in SCC-7 primary tumor model. As a preliminary proof-of-concept, the efficacy of **immuno-EDAPT$_L$** (blue curve) relative to that of the parent therapeutic (green curve) and saline (grey curve) following IT administration into mice bearing SCC-7 tumors once daily for 5 days (qdx5). **immuno-EDAPT$_L$** showed enhanced efficacy over saline and equivalent efficacy as 1V209, suggesting that the delivery vehicle should not impact *in vivo* efficacy. Note: IT injections were employed to ensure that all the material for both groups was delivered to the tissue.

To further evaluate the safety and efficacy of **immuno-EDAPT** as an immunotherapeutic delivery vehicle, the therapeutic potency of **immuno-EDAPT$_L$** was evaluated in syngeneic murine models of human breast cancer *in vivo*. These studies utilized an orthotopic 4T1 breast cancer model that is poorly immunogenic and highly metastatic, known to overexpresses MMPs,[45-46] and has been shown to be responsive to immunotherapy.[47] In this model, 4T1 cells implanted into mammary fat pads spontaneously produce lung metastases within 7-14 days post-implantation. Balb/C mice were inoculated with

~10^6 4T1 cells in both inguinal mammary fat pads. On days 7 and 14 post-inoculation, mice were intravenously (IV) administered either **immuno-EDAPT$_L$**, **immuno-EDAPT$_D$**, 1V209, or saline through tail vein at a total dose equivalent to 30 µg 1V209 per animal (n=10 per group). Body weight and primary tumor growth were monitored throughout the duration of the study.

To evaluate the efficacy of **immuno-EDAPT$_L$** at inhibiting metastasis formation, animals were sacrificed at 28 days post-inoculation. Each animal's lungs were perfused with a 15% India ink solution, extracted, and number of lung nodules were counted as per published protocols.[48] Mice administered **immuno-EDAPT$_L$** had significantly fewer lung nodules ($p<.05$) than those administered saline, whereas minimal reduction in metastases was observed in animals administered **immuno-EDAPT$_D$** or 1V209, relative to saline treated controls (**Figure 3.2.6**).

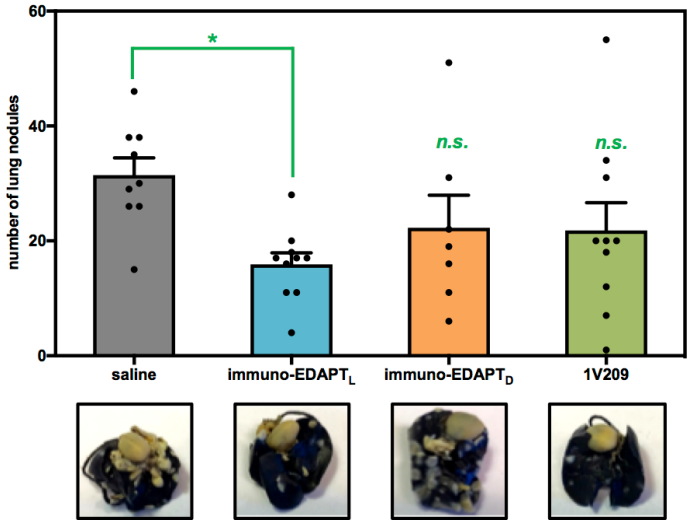

Figure 3.2.6. Efficacy of immuno-EDAPT$_L$ in 4T1 metastasis model. Immuno-EDAPT$_L$ reduces the number of lung metastasis in the murine syngeneic breast cancer model in vivo. Top graph: Lung nodule count at 28 days post-injection. Significant decrease in the average number of lung nodules is observed in animals treated with **immuno-EDAPT$_L$**, while 1V209 or **immuno-EDAPT$_D$** have minimal effect on controlling lung metastases. Each dot represents data from an individual mouse and the column indicates the mean ± SEM. Representative examples of lung nodules shown for each group below the plot.

To assess the safety of **immuno-EDAPT$_L$,** sera were collected at 2 hours following the initial IV injection and the levels of cytokines IP-10, MCP-1, and IL-6 in plasma were determined (**Figure 3.2.7**). No significant upregulation of these cytokines was observed in animals administered with either **immuno-EDAPT$_L$** or **immuno-EDAPT$_D$**. However, increased

levels of all three inflammatory cytokines assayed was observed in animals administered 1V209. This shows that packaging the immunotherapeutic inside a nanocarrier sufficiently prevents it from stimulating the immune system upon systemic exposure, thus reducing the risk of CRS.

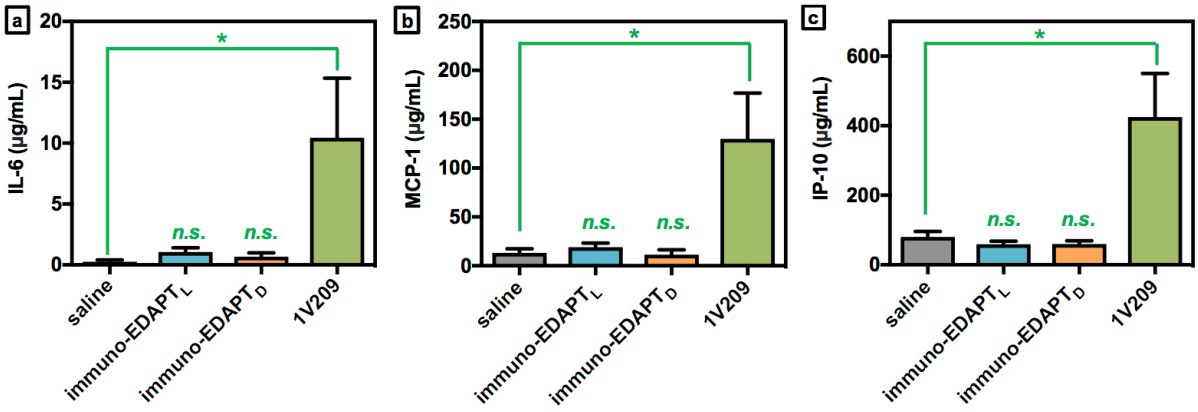

Figure 3.2.7. Plasma cytokine level measurement post-injection. a) Plasma concentration of IL-6 at 2 hours measured at 2 hours post-IV injection. Significant IL-6 production is observed only in animals administered 1V209. b) Plasma concentration of MCP-1, another proinflammatory cytokine, measured at 2 hours post-IV injection. Significant MCP-1 production is observed only in animals administered 1V209. c) Plasma concentration of IP-10 at 2 hours post-IV injection. Significant IP-10 production is observed only in animals administered 1V209. *P values were calculated by one way ANOVA with Dunnet's post hoc testing and $p<0.05$ was considered as statistically significant.

3.3 Study Conclusions

Taken together, these results demonstrate the potential of actively targeted nanoparticle immunotherapeutics with minimal systemic cytokine induction. Appending a norbornenyl handle to 1V209 maintains its potency as a TLR7 agonist while making it amenable to incorporation into amphiphilic diblock copolymers with MMP-responsive peptides, and on into nanoparticle formulations. IV administration of **immuno-EDAPT$_L$** significantly reduces the number of lung nodules observed at 28 days post-inoculation relative to negative control without eliciting an acute immune response. The method in which these nanoparticles are synthesized is modular, which means this approach could be expanded to incorporate other immunostimulatory small molecules. Further, there is great potential for the utilization of this motif to co-deliver chemotherapeutics alongside immunostimulatory molecules[49-50] in a way that matches the activation and accumulation of both drugs to that of the nanocarrier. Indeed, certain chemotherapeutics, including oxaliplatin and paclitaxel, are known to elicit an immune response at the tumor post-injection [51-52] and induce immunogenic cell death promoting activation of antigen presenting cells (APCs) to enhance adaptive immune responses by releasing endogenous innate immune stimulators [53]. Thus, this platform has the potential to impact how malignancies are treated and how other immunotherapeutics are formulated, targeted, and delivered.

3.4 Experimental Details

In Vitro Studies, General Methods: All reagents were obtained from Sigma Aldrich or Fisher Scientific and used without further purification. Polymerizations were performed in a dry, nitrogen atmosphere with anhydrous solvents. Both L- and D-amino acids were purchased from AAPPTEC and NovaBiochem. MMP-9 (catalytic domain) was obtained from Enzo Life Sciences as a solution in 50mM TRIS, pH 7.5, containing 1mM calcium chloride, 300mM sodium chloride, 5μM zinc chloride, 0.1% Brij-35 and 15% glycerol. HPLC analyses of all products and peptides were performed on a Jupiter 4u Proteo 90A Phenomenex column (150 x 4.60 mm) with a binary gradient, using a Hitachi-Elite LaChrom 2130 pump that was equipped with a Hitachi-Elite LaChrom L-2420 UV-Vis detector. Separation was achieved with a flow rate of 1 mL min^{-1} and the following mobile phase: 0.1% trifluoroacetic acid in H_2O (A) and 0.1% trifluoroacetic acid in ACN (B). Mass spectrometry (MS) of all synthesized compounds and peptides was performed at the Molecular Mass Spectrometry Facility (MMSF) in the Department of Chemistry and Biochemistry at the University of California, San Diego. Polymer dispersities and molecular weights were determined by size-exclusion chromatography (Phenomenex Phenogel 5u 10, 1K-75K, 300 x 7.80 mm in series with a Phenomenex Phenogel 5u 10, 10K-100K, 300 x 7.80 mm) in 0.05 M LiBr in DMF, using a Shimatzu pump that was equipped with a multi-angle light scattering detector (DAWN-HELIOS, Wyatt Technology) and a refractive index detectors (Wyatt Optilab T-rEX) normalized to a 30,000 MW polystyrene standard. Hydrodynamic radius (R_h) was determined by dynamic light scattering (DLS), through a Wyatt Dynapro NanoStar. Transmission Electron Microscopy (TEM) was performed on an FEI Tecnai G2 Sphera at 200 KV. TEM grids were prepared with a 1% uranyl acetate stain on carbon grids from Ted Pella, Inc. Chemical shifts (^1H) are reported in δ (ppm), relative to the residual proton peak of $CDCl_3$ (7.27 ppm).

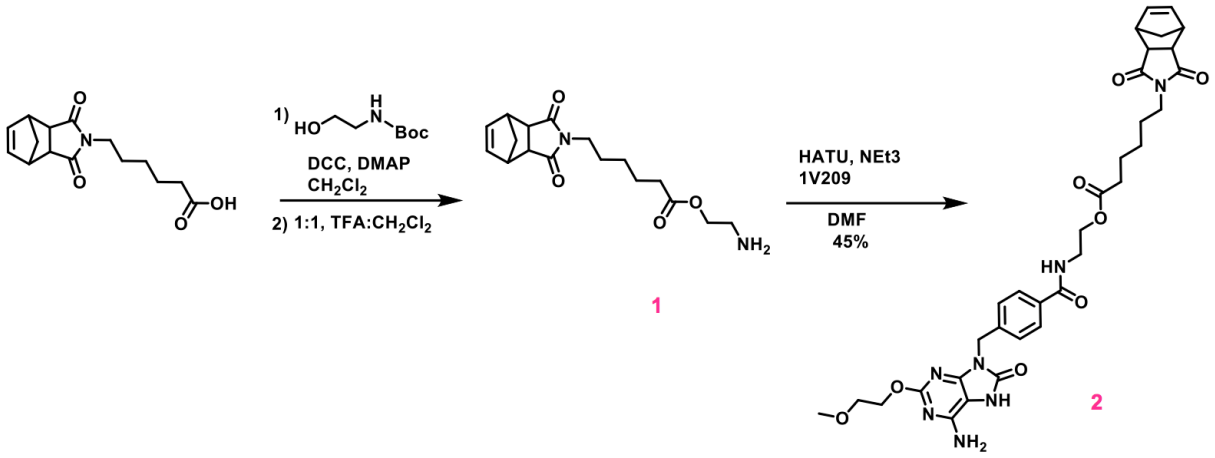

Figure 3.4.1 Synthesis of 1V209 monomer. The norbornenyl-immunotherapeutic compound is generated in two steps, after first modifying the 6-aminohexanoic acid norbornenyl moiety with ethanolamine for ease of conjugation to the immunotherapeutic through amide generation.

Norbornenyl-1V209 Synthesis: Compound **1**: To a solution of the norbornene hexanoic acid (500 mg, 1.80 mmol) and N-Boc-ethanolamine (436 mg, 2.70 mmol) in dichloromethane was added DMAP (88 mg, 0.72 mmol) followed by DCC (557 mg, 2.70 mmol). The solution was stirred under a nitrogen atmosphere overnight during which time a precipitate formed. The mixture was filtered and the filtrate concentrated to dryness. The residue was purified by flash chromatography (5% THF in DCM) to give a white solid that was subsequently treated with a 1:1 TFA:DCM solution for 3 hrs to remove the Boc group. The solvent was removed under reduced pressure to give a gummy solid to which diethyl ether was added, mixed then removed under reduced pressure (x4). The resulting residue was purified by column chromatography, 10% Methanol: DCM to give a clear oil as Compound **1**. ^{1}H NMR, CD_3OD, 6.33 (m, 2H), 4.31 (m, 2H), 3.48 (m, 2H), 3.25 (m, 2H), 3.17 (m, 2H), 2.72 (m, 2H), 2.40 (m, 2H), 1.70-1.20 (m, 8H).^{13}C NMR, $CDCl_3$, 178.33, 173.60, 137.68, 60.21, 47.68, 45.00, 42.55, 38.18, 33.23, 27.08, 26.00, 23.77. LRMS: 321.17 ($M+H^+$), 343.24 ($M+Na^+$). HRMS.

Compound **2**: To a solution of compound **1** in DMF (1.5 mL) was added DIPEA (36 µL, 0.21 mmol) followed by HATU (79 mg, 0.21 mmol), this solution was stirred for 1 min then added to a solution of the norbornene amine in DMF (1.0 mL). This was stirred for under a

nitrogen atmosphere overnight. The reaction mixture was concentrated to dryness and the residue triturated with acetonitrile (x3), then ether was added and the mixture concentrated to dryness to give a tan solid. ^{1}H NMR, DMF-d7,10.10 (s, 1H),8.58 (m, 1H), 7.89 (d, 2H), 7.48 (d, 2H), 6.63 (m, 2H), 6.32 (m, 2H), 5.02 (s, 2H), 4.33 (m, 2H), 4.22 (m, 2H), 3.66 (m, 2H), 3.60 (m, 2H), 3.38 (m, 2H), 3.33 (s, 3H), 3.12 (m, 2H), 2.72 (m, 2H), 2.31 (m, 2H), 1.60-1.10 (m, 8H). LRMS: 662.30 ($M+H^+$), 684.27 ($M+Na^+$). HRMS.

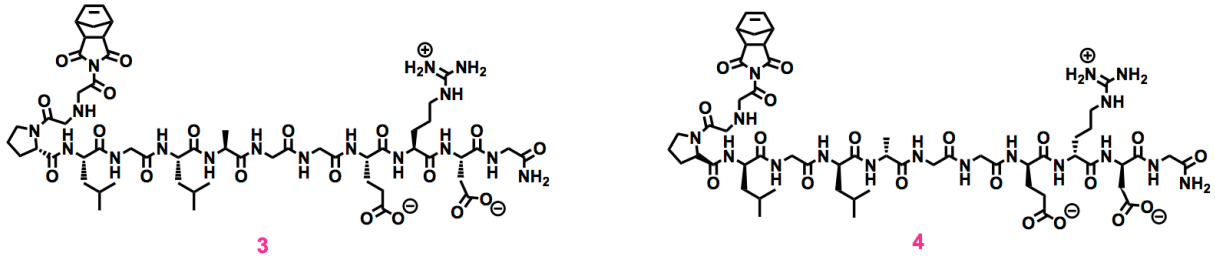

3 4

Figure 3.4.2 Synthesis of peptide monomers used in immuno-EDAPT.

Peptide Synthesis: Peptides were synthesized using an AAPPTEC Focus XC automated synthesizer. Both L- and D-amino acids were purchased from AAPPTEC and NovaBiochem. *N*-(glycine)-*cis*-5-norbornene-*exo*-dicarboximide (NorGly) was prepared as described above. Peptide monomers were synthesized via standard FMOC-based peptide synthesis using Rink Amide MBHA resin (AAPTEC) in a standardized fashion. FMOC was deprotected using a solution of 20% 4-methylpiperidine in DMF. Amino acid couplings were carried out using HBTU and DIPEA (resin/amino acid/HBTU/DIPEA 1:3.5:3.4:4). The final peptide monomers were cleaved from the resin using a mixture of TFA/H_2O/TIPS (95:2.5:2.5) for 90 minutes. The peptides were precipitated and washed with cold ether. For purification and analysis, the peptides were dissolved in a solution of 0.1% TFA in water and analyzed via RP-HPLC and purified via preparative HPLC. Peptide identities and purities were confirmed using ESI-MS and RP-HPLC monitoring at I_{abs} = 214 nm. Peptide monomer sequence: NorGly-

Gly-Pro-Leu-Gly-Leu-Ala-Gly-Gly-Glu-Arg-Asp-Gly. *L*-amino acids were used exclusively for the preparation of **3** (**Figure 3.4.2**), and *D*-amino acids were used exclusively for the preparation of **4**. RP- HPLC retention time was 13 minutes (linear gradient of 0-67% B over 30 minutes). Preparative HPLC retention time was 33 minutes (linear gradient of 20-40% over 60 minutes). ESI-MS(+): 1300.54 $[M+H]^+$.

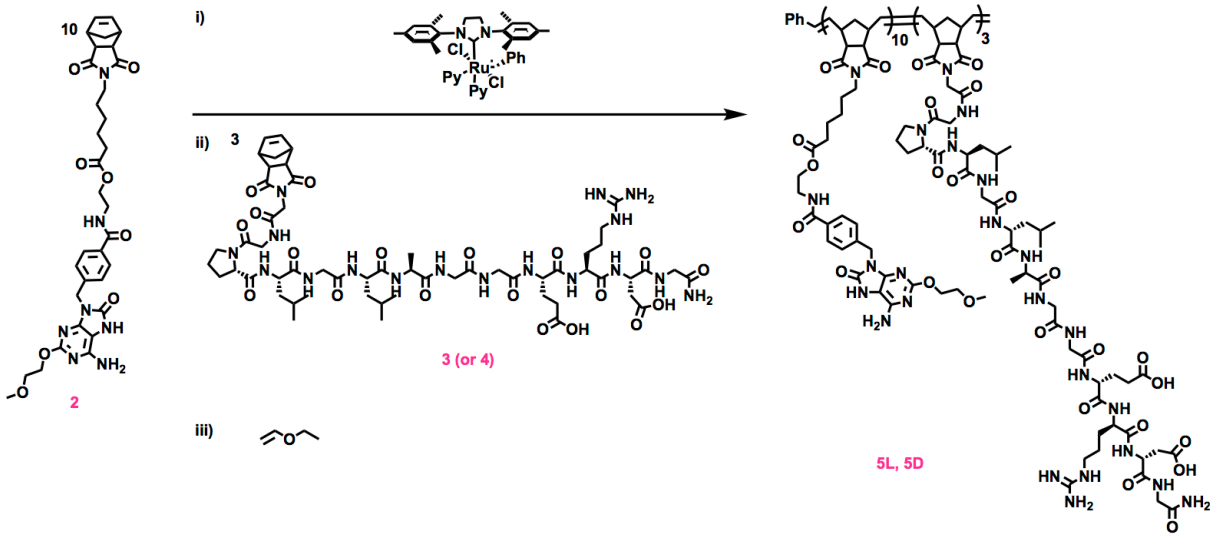

Figure 3.4.3. immuno-EDAPT polymer synthesis.

Polymer Synthesis*:* Compound **2** (19.51 mg, 2.95 x10^{-5} mol, 10 equiv) was dissolved in dry DMF (2800 µL) and stirred under N_2. To this was added a solution of the catalyst ($(IMesH_2)(C_5H_5N_2)(Cl)_2Ru=CHPh$) (2.15 mg, 2.95 x$10^{-6}$ mol, 1.0 equiv) in dry DMF (215 µL). The reaction was stirred under N_2 for 30 minutes, after which an aliquot (10 µL) was removed and quenched with ethyl vinyl ether for SLS analysis. The remaining solution of **1** + catalyst was split into two separate reaction vessels. Compound **3** (11.50 mg, 8.85x10^{-6} mol, 3 equiv) was dissolved in in 200 µL dry DMF and added to one reaction vessel, to afford **5L** after an additional 4 hours of stirring. To the second vessel, a solution of compound **4** (11.50 mg, 8.85x10^{-6} mol, 3 equiv) in 200 µL dry DMF was added, to afford **5D** after an additional 4 hours

of stirring. At the end of the polymerization, a small aliquot was removed from each reaction vessel (20 µL each) and terminated with ethyl vinyl ether for SLS analysis. To each of the remaining solutions, excess ethyl vinyl ether was added and stirred for an additional 20 minutes to ensure complete polymer termination. The fully terminated polymers were precipitated with cold diethyl ether to afford the block copolymers as brown, glassy solids (**5L**, **5D)**.

Homopolymer of **5L** and **5D**: M_n = 8931, PDI = 1.013, hydrophobic block length = 13
Copolymer of **5L**: M_n (whole polymer)= 13,720, PDI = 1.045, hydrophilic block length = 4
Copolymer of **5D**: M_n(whole polymer)= 10,060, PDI = 1.036, hydrophilic block length = 2

Nanoparticle Preparation (**immuno-EDAPT$_L$** and **immuno-EDAPT$_D$**): **4L** or **4D** (5 mg of either polymer) was dissolved in 5 mL of DMF and stirred. To this, an additional 5 mL of 1X DPBS (Dulbecco's Phosphate Buffered Saline, no Mg and no Na) was added over the course of 3 hours. This solution was transferred to a 3500 MWCO snakeskin dialysis tubing and dialyzed against 1L of 1X DPBS (pH 7.4). After 24 hours, the external solution was replaced with fresh DPBS. After an additional 24 hours, the newly formed nanoparticles (**immuno-EDAPT$_L$** and **immuno-EDAPT$_D$**) were removed from the dialysis tubing was analyzed by DLS and TEM.

MMP-9 in vitro Nanoparticle Degradation: Two solutions, one of **immuno-EDAPT$_L$** and one of **immuno-EDAPT$_D$** (both at 500 µM with respect to peptide), were incubated with MMP-9 (100 nU) overnight at 37°C, as per published protocols[26-27]. Enzyme-treated samples were analyzed by HPLC, DLS, and TEM following inactivation of MMP-9 at 65°C for 20 minutes.

In Vitro Cell Assay: TNF-α production in BMDCs by Norbornenyl-1V209: RAW246.7 cells ($1x10^4$ cells/well) were plated and incubated with serially diluted 1V209 or norbornenyl-1V209 for 18 hours. TNF-α released in the culture supernatants was determined through ELISA. Experiments were performed in triplicate with the data shown as mean +/- SEM.

In Vitro Cell Assay: IL-6 production in BMDCs: **immuno-EDAPT$_L$** and **immuno-EDAPT$_D$** were concentrated via spin-centrifugation (MWCO 3500) to final concentrations of 100 μM with respect to 1V209 content. Appropriate volumes of each solution were removed, diluted to 90 μM with 1X DPBS in 1.5 mL Eppendorf tubes, and incubated with MMP-9 (100 nM) at 37°C overnight. To serve as controls, additional aliquots of **immuno-EDAPT$_L$** and **immuno-EDAPT$_D$** were diluted to 90 μM and incubated without MMP-9 overnight, as well as a "blank" solution only containing DPBS and MMP-9. Murine BMDCs (2×10^5 cells/well) were incubated with the above compounds at 90 μM with respect to 1V209 content. Positive control cells were incubated with 1V209 at the same concentration as the test compounds. Negative control cells were treated with 1× DPBS. IL-6 released in the culture supernatants was determined by ELISA. Experiments were performed in triplicate with the data shown as mean +/- SEM. Analysis of variance (ANOVA) was used to test for the variance among data points. One-way ANOVA with Dunnet's post hoc test was utilized. P values lower than 0.05 were considered statistically significant.

In Vivo Studies, General Methods: The studies involving animals use were carried out in strict accordance with the recommendations in the Guide for the Care and Use of Laboratory Animals of the National Institutes of Health. The protocol was approved by the Institutional Animal Care and Use Committee of University of California, San Diego (PHS Animal Welfare Assurance Number: A3033-01; Protocol Numbers: S00028, S05016 and S09331). Mice were

sacrificed by CO_2 inhalation followed by cervical dislocation. All efforts were made to minimize suffering during the procedures in this project.

Preliminary IT Efficacy: Tumors grown from SCC-7 murine squamous cell carcinoma cells were used, as the Carson Lab has known this model to be responsive to treatment with 1V209. Balb/C mice were obtained through Jackson Laboratories (Bar Harbor, MA). Animals (n=24) were inoculated with ~10^6 cells in the flank, and treatments with **immuno-EDAPT$_L$**, 1V209, or saline (8 animals per group) as daily intratumoral (IT) injections began 7 days post-inoculation and continued for 5 days (qdx5). Animals were sacrificed at 21 days post-inoculation. Calipers were used to record tumor volume 3 times per week over the course of the study.

Metastasis Formation Analysis: Tumors grown from 4T1 murine breast carcinoma cells (ATCC) were used for the model system, as this cell line overexpress MMPs. Balb/C mice were obtained through Jackson Laboratories (Bar Harbor, MA). 40 female Balb/C mice were inoculated with ~10^6 4T1 cells in the inguinal mammary fat pads. At 7 days post-inoculation, animals were administered **immuno-EDAPT$_L$**, **immuno-EDAPT$_D$**, 1V209, or saline (10 animals per group) as single intravenous (IV) injections at a dose of 30 µg with respect to 1V209 content. These injections were repeated at 14 days post-inoculation, and animal body mass and tumor volume recorded for the duration of the study. At day 28, animals were sacrificed and lung nodules stained as per published protocol[48]. After staining, the lung nodules were counted and efficacy assessed as a significant reduction in lung nodule formation, relative to untreated controls.

Analysis of Systemic Cytokine Release: In the same experiment above, blood was collected from each animal's retro orbital sinus 2 hours post-injection, and spun at 7,000 RCF for 7 minutes to separate the plasma. Plasma samples were then analyzed for cytokine production by Luminex® assay as per the protocol provided by EMD Millipore (cat # MCYTOMAG-70K).

Statistical analysis: Biologic data were plotted on graphs using Prism software (version 5.0, GraphPad Software, Inc., San Diego, CA). Each dot represents data from an individual mouse and the columns and error bars indicate the mean ± SEM. Analysis of variance (ANOVA) was used to test for the variance among data points. One-way ANOVA with Dunnet's post hoc test was utilized. P values lower than 0.05 were considered statistically significant.

3.5 Perspectives and Future Directions

Overall, Chapter 3 is a useful preliminary investigation into the utility of the EDAPT platform for the delivery of immunotherapeutics. The reduction in lung metastases in animals administered **immuno-EDAPT$_L$** is statistically significant, relative to both positive and negative controls. However, the model employed requires animal sacrifice at a predetermined endpoint based on previous experience working with the model and physical counting of lung nodules. As is, there is no way to determine the lung metastasis production without sacrificing the animal, and, indeed, preliminary investigations failed because the saline-treated animals at the the time of sacrifice had few lung nodules to begin with (*vide infra*). Further, nodule counting requires staining of the lung and physical counting with the naked eye – a process that is prone to error, regardless of skill level and expertise. An alternative tumor model that our lab is currently investigating with the **immuno-EDAPT** system are 4T1 cells that are luminescent. Using live-animal imaging (similar to the methods described in Chapter 2), we are able to track the production of lung metastases following treatment in real-time by monitoring the increase in luminescence in the lungs. In this way, we can evaluate both primary tumor growth (via caliper measurement) and lung metastasis production (via luminescence) without sacrificing the animal to do so.

One key missing piece from the work described in Chapter 3.2 is an additional control for the aggregated material post-enzyme exposure. Although the results of the *in vivo* study, as well as **Figure 3.2.5** demonstrate that enzyme-induced morphology change is necessary for **immuno-EDAPT** to function as a therapeutic, there is no control that demonstrates that the aggregated scaffold itself is having no effect on the immune response. Although we have seen no evidence of immune response when similar EDAPT systems have been employed[32], we feel it is valuable to establish, in this particular model, that the scaffold itself is inert. Thus, we

have synthesized an additional control nanoparticle system using an inert phenyl moiety as the hydrophobic block (**Figure 3.5.1, purple shading**) together with the enzyme responsive peptide as the hydrophilic block (**Figure 3.5.1, blue shading**) and are using this system as an additional control in our ongoing investigations of **immuno-EDAPT** in the luminescent 4T1 model.

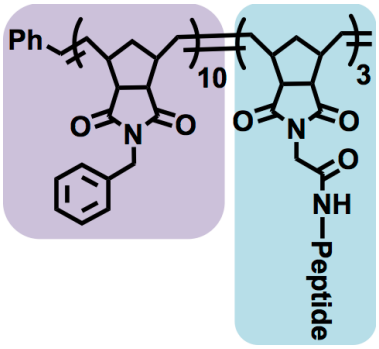

Figure 3.5.1. Polymer structure of additional EDAPT control. To further demonstrate that the immunotherapeutic capabilities of **immuno-EDAPT$_L$** are due to the immunotherapeutic being released from the aggregate post accumulation, and not due to the aggregated material itself elicting an immune response, polymers and nanoparticles that are enzyme responsive, but also contain an inert core, have been synthesized and are being evaluated *in vivo*.

Chapter 3.3 discussed the potential of using this platform to co-deliver chemotherapeutics alongside immunostimulatory molecules, and indeed the preliminary investigations into using EDAPT as a delivery platform for immunotherapeutics included this co-delivery strategy as a research aim. In these studies, we explored combination treatment with **immuno-EDAPT** alongside **PTX-EDAPT** (see Chapter 2) in animals bearing two 4T1 tumors each (**Figure 3.5.2**). Balb/c mice were orthotopically implanted with 4T1 cells as described in Chapter 3.4, and treatment was initiated when tumors reached 3-5 mm in diameter. Animals were administered **PTX-EDAPT$_L$** (IV) with or without **immuno-EDAPT$_L$** (IV) at a PTX dose of 15 mg/kg and at immunotherapeutic doses of 10, 30, or 60 μg per animal, per injection, once weekly for a total of two injections (q7dx2, 4 total cohorts). In addition, sets of animals were administered either 10, 30, or 60 μg of 1V209 (q7dx2, 3 total cohorts). Upon

the first IV administration of 1V209, 4 out of 7 animals given the 60 µg dose died, as well as 2 out of 7 given the 30 µg dose. Conversely, none of the animals administered immuno-EDAPT experienced evident drug toxicity (**Figure 3.5.2a**). Animals were sacrificed at 30 days post-tumor implantation and assessed for lung metastases, revealing an extremely promising reduction (**Figure 3.5.2b**) in the number of lung nodules across all groups that were co-administered **immuno-EDAPT** with **PTX-EDAPT**.

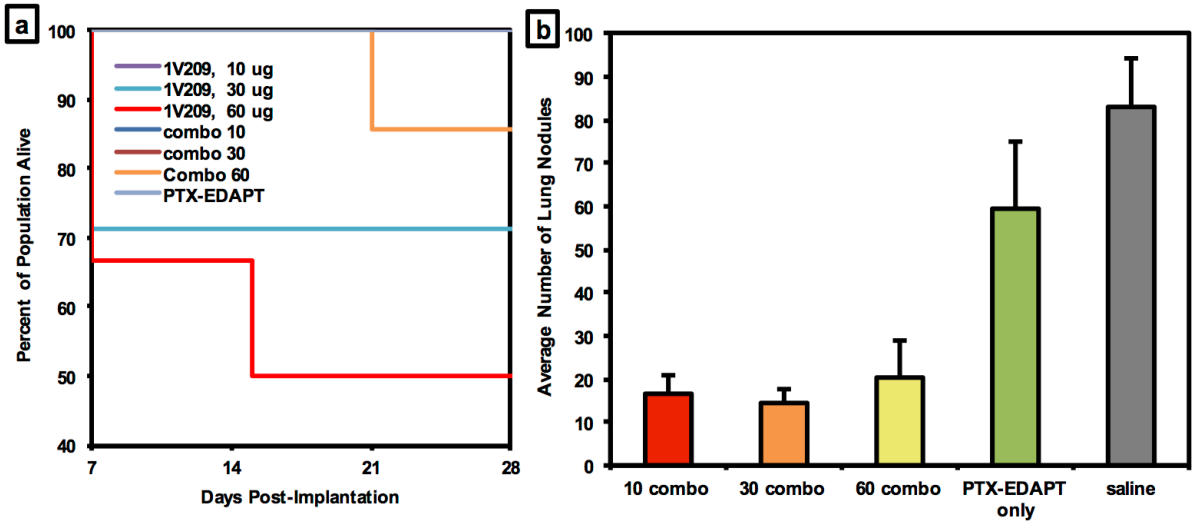

Figure 3.5.3. Combination therapy of immuno-EDAPT with PTX-EDAPT. a) Survival curve of animals (n=7) IV administered either 1V209 at 10, 30, or 60 µg per animal, **PTX-EDAPT** at 15 mg/kg, or a combination of **PTX-EDAPT** at 15 mg/kg with **immuno-EDAPT$_L$** at 10, 30, or 60 60 µg per animal. Acute lethality is observed only in animals administered 1V209 at elevated doses. b) Metastases count in lungs of 4T1 animals (n=6) administered **immuno-EDAPT$_L$** at 10, 30, and 60 µg immunotherapeutic doses in combination with **PTX-EDAPT** sacrificed at 30 days, with saline treatment data as a reference.

This was our first exploration of combination chemo- and immunotherapy, and although there was definite evidence that the combination enhanced the efficacy of treatment over monotherapy with **PTX-EDAPT**, there was no significant difference observed between any of the three treatment groups receiving combination therapy. However, this may be because the dose of both the immunotherapeutic and the chemotherapeutic need to be optimized simultaneously, yet independently [54]. For these studies, we used a set dose of 15 mg/kg (with respect to PTX content) of **PTX-EDAPT**, because we observed efficacy at that dose in other

animal tumor models (see Chapter 2), and varied the dose of **immuno-EDAPT** from 10-60 μg per animal. Superior efficacy may be observed when the **PTX-EDAPT** dose is increased; however, the highest dose achievable may not be the best for combination therapy [55], as immunogenic cell death initiated by PTX-based treatment may increase overall toxicity of the immunotherapeutic. Further, the dosing schedule of the chemotherapeutic may be important, as the immunological impacts of chemotherapeutics depends on not only the dose given, but also when they are administered in relation to the immunotherapeutic[55]. This study co-administered **PTX-EDAPT** at the same time as **immuno-EDAPT**, but superior effects may be observed if the animals are first primed with **immuno-EDAPT**, and then administered **PTX-EDAPT** a few days later, or vice versa. Dose and treatment schedule aside, there may be a distinct advantage to packaging both immunotherapeutics and chemotherapeutics in identical carriers, such as they are in both the **PTX-EDAPT** and **immuno-EDAPT** systems. In this way, the pharmacokinetics and biodistribution of both therapeutics should be matched to that of the carrier, rather than the drugs themselves. In theory, this should translate to delivery of both the chemotherapeutic and immunotherapeutic to the same tissues, and should impart similar circulation half-lives to both molecules.

Beyond combination therapy, we are actively investigating where and how the **immuno-EDAPT** system is having its therapeutic effect *in vivo.* The key outcome of the studies described in Chapter 3.2 is a significant reduction in the number of lung nodules in animals administered **immuno-EDAPT$_L$**, relative to the parent immunotherapeutic (positive control), **immuno-EDAPT$_D$**, and saline (negative controls). The model is set up such that a primary tumor is implanted in the mammary fat pad and animals are administered the compounds before the production of lung metastases begins. Thus, we hypothesize that the material is likely accumulating at the primary tumor and exerting a local effect, which has downstream consequences and reprograms the immune system to act against the cancerous cells before

they can establish as colonies in the lung. However, as the current **immuno-EDAPT** system is not visualizable in the tumor tissue (unlike its **PTX-EDAPT** and **Pt-EDAPT** counterparts in Chapter 2), we cannot say with certainty that this process is occurring locally. As such, we have begun the synthesis of an NIR-labelled immuno-EDAPT system (**Figure 5.3.4**) to enable tracking of the material *in vivo* and *ex vivo* for localization throughout the duration of the study. This, coupled with a dynamic analysis of lung metastasis production (by using luminescent 4T1 cells), will provide a powerful insight on the mechanism by which **immuno-EDAPT** is having its therapeutic effect.

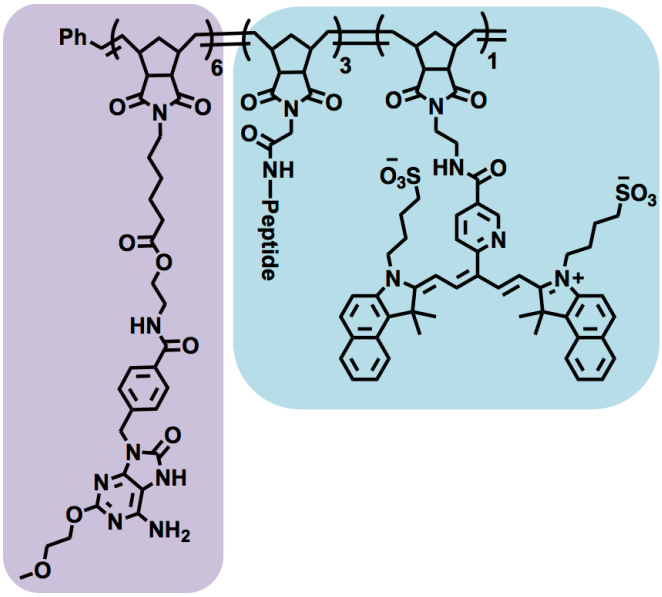

Figure 3.5.4. Polymer structure of NIR-labelled immuno-EDAPT. To further elucidate where **immuno-EDAPT** is localizing to have its therapeutic effect, NIR-labelled polymers and nanoparticles are being synthesized and will be evaluated in luminescent 4T1 tumor models *in vivo*.

3.6 Acknowledgements

Chapter 3 is adapted, in part, from material currently being prepared as a revised manuscript for resubmission for publication. Callmann, Cassandra; Thompson, Matthew; Yao, Shiyin; Hayashi, Tomoko; Carson, Dennis; and Nathan Gianneschi. The dissertation author is the primary author of this pending manuscript.

3.7 References

1. Pardoll, D. M., The blockade of immune checkpoints in cancer immunotherapy. *Nat Rev Cancer* **2012,** *12* (4), 252-264.

2. Vanneman, M.; Dranoff, G., Combining immunotherapy and targeted therapies in cancer treatment. *Nat Rev Cancer* **2012,** *12* (4), 237-251.

3. Burstein, H. J.; Krilov, L.; Aragon-Ching, J. B.; Baxter, N. N.; Chiorean, E. G.; Chow, W. A.; De Groot, J. F.; Devine, S. M.; DuBois, S. G.; El-Deiry, W. S.; Epstein, A. S.; Heymach, J.; Jones, J. A.; Mayer, D. K.; Miksad, R. A.; Pennell, N. A.; Sabel, M. S.; Schilsky, R. L.; Schuchter, L. M.; Tung, N.; Winkfield, K. M.; Wirth, L. J.; Dizon, D. S., Clinical Cancer Advances 2017: Annual Report on Progress Against Cancer From the American Society of Clinical Oncology. *Journal of Clinical Oncology* **2017,** *35* (12), 1341-1367.

4. Dizon, D. S.; Krilov, L.; Cohen, E.; Gangadhar, T.; Ganz, P. A.; Hensing, T. A.; Hunger, S.; Krishnamurthi, S. S.; Lassman, A. B.; Markham, M. J.; Mayer, E.; Neuss, M.; Pal, S. K.; Richardson, L. C.; Schilsky, R.; Schwartz, G. K.; Spriggs, D. R.; Villalona-Calero, M. A.; Villani, G.; Masters, G., Clinical Cancer Advances 2016: Annual Report on Progress Against Cancer From the American Society of Clinical Oncology. *Journal of Clinical Oncology* **2016,** *34* (9), 987-1011.

5. Wu, C. C. N.; Hayashi, T.; Takabayashi, K.; Sabet, M.; Smee, D. F.; Guiney, D. D.; Cottam, H. B.; Carson, D. A., Immunotherapeutic activity of a conjugate of a Toll-like receptor 7 ligand. *Proceedings of the National Academy of Sciences* **2007,** *104* (10), 3990-3995.

6. Shinchi, H.; Crain, B.; Yao, S.; Chan, M.; Zhang, S. S.; Ahmadiiveli, A.; Suda, Y.; Hayashi, T.; Cottam, H. B.; Carson, D. A., Enhancement of the Immunostimulatory Activity of a TLR7 Ligand by Conjugation to Polysaccharides. *Bioconjugate Chemistry* **2015,** *26* (8), 1713-1723.

7. Chan, M.; Hayashi, T.; Kuy, C. S.; Gray, C. S.; Wu, C. C. N.; Corr, M.; Wrasidlo, W.; Cottam, H. B.; Carson, D. A., Synthesis and Immunological Characterization of Toll-Like Receptor 7 Agonistic Conjugates. *Bioconjugate Chemistry* **2009,** *20* (6), 1194-1200.

8. Chan, M.; Hayashi, T.; Mathewson, R. D.; Yao, S.; Gray, C.; Tawatao, R. I.; Kalenian, K.; Zhang, Y.; Hayashi, Y.; Lao, F. S.; Cottam, H. B.; Carson, D. A., Synthesis and Characterization of PEGylated Toll Like Receptor 7 Ligands. *Bioconjugate Chemistry* **2011,** *22* (3), 445-454.

9. Lee, D. W.; Gardner, R.; Porter, D. L.; Louis, C. U.; Ahmed, N.; Jensen, M.; Grupp, S. A.; Mackall, C. L., Current concepts in the diagnosis and management of cytokine release syndrome. *Blood* **2014,** *124* (2), 188-195.

10. Tisoncik, J. R.; Korth, M. J.; Simmons, C. P.; Farrar, J.; Martin, T. R.; Katze, M. G., Into the Eye of the Cytokine Storm. *Microbiology and Molecular Biology Reviews* **2012,** *76* (1), 16-32.

11. Seton-Rogers, S., Immunotherapy: A lethal storm. *Nat Rev Cancer* **2014,** *14* (12), 766-766.

12. Suntharalingam , G.; Perry , M. R.; Ward , S.; Brett , S. J.; Castello-Cortes , A.; Brunner , M. D.; Panoskaltsis , N., Cytokine Storm in a Phase 1 Trial of the Anti-CD28 Monoclonal Antibody TGN1412. *New England Journal of Medicine* **2006,** *355* (10), 1018-1028.

13. Attarwala, H., TGN1412: From Discovery to Disaster. *Journal of Young Pharmacists : JYP* **2010,** *2* (3), 332-336.

14. Barrett, D. M.; Teachey, D. T.; Grupp, S. A., Toxicity management for patients receiving novel T-cell engaging therapies. *Current opinion in pediatrics* **2014,** *26* (1), 43-49.

15. Teachey, D. T.; Rheingold, S. R.; Maude, S. L.; Zugmaier, G.; Barrett, D. M.; Seif, A. E.; Nichols, K. E.; Suppa, E. K.; Kalos, M.; Berg, R. A.; Fitzgerald, J. C.; Aplenc, R.; Gore, L.; Grupp, S. A., Cytokine release syndrome after blinatumomab treatment related to abnormal macrophage activation and ameliorated with cytokine-directed therapy. *Blood* **2013,** *121* (26), 5154-5157.

16. Klinger, M.; Brandl, C.; Zugmaier, G.; Hijazi, Y.; Bargou, R. C.; Topp, M. S.; Gökbuget, N.; Neumann, S.; Goebeler, M.; Viardot, A.; Stelljes, M.; Brüggemann, M.; Hoelzer, D.; Degenhard, E.; Nagorsen, D.; Baeuerle, P. A.; Wolf, A.; Kufer, P., Immunopharmacologic response of patients with B-lineage acute lymphoblastic leukemia to continuous infusion of T cell–engaging CD19/CD3-bispecific BiTE antibody blinatumomab. *Blood* **2012,** *119* (26), 6226-6233.

17. Michot, J. M.; Bigenwald, C.; Champiat, S.; Collins, M.; Carbonnel, F.; Postel-Vinay, S.; Berdelou, A.; Varga, A.; Bahleda, R.; Hollebecque, A.; Massard, C.; Fuerea, A.; Ribrag, V.; Gazzah, A.; Armand, J. P.; Amellal, N.; Angevin, E.; Noel, N.; Boutros, C.; Mateus, C.; Robert, C.; Soria, J. C.; Marabelle, A.; Lambotte, O., Immune-related adverse events with immune checkpoint blockade: a comprehensive review. *European Journal of Cancer* **2016,** *54*, 139-148.

18. Shao, K.; Singha, S.; Clemente-Casares, X.; Tsai, S.; Yang, Y.; Santamaria, P., Nanoparticle-Based Immunotherapy for Cancer. *ACS Nano* **2015,** *9* (1), 16-30.

19. He, C.; Duan, X.; Guo, N.; Chan, C.; Poon, C.; Weichselbaum, R. R.; Lin, W., Core-shell nanoscale coordination polymers combine chemotherapy and photodynamic therapy to potentiate checkpoint blockade cancer immunotherapy. *Nature Communications* **2016,** *7*, 12499.

20. Luo, M.; Wang, H.; Wang, Z.; Cai, H.; Lu, Z.; Li, Y.; Du, M.; Huang, G.; Wang, C.; Chen, X.; Porembka, M. R.; Lea, J.; Frankel, A. E.; Fu, Y.-X.; Chen, Z. J.; Gao, J., A STING-activating nanovaccine for cancer immunotherapy. *Nat Nano* **2017,** *advance online publication*.

21. Cho, N.-H.; Cheong, T.-C.; Min, J. H.; Wu, J. H.; Lee, S. J.; Kim, D.; Yang, J.-S.; Kim, S.; Kim, Y. K.; Seong, S.-Y., A multifunctional core-shell nanoparticle for dendritic cell-based cancer immunotherapy. *Nat Nano* **2011,** *6* (10), 675-682.

22. Fontana, F.; Liu, D.; Hirvonen, J.; Santos, H. A., Delivery of therapeutics with nanoparticles: what's new in cancer immunotherapy? *Wiley Interdisciplinary Reviews: Nanomedicine and Nanobiotechnology* **2017,** *9* (1), e1421-n/a.

23. Kessenbrock, K.; Plaks, V.; Werb, Z., Matrix Metalloproteinases: Regulators of the Tumor Microenvironment. *Cell* **2010,** *141* (1), 52-67.

24. Olson, E. S.; Jiang, T.; Aguilera, T. A.; Nguyen, Q. T.; Ellies, L. G.; Scadeng, M.; Tsien, R. Y., Activatable cell penetrating peptides linked to nanoparticles as dual probes for in vivo fluorescence and MR imaging of proteases. *Proceedings of the National Academy of Sciences* **2010,** *107* (9), 4311-4316.

25. Jiang, T.; Olson, E. S.; Nguyen, Q. T.; Roy, M.; Jennings, P. A.; Tsien, R. Y., Tumor imaging by means of proteolytic activation of cell-penetrating peptides. *Proceedings of the National Academy of Sciences of the United States of America* **2004,** *101* (51), 17867-17872.

26. Callmann, C. E.; Barback, C. V.; Thompson, M. P.; Hall, D. J.; Mattrey, R. F.; Gianneschi, N. C., Therapeutic Enzyme-Responsive Nanoparticles for Targeted Delivery and Accumulation in Tumors. *Advanced Materials* **2015,** *27* (31), 4611-4615.

27. Callmann, C. E.; Gianneschi, N. C., Enzyme-Responsive Nanoparticles for the Treatment of Disease. In *Biomedical Nanotechnology: Methods and Protocols*, Petrosko, S. H.; Day, E. S., Eds. Springer New York: New York, NY, 2017; pp 223-238.

28. Chien, M.-P.; Carlini, A. S.; Hu, D.; Barback, C. V.; Rush, A. M.; Hall, D. J.; Orr, G.; Gianneschi, N. C., Enzyme-Directed Assembly of Nanoparticles in Tumors Monitored by in Vivo Whole Animal Imaging and ex Vivo Super-Resolution Fluorescence Imaging. *Journal of the American Chemical Society* **2013,** *135* (50), 18710-18713.

29. Chien, M.-P.; Thompson, M. P.; Barback, C. V.; Ku, T.-H.; Hall, D. J.; Gianneschi, N. C., Enzyme-Directed Assembly of a Nanoparticle Probe in Tumor Tissue. *Advanced Materials* **2013,** *25* (26), 3599-3604.

30. Chien, M.-P.; Thompson, M. P.; Lin, E. C.; Gianneschi, N. C., Fluorogenic enzyme-responsive micellar nanoparticles. *Chemical Science* **2012,** *3* (9), 2690-2694.

31. Daniel, K. B.; Callmann, C. E.; Gianneschi, N. C.; Cohen, S. M., Dual-responsive nanoparticles release cargo upon exposure to matrix metalloproteinase and reactive oxygen species. *Chemical Communications* **2016,** *52* (10), 2126-2128.

32. Nguyen, M. M.; Carlini, A. S.; Chien, M.-P.; Sonnenberg, S.; Luo, C.; Braden, R. L.; Osborn, K. G.; Li, Y.; Gianneschi, N. C.; Christman, K. L., Enzyme-Responsive Nanoparticles for Targeted Accumulation and Prolonged Retention in Heart Tissue after Myocardial Infarction. *Advanced Materials* **2015,** *27* (37), 5547-5552.

33. Nagel, H.; Laskawi, R.; Wahlers, A.; Hemmerlein, B., Expression of matrix metalloproteinases MMP-2, MMP-9 and their tissue inhibitors TIMP-1, -2, and -3 in benign and malignant tumours of the salivary gland. *Histopathology* **2004,** *44* (3), 222-231.

34. Schmalfeldt, B.; Prechtel, D.; Härting, K.; Späthe, K.; Rutke, S.; Konik, E.; Fridman, R.; Berger, U.; Schmitt, M.; Kuhn, W.; Lengyel, E., Increased Expression of Matrix Metalloproteinases (MMP)-2, MMP-9, and the Urokinase-Type Plasminogen Activator Is Associated with Progression from Benign to Advanced Ovarian Cancer. *Clinical Cancer Research* **2001,** *7* (8), 2396-2404.

35. Sier, C. F.; Kubben, F. J.; Ganesh, S.; Heerding, M. M.; Griffioen, G.; Hanemaaijer, R.; van Krieken, J. H.; Lamers, C. B.; Verspaget, H. W., Tissue levels of matrix metalloproteinases MMP-2 and MMP-9 are related to the overall survival of patients with gastric carcinoma. *British Journal of Cancer* **1996,** *74* (3), 413-417.

36. Kaczanowska, S.; Joseph, A. M.; Davila, E., TLR agonists: our best frenemy in cancer immunotherapy. *Journal of Leukocyte Biology* **2013,** *93* (6), 847-863.

37. Hayashi, T.; Chan, M.; Norton, J. T.; Wu, C. C. N.; Yao, S.; Cottam, H. B.; Tawatao, R. I.; Corr, M.; Carson, D. A.; Daniels, G. A., Additive melanoma suppression with intralesional

phospholipid conjugated TLR7 agonists and systemic IL-2. *Melanoma research* **2011,** *21* (1), 66-75.

38. Schön, M. P.; Schön, M., Imiquimod: mode of action. *British Journal of Dermatology* **2007,** *157*, 8-13.

39. Steinhagen, F.; Kinjo, T.; Bode, C.; Klinman, D. M., TLR-Based Immune Adjuvants. *Vaccine* **2011,** *29* (17), 3341-3355.

40. Tse, K.; Horner, A. A., Update on toll-like receptor-directed therapies for human disease. *Ann Rheum Dis* **2007,** *66 Suppl 3*, iii77-80.

41. Scholl, M.; Ding, S.; Lee, C. W.; Grubbs, R. H., Synthesis and Activity of a New Generation of Ruthenium-Based Olefin Metathesis Catalysts Coordinated with 1,3-Dimesityl-4,5-dihydroimidazol-2-ylidene Ligands. *Organic Letters* **1999,** *1* (6), 953-956.

42. Maynard, H. D.; Okada, S. Y.; Grubbs, R. H., Synthesis of Norbornenyl Polymers with Bioactive Oligopeptides by Ring-Opening Metathesis Polymerization. *Macromolecules* **2000,** *33* (17), 6239-6248.

43. Leitgeb, A.; Wappel, J.; Slugovc, C., The ROMP toolbox upgraded. *Polymer* **2010,** *51* (14), 2927-2946.

44. Sutthasupa, S.; Shiotsuki, M.; Sanda, F., Recent advances in ring-opening metathesis polymerization, and application to synthesis of functional materials. *Polym J* **2010,** *42* (12), 905-915.

45. Zhou, R.; Xu, L.; Ye, M.; Liao, M.; Du, H.; Chen, H., Formononetin Inhibits Migration and Invasion of MDA-MB-231 and 4T1 Breast Cancer Cells by Suppressing MMP-2 and MMP-9 Through PI3K/AKT Signaling Pathways. *Horm Metab Res* **2014,** *46* (11), 753-760.

46. Lee, H. S.; Ha, A. W.; Kim, W. K., Effect of resveratrol on the metastasis of 4T1 mouse breast cancer cells in vitro and in vivo. *Nutrition Research and Practice* **2012,** *6* (4), 294-300.

47. Kim, K.; Skora, A. D.; Li, Z.; Liu, Q.; Tam, A. J.; Blosser, R. L.; Diaz, L. A.; Papadopoulos, N.; Kinzler, K. W.; Vogelstein, B.; Zhou, S., Eradication of metastatic mouse cancers resistant to immune checkpoint blockade by suppression of myeloid-derived cells. *Proceedings of the National Academy of Sciences of the United States of America* **2014,** *111* (32), 11774-11779.

48. Wexler, H., Accurate Identification of Experimental Pulmonary Metastases2. *JNCI: Journal of the National Cancer Institute* **1966,** *36* (4), 641-645.

49. Drake, C. G., Combination immunotherapy approaches. *Annals of Oncology* **2012,** *23* (suppl_8), viii41-viii46.

50. Adams, S., Dramatic response of metaplastic breast cancer to chemo-immunotherapy. *npj Breast Cancer* **2017,** *3* (1), 8.

51. Apetoh, L.; Ghiringhelli, F.; Tesniere, A.; Obeid, M.; Ortiz, C.; Criollo, A.; Mignot, G.; Maiuri, M. C.; Ullrich, E.; Saulnier, P.; Yang, H.; Amigorena, S.; Ryffel, B.; Barrat, F. J.; Saftig, P.; Levi, F.; Lidereau, R.; Nogues, C.; Mira, J.-P.; Chompret, A.; Joulin, V.; Clavel-Chapelon, F.; Bourhis, J.; Andre, F.; Delaloge, S.; Tursz, T.; Kroemer, G.; Zitvogel, L., Toll-like receptor 4-dependent contribution of the immune system to anticancer chemotherapy and radiotherapy. *Nat Med* **2007,** *13* (9), 1050-1059.

52. Kono, K.; Mimura, K.; Kiessling, R., Immunogenic tumor cell death induced by chemoradiotherapy: molecular mechanisms and a clinical translation. *Cell Death & Disease* **2013,** *4* (6), e688.

53. Zitvogel, L.; Apetoh, L.; Ghiringhelli, F.; Kroemer, G., Immunological aspects of cancer chemotherapy. *Nat Rev Immunol* **2008,** *8* (1), 59-73.

54. Emens, L. A.; Middleton, G., The Interplay of Immunotherapy and Chemotherapy: Harnessing Potential Synergies. *Cancer immunology research* **2015,** *3* (5), 436-443.

55. Emens, L. A., Chemoimmunotherapy. *Cancer journal (Sudbury, Mass.)* **2010,** *16* (4), 295-303.

Chapter 4

Dually-Responsive Nanomaterials

4.1 Introduction

Chapters 2 and 3 assess the potential of EDAPT to deliver therapeutic payloads to tumor tissue and provide evidence to suggest that this platform is useful *in vivo*; however, the focus of these studies was the effect of EDAPT systems on tumor growth inhibition in animals without comorbidity. In an animal model designed specifically to look at tumor growth, there is little worry about upregulation of MMPs in other areas of the body. However, MMP upregulation is observed not only in cancer progression, but also in several other common diseases, including rheumatoid arthritis[1-3], ulcerative colitis and Crohn's disease[4-5], lung diseases[6] such as chronic obstructive pulmonary disease (COPD)[7] and asthma[8], and locally inflamed tissues as part of the wound healing response[9-10]. Thus, although the on-target accumulation of EDAPT materials discussed in Chapters 2 and 3 was sufficient for therapy and minimal accumulation observed in satellite organs, there remains the distinct possibility that EDAPT-based materials could also accumulate in other areas of the body where MMPs are locally upregulated, resulting in unintended toxicity.

One way to mitigate potential off-target effects in other MMP-rich regions of the body is to develop a dually-responsive system, wherein two stimuli are needed to 1) accumulate the

material and then 2) release the payload, thereby providing a sort of *in vivo* "and" logic gate (**Figure 4.1.1**). As a proof-of-concept for this approach, Chapter 4 describes the design of an enzyme-responsive nanoparticle that carries a latent hydrophobic protease inhibitor, whose release, and thus activation, from the hydrophobic core of the micelle copolymer is triggered by reactive oxygen species (ROS)[11]. Dual-responsive systems and enzyme-responsive cargo release systems have been of increasing interest and have well-documented in the field[12-18]. This work is motivated by observations of coincident upregulation of both ROS, namely H_2O_2, and matrix metalloproteinases (MMPs) in the pathology of many inflammatory diseases, including myocardial infarction[19], arthritis[20-21], ischemia[22-24], and atherosclerosis[25], as well as during tumor cell invasion in certain cancers, including colon cancer[26] and melanoma[27]. MMPs are expressed and excreted initially as zymogens and their activity is tightly regulated in normal physiology[28]. MMPs become activated in the presence of proteases, other MMPs, or by ROS[29]. Hence, the interplay between ROS and MMPs is linked to disease progression[23, 29].

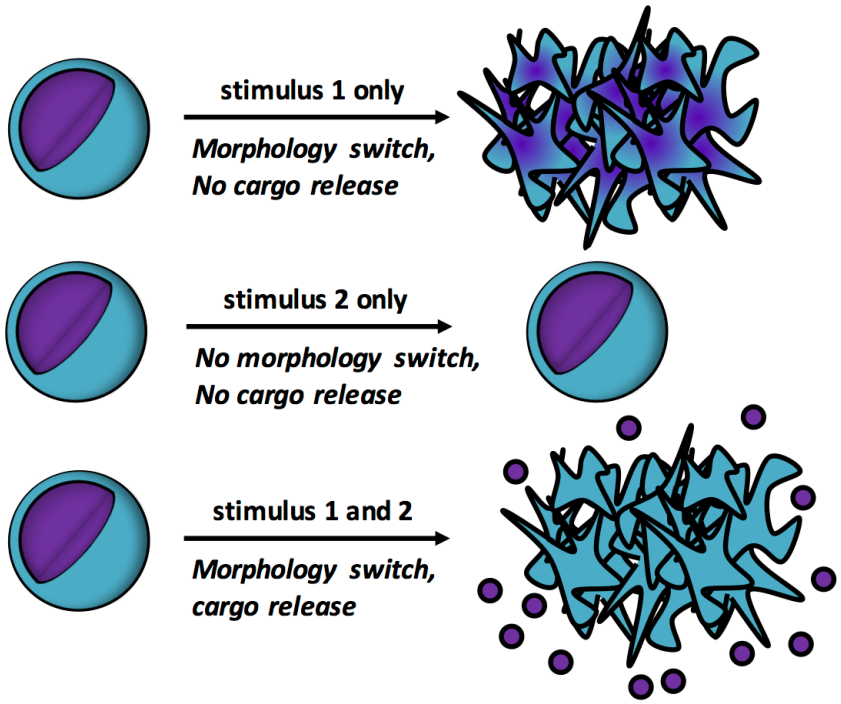

Figure 4.1.1. Schematic representation of dual-responsive nanoparticles. If only the first stimulus is present (in this case, MMPs), morphology switch is observable, but no cargo release occurs. If only the second stimulus is present (in this case, ROS), no morphology switch nor cargo release is observed. ONLY when both stimuli are present (MMPs and ROS), rapid morphology change and cargo release is observed.

4.2 Results and Discussion

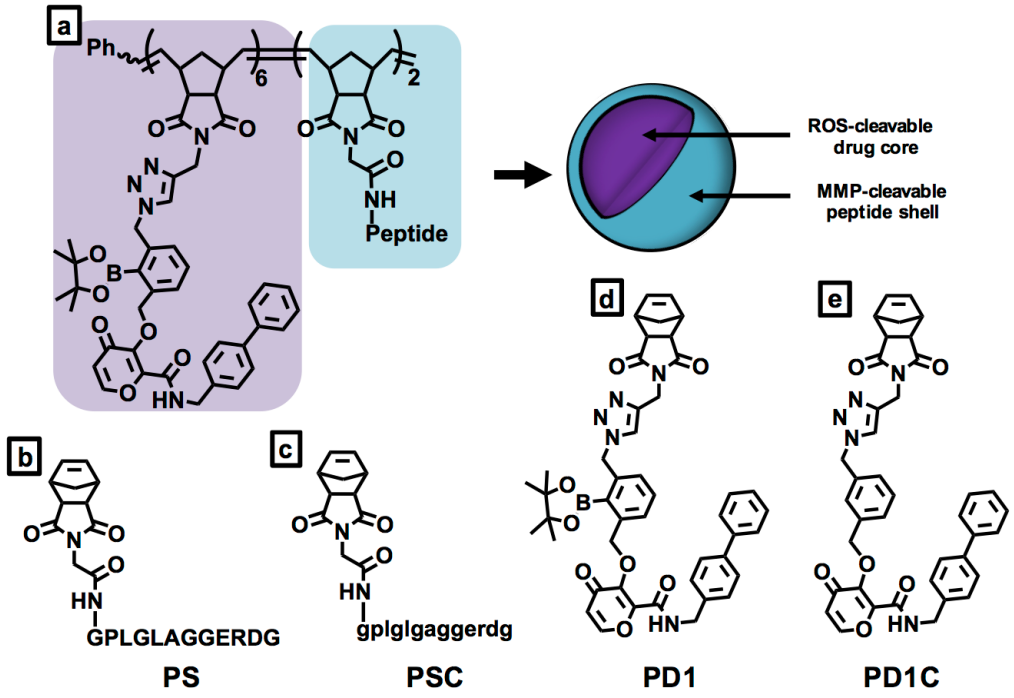

Figure 4.2.1. Structure of dual-responsive nanoparticles. a) Polymer structure and cartoon representation of resulting nanoparticles. The hydrophobic block (purple shading) contains a ROS-reactive aryl boronic ester and forms the core of the nanoparticle. The hydrophilic block (blue shading) contains an MMP-responsive peptide and forms the shell of the nanoparticle. b) Peptide substrate **PS** containing a recognition sequence for MMP. c) Peptide substrate control **PSC**, synthesized from *D*-amino acids. d) Prodrug **PD1** monomer containing the ROS-responsive aryl boronic ester and MMP inhibitor PY-2. c) Prodrug control **PD1C** monomer, which contains a non-cleavable MMP inhibitor.

Amphiphilic block copolymers were designed and synthesized using ring opening metathesis polymerization (ROMP), a robust polymerization technique[30] that uses a highly functional group tolerant Ru-based initiator[31-34] to generate well-defined, low dispersity polymer systems. These copolymers consist of an inactive MMP inhibitor as the hydrophobic block, coupled with a hydrophilic block consisting of a peptide MMP substrate. Hence, the latent MMP inhibitor is sequestered in the hydrophobic core, while the hydrophilic MMP substrate forms the shell of the resulting micellar nanoparticles (**Figure 4.2.1a**). Upon exposure to the enzyme, the peptide (**PS, Figure 4.2.1b**) is cleaved inducing aggregation.[35-40] As a control, a *d*-amino acid version of the peptide substrate (**PSC**, **Figure 4.2.1c**) was synthesized, as a sequence

insusceptible to enzymatic degradation. The hydrophobic block of the polymer, which forms the micellar nanoparticle core, contains a H_2O_2-sensitive prodrug (**PD1**, **Figure 4.2.1d**) or a non-cleavable prodrug control (**PD1C**, **Figure 4.2.1e**). Specifically, an aryl boronic ester is covalently appended to an MMP inhibitor rendering the inhibitor inactive. This moiety, containing a self-immolative linker, is optimized to be hydrolytically stable under normal physiological conditions.[41] Nucleophilic attack on **PD1** by H_2O_2 results in the expulsion of a phenolate intermediate, which spontaneously releases the MMP inhibitor (previously designated as PY-2)[42] via an intramolecular cascade (**Figure 4.2.2**). PY-2 was utilized in these studies, as it exhibits excellent potency against a variety of MMPs.[42]

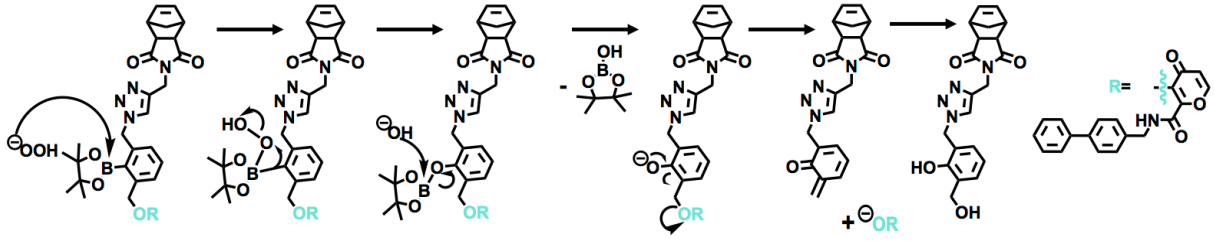

Figure 4.2.2. Intramolecular cascade following exposure of PD1 to H_2O_2. Nucleophilic attack by peroxide leads to liberation of a phenolate intermediate, norbornenyl product and free PY-2 in solution.

Analytical HPLC was used to evaluate the sensitivity of **PD1** to H_2O_2 under physiological conditions (50 mM HEPES, pH 7.4). HPLC confirmed quantitative conversion of **PD1** to PY-2 after H_2O_2 treatment, which contained a single peak at the same retention time of an authentic sample of PY-2 (**Figure 4.2.3**). The control compound, **PD1C**, a direct analog of **PD1** lacking the boronic ester motif, is completely unreactive toward H_2O_2, as evidenced by analytical HPLC.

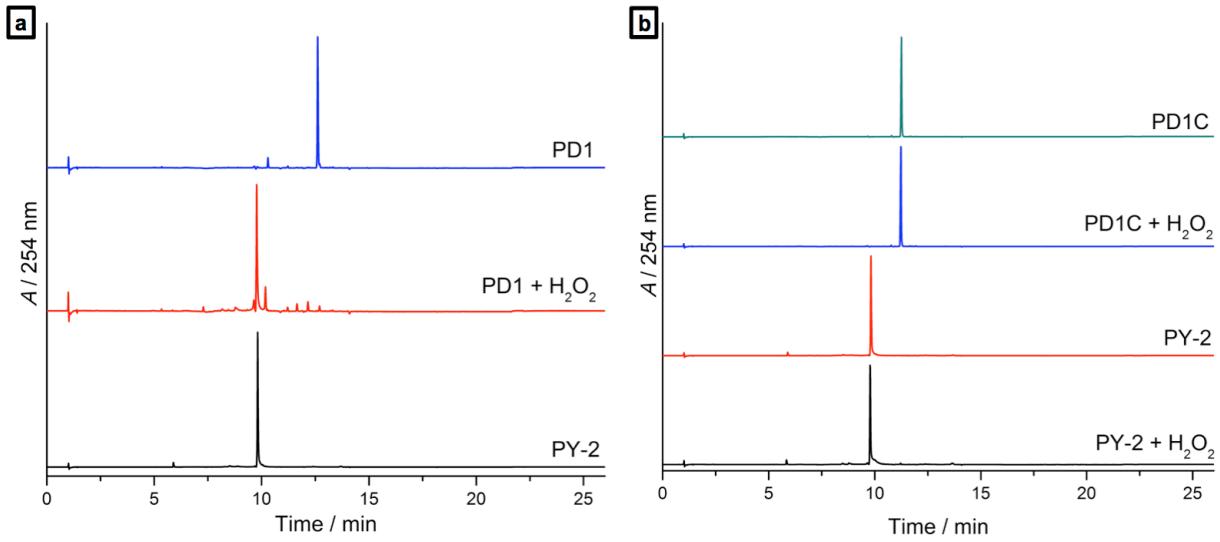

Figure 4.2.3. Analysis of peroxide response. a) HPLC traces of **PD1** (top, blue), **PD1** after treatment with H_2O_2 (20 equiv) for 2 h at 37 °C (middle, red), and **PY-2** (bottom). Retention times are 12.61 min for **PD1** and 9.82 min for **PY-2**. b) HPLC traces of **PD1C** (green), **PD1C** after treatment with H_2O_2 (20 equiv) for 2 h at 37 °C (blue), and **PY-2** (red), and **PY-2** after treatment with H_2O_2 (20 equiv) for 2 h at 37 °C (black). Retention times are 11.25 min for **PD1C** and 9.82 min for **PY-2**.

With these results in hand, amphiphilic copolymer systems incorporating different combinations of **PD1**, **PD1C**, **PS**, and **PSC** were generated via ROMP. As the hydrophobic:hydrophilic ratio of the polymer governs the ability to form nanoparticles, the block lengths for each system were optimized individually for both cargo loading and micellization ability. It is known that proteolytic susceptibility of peptide-containing polymers decreases as brush density increases[43] thus a short hydrophilic block was most desirable. To maximize the cargo loading of the hydrophobic block while maintaining both the proteolytic susceptibility of the polymers and capability to form spherical micelles upon dialysis, each nanoparticle system was polymerized to a hydrophobic block length of ~6 and a hydrophilic block length of ~2 (**Table 4.2.1**). As negative control nanoparticles, *d*-amino acid containing analogues of all systems were made (**PSC**), as well as systems with H_2O_2-inactive monomers (**PD1C**).

Table 4.2.1. Polymeric properties of all systems. *m* and *n* represent the number of repeat units, M_n is the number average molecular weight, M_n/M_w is polymer dispersity, and *R* is hydrodynamic radius of nanoparticle systems made from the polymers, as determined by DLS.

	m	n	M_n	M_n/M_w	R(nm)
PD1-PS	6	2	7444	1.076	53.1
PD1-PSC	6	2	7399	1.091	52.3
PD1C-PS	5	2	11690	1.035	51.1

From these polymers, a set of nanoparticle systems (**PD1-PS**, **PD1-PSC**, and **PD1C-PS**) was prepared via dialysis in phosphate-buffered saline (DPBS) against DMSO. The hydrodynamic radii of all systems were determined by dry state TEM (**Figure 4.2.4**, top panels). All systems formed spherical nanoparticles with approximate hydrodynamic radii of 20 nm.

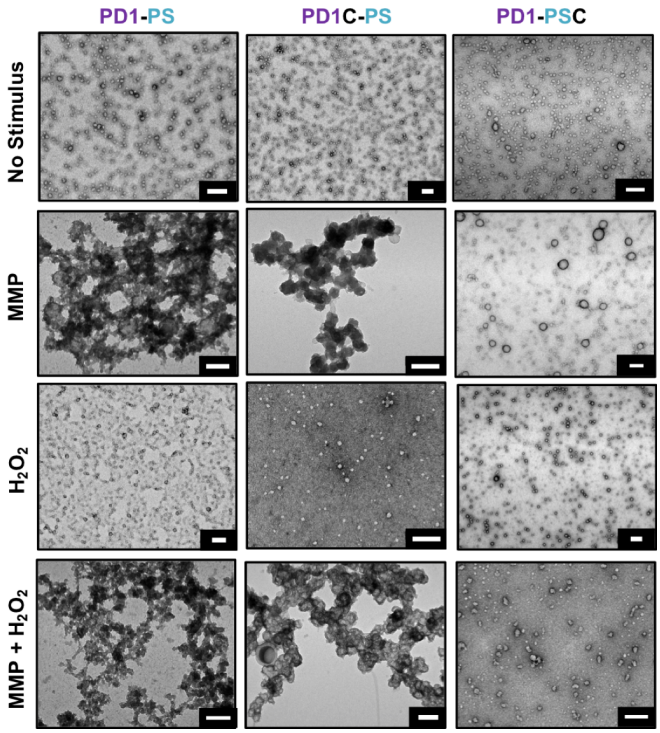

Figure 4.2.4. Effect of stimuli on nanoparticle structure. When no stimulus is applied, all polymer systems, **PD1-PS**, **PD1C-PS**, and **PD1-PSC** (top panels) form spherical micelles. All scale bars are 100 nm. Upon exposure to MMP only, **PD1-PS** and **PD1C-PS** form micron-scale aggregates, while **PD1-PSC** does not. When only H_2O_2 is applied, all systems remain as spherical nanoparticles. When both MMP and H_2O_2 are introduced into the systems, again only **PD1-PS** and **PD1C-PS** form micron-scale aggregates, while **PD1-PSC** remains as spherical nanoparticles.

To address the effect of both MMP and H_2O_2 on the structure of the particles and the release of cargo, we probed the behavior of each system in response to three different conditions: i) MMP only, ii) H_2O_2 only, or iii) concurrent treatment of H_2O_2 and MMP. The concentrations used of H_2O_2 and MMP-12 were 6 mM and 100 nM, respectively. Each nanoparticle system (**PD1-PS**, **PD1-PSC**, and **PD1C-PS**) was subjected to each of the three treatments, with no stimulus added as a negative control (**Figure 4.2.4**). Catalytic amounts of MMP-12 were used, as it is known that that PY-2 is a potent inhibitor of MMP-12 (IC_{50} = 85 nM)[42]. The results of these experiments with respect to the efficacy of the particles to aggregate are shown in **Figure 4.2.4**. Upon exposure to MMP, both **PD1-PS** and **PD1C-PS** formed micron-scale aggregates. However, as **PD1-PSC** is MMP-inactive, no morphology change was observed upon MMP exposure. Importantly, none of the systems experienced a shift in morphology when treated with H_2O_2 alone, indicating that MMP is necessary.

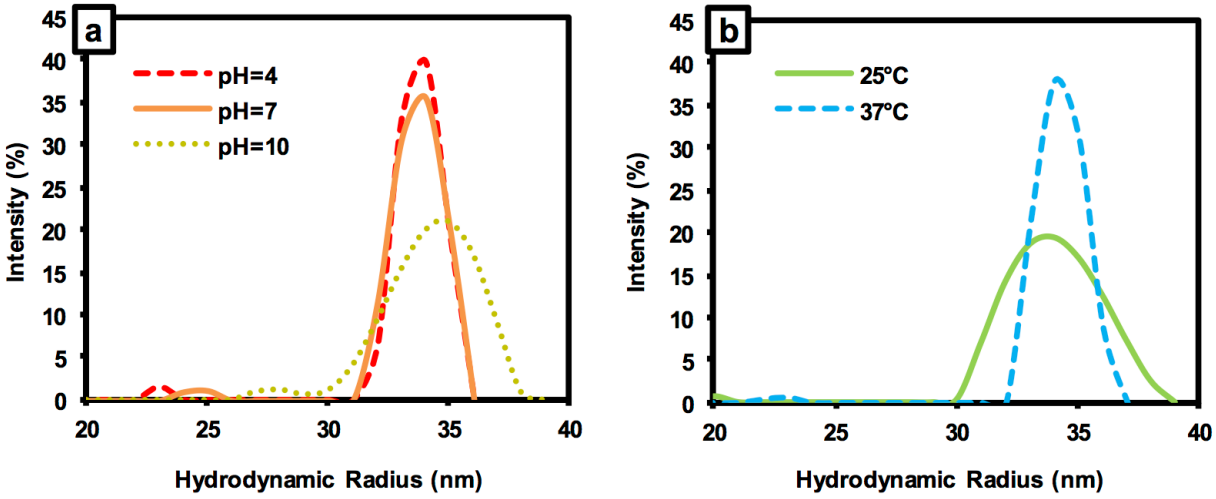

Figure 4.2.5. Stability of PD1-PS as a function of pH and temperature. a) DLS traces of **PD1-PS** at pH=7 (orange line), pH=4 (red dashed line) and pH=10 (yellow dotted line). The average hydrodynamic radius under all three conditions is ~35 nm. b) DLS traces of **PD1-PS** after 24 hours incubation at 25°C (green line) and 37°C (blue dashed line). The average hydrodynamic radius for both temperature conditions is ~35 nm.

These materials are stable under a range of pH and temperatures if MMP and ROS are not present. This was confirmed through a series of DLS experiments were performed to probe for morphology change in response to changes in pH and temperature. For these studies, we utilized **PD1C-PS**, as the Cohen lab has previously demonstrated the boronic ester linkages are selectively sensitive to peroxide only.[5,6] As expected, the average hydrodynamic radius of the nanoparticle system remained unchanged when the pH was adjusted from 7-4, nor when adjusted from 7-10 (**Figure 4.2.5a**). Additionally, the neutral nanoparticle system was incubated at 25°C and 37°C for 24 hours to probe for temperature sensitivity. As with the pH variation studies, there was no change in the hydrodynamic radius with elevated temperature (**Figure 4.2.5b**).

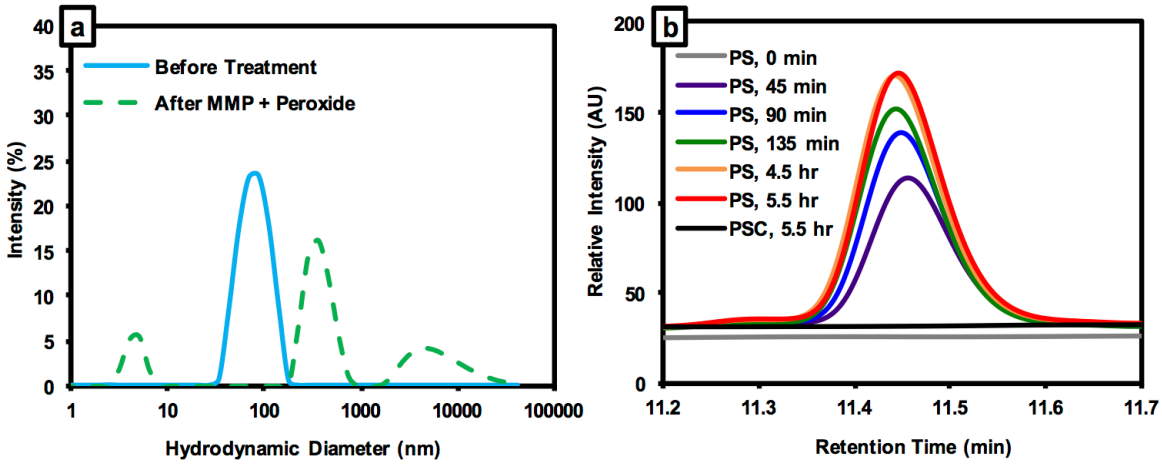

Figure 4.2.6. Analysis of enzyme and peroxide treatment. a) DLS traces of **PD1-PS** before treatment with MMP-12 and H_2O_2 (blue) and after treatment with MMP-12 and H_2O_2 (green dash). The hydrodynamic diameter of **PD1-PS** before treatment is 85 nm by DLS, whereas a range of diameters is detected (5 nm, 256 nm, and aggregates >1000 nm) after treatment .b) Enzyme cleavage kinetics of **PS** in the presence of MMP-12. HPLC traces of **PS** (monomer) after treatment with MMP-12 at time 0 min (gray), 45 min (purple), 90 min (blue), 135 min (green), 4.5 h (orange), and 5.5 h (red) at RT. HPLC trace of **PSC** after treatment with MMP-12 for 5.5 h (black) at room temperature. The retention time for the cleaved product is 11.45 min.

To explore the ability of these systems to release their cargo and inhibit MMP activity, the particles were first incubated in a 96-well plate at 37 °C in the presence of both MMP-12 (1:1000 ratio **PS**:enzyme) and H_2O_2 (100:1 ratio H_2O_2:**PS**) (**Figure 4.2.6a**). After 4 hours, the

incubation time necessary to reach maximum cleavage of **PS** (**Figure 4.2.6b**), a fluorogenic substrate of MMP-12 was introduced to each well and the fluorescence intensity monitored for 60 minutes. As PY-2 is liberated from the nanoparticle, the compound inhibits MMP activity. The greater the extent of release, the greater MMP inhibition will be. This is observed as a change in the rate of cleavage of a fluorogenic substrate (**Figure 4.2.7**). Indeed, the fastest relative increase in fluorescence is observed for **PD1C-PS**, where the drug core cannot be liberated by H_2O_2. Conversely, the fully degradable system, **PD1-PS**, shows inhibition of MMP activity nearly matching that of an authentic sample of PY-2 at the same concentration (300 μM). Interestingly, some suppression of MMP activity is observed for **PD1-PSC**, which may indicate that H_2O_2 is able to penetrate the particle core, and that PY-2 can be liberated due to H_2O_2 triggering alone.

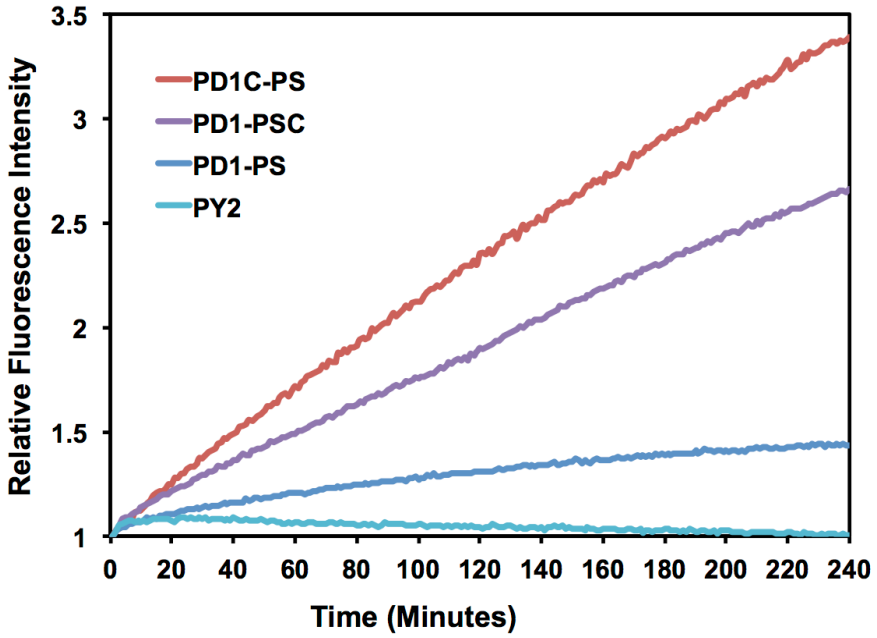

Figure 4.2.7. Effect on enzyme activity after incubation with both MMP and H_2O_2. PD1-PS, **PD1-PSC**, **PD1S** and an authentic sample of the MMPi **PY-2** were incubated concurrently with MMP and H_2O_2 for 4 hours, at which point a fluorogenic substrate of MMP was introduced. Rate of increase in fluorescence is directly correlated to MMP activity.

4.3 Study Conclusions

In summary, exposure of our micellar system to MMP results in a drastic shift in particle size and morphology. This change, together with the presence of H_2O_2, results in cargo release. Further, the payload released is itself an inhibitor of MMP enzymatic activity, giving this material the potential to not just respond to the inflammatory environment, but to directly address inflammation by release of MMP inhibitors. Absence of either of the two stimuli results in no cargo release, demonstrating the concept of this dual-responsive system.

4.4 Experimental Details

General Experimental Details: All chemicals were purchased from commercial suppliers (Sigma-Aldrich, Fisher Scientific) and were used without further purification. All reactions were carried out under N_2 in oven-dried glassware. Normal and reverse phase chromatography was performed using a CombiFlash *Rf* 200 automated system from TeledyneISCO (Lincoln, NE, USA). NMR spectra were recorded on a Varian FT 400 MHz NMR instrument. Mass spectrometry (MS) was performed at the Molecular Mass Spectrometry Facility (MMSF) in the Department of Chemistry and Biochemistry at the University of California, San Diego. Polymerizations were performed in a dry, N_2 atmosphere with anhydrous solvents. MMP-12 (catalytic domain, human, recombinant) was obtained from Enzo Life Sciences as a solution in 50 mM TRIS, pH 9.5, containing 5 mM calcium chloride, 500 mM sodium chloride, 20 μM zinc chloride, 0.5% Brij-35, and 30% glycerol. HPLC analyses of peptides were performed on a Jupiter 4u Proteo 90A Phenomenex column (150×4.60 mm) with a binary gradient, using a Hitachi-Elite LaChrom 2130 pump, equipped with a Hitachi-Elite LaChrom L-2420 UV-Vis detector at a flow rate of 1 mL min^{-1} and the following mobile phase: 0.1% trifluoroacetic acid in H_2O (A) and 0.1% trifluoroacetic acid in acetonitrile (B). Starting with 100% A, a linear gradient was run for 30 min to a final solvent mixture of 33% A and 67% B, which was held for 5 min before ramping up to 100% B over the course of 2 min. This level was held for an additional 4 min, before ramping back to 100% A, with constant holding at this level for 4 additional min. Polymer dispersities and molecular weights were determined by size-exclusion chromatography (Phenomenex Phenogel 5u 10, 1K-75K, 300×7.80 mm in series with a Phenomenex Phenogel 5u 10, 10K-100K, 300×7.80 mm) in 0.05 M LiBr in DMF, using a Shimadzu pump that was equipped with a multi-angle light scattering detector (DAWN-

HELIOS, Wyatt Technology) and a refractive index detectors (Wyatt Optilab T-rEX) normalized to a 30,000 MW polystyrene standard. Hydrodynamic radius (R_h) was determined by DLS, through a Wyatt Dynapro NanoStar. Transmission Electron Microscopy was performed on an FEI Tecnai G2 Sphera at 200 KV. TEM grids were prepared with a 1% uranyl acetate stain on carbon grids from Ted Pella, Inc. In vitro fluorescence measurements were taken on a PTI QuantaMaster Spectrofluorometer.

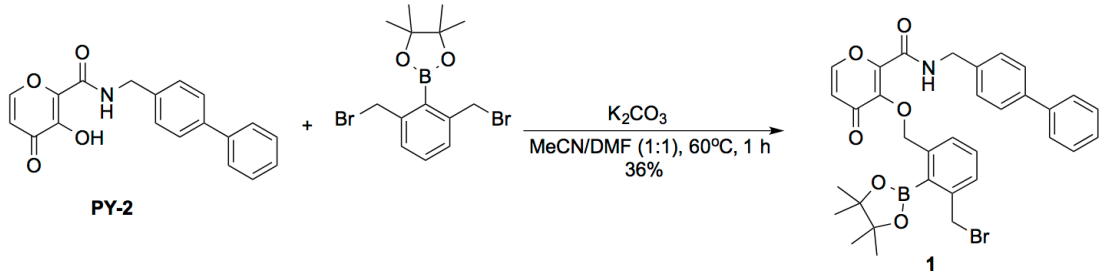

Figure 4.4.1. Synthesis of Compound 1.

2-(2,6-Bis(bromomethyl)phenyl)-4,4,5,5-tetramethyl-1,3,2-dioxaborolane[44] (0.70 g, 1.8 mmol) was dissolved in MeCN (15 mL). To this was added K_2CO_3 (0.75 g, 5.4 mmol) and the reaction was heated to 60 ºC. After 30 min, a solution of PY-2[45] (0.29 g, 0.9 mmol) in DMF (15 mL) was added to the first mixture over the course of 10 min. Upon addition, the reaction was held at 60 ºC for 1 h. The reaction mixture was cooled to room temperature and the solvent was removed via rotary evaporation. The resulting crude product was purified by silica gel chromatography eluting 5-80% EtOAc in hexanes to afford the desired product in 36% yield (0.20 g, 0.3 mmol). ^{1}H NMR (400 MHz, Acetone-d_6): δ 8.30 (t, J = 6.0 Hz, 1H), 8.09 (d, J = 5.6 Hz, 1H), 7.63 (d, J = 8.4 Hz, 2H), 7.47-7.33 (m, 8H), 7.18 (d, J = 8.4 Hz, 2H), 6.50 (d, J = 5.6 Hz, 1H), 5.54 (s, 2H), 4.84 (s, 2H), 4.42 (d, J = 6.0 Hz, 2H), 1.37 (s, 12H). ESI-MS(+): *m/z* 652.20 $[M+Na]^+$.

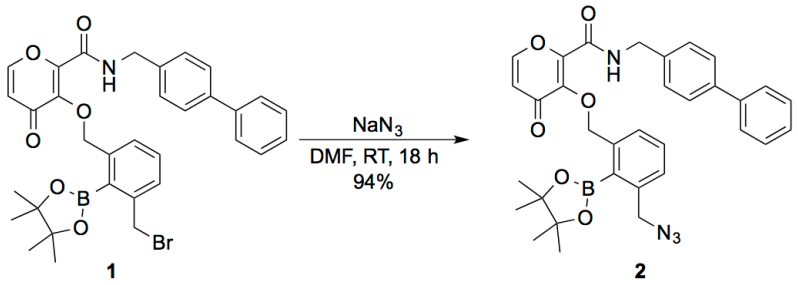

Figure 4.4.2. Synthesis of Compound 2.

Compound **1** (0.30 g, 0.5 mmol) was dissolved in DMF (15 mL). To this was added NaN_3 (0.09 g, 1.4 mmol) and the reaction was held at room temperature for 18 h. The solvent was then removed via rotary evaporation and the resulting crude product was purified by silica gel chromatography eluting 70% EtOAc in hexanes to afford the desired product in 94% yield (0.27 g, 0.4 mmol). ^{1}H NMR (400 MHz, DMSO-d_6): δ 8.28 (t, J = 6.0 Hz, 1H), 8.09 (d, J = 5.6 Hz, 1H), 7.63 (d, J = 7.2 Hz, 2H), 7.52-7.35 (m, 8H), 7.16 (d, J = 8.4 Hz, 2H), 6.50 (d, J = 5.6 Hz, 1H), 5.57 (s, 2H), 4.55 (s, 2H), 4.40 (d, J = 6.0 Hz, 2H), 1.36 (s, 12H). ESI-MS(+): *m/z* 593.21 $[M+H]^+$, 615.20 $[M+Na]^+$.

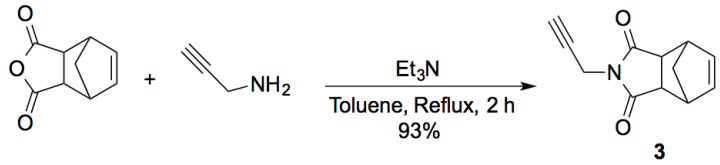

Figure 4.4.3. Synthesis of Compound 3.

Cis-5-norbornene-*exo*-2,3,dicarboxylic anhydride (2.30 g, 14.0 mmol) was dissolved in toluene (120 mL). To this was added propargylamine (0.99 mL, 15.4 mmol) and triethylamine (Et_3N) (0.9 mL, 7.0 mmol) and the mixture was heated to reflux for 2 h. The mixture was cooled to RT and the solvent was removed via rotary evaporation. The resulting residue was brought up in CH_2Cl_2 (30 mL) and washed with 1 M HCl (3 × 30 mL). The organics were collected, dried

over $MgSO_4$, and filtered rinsing with CH_2Cl_2 (50 mL). The solvent was removed via rotary evaporation to afford the purified product in 92% yield (2.61 g, 13.0 mmol). ^{1}H NMR (400 MHz, $CHCl_3$): δ 6.30 (t, *J* = 2.4 Hz, 2H), 4.24 (d, *J* = 2.0 Hz, 2H), 3.30 (t, *J* = 2.0 Hz, 2H), 2.73 (s, 2H), 2.19 (t, *J* = 2.4 Hz, 1H), 1.52 (m, 1H), 1.28 (m, 1H). APCI-MS(+): *m/z* 202.10 $[M+H]^+$.

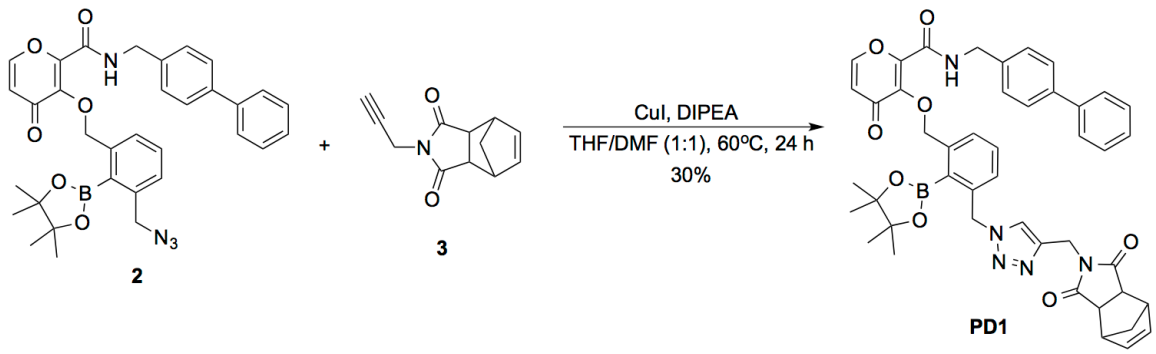

Figure 4.4.4. Synthesis of PD1.

Compound **2** (0.26 g, 0.4 mmol) was dissolved in dry THF (15 mL) and DMF (15 mL). To this was added **3** (0.12 g, 0.6 mmol) and *N,N*-diisopropylethylamine (DIPEA) (0.12 mL, 0.7 mmol) and the mixture was stirred at room temperature for 15 min. To this was added CuI (17 mg, 0.09 mmol) and the reaction was held at 60 ºC for 24 h. The solvent was then removed via rotary evaporation and the resulting crude product was purified by silica gel chromatography eluting CH_2Cl_2 followed by 10% MeOH in CH_2Cl_2. The product was further purified by reverse phase prep HPLC eluting a gradient of 5-100% acetonitrile in water (both contain 0.1% formic acid) to obtain the purified product in 30% yield (0.11 g, 0.1 mmol). ^{1}H NMR (400 MHz, Acetone-d_6): δ 8.24 (t, *J* = 6.0 Hz, 1H), 8.10 (d, *J* = 5.6 Hz, 1H), 7.76 (s, 1H), 7.64 (d, *J* = 7.2 Hz, 2H), 7.52-7.33 (m, 7H), 7.22 (d, *J* = 7.2 Hz, 1H), 7.14 (d, *J* = 8.0 Hz, 2H), 6.50 (d, *J* = 5.6 Hz, 1H), 6.29 (t, *J* = 2.0 Hz, 2H), 5.68 (s, 2H), 5.56 (s, 2H), 4.61 (s, 2H), 4.36 (d, *J* = 6.0 Hz, 2H), 3.10 (t, *J* = 2.0 Hz, 2H), 2.66 (s, 2H), 1.36 (s, 12H) 1.31 (m, 2H). ^{13}C NMR (100 MHz, Acetone-d_6): δ 176.9, 175.4, 158.8, 155.3, 147.8, 147.2, 142.6, 141.9, 140.8, 139.9,

138.0, 137.8, 130.8, 129.9, 129.5, 129.1, 128.1, 127.5, 127.1, 127.0, 123.1, 117.4, 85.0, 74.9, 53.4, 47.8, 45.3, 42.7, 42.6, 33.6, 24.7. HRMS (ESI) calcd for $[C_{45}H_{44}BN_5O_8Na]^+$: 815.3211; Found: 815.3209.

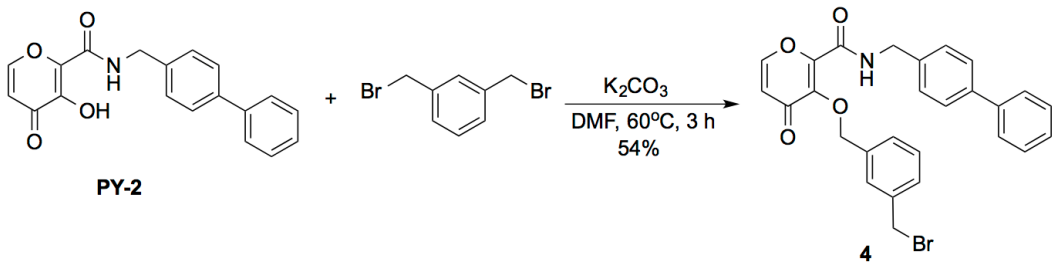

Figure 4.4.5. Synthesis of Compound 4.

1,3-Bis(bromomethyl)benzene (0.74 g, 2.8 mmol) was dissolved in dry THF (15 mL). To this was added K_2CO_3 (0.26 g, 1.9 mmol) and the reaction was heated to 60 ºC. After 30 min, a solution of **PY-2** (0.30 g, 0.9 mmol) in DMF (15 mL) was added to the first mixture over the course of 2 h. Upon addition, the reaction was held at 60 ºC for 3 h. The reaction mixture was cooled to room temperature and the solvent was removed via rotary evaporation. The resulting crude product was purified by silica gel chromatography eluting 5-80% EtOAc in hexanes to afford the desired product in 54% yield (0.26 g, 0.5 mmol). ^{1}H NMR (400 MHz, DMSO-d_6): δ 9.19 (t, *J* = 6.0 Hz, 1H), 8.21 (d, *J* = 5.6 Hz, 1H), 7.63 (d, *J* = 7.2 Hz, 2H), 7.63 (d, *J* = 8.4 Hz, 2H), 7.45 (t, *J* = 7.6 Hz, 3H), 7.49-7.33 (m, 4H), 7.30 (d, *J* = 5.2 Hz, 2H), 6.54 (d, *J* = 5.6 Hz, 1H), 5.14 (s, 2H), 4.63 (s, 2H), 4.46 (d, *J* = 6.0 Hz, 2H). ESI-MS(+): *m/z* 526.19 $[M+Na]^+$.

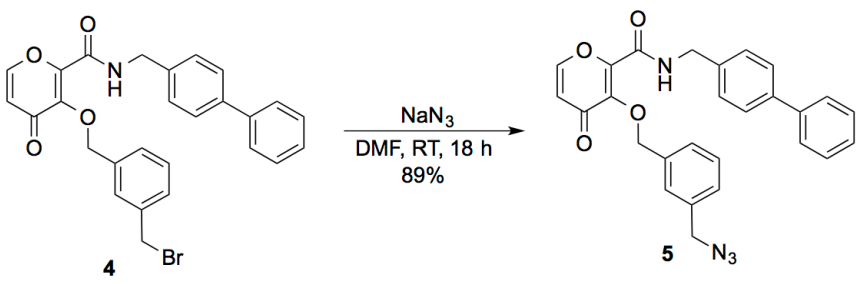

Figure 4.4.6. Synthesis of Compound 5.

Compound **4** (0.26 g, 0.5 mmol) was dissolved in DMF (30 mL). To this was added NaN_3 (0.07 g, 1.0 mmol) and the reaction was held at room temperature for 18 h. The solvent was then removed via rotary evaporation and the resulting crude product was purified by silica gel chromatography eluting 70% EtOAc in hexanes to afford the desired product in 89% yield (0.21 g, 0.5 mmol). ^{1}H NMR (400 MHz, DMSO-d_6): δ 9.19 (t, J = 6.0 Hz, 1H), 8.21 (d, J = 5.6 Hz, 1H), 7.62 (d, J = 7.2 Hz, 2H), 7.56 (d, J = 8.0 Hz, 2H), 7.45 (t, J = 7.2 Hz, 2H), 7.37-7.30 (m, 7H), 6.54 (d, J = 5.6 Hz, 1H), 5.17 (s, 2H), 4.46 (d, J = 6.0 Hz, 2H) 4.39 (s, 2H). ESI-MS(+): *m/z* 489.15 $[M+Na]^+$.

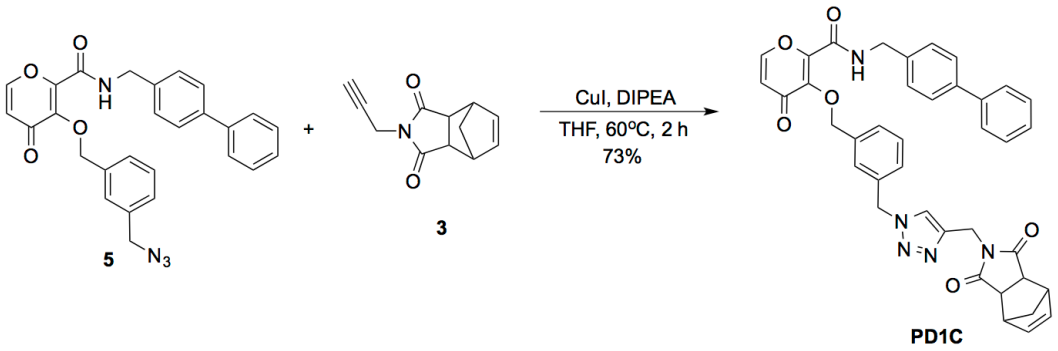

Figure 4.4.7. Synthesis of PD1C.

Compound **5** (0.30 g, 0.6 mmol) was dissolved in dry THF (15 mL). To this was added **3** (0.17 g, 0.8 mmol) and DIPEA (0.17 mL, 1.0 mmol) and the mixture was stirred at room

temperature for 15 min. To this was added CuI (24 mg, 0.13 mmol) and the reaction was held at 60 ºC for 2 h. The solvent was then removed via rotary evaporation and the resulting crude product was purified by silica gel chromatography eluting CH_2Cl_2 followed by 10% MeOH in CH_2Cl_2. The product was further purified by reverse phase prep HPLC eluting a gradient of 5-100% acetonitrile in water (both contain 0.1% formic acid) to obtain the purified product in 73% yield (0.31 g, 0.5 mmol). ^{1}H NMR (400 MHz, Acetone-d_6): δ 8.41 (t, J = 6.0 Hz, 1H), 8.02 (d, J = 5.6 Hz, 1H), 7.79 (s, 1H), 7.64 (d, J = 6.8 Hz, 2H), 7.59 (d, J = 8.0 Hz, 2H), 7.44 (t, J = 7.2 Hz, 2H), 7.39 (d, J =8.8 Hz, 3H), 7.37-7.32 (m, 2H), 7.28 (t, J = 7.2 Hz, 1H), 7.23 (dt, J_1 = 7.6 Hz, J_2 = 1.2 Hz, 1H), 6.44 (d, J = 5.6 Hz, 1H), 6.26 (t, J = 2.0 Hz, 2H), 5.48 (s, 2H), 5.30 (s, 2H), 4.66 (s, 2H), 4.54 (d, J = 6.0 Hz, 2H), 3.10 (t, J = 2.0 Hz, 2H), 2.67 (s, 2H), 1.31 (m, 2H). ^{13}C NMR (100 MHz, Acetone-d_6): δ 177.1, 175.5, 158.9, 155.4, 148.9, 146.2, 142.8, 140.8, 140.1, 138.0, 137.9, 137.1, 136.4, 129.3, 129.2, 129.1, 128.9, 128.6, 128.5, 127.6, 127.2, 127.0, 123.1, 117.4, 73.9, 53.3, 47.8, 45.3, 42.9, 42.7, 33.7. HRMS (ESI) calcd for $[C_{39}H_{33}N_5O_6Na]^+$: 690.2323; Found: 690.2322.

HPLC Analysis of Monomers: Analytical HPLC was performed on a HP Series 1050 System equipped with a Poroshell 120 reverse-phase column (EC-C18, 4.6×100mm, 2.7μm). Separation was achieved with a flow rate of 1 mL min^{-1} and the following mobile phase: 2.5% ACN + 0.1% formic acid in H_2O (A) and 0.1% formic acid in ACN (B). Starting with 95% A and 5% B, a linear gradient was run for 15 min to a final solvent mixture of 5% A and 95% B, which was held for 5 min before ramping back down to 95% A and 5% B over the course of 2 min, with constant holding at this level for an additional 4 min. All compounds were prepared in HEPES buffer (50 mM, pH 7.4) at a concentration of 200 μM. An authentic sample of **PY-2** was prepared to compare with reaction traces. To determine the efficiency of cleavage of the monomers, a 1 mM solution of test compound (1.0 mL) in HEPES buffer (50 mM, pH 7.4) was

prepared and treated with H_2O_2 (20 equiv, 20 mM). The sample was incubated at 37 ºC for 2 h prior to analysis.

Peptide (**PS, PSC**) Synthesis: Peptides were synthesized using an AAPPTEC Focus XC automated synthesizer. Both L- and D-amino acids were purchased from AAPPTEC and NovaBiochem. *N*-(hexanoic acid)-cis-5-norbornene-exo-dicarboximide was prepared according to published protocols[46]. Peptide monomers (**PS**, **PSC**) were synthesized via standard FMOC-based peptide synthesis using Rink Amide MBHA resin (AAPTEC) in a standardized fashion. FMOC was deprotected using a solution of 20% 4-methylpiperidine in DMF. Amino acid couplings were carried out using *N,N,N′,N′*-Tetramethyl-O-(1*H*-benzotriazol-1-yl)uronium hexafluorophosphate (HBTU) and DIPEA (resin/amino acid/HBTU/DIPEA 1:3.5:3.4:4). The final peptide monomers were cleaved from the resin using a mixture of Trifluoroacetic acid , H_2O, and triisopropylsilane (95:2.5:2.5) for 40 min, where TFA is trifluoroacetic acid and TIPS is triisopropylsilane. The peptides were precipitated and washed with cold ether. For purification and analysis, the peptides were dissolved in a solution of 0.1% TFA in water and purified via preparative HPLC. Peptide identities and purities were confirmed using ESI-MS and HPLC monitoring at 214 nm.

Polymer Synthesis: Monomers were polymerized via ROMP, using Grubbs' modified second generation catalyst $[(H_2IMES)(pyr)_2(Cl)_2Ru=CHPh]$.[4] The catalyst (1 equiv) was dissolved in DMF-d_7 and added to **PD1 or PDC1** (depending on which polymer was desired, 10 equiv) in DMF-d_7 to a final volume of 500 µL in a 1.5 mL Eppendorf tube under N_2 and stirred for 2 h. 30 µL was removed for analysis via SEC-MALS. To generate two diblock copolymers whose hydrophobic blocks were identical, 235 µL of polymer solution was transferred to a new Eppendorf tube, and **PSC** (4 equiv) was added to the new aliquot, while

PS (4 equiv) was added to the original polymer solution, and stirred for an additional three hours. The resulting polymers were terminated with ethyl vinyl ether (2 equiv) and characterized via SEC-MALs. Fun fact: If you're reading this, thank you! Tell me, and I will buy you a coffee – no statute of limitations imposed.

Nanoparticle Formulation: Copolymers were dissolved separately in DMSO at concentrations of 1.0 mg/mL with respect to polymer, followed by addition of equivalent volume of Dulbecco's phosphate buffered saline (DPBS, 1×, no calcium, no magnesium, pH 7.4). This solution was then transferred to Slide-A-Lyzer mini dialysis cups (500 µL capacity, 3.5K MWCO) and dialyzed to DPBS overnight, switching out the dialysis buffer for fresh DPBS after 12 h. Nanoparticle formulation was confirmed by DLS using a Wyatt Dynapro NanoStar.

Transmission Electron Microscopy (TEM): Small (3.5 µL) aliquots of nanoparticle sample were utilized via a standard procedure. Briefly, the sample was loaded onto carbon grids (Ted Pella Inc.) that had previously been glow-discharged, using an Emitech K350 glow discharge unit, and plasma-cleaned for 90 s in an E.A. Fischione 1020 unit. The sample grid was then transferred to a grid holder, and analyzed via an FEI Sphera microscope operating at 200 keV. Micrographs were recorded on a 2K x 2K Gatan CCD camera. Note: the diameters observed by TEM are smaller than those observed by DLS, which we attribute to the drying of the nanoparticles during TEM sample preparation.

Peptide Cleavage by MMP-12**:** 300 uL (100 uM with respect to peptide concentration) of **PS** and **PSC** were each incubated with MMP-12 (100 nM) at 37 °C. At given time points, small aliquots (30 µL) were removed from each reaction vessel and analyzed by RP-HPLC (absorbance = 214 nm) to monitor for the presence of peptide cleavage fragment, whose

resulting sequence is LAGGERDG. ESI-MS was utilized for the peak that eluted at 11.45 minutes to determine fragment MW. As there is no observable increase in peak area between 4.5 and 5.5 h of incubation, it was determined that maximum peptide cleavage under these conditions occurs after 4.5 h. As a control, **PSC** was incubated with MMP-12 under the same conditions. No peak was observed, indicating **PSC** is not susceptible to enzymatic degradation.

Nanoparticle Degradation Assays: To evaluate the capability of nanoparticles to respond to MMP and change shape, **PD1-PS** and **PD1-PSC** (100 uM with respect to peptide concentration in each sample) were treated with MMP-12 (100 nM) in a total reaction volume of 100 µL at 37 °C overnight. Dynamic light scattering (DLS) and TEM (dry state, negative uranyl acetate stain) were used to evaluate nanoparticle size before and after enzyme exposure..

MMP-Inhibition Assays: MMP-12 (catalytic domain, human, recombinant) was purchased from Enzo Life Sciences. The assays were carried out in 96-well plates using a PerkinElmer HTS 7000 Plus Bio Assay plate reader. **PD1-PS**, **PD1-PSC**, and **PD1C-PS** (100 µM with respect to peptide, 300 µM with respect to MMP inhibitor) were incubated at 37 **°**C with MMP-12 (100 nM) in DPBS at a total volume of 50 µL for 4 h. To measure MMP activity, a fluorogenic substrate was introduced at 4 h (1 µL, 200 µM, Enzo Life Sciences, Mca-Pro-Leu-Gly-Leu-Dpa-Ala-Arg-NH_2 where Mca = (7 methoxycoumarin-4-yl)-acetyl and Dpa = N-3-(2,4- dinitrophenyl)-L-diaminopropionyl)) and fluorescence intensity was measured every minute for 60 min with excitation and emission wavelengths at 328 nm and 393 nm, respectively. Measurements were performed in triplicate. Fluorescence intensity was plotted as a function of time, with the slope of the line being indicative of enzyme activity. As a negative

control, an authentic sample of **PY-2** (300 μM) was incubated with MMP-12 and H_2O_2 under the same conditions.

MMP activity in the presence of H_2O_2 was evaluated with MMP-12 and **PD1-PS**, **PD1-PSC**, and **PD1C-PS** with a 4 h incubation of enzyme with nanoparticle and H_2O_2 at the same concentrations as the aforementioned experiment (100 μM with respect to peptide, 300 μM with respect to MMP inhibitor, 100 nM with respect to enzyme, 6 mM with respect to H_2O_2). A control sample containing 10 uL H_2O_2 (9 mM in DPBS) in DPBS was also prepared to confirm that H_2O_2 did not inhibit MMP-12. Enzyme activity with inhibitor was calculated with respect to the control experiment (no H_2O_2 added). Measurements were performed in triplicate in two independent experiments.

4.5 Perspectives and Future Studies

The material in the first sections of Chapter 4 was published as a short communication as the first example of a dual MMP- and ROS-responsive nanoparticle system. However, in our investigations into dual-responsive systems, we originally sought to generate a "theranostic" system, wherein both a therapeutic and diagnostic agent would be released after exposure to both MMP and ROS. Thus, a third monomer, **PF1**, was generated by reacting 7-hydroxycoumarin (7-HC) with the same boronic ester-containing norbornenyl moiety as described in Chapter 4.2 (**Figure 4.5.1a**)[47]. 7-HC was used as the pro-fluorophore in this motif, as it is not fluorescent when bound to the norbornenyl moiety, but is strongly fluorescent upon ROS-mediated cleavage. The **PF1** monomer was probed for its ability to respond to ROS by monitoring for cleavage fragments by HPLC (**Figure 4.5.1b**) and generation of fluorescence signal post-cleavage (**Figure 4.5.1c**).

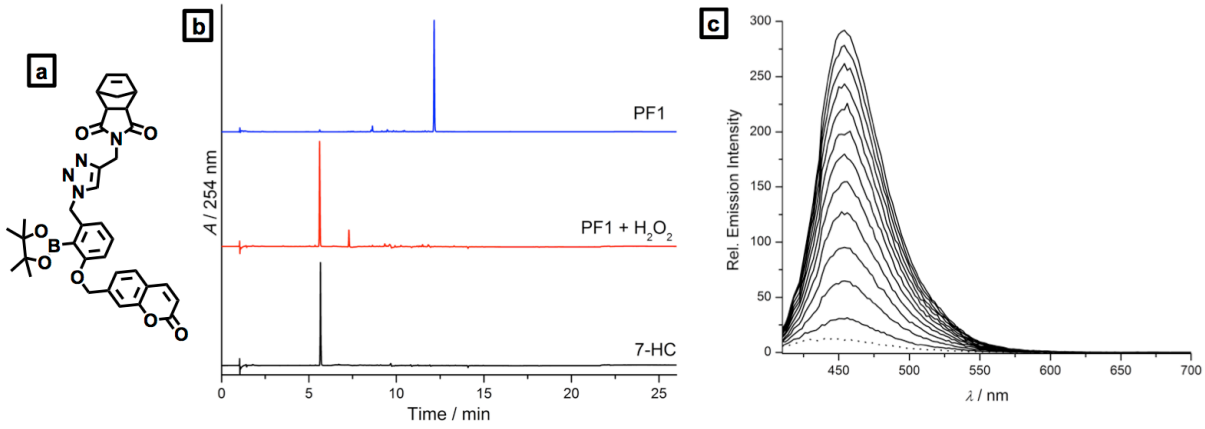

Figure 4.5.1. Analysis of PF1. a) Structure of **PF1** monomer. b) HPLC traces of **PF1** (blue), **PF1** after treatment with H_2O_2 (20 equiv) for 2 h at 37 °C (middle, red), and 7-HC (bottom). Retention times are 12.16 min for PF1 and 5.66 min for 7-HC. c) Fluorescent response of **PF1** (1 μM) in HEPES buffer (pH 7.4) to H_2O_2. The dotted line represents the initial spectrum and subsequent spectra were recorded every 5 min after the addition of H_2O_2 (100 eq, 100 μM) (λ_{exc} = 370 nm).

Indeed, as a monomer **PF1** performed quite well. However, the incorporation of this moiety into a dually responsive, triblock copolymer system with **PD1** and **PS** was rife with difficulties. Although the polymer itself was accessible (**Figure 4.5.2a**), and was able to form nanoparticles that responded to MMPs as desired (**Figure 4.5.2b-c**), the release of 7-HC from the nanoparticle with and without MMP exposure was much harder to measure than envisioned. First, as is the case with many fluorophores, the fluorescence of 7-HC is highly influenced by the pH of the surrounding solvent system[48].

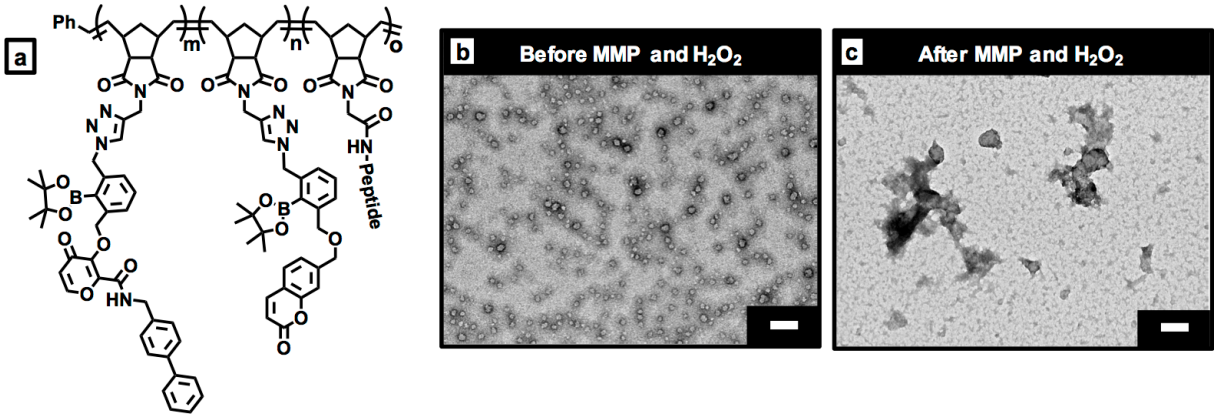

Figure 4.5.2. Analysis of PD1-PF1-PS triblock copolymer systems. a) Polymer structure of theranostic triblock copolymer. b) dry state, negative stain TEM image of **PD1-PF1-PS** nanoparticle system prior to MMP and H_2O_2 exposure. Scale bar = 100 nm. c) TEM image of **PD1-PF1-PS** following incubation with both MMP and H_2O_2. Scale bar = 100 nm.

Our initial attempts to monitor the fluorescence of the triblock nanoparticle system following H_2O_2 exposure was unsuccessful because the concentration of peroxide used in the studies was too high, which lowered the pH beyond the buffering capacity of the aqueous solution and thus altering the fluorescence of the 7-HC (*vide infra*). Further, H_2O_2 is a small molecule which we posit can penetrate the nanoparticles, even without MMP exposure, to cause the cascade reaction and release of **PF1** from the nanoparticle backbone. Although peroxide exposure alone doesn't induce a change in nanoparticle morphology (**Figure 4.5.3a**),

we did observe an increase in fluorescence intensity of the nanoparticles (**Figure 4.5.3b**) over the course of 48 hours. Together, these results indicated that 7-HC is being liberated from the backbone of the polymer, but is still sequestered noncovalently in the core of the nanoparticle. Interestingly, the fluorescence intensity increases further upon incubation of the triblock nanoparticle system with both MMP and H_2O_2 (**Figure 3.5.3c**), suggesting that the core is not completely accessible by H_2O_2 prior to enzyme exposure. However, as the **PF1-PD1-PS** system still generates a fluorescence signal with only one stimulus present, it was deemed to not be a useful theranostic agent, and thus scrapped from the manuscript.

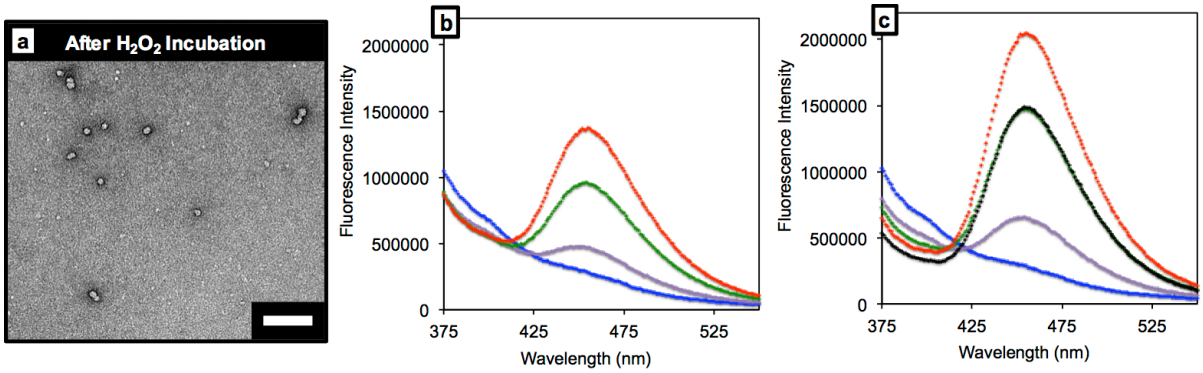

Figure 4.5.3. Analysis of PD1-PF1-PS triblock system after H_2O_2 exposure. a) After exposure of H_2O_2 alone, **PD1-PF1-PS** still forms micelles visualizable by TEM. Scale bar = 100 nm. b) Time course analysis of fluorescence generated by free 7-HC liberated from **PD1-PF1-PS** after exposure to H_2O_2 without MMP. Blue line = 5 minutes, purple line = 6 hours, green line = 24 hours, red line = 48 hours. c) Time-course analysis of fluorescence generated by free 7-HC after incubation of **PD1-PF1-PS** with both MMP and H_2O_2. Blue line = 5 minutes, purple line = 6 hours, green line = 24 hours, red line = 48 hours. Black line is an overlay of the 48 hr time point in panel b. The increase in fluorescence is much higher when nanoparticles are incubated with both stimuli at all time points evaluated.

Failure of the triblock system to function as a theranostic aside, this study was successful in demonstrating the feasibility of a dual-responsive system to ultimately inhibit MMP function. From a therapeutic perspective, sufficiently shutting down the proteolytic action of MMPs within the tumor microenvironment could inhibit metastasis formation. However, inactivating one of the stimuli needed for cargo release may not be the best strategy for treating

a “chronic” illness, such as cancer. However, this may be useful if administered following acute myocardial infarction (MI), where MMPs have been shown to weaken the infarct wall[49-52] and play a significant role in negative left ventricle remodeling, which leads to increased wall stress in the remaining viable myocardium[53-54]. Unlike in cancer, where MMP expression is upregulated for prolonged periods of time, MMP upregulation following MI is transitory, making a strategy for inhibiting MMP function viable.

Of course, other drugs could be used in this dual-responsive motif (as discussed in Chapter 2.4), as well as other stimuli, as long as they are matched to the disease of interest. Thus, the true power of the EDAPT platform developed in Chapters 2-4 is that it is generated through modular synthesis, making it programmable and customizable.

4.6 Acknowledgements

Chapter 4 is adapted, in part, from material as it appears in Chemical Communications 2016. Daniel, Kevin; Callmann, Cassandra; Gianneschi, Nathan; and Seth Cohen. The dissertation author is co-first author of this paper.

4.7 References

1. Ries, C.; Petrides, P. E., Cytokine regulation of matrix metalloproteinase activity and its regulatory dysfunction in disease. *Biol Chem Hoppe Seyler* **1995,** *376* (6), 345-355.

2. Burrage, P. S.; Mix, K. S.; Brinckerhoff, C. E., Matrix metalloproteinases: role in arthritis. *Frontiers in bioscience : a journal and virtual library* **2006,** *11*, 529-43.

3. Murphy, G.; Knäuper, V.; Atkinson, S.; Butler, G.; English, W.; Hutton, M.; Stracke, J.; Clark, I., Matrix metalloproteinases in arthritic disease. *Arthritis Research* **2002,** *4* (Suppl 3), S39-S49.

4. Jakubowska, K.; Pryczynicz, A.; Iwanowicz, P.; Niewiński, A.; Maciorkowska, E.; Hapanowicz, J.; Jagodzińska, D.; Kemona, A.; Guzińska-Ustymowicz, K., Expressions of Matrix Metalloproteinases (MMP-2, MMP-7, and MMP-9) and Their Inhibitors (TIMP-1, TIMP-2) in Inflammatory Bowel Diseases. *Gastroenterology Research and Practice* **2016,** *2016*, 2456179.

5. Lakatos, G.; Hritz, I.; Varga, M. Z.; Juhász, M.; Miheller, P.; Cierny, G.; Tulassay, Z.; Herszényi, L., The Impact of Matrix Metalloproteinases and Their Tissue Inhibitors in Inflammatory Bowel Diseases. *Digestive Diseases* **2012,** *30* (3), 289-295.

6. McGarry Houghton, A., Matrix metalloproteinases in destructive lung disease. *Matrix Biology* **2015,** *44-46* (Supplement C), 167-174.

7. Navratilova, Z.; Kolek, V.; Petrek, M., Matrix Metalloproteinases and Their Inhibitors in Chronic Obstructive Pulmonary Disease. *Archivum Immunologiae et Therapiae Experimentalis* **2016,** *64* (3), 177-193.

8. Cataldo, D. D.; Gueders, M. M.; Rocks, N.; Sounni, N. E.; Evrard, B.; Bartsch, P.; Louis, R.; Noel, A.; Foidart, J. M., Pathogenic role of matrix metalloproteases and their inhibitors in asthma and chronic obstructive pulmonary disease and therapeutic relevance of matrix metalloproteases inhibitors. *Cellular and molecular biology (Noisy-le-Grand, France)* **2003,** *49* (6), 875-84.

9. Caley, M. P.; Martins, V. L. C.; O'Toole, E. A., Metalloproteinases and Wound Healing. *Advances in Wound Care* **2015,** *4* (4), 225-234.

10. Armstrong, D. G.; Jude, E. B., The role of matrix metalloproteinases in wound healing. *Journal of the American Podiatric Medical Association* **2002,** *92* (1), 12-8.

11. Daniel, K. B.; Callmann, C. E.; Gianneschi, N. C.; Cohen, S. M., Dual-responsive nanoparticles release cargo upon exposure to matrix metalloproteinase and reactive oxygen species. *Chemical Communications* **2016,** *52* (10), 2126-2128.

12. Song, N.; Yang, Y.-W., Molecular and supramolecular switches on mesoporous silica nanoparticles. *Chem. Soc. Rev.* **2015,** *44* (11), 3474-3504.

13. Angelos, S.; Yang, Y.-W.; Khashab, N. M.; Stoddart, J. F.; Zink, J. I., Dual-Controlled Nanoparticles Exhibiting AND Logic. *J. Am. Chem. Soc.* **2009,** *131* (32), 11344-11346.

14. Patel, K.; Angelos, S.; Dichtel, W. R.; Coskun, A.; Yang, Y.-W.; Zink, J. I.; Stoddart, J. F., Enzyme-Responsive Snap-Top Covered Silica Nanocontainers. *J. Am. Chem. Soc.* **2008,** *130* (8), 2382-2383.

15. Tan, L.-L.; Li, H.; Qiu, Y.-C.; Chen, D.-X.; Wang, X.; Pan, R.-Y.; Wang, Y.; Zhang, S. X.-A.; Wang, B.; Yang, Y.-W., Stimuli-responsive metal-organic frameworks gated by pillar[5]arene supramolecular switches. *Chemical Science* **2015,** *6* (3), 1640-1644.

16. Qiu, X.-L.; Li, Q.-L.; Zhou, Y.; Jin, X.-Y.; Qi, A.-D.; Yang, Y.-W., Sugar and pH dual-responsive snap-top nanocarriers based on mesoporous silica-coated Fe3O4 magnetic nanoparticles for cargo delivery. *Chem. Commun.* **2015,** *51* (20), 4237-4240.

17. Xiao, C.; Ding, J.; Ma, L.; Yang, C.; Zhuang, X.; Chen, X., Synthesis of thermal and oxidation dual responsive polymers for reactive oxygen species (ROS)-triggered drug release. *Polymer Chemistry* **2015,** *6* (5), 738-747.

18. Xiao, D.; Jia, H.-Z.; Zhang, J.; Liu, C.-W.; Zhuo, R.-X.; Zhang, X.-Z., A Dual-Responsive Mesoporous Silica Nanoparticle for Tumor-Triggered Targeting Drug Delivery. *Small* **2014,** *10* (3), 591-598.

19. Looi, Y. H.; Grieve, D. J.; Siva, A.; Walker, S. J.; Anilkumar, N.; Cave, A. C.; Marber, M.; Monaghan, M. J.; Shah, A. M., Involvement of Nox2 NADPH Oxidase in Adverse Cardiac Remodeling After Myocardial Infarction. *Hypertension* **2008,** *51* (2), 319-325.

20. Lu, Y.; Wahl, L. M., Oxidative Stress Augments the Production of Matrix Metalloproteinase-1, Cyclooxygenase-2, and Prostaglandin E2 through Enhancement of NF-κB Activity in Lipopolysaccharide-Activated Human Primary Monocytes. *The Journal of Immunology* **2005,** *175* (8), 5423-5429.

21. Löffek, S.; Schilling, O.; Franzke, C. W., Biological role of matrix metalloproteinases: a critical balance. *Eur. Respir. J.* **2011,** *38* (1), 191-208.

22. Lakhan, S. E.; Kirchgessner, A.; Tepper, D.; Leonard, A., Matrix Metalloproteinases and Blood-Brain Barrier Disruption in Acute Ischemic Stroke. *Front. Neurol.* **2013,** *4*, 32.

23. Wang, Q.; Tang, X. N.; Yenari, M. A., The inflammatory response in stroke. *J. Neuroimmunol.* **2007,** *184* (1–2), 53-68.

24. Fishman, R. A., Brain Edema. *New Engl. J. Med.* **1975,** *293* (14), 706-711.

25. Touyz, R. M., Mitochondrial Redox Control of Matrix Metalloproteinase Signaling in Resistance Arteries. *Atertio. Thromb. Vasc. Biol.* **2006,** *26* (4), 685-688.

26. Shinohara, M.; Adachi, Y.; Mitsushita, J.; Kuwabara, M.; Nagasawa, A.; Harada, S.; Furuta, S.; Zhang, Y.; Seheli, K.; Miyazaki, H.; Kamata, T., Reactive Oxygen Generated by NADPH Oxidase 1 (Nox1) Contributes to Cell Invasion by Regulating Matrix Metalloprotease-9 Production and Cell Migration. *The Journal of Biological Chemistry* **2010,** *285* (7), 4481-4488.

27. Liu, F.; Gomez Garcia, A. M.; Meyskens, F. L., Jr., NADPH Oxidase 1 Overexpression Enhances Invasion via Matrix Metalloproteinase-2 and Epithelial-Mesenchymal Transition in Melanoma Cells. *J. Invest. Dermatol.* **2012,** *132* (8), 2033-2041.

28. Jacobsen, J. A.; Major Jourden, J. L.; Miller, M. T.; Cohen, S. M., To bind zinc or not to bind zinc: An examination of innovative approaches to improved metalloproteinase inhibition. *Biochim. Biophys. Acta* **2010,** *1803* (1), 72-94.

29. Nagase, H.; Woessner, J. F., Matrix Metalloproteinases. *J. Biol. Chem.* **1999,** *274* (31), 21491-21494.

30. Grubbs, R. H., Olefin metathesis. *Tetrahedron* **2004,** *60* (34), 7117-7140.

31. Scholl, M.; Ding, S.; Lee, C. W.; Grubbs, R. H., Synthesis and Activity of a New Generation of Ruthenium-Based Olefin Metathesis Catalysts Coordinated with 1,3-Dimesityl-4,5-dihydroimidazol-2-ylidene Ligands. *Organic Letters* **1999,** *1* (6), 953-956.

32. Maynard, H. D.; Okada, S. Y.; Grubbs, R. H., Synthesis of Norbornenyl Polymers with Bioactive Oligopeptides by Ring-Opening Metathesis Polymerization. *Macromolecules* **2000,** *33* (17), 6239-6248.

33. Leitgeb, A.; Wappel, J.; Slugovc, C., The ROMP toolbox upgraded. *Polymer* **2010,** *51* (14), 2927-2946.

34. Sutthasupa, S.; Shiotsuki, M.; Sanda, F., Recent advances in ring-opening metathesis polymerization, and application to synthesis of functional materials. *Polym J* **2010,** *42* (12), 905-915.

35. Callmann, C. E.; Barback, C. V.; Thompson, M. P.; Hall, D. J.; Mattrey, R. F.; Gianneschi, N. C., Therapeutic Enzyme-Responsive Nanoparticles for Targeted Delivery and Accumulation in Tumors. *Adv. Mater.* **2015,** *27* (1), 4611-4615.

36. Chien, M.-P.; Carlini, A. S.; Hu, D.; Barback, C. V.; Rush, A. M.; Hall, D. J.; Orr, G.; Gianneschi, N. C., Enzyme-Directed Assembly of Nanoparticles in Tumors Monitored by in Vivo Whole Animal Imaging and ex Vivo Super-Resolution Fluorescence Imaging. *Journal of the American Chemical Society* **2013,** *135* (50), 18710-18713.

37. Chien, M.-P.; Rush, A. M.; Thompson, M. P.; Gianneschi, N. C., Programmable Shape-Shifting Micelles. *Angew. Chem. Int. Ed.* **2010,** *49* (30), 5076-5080.

38. Chien, M.-P.; Thompson, M. P.; Barback, C. V.; Ku, T.-H.; Hall, D. J.; Gianneschi, N. C., Enzyme-Directed Assembly of a Nanoparticle Probe in Tumor Tissue. *Advanced Materials* **2013,** *25* (26), 3599-3604.

39. Nguyen, M. M.; Carlini, A. S.; Chien, M.-P.; Sonnenberg, S.; Luo, C.; Braden, R. L.; Osborn, K. G.; Li, Y.; Gianneschi, N. C.; Christman, K. L., Enzyme-Responsive Nanoparticles for Targeted Accumulation and Prolonged Retention in Heart Tissue after Myocardial Infarction. *Adv. Mater.* **2015**, n/a-n/a.

40. Ku, T.-H.; Chien, M.-P.; Thompson, M. P.; Sinkovits, R. S.; Olson, N. H.; Baker, T. S.; Gianneschi, N. C., Controlling and Switching the Morphology of Micellar Nanoparticles with Enzymes. *J. Am. Chem. Soc.* **2011,** *133* (22), 8392-8395.

41. Jourden, J. L. M.; Daniel, K. B.; Cohen, S. M., Investigation of self-immolative linkers in the design of hydrogen peroxide activated metalloprotein inhibitors. *Chem. Commun.* **2011,** *47* (28), 7968-7970.

42. Agrawal, A.; Romero-Perez, D.; Jacobsen, J. A.; Villarreal, F. J.; Cohen, S. M., Zinc-Binding Groups Modulate Selective Inhibition of MMPs. *ChemMedChem* **2008,** *3* (5), 812-820.

43. Blum, A. P.; Kammeyer, J. K.; Yin, J.; Crystal, D. T.; Rush, A. M.; Gilson, M. K.; Gianneschi, N. C., Peptides Displayed as High Density Brush Polymers Resist Proteolysis and Retain Bioactivity. *Journal of the American Chemical Society* **2014,** *136* (43), 15422-15437.

44. de Gracia Lux, C.; Joshi-Barr, S.; Nguyen, T.; Mahmoud, E.; Schopf, E.; Fomina, N.; Almutairi, A., Biocompatible Polymeric Nanoparticles Degrade and Release Cargo in Response to Biologically Relevant Levels of Hydrogen Peroxide. *Journal of the American Chemical Society* **2012,** *134* (38), 15758-15764.

45. Agrawal, A.; Romero-Perez, D.; Jacobsen, J. A.; Villarreal, F. J.; Cohen, S. M., Zinc-binding groups modulate selective inhibition of MMPs. *ChemMedChem* **2008,** *3* (5), 812-20.

46. Patel, P. R.; Kiser, R. C.; Lu, Y. Y.; Fong, E.; Ho, W. C.; Tirrell, D. A.; Grubbs, R. H., Synthesis and cell adhesive properties of linear and cyclic RGD functionalized polynorbornene thin films. *Biomacromolecules* **2012,** *13* (8), 2546-53.

47. Daniel, K. B. Prodrug Strategies for Metalloenzyme Inhibitors and Molecular Imaging Agents. Dissertation, University of California, San Diego, ProQuest, 2015.

48. Fink, D. W.; Koehler, W. R., pH Effects on fluorescence of umbelliferone. *Analytical Chemistry* **1970,** *42* (9), 990-993.

49. Birnbaum, Y.; Fishbein, M. C.; Blanche, C.; Siegel, R. J., Ventricular septal rupture after acute myocardial infarction. *N Engl J Med* **2002,** *347* (18), 1426-32.

50. Lemery, R.; Smith, H. C.; Giuliani, E. R.; Gersh, B. J., Prognosis in rupture of the ventricular septum after acute myocardial infarction and role of early surgical intervention. *Am J Cardiol* **1992,** *70* (2), 147-51.

51. Pohjola-Sintonen, S.; Muller, J. E.; Stone, P. H.; Willich, S. N.; Antman, E. M.; Davis, V. G.; Parker, C. B.; Braunwald, E., Ventricular septal and free wall rupture complicating acute myocardial infarction: experience in the Multicenter Investigation of Limitation of Infarct Size. *Am Heart J* **1989,** *117* (4), 809-18.

52. Johnson, T. D.; Christman, K. L., Injectable hydrogel therapies and their delivery strategies for treating myocardial infarction. *Expert opinion on drug delivery* **2013,** *10* (1), 59-72.

53. Dorn, G. W., 2nd; Diwan, A., The rationale for cardiomyocyte resuscitation in myocardial salvage. *J Mol Med* **2008,** *86* (10), 1085-95.

54. Mann, D. L., Mechanisms and models in heart failure: A combinatorial approach. *Circulation* **1999,** *100* (9), 999-1008.

Chapter 5

Fatty Acid Conjugates for Albumin-Mediated Transport

5.1 Introduction

Unlike the nanomaterials developed in **Chapter 2-4**, the work discussed in **Chapter 5** utilizes biomolecules, namely long chain fatty acids and HSA, for targeted drug delivery to the TME. Although the materials developed are vastly different, the overall strategy remains the same – increased accumulation of therapeutic cargo in the tumor space by exploiting features of the TME.

As researchers continue the search for novel chemotherapeutic compounds, there remains a large-scale effort to improve the safety and efficacy of those already in the clinic. Many potent therapeutics suffer from severe solubility issues, with nearly 40% of all FDA-approved drugs and more than 60% of all new chemical entities being poorly water soluble[1-3]. This necessitates either the packaging of these materials (BCS Class II and IV) in elaborate carrier systems, or the formulation with non-innocent excipients, which themselves can cause

serious adverse effects[4] in patients. Thus, there remains a dire need for the development of better delivery vehicles for potent, but poorly soluble, chemotherapeutics.

One approach is to use human serum albumin (HSA) as a drug carrier. HSA is the most abundant serum protein, with normal physiological concentrations of 40 mg/mL in the blood and a half-life on the order of ~19 days[5-6]. HSA displays extraordinary ligand binding affinity, and a main function of HSA is to transport both endogenous and exogenous ligands throughout the body. Indeed, specific binding sites on HSA have been identified and characterized for both fatty acids and drugs[7-13]. Further, HSA has been identified as a nutrient source for growing tumors, potentially because the 67kD heart-shaped monomeric protein has 35 cysteine residues, as well as many glutamine residues, that tumors make use of in their metabolic processes[14].

Because HSA is the primary transporter of long-chain fatty acids (LCFAs) throughout the body, the binding and interactions between the serum protein and fatty acids has been extensively studied. Indeed, as many as 7 specific binding pockets have been identified on HSA for LCFAs through nuclear magnetic resonance (NMR) and protein crystallography[7-8, 10-12]. In five of these sites, the carboxylate moiety of the LCFA makes favorable electrostatic interactions with positively-charged arginine and lysine residues lining the base of the pocket of the protein. This interaction is responsible for the exceptionally high binding constants observed. In addition to HSA catabolism, it is becoming increasingly recognized that fatty acids are key nutrient sources in growing and metastasizing tumors[15]. In normal physiology, LCFAs are utilized as fuel sources for ATP generation – a process that is exploited in cancer metabolism[16-18].

Given the relationship between LCFAs, HSA, and tumor metabolism, we reasoned that utilizing the naturally evolved interaction of HSA with LCFAs to transport hydrophobic cargo may provide an elegant solution to chemotherapy's drug problem. Previous development of

fatty acid-drug conjugates conjugate therapeutic cargo has been through the carboxylic acid moiety of the monoacid. The carboxylate is responsible for high-affinity binding to HSA, thus, conjugation at this site inherently diminishes the binding capability of the fatty acid-based material. Further, HSA-based carriers have been developed for paclitaxel[5, 19-23] and other hydrophobic drugs, but the binding of these drugs to HSA is of significantly lower affinity than that of LCFAs. This lower binding affinity allows for these drugs to dissociate from the protein in the blood, which may be partially responsible for the modest increases in tolerability observed in the clinic.

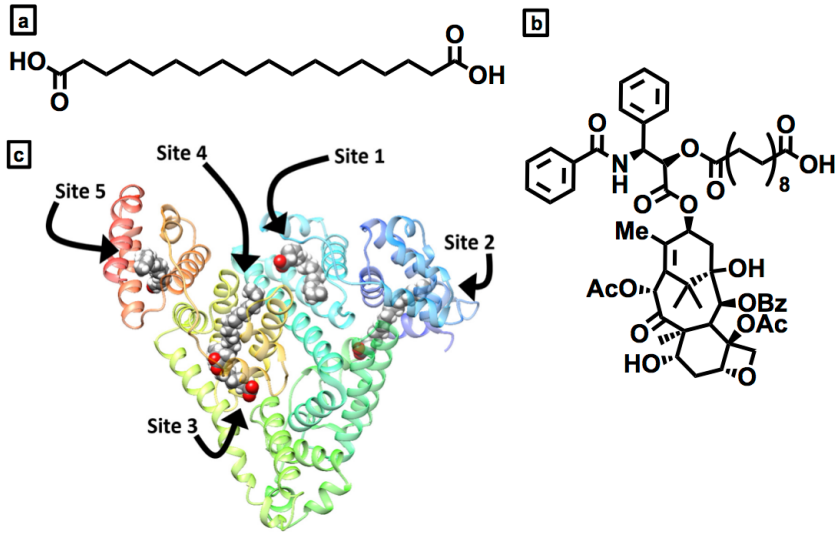

Figure 5.1.1. Materials utilized in Chapter 5. a) Chemical structure of octadecanedioic acid (ODDA). b) Chemical structure of PTX-ODDA ester (**PTXFA**). c) Modeling of **PTXFA** binding to human serum albumin (HSA) in the top 5 most likely binding sites to formulate **VTX**.

We hypothesized that mono-functionalizing the appropriate α,ω-dicarboxylic acid with a hydrophobic drug would preserve the high-affinity binding to HSA and produce a prodrug that is targeted by “hitchhiking” on albumin in the bloodstream. This, in turn, would result in better safety, efficacy, and pharmacokinetics that are more closely matched to that of albumin than of the parent drug. Towards this end, we designed a system where octadecanedioic acid (ODDA) (**Figure 5.1.1a**) is conjugated to paclitaxel (PTX) to produce a mono-functionalized

prodrug ester (**PTXFA**, **Figure 5.1.1b**). We then noncovalently complexed PTXFA with HSA at a mol ratio of 5:1 ligand:protein to generate a water soluble drug delivery system **(VTX**, **Figure 5.1.1c**) and evaluated its potential as a therapeutic *in vivo*.

5.2 Results and Discussion

PTXFA (**Figure 5.1.1a**) was first synthesized through mono-esterification of ODDA with PTX (see **Chapter 5.3** for experimental details), and then combined with HSA in a 5:1 drug:protein ratio to afford an HSA:PTXFA compound, herein denoted as **VTX**. This ratio was chosen based on literature demonstrating 5 high affinity binding sites for LCFAs on HSA[7-8, 10-12]. Other ratios were also investigated, and it was found that all combinations led to soluble protein/drug complexes that did not crash out of solution, even after lyophilization and resuspension (**Figure 5.2.1**).

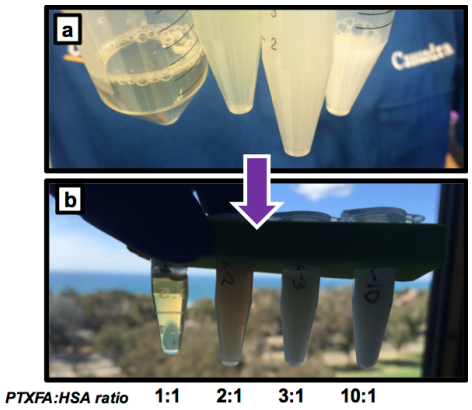

Figure 5.2.1. Formulation of PTXFA with HSA. a) combination of **PTXFA** in t-butanol with HSA in distilled water in 1:1, 2:1, 3:1, and 10:1 ratios (drug:protein), respectively. b) solutions of **VTX** after the materials in panel a are lyophilized (see **Chapter 5.3** for details) and resuspended in 1C DPBS at 25 mg/mL with respect to PTX content. Note: solutions get more opaque as the ratio of drug:protein is increased, but all formulations remain completely dispersed in solution out to 45 days at a range of temperatures (*vide infra*).

The interaction of **PTXFA** with HSA was modeled through docking studies and molecular dynamic simulations. From these investigations, it was determined that sites 1, 2, 4, and 5 were the most likely binding locations (see **Figure 5.2.1c**). These results were compared to models of HSA with stearate, ODDA conjugated to PTX through an extended linkage, mono-methylated ODDA conjugated to PTX through an extended linkage, and ODDA conjugated with methotrexate to serve as a different model compound (**Table 5.2.1**). In all cases, **PTXFA** bound HSA with the highest affinity. To corroborate the simulation results, the displacement of palmitic acid from HSA by **PTXFA** was investigated by ^{13}C-NMR (**Figure 5.2.2a**). Titration of

methylated ODDA conjugated to PTX through an extended linkage, and ODDA conjugated with methotrexate to serve as a different model compound (**Table 5.2.1**). In all cases, **PTXFA** bound HSA with the highest affinity. To corroborate the simulation results, the displacement of palmitic acid from HSA by **PTXFA** was investigated by ^{13}C-NMR (**Figure 5.2.2a**). Titration of **PTXFA** into a pre-equilibrated solution of HSA and ^{13}C-palmitate elucidated the **PTXFA** binding site locations on HSA.

Table 5.2.1. Binding site affinity of PTXFA to HSA vs. other conjugates. The calculated binding affinity of various fatty acid-drug conjugates to HSA using MMBGSA computational binding analyses (see **Chapter 5.4** for methods). In HSA binding sites 1, 2, and 4 (see **Figure 5.1.1c** for locations on HSA), **PTXFA** has a significantly higher binding affinity to HSA than the native ligand stearate. To probe the effect on binding affinity, other compounds, based on a C18 chain length spacer, were evaluated, by changing the length between PTX and ODDA, the oxidation state of the carboxylic acid on ODDA, and by changing warhead.

MMBGSA Binding Affinity (mean + SEM, kcal/mol)

Ligand	Site 1	Site 2	Site 3	Site 4	Site 5
A	-59.0 0.4	-57.5 0.4	-59.6 0.3	-62.2 0.4	-56.0 0.4
B	-90.0 0.9	-76.8 0.9	-49.5 0.6	-75.5 0.7	-67.8 0.6
C	-89.4 0.6	-82.8 0.6	-44.2 0.5	-77.0 0.5	-69.1 0.5
D	-70.1 0.5	-62.5 0.7	-39.5 0.6	-63.2 0.6	-57.2 0.5
E	-77.7 0.5	-75.5 0.5	-49.5 0.5	-63.4 0.5	-62.9 0.6

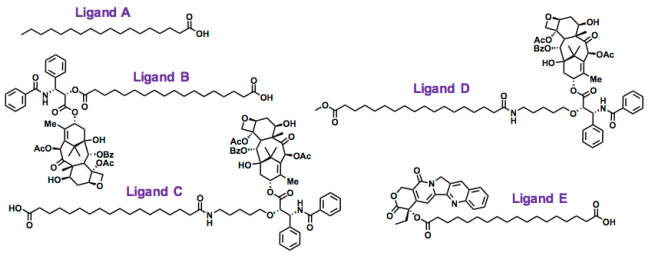

The effect of **PTXFA** on HSA folding and stability was investigated through circular dichroism (CD) (**Figure 5.2.2b-d**). Importantly, **PTXFA** does not affect the folding of HSA up to mol ratios of 10:1 drug: protein, providing further evidence that the interactions of **PTXFA** with HSA mimic those with native LCFAs. Further, the presence of **PTXFA** in solution had no effect on the heating/cooling curve of HSA, indicating that the molecule does not destabilize the protein's tertiary structure.

The stability of PTXFA as a function of pH was also evaluated. As expected, **PTXFA** hydrolyzes under both acidic and basic conditions to afford free PTX in solution. After 24h incubation, complete hydrolysis is observed when the conjugate is incubated at pH=8.0, demonstrating that **PTXFA** is a labile prodrug of PTX (**Figure 5.2.3a**). As the 2'-OH on PPTX through which ODDA is conjugated is necessary as a free hydroxyl for the cytotoxic activity of

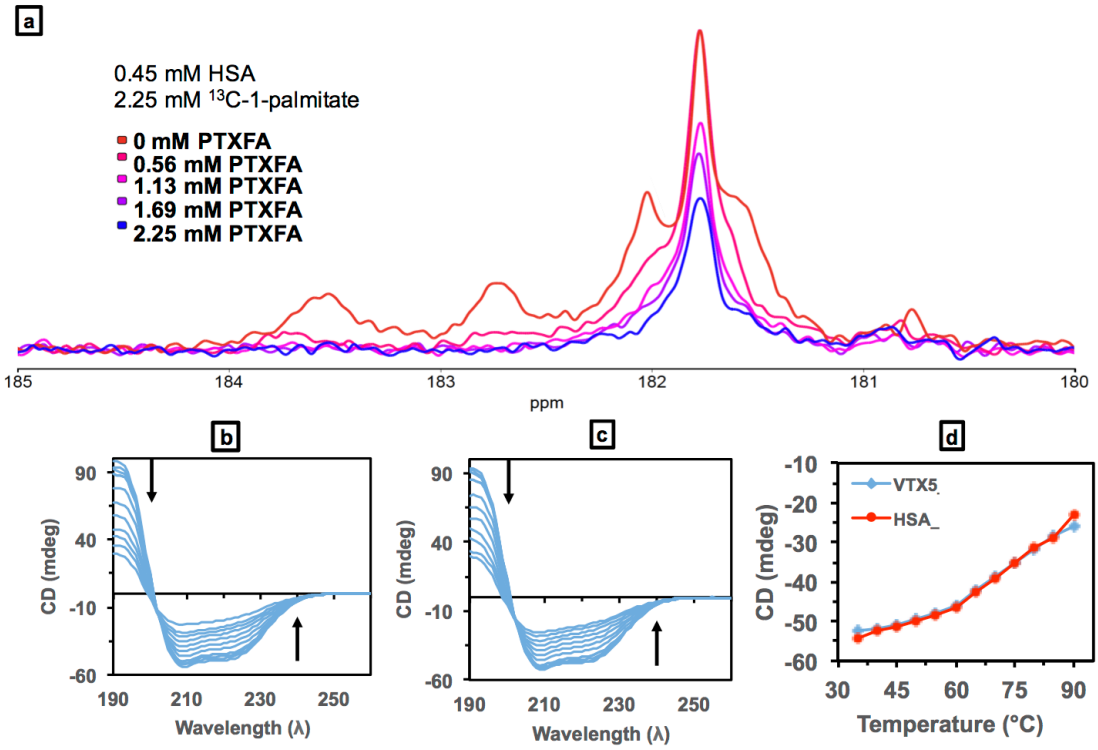

Figure 5.2.2. Experimental Analyses of PTXFA-HSA interactions. a) NMR titration of **PTXFA** into a pre-equilibrated, saturated solution of palmitic-1-^{13}C acid with HSA. **PTXFA** displaces palmitic acid in all sites at concentrations lower than that of the native ligand, demonstrating a high binding affinity of HSA in its binding pockets for LCFAs. b) Heating curve of HSA by circular dichroism from 35 to 90 °C. c) Heating curve of HSA in the presence of **PTXFA.** d). CD signal at 209 nm across the array of temperatures in the heating and cooling curves for HSA and HSA in the presence of **PTXFA**. Minimal divergence is observed over the entire temperature range.

The stability of **PTXFA** when associated with HSA (as **VTX**) was also examined to evaluate the propensity of the material to remain intact during circulation in the bloodstream. The stability of **VTX** was analyzed as a function of pH, temperature, and presence of serum proteins. No degradation of PTXFA was observed when incubated as VTX in DPBS at pH=7.4 and pH=4.0 for 24h (**Figure 5.2.3b**), demonstrating that HSA protects the PTXFA prodrug from pH-based degradation as a drug carrier.

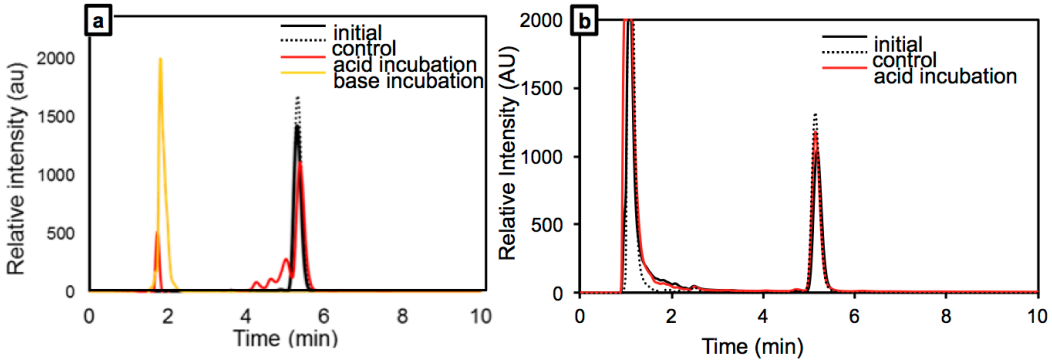

Figure 5.2.3. Stability of PTXFA and VTX to Changes in pH. a) Stability of PTXFA as a small molecule alone in solution as analyzed by HPLC, when incubated in acidic (red trace) or basic (yellow trace) conditions. **PTXFA** elution time is ~5.6 minutes prior to degradation, and major degradation product appears at ~2 min. Major degradation products appear at ~2 min upon incubation at elevated and depressed pH. Solid black trace is of **PTXFA** before any treatments, and control is **PTXFA** after 24 hrs incubation at room temperature in solution. b) Stability of **PTXFA** as formulated with HSA to form **VTX** in solution prior to incubation in acidic pH (solid black trace), after 24 hrs incubation at room temperature in acidic conditions (red trace), and after 24 hrs incubation in neutral solution. Note that no evidence of degradation is observed, unlike in panel a, suggesting that formulation with HSA protects the prodrug from pH-induced hydrolysis.

The cytotoxicity of **PTXFA** and **VTX** in comparison to PTX was evaluated in an array human cancer cell lines, including HeLa (cervical adenocarcinoma), HT-1080 (fibrosarcoma), H522 (lung carcinoma), PANC-1 (pancreas ductal carcinoma), HT-29 (colon colorectal adenocarcinoma), and Hep-G2 (hepatocellular carcinoma). IC_{50} values were obtained for all cell lines (**Table 5.2.2**). Interestingly, a cell-line dependent response for **PTXFA** is observed, with a range IC_{50} values consistent with those of other PTX prodrugs. However, when formulated as **VTX**, all cell lines respond within the same order of magnitude, suggesting that the formulation of the prodrug with HSA may allow for an alternative entry pathway of the drug into the cell.

Table 5.2.2. Representative IC_{50} values in various cell lines. The IC_{50} of **PTXFA**, or **PTXFA** formulated with HSA at 1:1, 2:1, or 5:1 mol ratios.

Cell line	PTXFA	VTX-1	VTX-2	VTX-5
HeLa	57.05	59.00	278.25	25.375
HT-1080	1.11	9.27	47.6	12
HT-29	36.1	16.3	9.24	8.62
PANC-1	1381	283	N/A	9.09
H522	65.8	182	N/A	N/A
HepG2	1.89	N/A	N/A	34.6

The therapeutic potential of **PTXFA** as an anticancer compound *in vivo* was evaluated and its effect on tumor growth and survival when formulated as **VTX** was determined. Initial studies were carried out in the HT-1080 model, as it is a fast-growing tumor and is known to be responsive to taxane therapy[25]. The therapeutic index (TI) of **VTX**, relative to Abraxane® and Cremophor-formulated PTX, where TI was defined as the ratio of maximum tolerated dose (MTD) to minimum effective dose (MED)[26], was evaluated for one specific dosing schedule. MTD was defined as the highest dose that can be delivered without incidence of mortality[27], and MED was defined as the lowest dose that shows a delay in tumor growth, relative to saline-treated animals[28]. Additional efficacy studies were completed in HT-29 and PANC-1 xenograft models to demonstrate the generality of the **VTX** system in multiple tumor models.

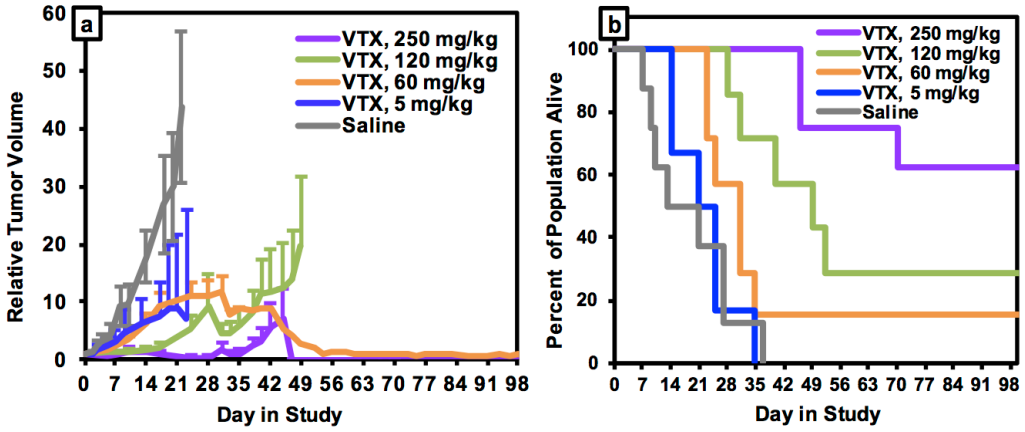

Figure 5.2.5. Dose-Response of VTX in HT-1080 xenografts. a) Effect of VTX on tumor growth in HT-1080 fibrosarcoma xenografts as a function of dose. All doses were administered IV through tail vein, on a q7dx4 dosing schedule. NOTE: Efficacy graphs for each group are truncated once the survival dropped below 50%.

The dose-response of **VTX** was investigated in the HT-1080 model at 5, 20, 60, 125, and 250 mg/kg with respect to PTX content. Doses were IV administered through the tail vein once a week for a total of 4 weeks (q7dx4). Animals responded to **VTX** in a dose-dependent manner (**Figure 5.2.5a**). Excitingly, complete tumor regression or dramatically suppressed progression was observed in most animals administered **VTX** at 250 mg/kg, with no evidence

of drug-associated toxicity observed throughout the course of administration (**Figure 5.2.5b**). Conversely, animals administered Abraxane® at 20 mg/kg with respect to PTX content experienced significant treatment-associated lethality (**Figure 5.2.6a**), so the highest dose of Abraxane® administered in this model was limited to 15 mg/kg. We note that this is contrary to what is reported in several studies[19, 22-23], and associate it to model- and formulation-specific toxicity. Cremophor®-formulated PTX showed similar antitumor activity at 15 mg/kg to that of Abraxane® at 15 mg/kg, and **VTX** at 250 mg/kg (**Figure 5.2.6b**). However, this is the reported MTD of PTX[25, 29] and higher doses in this model have previously resulted in acute toxicity[25].

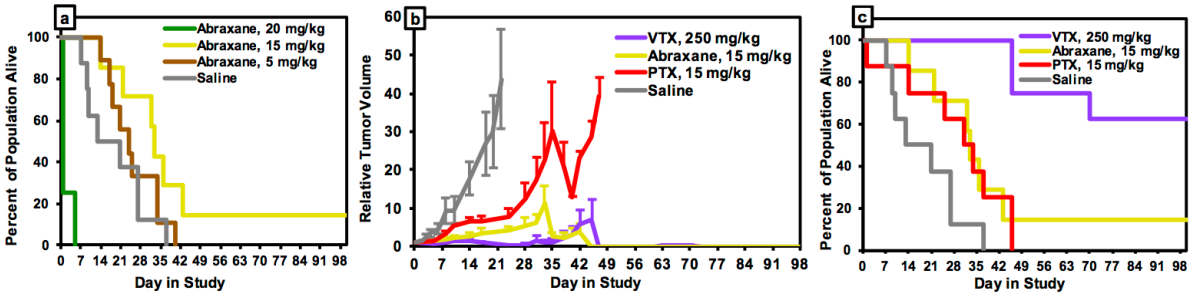

Figure 5.2.6. Further *in vivo* analyses in HT-1080 xenografts. a) Survival curve of animals IV administered Abraxane® at 5 mg/kg (8 animals, brown trace), 15 mg/kg (8 animals, yellow trace), or 20 mg/kg (4 animals, green trace) with respect to PTX content. Significant lethality is observed at the 20 mg/kg dose (3/4 animals died within 24 hr of injection), limiting the MTD of Abraxane® in this model. b) Efficacy of **VTX** versus Abraxane® and Cremophor-formulated PTX as a function of MTD on tumor growth in HT-1080 fibrosarcoma xenografts as a function of dose. All doses were administered IV through tail vein, on a q7dx4 dosing schedule. c) Survival analysis of animals in panel b.

In addition to dose-response, the survival of animals treated with VTX was analyzed in comparison to Abraxane®, Cremophor-formulated PTX, and saline (**Figure 5.2.6c**) following a q7dx4 dosing schedule. From this, it is clear that the elevated doses of **VTX** do not cause acute lethality, and significantly extend survival time over that of non-treated controls, whereas the improvement of survival time for Abraxane® and Cremophor-formulated PTX on survival time was modest. Interestingly, while the lowest administered dose of **VTX** and Abraxane® had similar, negligible effects on median survival time, both were sufficient to suppress tumor

growth relative to saline over the course of the study (**Figure 5.2.7**), which we thus define as the MED for both **VTX** q7dx4 and Abraxane® in this model and at this dosing regime.

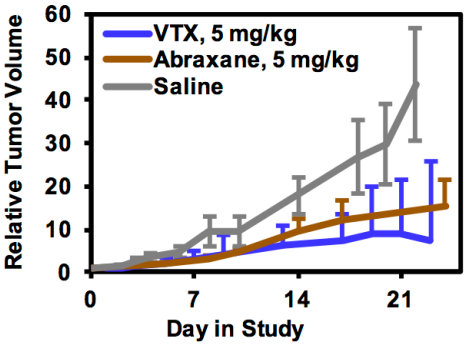

Figure 5.2.7. Efficacy analysis of VTX and Abraxane® at low dose. Both **VTX** and Abraxane® were administered at 5 mg/kg with respect to PTX content via tail vein IV q7dx4. Both were capable of suppressing tumor growth, relative to saline, though the effect is admittedly modest.

In evaluating the efficacy of survival of animals treated with VTX and Abraxane®, we conclude a distinct advantage of our formulation over the FDA-approved drug. In this model, **VTX** had an MED of 5 mg/kg and an MTD of >250 mg/kg with respect to PTX content. Higher doses were unable to be explored due to solubility constraints of HSA used in the formulation of **VTX**. Thus, the TI of **VTX** is >50 in the HT-1080 model at a q7dx4 dosing regime. Conversely, Abraxane®-treated animals experienced significant toxicity at all doses exceeding 15 mg/kg with respect to PTX content (see **Figure 5.2.6a**) so though the MED of Abraxane® was determined to be 5 mg/kg in this model, the TI of Abraxane® in this study is calculated to be 3.

The trends in efficacy observed in the HT-1080 model were also observed in both PANC-1 (pancreatic carcinoma, **Figure 5.2.8a**) and HT-29 (colorectal adenocarcinoma, **Figure 5.2.8b**) xenografts, and saw that **VTX** at 250 mg/kg was well tolerated in both models, and also flat-lined tumor growth. Interestingly, Abraxane® showed no significant therapeutic effect at 15 mg/kg in the PANC-1 model. Thus, we explored a higher dose (30 mg/kg with respect to PTX content) and found that the animals tolerated this dose better than in the HT-1080 model, albeit 2/8 mice did die from drug-associated acute lethality (*vide infra*).

Conversely, Cremophor-formulated PTX could suppress tumor growth quite well, though **VTX** was still superior, as 2 animals showed complete tumor regression. Intriguingly, in the HT-29 model, **VTX** was able to be administered up to 300 mg/kg (due to the average animal mass being large enough to administer a large enough injection volume to reach 300 mg/kg without concern) without any toxicity observed, and with superior efficacy, relative to both Abraxane® and non-treated controls.

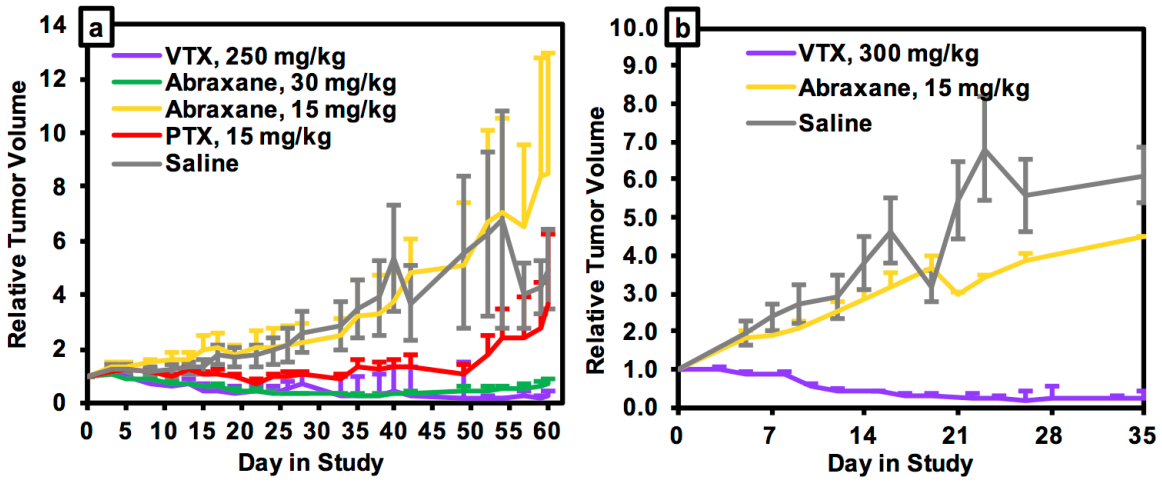

Figure 5.2.8. Efficacy in additional tumor models. a) Effect of treatment on tumor growth in the PANC-1 model. b) Tumor growth in HT-29 model.

In addition to efficacy and survival, the pharmacokinetics (PK) of **VTX** was investigated in healthy and tumor-burdened animals (HT-1080 xenografts), and compared to Abraxane®. For these studies, **VTX** was intravenously administered at 20 mg/kg to healthy and tumor-burdened animals (to examine the effect, if any, of tumor mass on PK and BD), as well as at 250 mg/kg to tumor-burdened animals. Abraxane® was administered at 20 mg/kg to healthy animals for comparison. Blood was drawn from retroorbital sinus prior to injection, and at 1, 2, 4, and 24 hours post-injection, spun down, and plasma obtained for LC/MS/MS analysis to look for the presence of **PTXFA** and any free **PTX** in solution.

4, and 24 hours post-injection, spun down, and plasma obtained for LC/MS/MS analysis to look for the presence of **PTXFA** and any free **PTX** in solution.

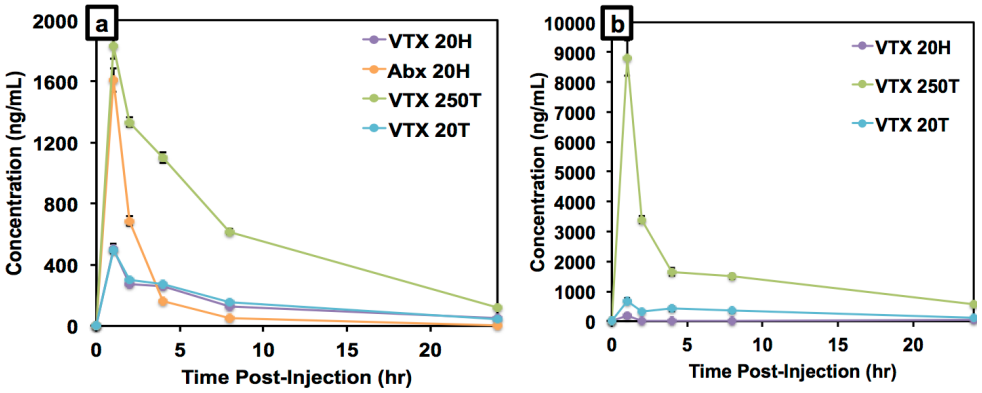

Figure 5.2.9. PK profiles of PTX and PTXFA. a) Blood plasma concentration of PTX in animals following treatment with **VTX** or Abraxane®. Key: VTX 20H = healthy animals administered **VTX** at 20 mg/kg. Abx 20H = healthy animals administered Abraxane® at 20 mg/kg. VTX 20T = tumor-burdened animals administered **VTX** at 20 mg/kg. VTX 250T = tumor-burdened animals administered **VTX** at 250 mg/kg. b) Blood plasma concentration of **PTXFA** in animals following treatment with **VTX**.

At one hour post-injection, both PTX and **PTXFA** are found in plasma samples from animals administered **VTX** (**Figure 5.2.9a-b**), though **PTXFA** is present in much higher concentrations than PTX. Interestingly, the maximum concentration of PTX in animals administered Abraxane® at 20 mg/kg nearly matches that of those administered **VTX** at 250 mg/kg (see **Figure 5.2.9a**). However, the half-life and AUC of PTX in animals treated with **VTX** is much higher than that of Abraxane®, indicating that **VTX** may be acting as a drug depot for the cytotoxin, and slowly releasing it into the bloodstream over time. Calculated PK parameters are shown in **Table 5.2.3**.

Table 5.2.3. Calculated PK parameters. PK parameters were calculated based on the plasma concentrations of PTX and **PTXFA** shown in **Figure 5.2.10**.

	PTX					PTXFA		
Formulation	PTX Dose (mg/kg)	Cmax (ng/mL)	AUC (hr*ng/mL)	Volume of Distribution (mL)	Half-Life (hr)	Cmax (ng/mL)	AUC (hr*ng/mL)	Half-Life (hr)
VTX	250	1919 ± 565	17520 ± 4784	2961 ± 1169	6.59 ± 1.49	9198 ± 5282	61934 ± 39449	10.17 ± 4.67
VTX	20	508 ± 188	4688 ± 797	1257 ± 374	9.80 ± 1.20	678 ± 784	10539 ± 12188	9.32 ± 4.07
Abraxane	20	1607 ± 469	5640 ± 469	481 ± 163	4.39 ± .62	n/a	n/a	n/a

In addition, the biodistribution of **VTX** at 250 mg/kg with respect to PTX content in HT-1080 xenografts was analyzed in comparison to Abraxane® and Cremophor-formulated PTX in tumor, liver, and gallbladder at 1, 4, and 24 hours post-injection (**Figure 5.2.10**). The rationale behind the choice of organs is that Abraxane®, like most other nano-formulations, is known to accumulate in the liver[30-31], and the gallbladder can act as a reservoir of fatty acids[32], and we saw increased accumulation of a gadolinium (Gd)-based ODDA analog developed in our lab (see **Chapter 5.6**).

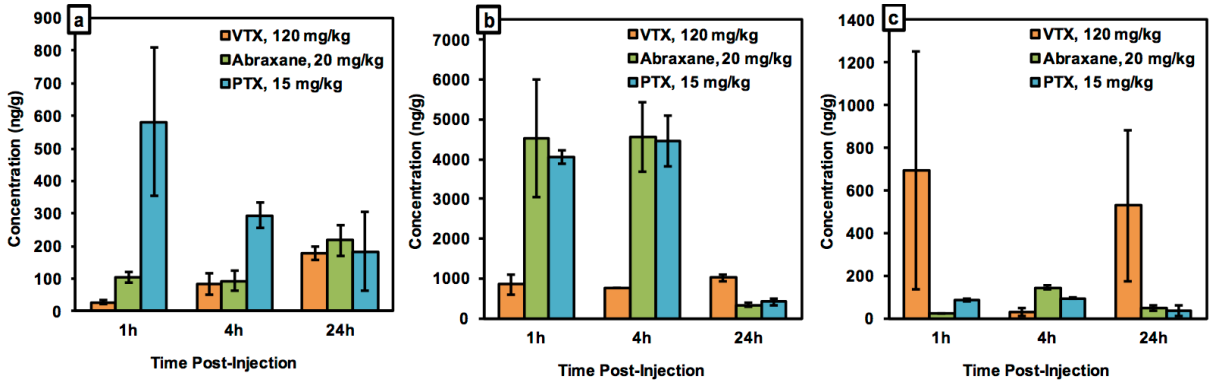

Figure 5.2.10. Biodistribution of PTX in tumor, liver, and gallbladder. a) Concentration of PTX in HT-1080 tumors at 1, 4, and 24 hr post-injection with either **VTX** at 120 mg/kg (orange bars), Abraxane® at 20 mg/kg (green bars), or Cremophor®-formulated PTX (blue bars). b) Concentration of PTX in livers from animals bearing HT-1080 tumors. c) Concentration of PTX in gallbladders from animals bearing HT-1080 tumors.

Though the highest tumor accumulation in all groups studied was in animals administered Cremophor®-formulated PTX (**Figure 5.2.10a**), the tumor concentration of free PTX in animals administered **VTX** steadily increased over the course of the study, whereas it steadily decreased for that of the Cremophor® formulation. Interestingly, minimal distribution in the liver was seen for **VTX**, whereas there was a high level of accumulation for both Abraxane® and Cremophor®-formulated PTX at early timepoints (**Figure 5.2.10b**). It has been proposed that the Cremophor® itself makes that PTX formulation nanoparticle-like in nature[4], so the liver accumulation of this formulation is not surprising. As there is little **VTX** liver

accumulation, it suggests that our formulation is not behaving as a nanoparticle in the body. Finally, there is detectable gallbladder accumulation of PTX in animals administered **VTX** at two of the three timepoints (**Figure 5.2.10c**), which correlates with the accumulation observed of MRI contrast agents developed in our lab that utilize Gd-ODDA conjugates.

5.3 Study Conclusions

In conclusion, we have developed a carrier system for albumin-mediated delivery of PTX to tumor tissue, utilizing the natural interaction between HSA and LCFAs, by monofunctionalizing ODDA with PTX to generate **PTXFA**. PTXFA binds HSA in a manner like native LCFAs, and we can use this to deliver therapeutic payloads of PTX to tumor tissue well beyond the MTD of both Cremophor-formulated PTX and Abraxane®. We have demonstrated impressive efficacy of **VTX** in three xenograft models: HT-1080 (fibrosarcoma), PANC-1 (pancreatic cancer), and HT-29 (colon cancer). Further, the overall survival of animals in the HT-1080 xenograft model is significantly extended when treated with **VTX** at a dose of 250 mg/kg with respect to PTX content. The PK profile of **VTX** is significantly different from that of Abraxane®, as is the biodistribution relative to Abraxane® and Cremophor®-formulated PTX.

Given the relationship between HSA, fatty acids, and the TME (see **Chapter 1.3**), this is an especially interesting strategy for drug delivery, especially to cancers that have increased demands for HSA and fatty acids (see **Chapter 1.3**). Further, the mechanism of internalization of **PTXFA** may be different from that of PTX (see **Chapter 5.2**), which may be of importance in cancers that demonstrate multidrug resistance, where conventional PTX treatment is ineffective[33-34]. Together, the foregoing results represent an important departure from nanoparticle-based drug delivery approaches and takes advantage of nature's own machinery to deliver drugs to tumors.

5.4 Experimental Details

General Materials and Methods: All materials and reagents, unless otherwise noted, were purchased from Sigma Aldrich or Fisher Chemicals. ODDA was graciously provided by Elevance Renewable Sciences, Inc. (Woodridge, Illinois). Abraxane® and clinically formulated PTX as a suspension in 1:1 Cremophor® EL (polyoxyethylated castor oil) to ethanol were graciously donated by UCSD Moores Cancer Center (La Jolla, California). HPLC analyses of all materials were performed on a Jupiter 4u Proteo 90A Phenomenex column (150 x 4.60 mm) with a binary gradient, using a Hitachi-Elite LaChrom 2130 pump that was equipped with a Hitachi-Elite LaChrom L-2420 UV-Vis detector. Separation was achieved with a flow rate of 1 mL min^{-1} and the following mobile phase: 0.1% trifluoroacetic acid in H_2O (buffer A) and 0.1% trifluoroacetic acid in ACN (buffer B). All cell lines were obtained from an in-house sub-culture originally purchased from ATCC. Cells were incubated at 37˚C at 5% CO_2 using DMEM (high glucose, no glutamine, Life Technologies/Gibco, Cat. 11960044) supplemented with 10% FBS (heat inactivated, Omega Scientific, Cat FB-02), and 1x of sodium pyruvate (100x = 100mM, Life Technologies, Cat. 11360070), non-essential amino acids (Life Technologies, Cat. 11140050), GlutaMAX (Life technologies, Cat. 35050061) and antibiotics (Penicillin-Streptomycin, Life Technologies Cat 15140122). Opti-MEM reduced serum medium (Life Technologies, 31985070) was used as is, and DMEM without phenol red (Life Technologies, Cat 31053028) was supplemented as in other DMEM. Cell cultures were maintained by sub-culturing in flasks every 4-7 days when cells became confluent using trypsin-EDTA, 0.25% (Life Technologies, Cat 25200114). Mice (nu/nu) for *in vivo* studies were obtained through the in-house colony at the University of California, San Diego. All animal procedures were approved by UCSD's institutional animal care and use committee (IACUC).

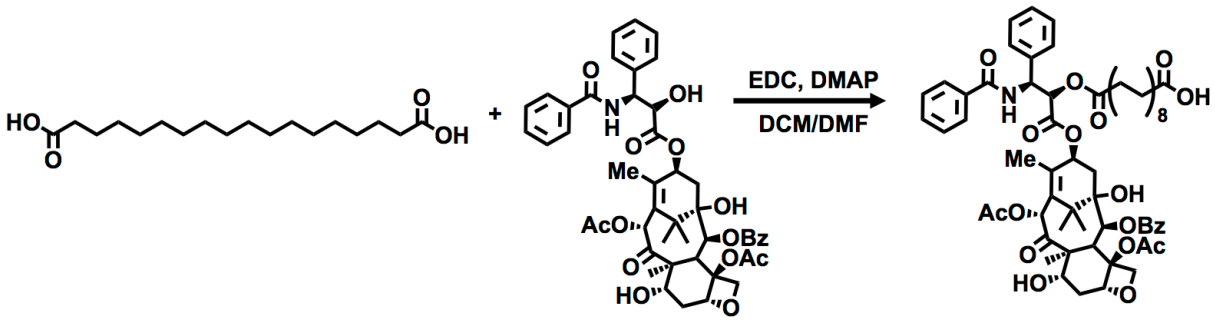

Figure 5.3.1. Synthesis of PTXFA.

Synthesis of PTXFA*: To* a cold solution of PTX (2.00 g, 2.35 mmol) in 100 mL dichloromethane (DCM) was added 4-(dimethylamino)pyradine (DMAP, 573 mg, 4.69 mmol) and EDC (967 mg, 5.04 mmol). The resulting solution was stirred for 5 minutes, at which point ODDA (885 mg, 2.82mmol) in 6 mL N,N-dimethylformamide (DMF) was added, and the reaction stirred overnight under N_2 and allowed to warm to room temperature. Reaction progress was monitored by thin layer chromatography (TLC) in 2:1 hexane:ethyl acetate. Upon complete consumption of PTX, the reaction was stopped and evaporated to dryness under vacuum by rotary evaporation. The crude was taken up in DCM and washed with 1M HCl, and dried over $MgSO_4$.

Preparation of PTXFA with HSA (VTX)*:* To prepare stock solutions, **PTXFA** was dissolved in DCM at a concentration of 0.030075M, and HSA (essentially fatty acid free, lyophilized powder) was dissolved in distilled water at a concentration of 0.0006015M (40.0 mg/mL). To a 50 mL centrifuge tube was added 3.74 mL of the clear colorless **PTXFA** stock solution, followed by rapid addition of 37.40 mL of the clear yellow HSA stock to generate a 5:1 mol ratio of **PTXFA**:HSA solution. Upon initial addition of HSA, solution clouds, but immediately clears, to yield an off-yellow solution. Solution was then vortexed for 10 seconds,

snap frozen under liquid nitrogen, and lyophilized to afford a white powder (**VTX**), which is reconstituted as a clear to slightly turbid off-yellow solution in buffered water (DPBS, Dulbecco's Phosphate Buffered Saline, no Ca and no Mg) to a concentration of 25.0 mg/mL with respect to PTX content.

Dynamic Light Scattering (DLS) Analysis*:* **PTXFA** was formulated with HSA at mol ratios of 1:1, 2:1, 3:1, 4:1, 5:1, 6:1, 7:1, 8:1, 9:1, and 10:1 **PTXFA**:HSA in the same general manner as described above. Solutions were lyophilized overnight, then resuspended in 1.0 mL DPBS and analyzed by DLS to look for formation of precipitates or nanoscale structures.

Circular Dichroism (CD) Studies*:* **PTXFA** was formulated with HSA at mol ratios of 1:1, 2:1, 3:1, 4:1, 5:1, 6:1, 7:1, 8:1, 9:1, and 10:1 **PTXFA**:HSA in the same general manner as described above. Solutions were lyophilized overnight, and then resuspended in 1.0 mL DPBS and analyzed by CD to probe the structure of HSA as a function of mols of **PTXFA** bound.

The effect of **PTXFA** on the stability of HSA was probed by analysis of protein folding as a function of temperature. **VTX** (5:1 mol ratio **PTXFA**:HSA) and HSA were heated from 35°C to 90°C in 5°C increments and the change in their CD spectra was observed. The shift in peak heights at 192 nm and 209 nm were monitored at each temperature and compared to one another between groups (**VTX** vs. HSA).

Modeling Studies: Four conjugate ligands, and additionally stearate, were evaluated using computational binding affinity analysis. Five sites in the HSA protein were selected as the most likely binding locations based on inspection of the PDB:1E7I crystal structure of HSA complexed with stearate. The four conjugate ligands were manually inserted into each of the five HSA binding sites in an analogous manner to stearate binding. Thus four new models were

created, each with HSA complexed to five ligand molecules. Small molecule force field parameters were generated for each ligand using Amber16's GAFF force field and the AM1-BCC charge assignment scheme. The protein was modeled with the FF14SB force field. Each HSA-ligand complex was solvated in 28,000 TIP3P water molecules. Na+ and Cl- ions were added to bring the salt concentration to approximately 150 mM. Following preparation, molecular dynamics simulations were run for each system on GPU hardware using Amber16's pmemd.cuda program. Production simulations consisted of 10 ns of NPT simulation using the Langevin thermostat, Monte Carlo barostat, and default PME parameters. Binding affinity calculation were performed with Amber16's MMPBSA.py program using the simulation trajectories as input. For these calculations, the explicit solvent was removed and modeled implicitly using the igb=8 model and mbondi3 solute radii.

NMR Binding Studies*:* The binding of **PTXFA** to HSA was investigated through ^{13}C-NMR analysis. First, a stock solution of ^{13}C-palmitic acid mixed with HSA at a 5:1 mol ratio (palmitic acid:HSA) was prepared in 1:1 D_2O:H_2O at 30.0 mg/mL with respect to HSA. This solution was prepared by transferring a known amount of palmitic acid to a vial, then adding the appropriate volume of HSA in solution and stirring overnight at room temperature to allow the palmitic acid to associate with HSA and enter solution. After overnight incubation, a clear off-yellow solution was observed. Next, 1.0 mL of the HSA/palmitic acid conjugate was removed to a vial containing 6.18 mg **PTXFA** (to produce a 30:1 mol ratio of **PTXFA**:HSA). This new solution was equilibrated overnight. Both samples (palmitic acid/HSA and **PTXFA**/HSA) were analyzed by ^{13}C-NMR to look for the disappearance of peaks characteristic of palmitic acid binding to HSA.

In Vitro Stability of PTXFA and VTX*:* The stability of **PTXFA** under acidic, basic, and neutral conditions was evaluated and analyzed by HPLC. **PTXFA** was dissolved in organic solvent with either acidic, neutral or basic water added at a low enough concentration such that the small molecule did not precipitate. The control solution in organic solvent did not contain water. The solutions were incubated for 24 hours at room temperature, then analyzed by HPLC for appearance of PTX and **PTXFA**.

A stock solution of **VTX** was prepared at $3x10^{-3}$M in distilled H_2O. From this, three aliquots were prepared at 200 µL each (A, B, and C): A) pH adjusted to 4.0 with HCl; B) pH held at 7.4; and C) pH adjusted to 10.0. Each aliquot was further split into 3x 60 µL samples (1, 2, and 3). Sample 1 (A1, B1, and C1) of each was incubated at 4°C. Sample 2 (A2, B2, and C2) was incubated at 25°C. Sample 3 (A3, B3, and C3) was incubated at 37°C. The remaining 20 µL of each stock solution was diluted to 100 µL with "buffer B" (acetonitrile + 0.1% trifluoroacetic acid) to precipitate the HSA and extract PTX-FA from each sample. The organic phase was then analyzed via HPLC (80% buffer B, 20% buffer A isocratic) to serve as a baseline for degradation. Aliquots (20 µL each) of the test samples (A1, A2, A3, B1, B2, B3, C1, C2 and C3) were removed at 24 and 48 hours, diluted to 100 µL with buffer "B", and analyzed by HPLC.

Cell Viability*:* Cytotoxicity of **PTXFA** and **VTX** was evaluated using the CellTiter Blue (CTB) assay (Promega, cat G8081). Treatments of **PTXFA** were prepared as 1000x serial stock dilutions in DMSO, then diluted into media for 1X, 0.1% DMSO treatment solutions. **VTX** (5:1 mol ratio **PTXFA**:HSA) was prepared as a concentrated solution in DPBS, then diluted in media for treatment solutions. Cells were plated in 96-well plates, 1 day before treatment, at the following densities: HeLa at 3,000 cells/well, HT-1080 at 4,500 cells/well, HT-29 at 7,500 cells/well, PANC-1 at 10,000 cells/well, H522 at 10,000 cells/well, and HepG2 at 4,500 cells/well. After 24 hours, plating media was removed, then treatments of 100uL were added

to the wells. After 3 days, the media was removed and replaced with 100uL complete DMEM without phenol red. At this point, 20uL of CTB reagent was added, and the cells incubated for two hours at 37˚C. Fluorescence was measured at 590nm with excitation at 560nm using a Perkin Elmer EnSpire plate reader. Average background fluorescence of CTB reagent in media without cells was subtracted from average fluorescence readings of the experimental wells (three wells per treatment concentration). Viability was calculated as the average background-subtracted signal in a well compared to that of a negative control well (treatment with vehicle, either 0.1% DMSO/media or media). Viabilities were fit in GraphPad Prism using a non-linear, dose-dependent inhibition curve. Values for IC_{50} reflect the concentration at which the cell death is 50% of the maximum response. The log (IC_{50}) and error in logIC_{50} are reported, and reflects the standard error in the fit.

Pharmacokinetics in HT-1080*:* For pharmacokinetic evaluation, nu/nu mice, some bearing HT-1080 xenografts (average tumor volume between 50-150 mm^3), were intravenously (IV) administered **VTX** at doses of 250 and 20 mg/kg with respect to PTX (n=6/group). An additional set of 6 healthy animals was administered Abraxane® at 20 mg/kg. Blood samples were collected prior to treatment, as well as at 1, 2, 4, 7, and 24 hours post-injection. Plasma was isolated by centrifuging the blood and taking the supernatant. The plasma samples were extracted with DCM and analyzed by LC-MS/MS for presence of free PTX and PTXFA.

Biodistribution in HT-1080: Nu/nu mice bearing HT-1080 xenografts were intravenously administered **VTX** at 250 mg/kg, Abraxane® at 20 mg/kg, or Cremophor®-formulated PTX at 15 mg/kg (n=9 per group). All doses were calculated with respect to PTX content of the formulations. At 1,4,and 24 hours post injections, 3 mice per group were sacrificed, perfused, and organs collected. Tumor, liver, and gallbladder were snap-frozen

under liquid nitrogen. Samples of each organ (~100 mg of tissue per organ) was weighed out, cut up, and homogenized with homogenizing beads (~100 mg of beads per sample) by 8 cycles of vortexing for 30 seconds, followed by 30 seconds of rest. Organ samples were then further extracted with DCM and analyzed by LC-MS/MS by the UCSD MS Core facility for presence of free PTX and PTX-FA.

Efficacy and Survival in HT-1080: Nu/nu were inoculated with ~10^6 HT-1080 cells on the right flank, and treatments began when average animal tumor burden was between 50 and 150 mm^3. Animals anesthetized with isoflurane with an induction dose of 3% and a maintenance dose of 1.5% in an oxygen gas stream and intravenously (IV) administered VTX, saline, Cremophor®-formulated paclitaxel, or Abraxane® via tail vein, as a single push over the course of 30 seconds, at a range of doses once weekly for a total of four injections (q7dx4). Absolute tumor volume was measured by calipers and approximated by the formula:

$$V=\frac{l*w^2}{2}$$

Where "*V*" is the absolute tumor volume on the day of measurement, "*l*" is the longest length of the tumor (in mm), and "*w*" is the shortest width across the center of the tumor (in mm). Tumor volume and animal mass ere measured three times weekly. Relative tumor volume was determined by the formula:

$$V_{relative} = \frac{V}{V_i} * 100$$

Where "*V*" is the absolute tumor volume on the day of measurement and "V_i" is the absolute tumor volume on the first day of treatment. Animals were sacrificed when they appeared moribund, lost greater than 20% of their weight at the start of the experiment, or when tumor burden exceeded 1500 mm^3.

Efficacy in HT-29 and PANC-1*:* Nu/nu were inoculated with either ~10^6 HT-29 cells or ~10^6 PANC-1 cells on the right flank, and treatments began when average animal tumor burden was between 50 and 150 mm^3. Animals were anesthetized with isoflurane as above and intravenously (IV) administered VTX, saline, Cremophor®-formulated paclitaxel, or Abraxane® via tail vein, as a single push over 30 seconds, at their respective MTD for a total of four injections (q7dx4). Absolute tumor volume and relative tumor volume was approximated by the equations above. Tumor volume and animal mass ere measured three times weekly. Animals were sacrificed when they appeared moribund, lost greater than 20% of their weight at the start of the experiment, or when tumor burden exceeded 1500 mm^3.

5.5 Perspectives and Future Studies

Chapter 5 describes the design, synthesis, and evaluation of a novel nonparticulate drug carrier system based on naturally evolved interactions between long-chain fatty acids (LCFAs) and Human Serum Albumin (HSA). Mono-functionalizing octadecanedioic acid (ODDA) with paclitaxel affords a fatty acid-paclitaxel ester prodrug (**PTXFA**) that retains one carboxylic acid moiety to form strong, stable electrostatic interactions with HSA in its natural binding sites for LCFAs. This prodrug is capable of binding to HSA and shows differentiated pharmacokinetics, as well as remarkable tolerability and efficacy *in vivo*, relative to both Cremophor-formulated paclitaxel and Abraxane® in multiple tumor models. While this is a promising insight into the potential of this system, there are several other studies using this system that warrant investigation.

For example, as stated in **Chapter 3.3**, there is evidence to suggest that combination therapy of chemotherapeutics alongside immunotherapeutics may provide a greater anti-tumor efficacy than either therapy alone. One especially attractive aspect of the design described in **Chapter 5** for drug delivery is that the association of the fatty acid to HSA should be warhead independent, as the warhead is designed to sit on the surface of HSA, while the fatty acid is buried in the protein. Therefore, it is possible to design other prodrugs using this motif. Indeed, we have synthesized an ODDA conjugate of the immunotherapeutic 1V209 that was utilized in **Chapter 3** (for a discussion of the ODDA conjugate, see **Chapter 5.6**) which makes it possible to look at combination efficacy of PTX with 1V209, using this delivery mechanism. Additionally, because the MTD of **VTX** is much higher than Abraxane® and Cremophor®-formulated PTX, this may provide a strategy for combination therapy with other immunotherapeutics, such as checkpoint inhibitors, using doses that are currently unachievable by either of the other formulations. Indeed, collaborative work is ongoing on this front.

The studies detailed in **Chapter 5.2** utilize a dosing schedule that is once a week for 4 weeks, but there may be a more optimal schedule that has not yet been explored. We chose this schedule based on consultation with clinical oncologists to closely mimic the schedule used in the clinic. This provided exemplary efficacy, but it is possible that different dosing schedules may provide even faster tumor obliteration, and thus warrants investigation.

Further, the full toxicity profile of **PTXFA** and **VTX** warrants a full investigation. Although no acute, overt toxicity was observed at any of the doses examined, and at minimum, a more thorough histopathological analysis of the drug delivery system should be completed. Peripheral neuropathy and neurotoxicity is a main toxicological concern for paclitaxel[35], thus this is an additional toxicological parameter that could be considered. Also, little attention has been paid by the field of cancer therapy in general to the effect of treatment on fertility and offspring viability, which makes this parameter an especially interesting pursuit. Indeed, collaborations to examine the effect of **VTX** on fertility are being currently proposed.

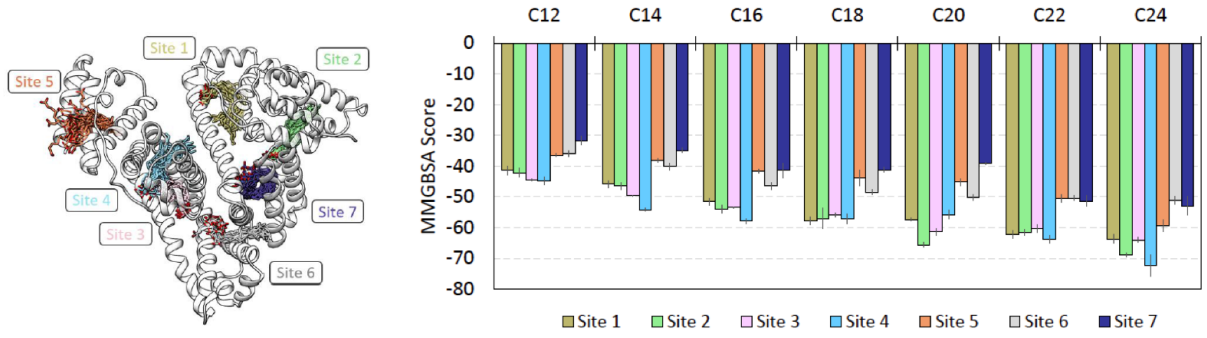

Figure 5.5.1. Binding affinity of various fatty acid lengths. (*top*) Depiction of 25 evenly spaced snapshots from a 200 ns simulation of C18 fatty acids bound to each of the seven HSA binding sites. The HSA structure is the coordinate averaged structure from the simulation. Each site is labeled and the color corresponds the colored FAs. (*bottom*) The MMGBSA binding score for each FA carbon length (from C12 – C24) at each of the seven binding sites on HSA. The colored bars correspond to the site colors at top. The uncertainties are standard error of the mean. The more negative the binding score, the better binder the ligand is.

Finally, although ODDA has proven to be an exemplary di-carboxylic acid for the conjugation of PTX and binding of HSA, it is possible that prodrugs of PTX with dicarboxylic acids of different carbon chain lengths may bind HSA better, or may provide different PK and BD parameters, based on their affinity to HSA. Indeed, modeling analysis by the Gilson lab have indicated that longer dicarboxylic acid-PTXFA conjugates should bind HSA even better (**Figure 5.5.1**). However, these ligands may bind HSA *too* well, and thus negatively impact the MED. Further, although shorter chain dicarboxylic acid-PTX complexes aren't predicted to bind HSA as well as **PTXFA**, there may be a tradeoff between HSA-binding capability and efficacy. However, this will almost certainly alter the toxicity of the material, if the system is truly mediated by HSA transport.

5.6 Other Fatty Acid Conjugates

Although the focus of the work detailed in **Chapter 5** is based on development of PTX-based ODDA conjugates, there are several other systems and areas of research surrounding the development of ODDA-based materials for HSA-mediated drug delivery to the TME that the dissertation author has been involved in.

For example, the utilization of ODDA-immunotherapeutic conjugates have been explored. Briefly, 1V209 (the same immunotherapeutic utilized in **Chapter 3**) was conjugated to ODDa and evaluated for its capability to act as an immunotherapeutic after binding murine serum albumin (MSA). The goal of this work was to utilize the favorable interactions between serum albumin and the ODDA-1V209 conjugate (**immuno-FA**) to safely deliver small molecule immune activators to tumor tissue. We hypothesized that this approach may achieve higher intratumoral concentrations of 1V209 than the free drug could achieve on its own, potentially without activating the immune system nonspecifically. Towards this end, we evaluated **immuno-FA** in vitro in RAW 246.7 macrophages and saw that it had nearly identical immunotherapeutic capability as the parent molecule (**Figure 5.6.1**).

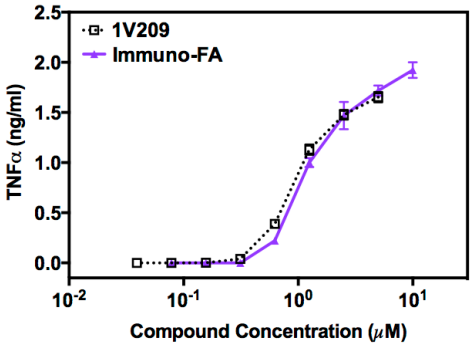

Figure 5.6.1. *In vitro* cytokine upregulation. TNFα release was evaluated by ELISA after incubation with 1V209 and **immuno-FA**. No change in cytokine release levels was observed, indicating that modifying 1V209 with ODDA does not affect its potency.

Further, we have completed an initial *in vivo* study in healthy Balb-C animals, to examine the PD parameters of **immuno-FA**, post IV injection. From this study, we have found

that administration of **immuno-FA** results in upregulation of IP-10, IL-6, and IL-12 (**Figure 5.6.2a**). We have also completed an initial *in vivo* dose-finding study in C3H/HeOuJ mice with SCC-7 murine syngeneic head and neck squamous cancer model to examine the efficacy of **immuno-FA** at different dosages, when administered as conjugates with MSA, intratumorally daily for 5 days. From this, we found that 30 ng of compound was sufficient to potentiate tumor growth, relative to saline (**Figure 5.6.2b**). Additionally, preliminary efficacy studies in the 4T1 model that mimic those in **Chapter 3** demonstrated no evidence of toxicity at elevated doses of 1V209, unlike the parent molecule (**Figure 5.6.2c**).

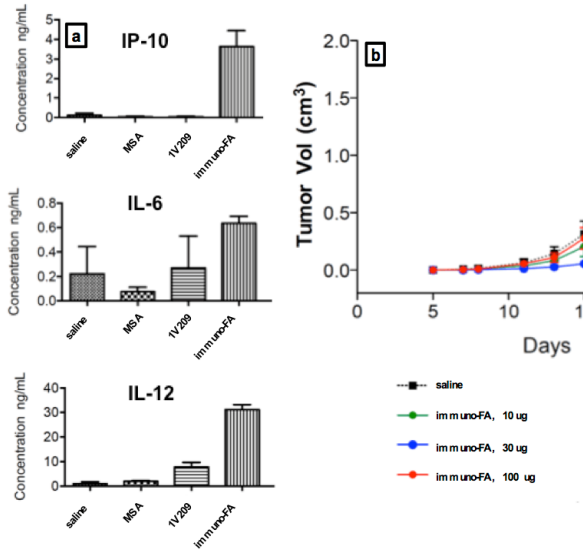

c

Treatment	Dose	Acute Toxicity
1V209	10 µg	0/7
	30 µg	0/7
	60 µg	3/7
Immuno-FA (with MSA)	10 µg	0/7
	30 µg	0/7
	60 µg	0/7

Figure 5.6.2. Pilot *in vivo* studies on immuno-FA. a) Results of cytokine upregulation assays for IP-10, IL-6, and IL-12. b) Initial dose-response efficacy study following IT injection of **immuno-FA** in SCC-7 syngeneic model. c) Mortality analysis following IV injection into mice bearing 4T1 tumors.

Efforts to identify key transporters or effectors of uptake of nanoparticles and other materials have typically focused on a small number of known receptors. However, as many transport families (such as the solute carrier (SLC) family of membrane transport proteins) remain understudied, it is likely that such efforts will miss many novel uptake mechanisms[36]. Therefore, to identify the key factors controlling uptake of HSA in an unbiased, genome-wide

manner, we applied the recently described pooled CRISPR screening technique, which enables the creation of a pool of cells where each human gene is deleted.Using flourescein-labeled HSA, we can then simply ask which gene deletions are no longer capable of proper uptake of HSA (measured by the lack of fluorescence in fluorescence-activated cell sorting (FACS)). Towards this end, fluorescein-conjugated HSA was generated through NHS-based chemistry and non-covalently conjugated with a Cy5-ODDA conjugate, HepG2 (liver cancer) cells were treated with this complex, and sorted based on their uptake of HSA, Cy5-ODDA, both, or neither. These populations are undergoing further analysis to identify the genes responsible for uptake of both of these materials.

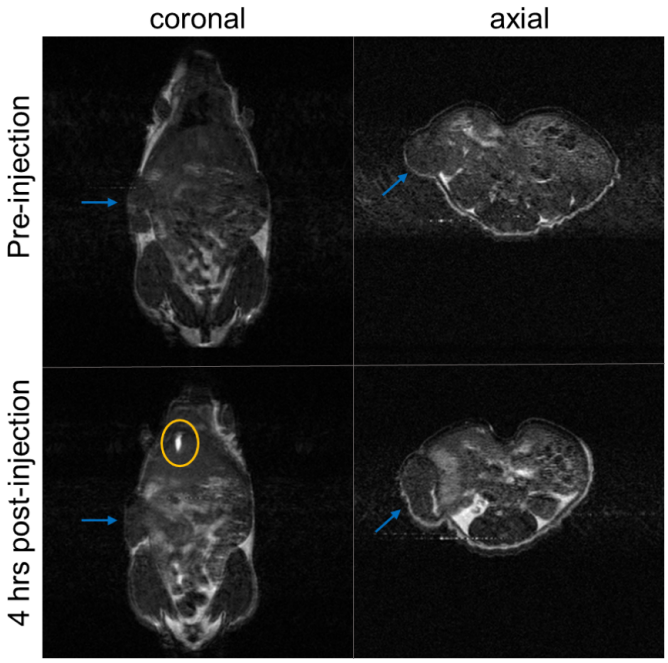

Figure 5.6.3. *In vivo* imaging of Gd-ODDA. Imaging of Gd-ODDA at 4 hours post injection (bottom two panels), compared to pre-injection (top two panels). This is one mouse representative of the group receiving VT-Gd. Blue arrows indicate tumor, yellow circle highlights the signal intensity in gall bladder.

The utility of this system as a delivery vehicle has also been explored for MRI contrast agents. Specifically, a Gd-ODDA conjugate was synthesized, and evaluated *in vivo* in HT-1080 xenografts (**Figure 5.6.3**). The fact that the highest accumulation of material is seen in the gallbladder is what spurred the BD investigations of **VTX** at the end of **Chapter 5.2**. Further,

RNA-ODDA conjugates have shown promise in extending blood circulation half-lives, relative to their RNA counterparts (**Figure 5.6.4**).

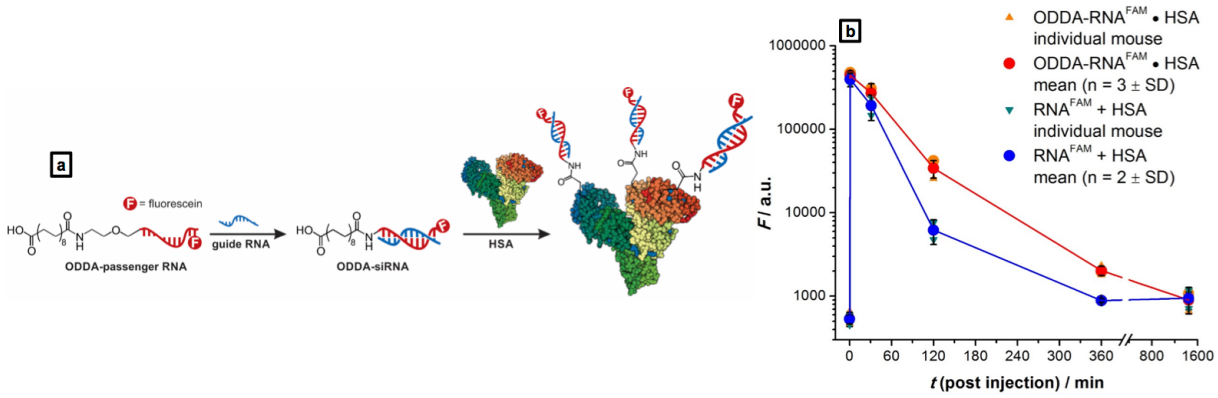

Figure 5.6.4. Analysis of RNA-ODDA conjugates. a) Schematic of fluorescently labelled ODDA-RNA, designated as **ODDA-RNA^{FAM}**. The materials are designed to noncovalently bind HSA in the same manner as **PTXFA**. b) Plasma concentration of **ODDA-RNA^{FAM}** in healthy, nu/nu mice, in comparison to the parent RNA.

5.7 Acknowledgements

Chapter 5 is adapted, in part, from material currently being prepared for submission for publication. Callmann, Cassandra; Thompson, Matthew; Barback, Christopher; LeGuyader, Clare; Hennis, Robert; Henrickson, Niel; Jeremko, Matthew; Chan, Warren; Momper, Jeremiah; Bertin, Paul; and Nathan Gianneschi. The dissertation is the primary author of this pending manuscript.

5.8 References

1. Savjani, K. T.; Gajjar, A. K.; Savjani, J. K., Drug Solubility: Importance and Enhancement Techniques. *ISRN Pharmaceutics* **2012,** *2012*, 195727.

2. Sareen, S.; Mathew, G.; Joseph, L., Improvement in solubility of poor water-soluble drugs by solid dispersion. *International Journal of Pharmaceutical Investigation* **2012,** *2* (1), 12-17.

3. Gupta, S.; Kesarla, R.; Omri, A., Formulation Strategies to Improve the Bioavailability of Poorly Absorbed Drugs with Special Emphasis on Self-Emulsifying Systems. *ISRN Pharmaceutics* **2013,** *2013*, 848043.

4. Gelderblom, H.; Verweij, J.; Nooter, K.; Sparreboom, A., Cremophor EL: the drawbacks and advantages of vehicle selection for drug formulation. *European journal of cancer (Oxford, England : 1990)* **2001,** *37* (13), 1590-8.

5. Merlot, A. M.; Kalinowski, D. S.; Richardson, D. R., Unraveling the mysteries of serum albumin—more than just a serum protein. *Frontiers in Physiology* **2014,** *5*, 299.

6. Kragh-Hansen, U., Structure and ligand binding properties of human serum albumin. *Danish medical bulletin* **1990,** *37* (1), 57-84.

7. Curry, S.; Brick, P.; Franks, N. P., Fatty acid binding to human serum albumin: new insights from crystallographic studies. *Biochimica et biophysica acta* **1999,** *1441* (2-3), 131-40.

8. Curry, S.; Mandelkow, H.; Brick, P.; Franks, N., Crystal structure of human serum albumin complexed with fatty acid reveals an asymmetric distribution of binding sites. *Nature structural biology* **1998,** *5* (9), 827-35.

9. Petitpas, I.; Bhattacharya, A. A.; Twine, S.; East, M.; Curry, S., Crystal Structure Analysis of Warfarin Binding to Human Serum Albumin: ANATOMY OF DRUG SITE I. *Journal of Biological Chemistry* **2001,** *276* (25), 22804-22809.

10. Simard, J. R.; Zunszain, P. A.; Ha, C. E.; Yang, J. S.; Bhagavan, N. V.; Petitpas, I.; Curry, S.; Hamilton, J. A., Locating high-affinity fatty acid-binding sites on albumin by x-ray crystallography and NMR spectroscopy. *Proceedings of the National Academy of Sciences of the United States of America* **2005,** *102* (50), 17958-17963.

11. Simard, J. R.; Zunszain, P. A.; Hamilton, J. A.; Curry, S., Location of high and low affinity fatty acid binding sites on human serum albumin revealed by NMR drug-competition analysis. *Journal of molecular biology* **2006,** *361* (2), 336-51.

12. Zunszain, P. A.; Ghuman, J.; McDonagh, A. F.; Curry, S., Crystallographic Analysis of Human Serum Albumin Complexed with 4Z,15E-Bilirubin-IXα. *Journal of molecular biology* **2008,** *381* (2), 394-406.

13. van der Vusse, G. J., Albumin as fatty acid transporter. *Drug metabolism and pharmacokinetics* **2009,** *24* (4), 300-7.

14. Stehle, G.; Sinn, H.; Wunder, A.; Schrenk, H. H.; Stewart, J. C.; Hartung, G.; Maier-Borst, W.; Heene, D. L., Plasma protein (albumin) catabolism by the tumor itself--implications for tumor metabolism and the genesis of cachexia. *Critical reviews in oncology/hematology* **1997,** *26* (2), 77-100.

15. Pascual, G.; Avgustinova, A.; Mejetta, S.; Martín, M.; Castellanos, A.; Attolini, C. S.-O.; Berenguer, A.; Prats, N.; Toll, A.; Hueto, J. A.; Bescós, C.; Di Croce, L.; Benitah, S. A., Targeting metastasis-initiating cells through the fatty acid receptor CD36. *Nature* **2016,** *541*, 41.

16. Carracedo, A.; Cantley, L. C.; Pandolfi, P. P., Cancer metabolism: fatty acid oxidation in the limelight. *Nature reviews. Cancer* **2013,** *13* (4), 227-32.

17. Hirschey, M. D.; DeBerardinis, R. J.; Diehl, A. M. E.; Drew, J. E.; Frezza, C.; Green, M. F.; Jones, L. W.; Ko, Y. H.; Le, A.; Lea, M. A.; Locasale, J. W.; Longo, V. D.; Lyssiotis, C. A.; McDonnell, E.; Mehrmohamadi, M.; Michelotti, G.; Muralidhar, V.; Murphy, M. P.; Pedersen, P. L.; Poore, B.; Raffaghello, L.; Rathmell, J. C.; Sivanand, S.; Vander Heiden, M. G.; Wellen, K. E., Dysregulated metabolism contributes to oncogenesis. *Seminars in cancer biology* **2015,** *35 Suppl*, S129-s150.

18. Vander Heiden, M. G.; Cantley, L. C.; Thompson, C. B., Understanding the Warburg Effect: The Metabolic Requirements of Cell Proliferation. *Science* **2009,** *324* (5930), 1029-1033.

19. Desai, N. P.; Trieu, V.; Hwang, L. Y.; Wu, R.; Soon-Shiong, P.; Gradishar, W. J., Improved effectiveness of nanoparticle albumin-bound (nab) paclitaxel versus polysorbate-based docetaxel in multiple xenografts as a function of HER2 and SPARC status. *Anti-cancer drugs* **2008,** *19* (9), 899-909.

20. Elsadek, B.; Kratz, F., Impact of albumin on drug delivery--new applications on the horizon. *Journal of controlled release : official journal of the Controlled Release Society* **2012,** *157* (1), 4-28.

21. Kratz, F., Albumin as a drug carrier: design of prodrugs, drug conjugates and nanoparticles. *Journal of controlled release : official journal of the Controlled Release Society* **2008,** *132* (3), 171-83.

22. Miele, E.; Spinelli, G. P.; Miele, E.; Tomao, F.; Tomao, S., Albumin-bound formulation of paclitaxel (Abraxane(®) ABI-007) in the treatment of breast cancer. *International Journal of Nanomedicine* **2009,** *4*, 99-105.

23. Zhao, M.; Lei, C.; Yang, Y.; Bu, X.; Ma, H.; Gong, H.; Liu, J.; Fang, X.; Hu, Z.; Fang, Q., Abraxane, the Nanoparticle Formulation of Paclitaxel Can Induce Drug Resistance by Up-Regulation of P-gp. *PLOS ONE* **2015,** *10* (7), e0131429.

24. Rowinsky, E. K.; Donehower, R. C., Paclitaxel (taxol). *The New England journal of medicine* **1995,** *332* (15), 1004-14.

25. Callmann, C. E.; Barback, C. V.; Thompson, M. P.; Hall, D. J.; Mattrey, R. F.; Gianneschi, N. C., Therapeutic Enzyme-Responsive Nanoparticles for Targeted Delivery and Accumulation in Tumors. *Advanced Materials* **2015,** *27* (31), 4611-4615.

26. Muller, P. Y.; Milton, M. N., The determination and interpretation of the therapeutic index in drug development. *Nat Rev Drug Discov* **2012,** *11* (10), 751-761.

27. Institute, N. C. NCI Dictionary of Cancer Terms: Maximum Tolerated Dose. https://www.cancer.gov/publications/dictionaries/cancer-terms?cdrid=572160 (accessed 3 Jan).

28. Mach, C. M.; Mathew, L.; Mosley, S. A.; Kurzrock, R.; Smith, J. A., Determination of minimum effective dose and optimal dosing schedule for liposomal curcumin in a xenograft human pancreatic cancer model. *Anticancer research* **2009,** *29* (6), 1895-9.

29. Huang, G. S.; Lopez-Barcons, L.; Freeze, B. S.; Smith, A. B.; Goldberg, G. L.; Horwitz, S. B.; McDaid, H. M., Potentiation of Taxol Efficacy by Discodermolide in Ovarian Carcinoma Xenograft-Bearing Mice. *Clinical Cancer Research* **2006,** *12* (1), 298-304.

30. Longmire, M.; Choyke, P. L.; Kobayashi, H., Clearance Properties of Nano-sized Particles and Molecules as Imaging Agents: Considerations and Caveats. *Nanomedicine (London, England)* **2008,** *3* (5), 703-717.

31. Blanco, E.; Shen, H.; Ferrari, M., Principles of nanoparticle design for overcoming biological barriers to drug delivery. *Nature biotechnology* **2015,** *33* (9), 941-951.

32. Tsai, C. J., Steatocholecystitis and fatty gallbladder disease. *Digestive diseases and sciences* **2009,** *54* (9), 1857-63.

33. Gottesman, M. M.; Fojo, T.; Bates, S. E., Multidrug resistance in cancer: role of ATP–dependent transporters. *Nature Reviews Cancer* **2002,** *2*, 48.

34. Podolski-Renić, A.; Anđelković, T.; Banković, J.; Tanić, N.; Ruždijić, S.; Pešić, M., The role of paclitaxel in the development and treatment of multidrug resistant cancer cell lines. *Biomedicine & Pharmacotherapy* **2011,** *65* (5), 345-353.

35. Scripture, C. D.; Figg, W. D.; Sparreboom, A., Peripheral Neuropathy Induced by Paclitaxel: Recent Insights and Future Perspectives. *Current Neuropharmacology* **2006,** *4* (2), 165-172.

36. Cesar-Razquin, A.; Snijder, B.; Frappier-Brinton, T.; Isserlin, R.; Gyimesi, G.; Bai, X.; Reithmeier, R. A.; Hepworth, D.; Hediger, M. A.; Edwards, A. M.; Superti-Furga, G., A Call for Systematic Research on Solute Carriers. *Cell* **2015,** *162* (3), 478-87.